

Zika virus M protein as a viroporin drug target

Emma Tabitha Brown

Submitted in accordance with the requirements for the degree of Doctor of
Philosophy

The University of Leeds

Faculty of Medicine and Health

August 2020

The candidate confirms that the work submitted is their own and that appropriate credit has been given where reference has been made to the work of others.

Chapter 4

Figure 4.4 Grids stained by myself and transmission electron microscopy (TEM) images generated by Dr Daniel Maskell and Dr Rebecca Thompson

Figure 4.6 Images taken by Dr Daniel Maskell and Dr Rebecca Thompson, processing carried out by myself.

Figure 4.17 *In vivo* assay carried out by Dr Daniella Lefteri and Dr Clive McKimmie, sample processing carried out by myself.

Chapter 5

Figure 5.3 Identification of binding sites carried out by Dr Ravi Singh, Dr Stephen Griffin and by myself.

Figure 5.4 Docking and images generated by Dr Ravi Singh using PyMOL and Maestro

Table 5.2 & 5.3 High-throughput screen carried out by Ravi Singh using Maestro

Figure 5.7- 5.12 Maestro interaction images generated by Dr Ravi Singh

Acknowledgements

Thank you to my supervisor Dr Stephen Griffin for all his support throughout my PhD, encouraging and believing in me. Thank you to my co-supervisor Dr Antreas Kalli for joining my supervisory team, your MD training and endlessly answering my questions. I would also like to thank co-supervisors Dr Clive McKimmie and Dr Richard Foster for your support. Thank you to Dr Ravi Singh for your help using the modelling software and carrying out the *in silico* docking. Thank you to Dr Daniella Lefteri for carrying out the *in vivo* work. Thank you to Dr Daniel Maskell and Dr Rebecca Thompson for providing the TEM images. Thank you to Griffin group members Dr Matthew Bentham, Dr Abigail Bloy and Hannah Beaumont for your technical help throughout my first couple of months, answering my questions and ongoing moral support with lots of cups of tea and cake. Thank you also to newer group member Alex Kilvington, I wish you the best of luck in the future. Thank you to all the lovely people on level 5 who made my time enjoyable with endless support and baked goods! Thank you to Hyde Park Harriers for encouraging me to get out running on an evening and weekends, but most importantly for the amazing friendships and memories. I would like to thank all my friends and family for the support over the years. A special thank you to my parents Sally and Mick for your support and encouragement throughout my higher education. Last but not least, thank you to Brad for being understanding, cheering me up and ensuring that, outside of the lab and writing I got out for plenty of climbing adventures.

Abstract

Zika virus (ZIKV) an arbovirus that became widely known in 2015 due to the epidemic in Brazil, spreading across South and North America. Whilst previous Old World ZIKV outbreaks comprised largely mild, or even asymptomatic infections, the New World epidemic became notorious for its association with foetal microcephaly following maternal infection, and an increased incidence of various neurological symptoms, including Guillain-Barré syndrome.

Mature, infectious ZIKV particles comprise three structural proteins, Capsid (C), small Membrane (M) and the envelope (E) glycoprotein; the latter is responsible for receptor binding and mediates membrane fusion upon encountering low pH within the acidifying endosome. However, the function of M within this context is unknown.

Based upon its structural similarity to “viroporins”, a class of virus-coded ion channels mediating virus entry and uncoating, we investigated whether M could form alternative oligomeric forms to the dimeric structure seen within mature virions, and in so doing exhibit channel activity. Gratifyingly, M peptides adopted higher order structures within membrane-mimetic environments and displayed channel activity *in vitro*, sensitive to the prototypic viroporin inhibitor, Rimantadine. Accordingly, ZIKV entry was blocked in a dose-dependent fashion by the drug, which also prevented virus spread in mouse models of ZIKV infection. Molecular dynamics simulations supported that M protein is able to oligomerise into a hexameric viroporin channel, opening of which was within acidified environments via protonation of a conserved histidine residue. Rimantadine was predicted *in silico* to interact at a luminal binding site, against which we derived improved inhibitors from a library of generic, FDA-approved and other bio-active small molecules, providing a basis for novel M protein targeted drug discovery. Significantly, due to its role during virus entry, M-targeted drugs might either prevent or reduce the severity of ZIKV infections, including those crossing the placenta, and may also show activity against closely related M proteins from other *Flaviviruses*.

Table of Contents

Acknowledgements	ii
Abstract	iii
Table of Contents	iv
Table of Figures	viii
Abbreviations	xii
Chapter 1 Introduction	1
1.1 Flaviviruses	1
1.2 Zika virus (ZIKV).....	1
1.2.1 Origin and Discovery	1
1.2.2 Transmission.....	2
1.2.3 Symptoms	5
1.3 Epidemiology	6
1.4 Molecular biology of Zika virus (ZIKV).....	11
1.4.1 Zika virus genome structure	11
1.4.2 Zika virus structural proteins	11
1.4.3 Zika virus Non-structural proteins.....	21
1.5 Zika virus life cycle	29
1.5.1 Entry.....	29
1.5.2 Translation	33
1.5.3 Polyprotein processing.....	34
1.5.4 Virus genome replication.....	35
1.5.5 Capping.....	36
1.5.6 Virus assembly, budding, maturation and release.....	36
1.6 ZIKV model systems.....	38
1.7 Vaccines.....	39
1.8 Antivirals and pharmacological disease management.....	39
1.9 M protein as an antiviral target	41
1.9.1 M protein structure and function.....	41
1.10 Viroporins	42
1.10.1 Influenza A Virus (IAV) M2.....	44
1.10.2 Hepatitis C Virus (HCV) p7.....	46
1.10.3 Human immunodeficiency Virus type-1 (HIV-1) Vpu	48
1.10.4 Human Respiratory Syncytial Virus (hRSV) SH	49

1.10.5	Human Papillomavirus type 16 (HPV-16) E5	50
1.10.6	Enterovirus VP4	51
1.11	Aims	52
Chapter 2 Materials and Methods		53
2.1.1	Zika Virus	53
2.2	Mammalian Cell Culture	53
2.2.1	Recovery of frozen cells	53
2.2.2	Maintenance and Passage of Cells	53
2.2.3	Freezing cells	53
2.2.4	MTT Assay	54
2.2.5	EGF Uptake Assay	54
2.2.6	Immunofluorescence	54
2.3	Virus production and storage	55
2.3.1	Virus stock propagation	55
2.3.2	Freezing virus	55
2.3.3	Determination of Virus Titre	55
2.3.4	Virus assays	56
2.4	Preclinical <i>in vivo</i> models of ZIKV replication	56
2.5	Protein Biochemistry	57
2.5.1	Western blot	57
2.5.2	Native PAGE	58
2.5.3	Coomassie-blue staining	59
2.5.4	M peptide	59
2.6	<i>In vitro</i> liposome assay	59
2.6.1	Liposome preparation	59
2.6.2	End-point <i>in vitro</i> M protein liposome dye release assay	60
2.6.3	Inhibitor assays	60
2.6.4	pH Liposome assay	60
2.6.5	Lipids	61
2.6.6	Transmission Electron Microscopy	61
2.7	Molecular Dynamics	61
2.7.1	Coarse-grained simulations	61
2.7.2	Atomistic Simulations	62
2.7.3	Design of Hexamer and Heptamers	63
Chapter 3 <i>In silico</i> modelling of M protein		64
3.1	Introduction	64

3.2	<i>In silico</i> predictions of M protein secondary structure	69
3.3	Modelling M protein monomers <i>in silico</i>	73
3.3.1	Is M protein stable as a one or two transmembrane domain M protein in a POPC bilayer?	76
3.3.2	Is M protein stable as a two transmembrane domain protein (Model-1) in a representative <i>Flavivirus</i> virion bilayer?	80
3.4	Dimerisation of M protein <i>in silico</i>	82
3.4.1	M protein forms stable dimers in standard POPC bilayers	82
3.4.2	Dimerisation of M protein in WNV virion composition bilayer differs to a POPC bilayer.....	86
3.4.3	Restraining M protein conformation during dimerisation alters dimer class preferences	89
3.5	Simulating M protein channels <i>in silico</i>	94
3.5.1	Which TMD helix lines the M protein pore?.....	98
3.5.2	Are hexameric channels with pores lined by Helix 3 stable? .	98
3.5.3	Are channels with Helix 2 lining the pore stable?	122
3.6	Discussion	139
Chapter 4 M protein displays pH activated, rimantadine-sensitive, channel activity with a role during ZIKV entry		149
4.1	Introduction.....	149
4.2	ZIKV M protein forms oligomers in detergent micelles	153
4.2.1	M protein oligomerises in DHPC detergent	153
4.2.2	Visualisation of ZIKV M peptide oligomers by Transmission Electron Microscopy (TEM)	156
4.3	M peptides mediate dose-dependent release of carboxyfluorescein from liposomes	160
4.3.1	ZIKV M protein channel activity is enhanced at acidic pH...	162
4.4	M peptide channel activity displays sensitivity to Rimantadine <i>in vitro</i> 164	
4.5	Rimantadine mediates dose-dependent inhibition of ZIKV in cell culture.....	167
4.5.1	Rimantadine does not affect cell cytotoxicity or endocytic uptake of EGF	170
4.5.2	Rimantadine suppresses ZIKV replication in cell culture.....	170
4.5.3	Rimantadine targets an early stage of the ZIKV life cycle ...	174
4.6	Rimantadine inhibits ZIKV infection <i>in vivo</i>	176
4.7	Discussion	179
Chapter 5 Rational development of improved inhibitors targeting M protein channel activity		188
5.1	Introduction.....	188

5.2	M protein shows differential sensitivity to structurally distinct viroporin inhibitors	191
5.3	Identification of candidate drug binding sites and docking of adamantanes into M protein channel models <i>in silico</i>	194
5.4	Identification and HTS targeting of peripheral and luminal binding sites	198
5.4.1	Screening <i>in silico</i> selected compounds using dye release assays	198
5.4.2	<i>In silico</i> docking of generic hits into ZIKV M viroporin model	206
5.4.3	Testing selected screened compounds in cell culture	213
5.5	Discussion	218
Chapter 6 Final Conclusion.....		222
Appendix		263
	Appendix A Recipes.....	263
	Appendix B Supplementary Data	266
	Simulating M protein in the absence of the second TMD	266
	B.2 Simulating heptameric M protein channels <i>in silico</i>	268

Table of Figures

Figure 1.1 ZIKV transmission cycles schematic	3
Figure 1.2 Evolutionary timescales of ZIKV.....	8
Figure 1.3 ZIKV nucleotide and amino acid alignments	9
Figure 1.4 Countries and territories showing the spread of ZIKV (2013-2016)	10
Figure 1.5 ZIKV genome organisation schematics	13
Figure 1.6 Flavivirus maturation.....	15
Figure 1.7 E protein	18
Figure 1.8 Flavivirus membrane fusion schematic.....	19
Figure 1.9 Mature and Immature ZIKV structure	20
Figure 1.10 NS1 Structures	22
Figure 1.11 ZIKV NS5 Structure.....	28
Figure 1.12 Conformational states of the dengue virus E protein.....	33
Figure 1.13 IAV M2 as a proton transporter.....	44
Figure 3.1 Amino acid sequence alignment of <i>Flavivirus</i> M proteins ...	66
Figure 3.2 Cryo-EM structure of ZIKV E and M protein within the virion membrane.....	67
Figure 3.3 M protein dimer structure.....	68
Figure 3.4 Single TMD predictions of the ZIKV M protein structure from TMHMM, TOPCONS and Phobius servers.	71
Figure 3.5 Two TMD predictions of the ZIKV M protein structure from SPLIT and MEMSAT-SVM servers.	72
Figure 3.6 Structure and protein sequence of ZIKV M protein truncation	74
Figure 3.7 Simulation system of coarse-grained MD simulations of the M protein monomer	75
Figure 3.8 Monomeric M protein is not stable as a single TMD protein in a POPC lipid bilayer.....	78
Figure 3.9 Monomeric M protein with two TMDs is stable in a POPC bilayer	79
Figure 3.10 Monomeric M protein with two TMDs is stable in a WNV derived lipid bilayer	81
Figure 3.11. M protein dimerises in a POPC bilayer	84
Figure 3.12 Dimerisation analysis of monomers in a POPC bilayer	85
Figure 3.13 Dimerisation analysis of monomers in a <i>Flavivirus</i> derived lipid bilayer.....	87
Figure 3.14 M protein dimerises in a <i>Flavivirus</i> composed lipid bilayer.....	88

Figure 3.15 Dimerisation analysis of restrained monomers in a POPC lipid bilayer.....	92
Figure 3.16 Dimerisation analysis of restrained monomers in a <i>Flavivirus</i> derived lipid bilayer	93
Figure 3.17 Hexameric channel conformations based on dimeric classes.....	96
Figure 3.18 Simulation system visualisation of M protein channel.....	97
Figure 3.19 M protein amino acid properties determined by EMBOSS Pepinfo.....	100
Figure 3.20 Starting conformations of hexameric 'radial' channel with pore lined by Helix 3.....	101
Figure 3.21 Hexameric helix 3 pore-lining 'radial' channel luminal residues	102
Figure 3.22 200 ns conformation of hexameric 'radial' channel with pore lined by helix 3.....	103
Figure 3.23 Helix 3 pore lining radial start and end conformation overlay	105
Figure 3.24 Hexameric Helix 3 pore-lining 'compact' channel, starting conformations.....	108
Figure 3.25 Hexameric helix 3 pore-lining 'compact' channel luminal residues	109
Figure 3.26 Hexameric Helix 3 pore-lining 'compact' channel conformations after 200 ns simulation	110
Figure 3.27 Helix 3 pore lining compact start and end conformation overlay	112
Figure 3.28 Hexameric Helix 3 pore-lining 'radial' protonated channel starting conformations.....	115
Figure 3.29 Hexameric Helix 3 pore-lining 'radial' protonated channel conformation after 200 ns simulation	116
Figure 3.30 Hexameric Helix 3 pore-lining 'compact' protonated channel starting conformations.....	118
Figure 3.31 Hexameric Helix 3 pore-lining 'compact' protonated channel conformation after 200 ns simulation	119
Figure 3.32 Hexameric helix 3 pore lining channel simulations with truncated helix 1	121
Figure 3.33 Hexameric Helix 2 pore-lining 'radial' channel starting conformations.....	123
Figure 3.34 Hexameric helix 2 pore-lining 'radial' channel luminal residues and comparison of radial and compact conformations.	124
Figure 3.35 Hexameric Helix 2 pore-lining 'radial' channel conformation after 200 ns simulation.....	125
Figure 3.36 Hexameric Helix 2 pore-lining 'compact' channel starting conformations.....	128

Figure 3.37 Hexameric helix 2 pore-lining 'compact' channel luminal residues.....	129
Figure 3.38 Hexameric Helix 2 pore-lining 'compact' channel conformation after 200 ns simulation	130
Figure 3.39 Hexameric Helix 2 pore-lining 'radial' protonated channel starting conformations.....	133
Figure 3.40 Hexameric Helix 2 pore-lining 'radial' protonated channel conformation after 200 ns simulation	134
Figure 3.41 Hexameric Helix 2 pore-lining 'compact' protonated channel starting conformations.....	136
Figure 3.42 Hexameric Helix 2 pore-lining 'compact' protonated channel conformation after 200 ns simulation.....	137
Figure 4.1 Schematic comparing phospholipid structures	152
Figure 4.2 M peptide of 55 amino acids with an N terminal truncation	154
Figure 4.3 Oligomerisation of M protein in detergent environment by native PAGE	155
Figure 4.4 M oligomerisation at varying DH(6)PC concentrations, visualised by TEM.....	158
Figure 4.5 Pore diameter of M protein oligomers in a detergent environment	159
Figure 4.6 Oligomerisation of M protein in detergent environment by Transmission Electron Microscopy	159
Figure 4.7 M peptide displays channel activity in the liposome-based assay when reconstituted in DMSO.	161
Figure 4.8 The effect of pH titration on M protein channel activity	163
Figure 4.9 Rimantadine has a dose-dependent effect on M protein-mediated CF release	165
Figure 4.10 Rimantadine at 1 μ M reproducibly reduces M protein-mediated CF release	166
Figure 4.11 Optimisation of ZIKV specific antibodies for western blot and immunofluorescence	168
Figure 4.12 Optimisation of ZIKV antibodies by western blot.....	169
Figure 4.13 The effect of Rimantadine on cell viability.....	171
Figure 4.14 Rimantadine does not effect the uptake of fluorescently labelled EGF	172
Figure 4.15 Rimantadine has a dose-dependent effect on ZIKV infection in cell culture.....	173
Figure 4.16 Rimantadine targets entry step of virus life cycle shown by time of addition plaque assay.....	175
Figure 4.17 Rimantadine reduces viral titres of ZIKV infected mice ...	178
Figure 5.1 Representative JK compound chemical composition	192

Figure 5.2 Inhibition of M protein channel activity by small molecules	193
Figure 5.3 Identified drug binding sites on <i>in silico</i> M protein hexameric model	196
Figure 5.4 Docking of adamantane compounds into the luminal 1 site of optimal hexameric M protein <i>in silico</i> model	197
Figure 5.5 Inhibition of M peptide channels by lumen-targeting compounds using liposome-based channel activity assay	203
Figure 5.6 Inhibition of M peptide channels by peripherally targeting compounds using liposome-based channel activity assay	205
Figure 5.7 GNF 5837 and M protein predicted interaction data	207
Figure 5.8 GSK 2837808A and M protein predicted interaction data ...	208
Figure 5.9 KB SRC 4 and M protein predicted interaction data	209
Figure 5.10 AA 29504 and M protein predicted interaction data	210
Figure 5.11 L-732, 183 and M protein predicted interaction data	211
Figure 5.12 Formoterol and M protein predicted interaction data	212
Figure 5.13 The effect of lumen-targeting TOCRIS selected compounds on cell viability	214
Figure 5.14 The effect of peripherally targeting TOCRIS selected compounds on cell viability	215
Figure 5.15 Effects of selected TOCRIS compounds on viral titre	217

Abbreviations

λ_{ex}	Excitation wavelength
λ_{em}	Emission wavelength
$^{\circ}\text{C}$	Degrees centigrade
2D	Two dimensional
2K	2000Dalton protein
3'	Three prime
3D	Three dimensional
5'	Five prime
Å	Angstrom
aa	Amino acid(s)
ADE	Antibody mediated enhancement
<i>A. aegypti</i>	<i>Aedes Aegypti</i>
<i>A. albopictus</i>	<i>Aedes Albopictus</i>
<i>A. hensilli</i>	<i>Aedes hensilli</i>
<i>A. polynesiensis</i>	<i>Aedes polynesiensis</i>
AIDP	Acute Inflammatory Demyelinating Polyradiculoneuropathy
AMAN	Acute motor axonal neuropathy
ATP	Adenosine triphosphate
AXL	Axl receptor tyrosine kinase
BCA	Bicinchoninic acid
BHK-21	Baby hamster kidney cells 21
BLMs	Bilayer lipid membranes or black lipid membranes
bp	Base pairs
BSA	Bovine serum albumin
C	Capsid protein
C	Carboxyl
cDNA	Copy deoxyribonucleic acid
Ci	Intracellular Capsid protein
CD	Conductance domain
CD1	Cluster of differentiation 1
CF	Carboxyfluorescein
CG	Coarse-grained
CHIKV	Chikungunya virus
cHP	Capsid hairpin
CMC	Critical micellar concentration
CO ₂	Carbon dioxide
CPE	Cytopathic effect
Da	Dalton(s)
DAXX	Death Domain Associated Protein
DC-SIGN	Dendritic Cell-Specific Intercellular adhesion molecule-3-Grabbing Non-integrin
ddH ₂ O	Distilled deionised water
DDX56	DExD-Box Helicase 56

DENV	dengue Virus
DH(7)PC	1,2-diheptanoyl-sn-glycero-3-phosphocholine
DH(6)PC	1,2-dihexanoyl-sn-glycero-3-phosphocholine
DMEM	Dulbecco's modified Eagle's medium
DMSO	Dimethyl sulfoxide
DNA	Deoxyribose nucleic acid
dNTP	Deoxynucleoside triphosphate
ds	Double-stranded
DTT	Dithiothreitol
EBC	Enriched Broth Culture
ECL	Enhanced chemiluminescence
<i>E.coli</i>	Escherichia coli
ED	Ectodomain
EDTA	Ethylenediaminetetra-acetic acid
EGF	Epidermal growth factor
EGFR	Epidermal growth factor receptor
EM	Electron microscopy
E protein	Envelope protein
ER	Endoplasmic reticulum
ERK	Extracellular regulated kinase
FCS	Foetal calf serum
FRET	Fluorescence resonance energy transfer
g	Grams
<i>g</i>	Gravitational force
GBS	Guillain-Barré syndrome
GFP	Green fluorescent protein
GST	Glutathione-S-transferase
GTP	Guanosine triphosphate
H ⁺	proton(s)
HA	Hemagglutinin
HCoV-229	human coronavirus 229
HCV	Hepatitis C virus
HDM2	Mouse double minute 2
HEPES	N-2-hydroxyethylpiperazine-N'-2-ethanesulfonic acid
HIV-1	Human immunodeficiency virus 1
HMA	5-N(N-Hexamethylene)amiloride
HMM	hidden Markov model
Hpi	hours post infection
HPLC	High performance liquid chromatography
HPV(-16)	human papillomavirus (type 16)
hr	Hour(s)
HRP	Horseradish peroxidase
HRSV	Human respiratory syncytial virus
HRV	Human rhinovirus
Hsp70	Heat shock protein 70
HSV	Herpes simplex virus

HTS	High-throughput screen
IAV	Influenza A virus
IBV	Influenza B virus
IFN	Interferon
IL	Interleukin
INSANE	INSert membrANE
IPTG	Isopropyl- β -D-thiogalactopyranoside
IRES	Internal ribosome entry site
IRF	Interferon regulatory factor
ISRE	Interferon-Stimulated Response Element
JEV	Japanese Encephalitis Virus
JAK	Janus kinase
KUNV	Kunjin Virus
LARP	La-related protein 1
LB	Luria Bertani
LPPG	1-palmitoyl-2-hydroxy-sn-glycero-3-phospho-(1'-rac-glycerol)
LMPG	1-myristoyl-2-hydroxy-sn-glycero-3-phospho-(1'-rac-glycerol)
LY6E	lymphocyte antigen 6E
LYAR	Ly1 Antibody Reactive
μ g	Microgram(s)
μ g/ μ L	Microgram(s) per microlitre
μ g/mL	Microgram(s) per millilitre
μ m	Micrometre(s)
μ M	Micromolar
m7G	N-7 methylguanosine
M	Membrane protein
M	Molar
MAPK	Mitogen activated protein kinase
mg	Milligram(s)
mL	Millilitre(s)
MAC	Membrane Attack Complex
MAPK	Mitogen-activated protein kinase
MD	Molecular Dynamics
MDA5	melanoma differentiation-associated protein 5
MHV	mouse hepatitis virus
min	Minute(s)
mM	Millimolar
mNS1	membrane associated NS1
mRNA	messenger RNA
MT	Methyltransferase
MTT	(3-(4,5-dimethylthiazol-2-yl)-2,5-diphenyltetrazolium bromide)
MV006	Mark Verow compounds 006
MW	Molecular weight

N	Amino
NA	Neuraminidase
NFκB	Nuclear factor kappa beta
ng	Nanogram(s)
nM	Nanomolar
NGDN	neuroguidin
NHP	Non-human primate
nm	Nanometre(s)
NMR	Nuclear magnetic resonance
MN-DNJ	<i>N</i> -(<i>n</i> -Nonyl)deoxynojirimycin
NS	Non-structural
nt	nucleotide(s)
OD ₆₀₀	Optical density measured at 600 nm
ORF(s)	Open reading frame(s)
PA	Phosphatidic acid
PABP	poly-(A) binding protein
PBS	Phosphate buffered saline
PBSA	PBS with BSA
PC	Phosphatidylcholine
PCR	Polymerase chain reaction
PDB	Protein Data Bank
PFA	Paraformaldehyde
PFU	Plaque forming unit
pH	-log ₁₀ concentration of hydrogen ions
POPC	1-palmitoyl-2-oleoyl-sn-glycero-3-phosphocholine
POPE	1-Palmitoyl-2-oleoyl-sn-glycero-3-phosphoethanolamine
POPS	1-palmitoyl-2-oleoyl-sn-glycero-3-phospho-L-serine
prM	Precursor Membrane protein
RIG-I	retinoic acid-inducible gene I
PVDF	Polyvinylide fluoride
RdRp	RNA-dependent RNA polymerase
RMSD	Root mean square deviation
RMSF	Root mean square fluctuation
RNA	Ribose nucleic acid
RSV	Respiratory Syncytial virus
RT	Room Temperature
RTPase	RNA 5' triphosphatase
RV	Rotavirus
s	second(s)
SAR	Structure Activity Relationship
SDS	Sodium dodecyl sulphate
SDS-PAGE	Sodium dodecyl sulphate polyacrylamide gel electrophoresis
sfRNA	subgenomic <i>Flavivirus</i> RNA
SH	Small hydrophobic protein
SL	Stem-loop

SM	sphingomyelin
Ss	single-stranded
STAT	Signal transducer and activator of transcription
SVM	support vector machines
TASK	Twik-related acid sensitive K ⁺
TBEV	Tick-borne encephalitis virus
TBS	Tris buffered saline
TBST	Tris buffered saline containing 0.1 % v/v Tween-20
TBK1	Tank-Binding Kinase 1
TEM	Transmission electron microscopy
TGN	<i>Trans</i> -Golgi network
TIM-1	T-cell immunoglobulin and mucin domain 1
TLR3	Toll-like receptor 3
TLR8	Toll-like receptor 8
TM	<i>Trans</i> -membrane
TMD	<i>Trans</i> -membrane Domain
TNF	Tumour Necrosis Factor
Tyro3	Tyrosine-protein kinase receptor
UPF1	Regulator of nonsense transcripts 1
UPR	unfolded protease response
UTR	Untranslated region
UV	Ultraviolet
V	Volts
VCP	Valosin-Containing Protein
VLP	Virus-like particle
vRNPs	Viral ribonucleoprotein complexes
vsRNA	Virus-derived small interfering RNAs
v/v	Volume per unit volume
w/v	Weight per unit volume
WNV	West Nile Virus
XRN1	RNA exonuclease protein 5'-3' exoribonuclease 1
YFV	Yellow Fever Virus
ZC3HAV1	Zinc Finger CCCH-Type Containing Antiviral 1
ZIKV	Zika Virus

Chapter 1 Introduction

1.1 Flaviviruses

The *Flavivirus* genus within the *Flaviviridae* family comprises many viruses, all of which possess a genome with a unique 5' cap feature (m⁷GpppAmp). The positive sense viral single-stranded genomic RNA encodes an approx. 3000 kDa polyprotein, which is processed by both viral and host proteases. All have three structural proteins C, E and prM/M which organise to form the enveloped virion, along with the genomic RNA. There are also seven non-structural proteins encoded by the genome: NS1, NS2A, NS2B, NS3, NS4A, NS4B and NS5, which enable viral replication.

Flaviviruses are transmitted predominantly by arthropods and are known as arboviruses (arthropod-borne), utilising their capabilities to jump between hosts. Over half of *Flaviviruses* have been linked to human pathogenesis; many are well-known including yellow fever virus (YFV), dengue virus (DENV) and Zika virus (ZIKV). These infections often cause symptoms related to the central nervous system, fever, rashes and haemorrhagic fever. Fewer *Flaviviruses* are also known to cause pathogenesis in other animals including rodents.

There are over 50 *Flavivirus* species, yet there are currently only three viruses with commercial vaccines: first introduced in 1937 the YFV 17D vaccine (Theiler and Smith, 1937), the Tick-borne Encephalitis virus (TBEV) vaccine (Kunz et al., 1976) then Japanese encephalitis virus vaccine (Yun and Lee, 2014). However, highly pathogenic and prevalent *Flaviviruses* including well-known DENV, ZIKV, and lesser-known Kyassanur Forest virus and Louping Ill virus have no current vaccines or antivirals (Kasabi et al., 2013; Jeffries et al., 2014).

1.2 Zika virus (ZIKV)

1.2.1 Origin and Discovery

Discovered in 1947 in Uganda whilst surveying for yellow fever in the Zika forest, ZIKV was isolated from a sentinel rhesus monkey sample. The virus was isolated again in the following year, 1948, however, from an *Aedes africanus*

mosquito, again from within the Zika forest (Dick et al., 1952). It is not known when Zika crossed the species barrier and entered the human population, however in 1952 it was detected in human samples in both Uganda and Tanzania, and again in 1954 in Nigeria (Smithburn, 1952; Macnamara, 1954). In 1964 the first symptomatic patient had Zika isolated from them. Symptoms were described as mild with a rash covering the majority of their body, and differing to DENV and the alphavirus chikungunya (CHIKV) by the absence of joint/bone pain (Simpson, 1964). The similarity of these symptoms highlights why ZIKV may not have been investigated previously. Throughout the 1970s and 80s, ZIKV was detected across equatorial Africa within mosquitoes and sentinel rhesus monkeys, as well as rare cases within the human population (Moore et al., 1975; Jan et al., 1978; Robin and Mouchet, 1975; Fagbami, 1977; Saluzzo et al., 1981). However, during this time ZIKV spread across India, Indonesia, Malaysia and Pakistan, again predominantly within mosquitos and rarely within humans (Marchette et al., 1969; Olson et al., 1981; Darwish et al., 1983). However, the presence of clinically similar virus infections, including CHIKV and DENV, could have masked the volume of ZIKV cases.

1.2.2 Transmission

Two different transmission cycles exist for ZIKV, the sylvatic and urban cycles involving *Aedes* mosquitos and either non-human primates or humans (Figure 1.1).

ZIKV is thought to only display tropism within humans, non-human primates and mosquitos. However, ZIKV is commonly used in cell culture in cell lines of other vertebrates (e.g. Baby Hamster Kidney (BHK) cells), and antibodies specific to ZIKV have been identified in other vertebrates including rodents and cattle, highlighting that they may play a role in virus circulation (Johnson et al., 1977).

ZIKV is primarily transmitted to humans through a female *Aedes* mosquito bite, commonly *A. aegypti*, which are found only in tropical areas, or *A. albopictus*, which are more widespread and can survive in more temperate regions; the former species is thought to transmit the majority of ZIKV infections (Thomas et al., 2012; Ferreira-de-Brito et al., 2016; Peterson et al., 2016). However, the recent outbreaks in Yap and French Polynesia likely resulted from *A. aegypti* in addition to *A. hensilli* and *A. polynesiensis*, respectively (Duffy et al., 2009; Lazear and Diamond, 2016).

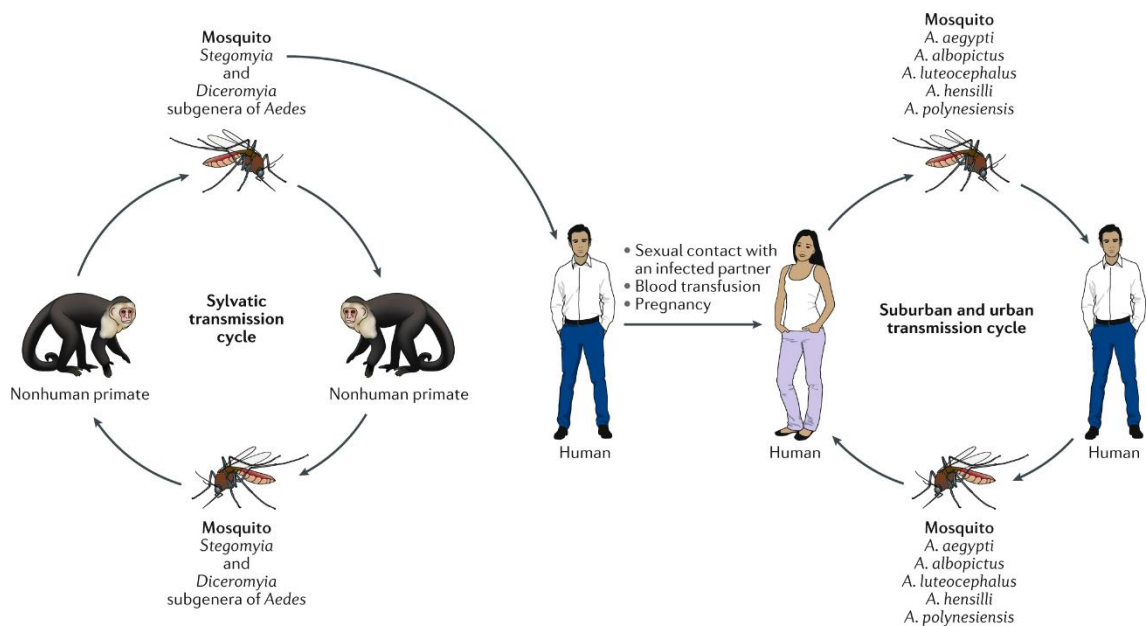


Figure 1.1 ZIKV transmission cycles schematic

In Africa ZIKV circulates in the sylvatic transmission cycle between non-human primates and forest-dwelling *Aedes* mosquitoes. However, in the suburban and urban environment ZIKV is primarily transmitted in a human – *Aedes* mosquito transmission cycle. Additionally, ZIKV can be transmitted between humans *in utero*, through sexual contact and blood transfusion. Figure taken from (Kurscheidt et al., 2019).

The African lineage of ZIKV is sustained predominantly via the sylvatic cycle (Figure 1.1) through non-human primates and mosquitos, whilst humans occasionally become incidental hosts (Althouse et al., 2016). However, critical amino acid substitutions led to the evolution of an Asian lineage of ZIKV (Gong et al., 2017), which predominantly infects humans as opposed to non-human primates, sustaining transmission via the urban transmission cycle (Saiz et al., 2016). This involves humans as the carrier, replicator and source of ZIKV for uninfected mosquitos, and the extrinsic incubation period of a mosquito is thought to be 10 days (Hayes, 2009; Boorman and Porterfield, 1956).

Non-mosquito modes of ZIKV transmission also exist, albeit with much lower incidence. The most reported non-mosquito transmission event occurs vertically from pregnant mothers transmitting ZIKV to their foetus through the placenta (Mysorekar, 2017). It is reported this is most likely to occur and cause congenital defects when the mother becomes infected in the 1st trimester (Rasmussen et al., 2016). In murine models, ZIKV RNA and antigens have been found in amniotic fluid, placenta and foetal brain, whilst both blood and cerebrospinal fluid (CSF) are positive in human studies. Furthermore, infectious

ZIKV particles have been isolated from the brain (Tai et al., 2019; Brito et al., 2018; Krauer et al., 2017).

Other routes of perinatal transmission are possible. ZIKV RNA and infectious particles have been detected in breast milk of infected mothers. A study in 2014 with two mother-infant pairs who were not infected throughout pregnancy detected ZIKV RNA in the milk and serum of the mothers, which then presented in the infants serum (Besnard et al., 2014). However, inoculation of Vero cells with breast milk did not result in virus replication. It is not certain ZIKV was transmitted via breast milk; other routes include transplacental, during delivery and by close contact between the mother and her newborn. However, breast milk transmission has previously been reported in DENV and WNV, but is thought to be very rare in both cases (Barthel et al., 2013; Hinckley et al., 2007). Furthermore, breastmilk has shown antiviral activity upon endogenous lipase-dependent production of fatty acids known to disrupt enveloped viruses (Cortese et al., 2017; Pfaender et al., 2013)

Additionally, sexual transmission has been reported. This was first indicated in 2008 after an American scientist returned home from Senegal, upon his return he became symptomatic with ZIKV. The scientists' wife had remained within the US and subsequently contracted ZIKV, likely to be transmitted sexually (Foy et al., 2011).

Sexual transmission was again indicated when ZIKV particles were isolated from the semen of a patient from French Polynesia in 2013 as he underwent treatment for haemospermia (Musso et al., 2015). There have since been further reports of sexually transmitted ZIKV. As of January 2018 in non-endemic areas there have been 27 reports of sexually transmitted ZIKV from 18 studies (Kim et al., 2018). ZIKV RNA and replicative ZIKV have both been isolated from semen, and viral RNA has been detected up to 62 days post symptoms (Atkinson et al., 2016).

Furthermore, Brazilian officials confirmed there had been two cases of ZIKV infections originating from blood transfusions, one of which was asymptomatic; these both happened in 2015 prior to the outbreak. Blood banks now only allow donations 30 days after a symptomatic infection of ZIKV (Magnus et al., 2018; Schnirring, 2016).

1.2.3 Symptoms

Only 20-25 % of infected individuals present with classical ZIKV symptoms, the majority remaining asymptomatic. Classical symptoms present as a non-specific malaise and can mimic flu-like symptoms or other arbovirus infections e.g. DENV, CHIKV, making identification difficult in the absence of molecular diagnostics (Patterson et al., 2016). Symptoms include: skin rash, headache, fever, conjunctivitis, muscle pain, joint pain & joint swelling (Cerbino-Neto et al., 2016).

During the South American outbreak in Columbia, 270 of 2603 ZIKV infected individuals displaying classical symptoms developed Guillain-Barré syndrome (GBS), increasing the baseline average from 20 to 90 cases/month (Parra et al., 2016). GBS comprises neurological symptoms including progressive weakness and loss of sensation in limbs, leading to paralysis of legs, arms, chest & facial muscles. GBS is an autoimmune disease attacking the peripheral nervous system and can be fatal due to ensuing respiratory failure occurring in 30 % of patients (Orlikowski et al., 2004). This was illustrated in 1976 when 5 % of GBS cases associated with a particular Influenza A virus (IAV) vaccine were fatal (Schonberger et al., 1979). The mechanism by which ZIKV causes GBS is unknown.

During an outbreak of ZIKV in French Polynesia, GBS incidence was estimated to be approximately 20-fold higher than the normal incidence rate of 1-2 cases per 100,000 per year (Oehler et al., 2014). GBS is triggered by a preceding event including infection or immunisation and comprises two main types: Acute motor axonal neuropathy (AMAN) and Acute Inflammatory Demyelinating Polyradiculoneuropathy (AIDP). AMAN is caused by pathogen cross-reactivity with epitopes on peripheral nerves, resulting in degeneration of the axons, whereas in AIDP epitopes are cross-reactive with Schwann cells and/or myelin, resulting in axonal demyelination (Kuwabara, 2004). Studies have shown T cells infiltrate GBS neuronal lesions, implying a role in mediating the production of auto-antibodies (Yang, M. et al., 2015).

Another serious ZIKV neurological consequence is microcephaly, where impaired foetal brain development results in heads of smaller than normal size and is associated with intellectual disability (Alcantara and O'Driscoll, 2014). During the 2015 Brazil outbreak, causal association between prenatal ZIKV

infection and microcephaly was documented, with a 405 % increase over baseline incidence (Microcephaly Epidemic Research, 2016; Magalhaes-Barbosa et al., 2016). Retrospectively, analysis of the 2013 ZIKV outbreak in French Polynesia revealed out of 8750 ZIKV cases, 7 cases of microcephaly occurred when the mother was infected during the first trimester of pregnancy (de Oliveira et al., 2017a).

The greatest loss of neurons in microcephaly occurs in the cerebral cortex found in the forebrain, encompassing 80 % of the total brain mass. The absence of a fully formed cortex results in impaired higher-order processes, including cognition and sensation (Geschwind and Rakic, 2013). Formation of the cortex during foetal development originates from three different types of cell divisions of the neural tube. Along with programmed cell death, the proportion of these different divisions is tightly regulated. Imbalances in the proportions of these divisions can impact the development of the central nervous system, therefore leading to microcephaly (Rakic, 2009).

ZIKV impacts the development of the developing cerebral cortex by infecting neural progenitor cells often resulting in cytotoxic effects (Brault, J.B. et al., 2016) and also infects cranial neural crest cells which develop into cranial bones and secrete hormones promoting neural differentiation (Bayless et al., 2016). Upon infection, ZIKV promotes cell cycle arrest and apoptotic cell death (Li, C. et al., 2016b; Tang et al., 2016; Hanners et al., 2016; Garcez et al., 2016) autophagy or possibly by early differentiation through hormone release (Merfeld et al., 2017).

1.3 Epidemiology

In 2007, the first large human ZIKV outbreak occurred on Yap, a small Pacific island of 11250 people. Surveys suspected 185 Zika cases and it was estimated 73 % of Yap residents were infected. However, there were no deaths, hospitalisations or neurological complications as a result of the outbreak (Duffy et al., 2009; Lanciotti et al., 2008). It is not known how ZIKV was introduced to Yap; it is possible mosquitoes can travel considerable distances by wind, yet it was most likely introduced by an infected person or mosquito by travel or trade. Unlike the African and Asian population, the Yap population are thought to lack herd immunity, an indirect protection occurring when the majority of the

population is immune to the pathogen, providing protection to those who are not.

In 2012 Zika virus strain research for African strains: MR 766 (Prototype, Uganda, 1947); IbH 30656 (Nigeria, 1968) and ArD 41519 (Senegal 1984) and Asian strains: P6-740 (Malaysia, 1966); EC Yap (Yap Island, Micronesia, 2007) and FSS13025 (Cambodia, 2010) were published, indicating differing Asian and African lineages, strengthening the thought the ZIKV outbreak in Yap originated from Asia (Haddock et al., 2012) (Figure 1.2 & Figure 1.3).

ZIKV subsequently caused outbreaks throughout 2013 and 2014 isolated to Pacific island groups including French Polynesia (Cao-Lormeau and Musso, 2014; Roth et al., 2014), which generated thousands of suspected infections. For the first time ZIKV was suggested to be associated with GBS and congenital malformations (Oehler et al., 2014). However, during this time French Polynesia was also experiencing a DENV outbreak, which prevented conclusive studies (Cao-Lormeau et al., 2014).

ZIKV was first detected in South America in 2015. In the February, an illness characterised by a rash was present in Brazil and by May it was identified as ZIKV and declared an outbreak by the National Ministry of Health. The illness was described as mild but caused 7000 cases in north-eastern states of Brazil. In July, reports of GBS associated with a prior virus infection were associated. However, by October, the cases of GBS had increased and Brazil first reported a rise in new-born microcephaly cases (de Oliveira et al., 2017b). Over the next year ZIKV spread throughout South America & Central America (Figure 1.4). As of 4th January 2018 throughout the Americas there have been over 1,000,000 cases of ZIKV, and 3720 cases of confirmed congenital syndrome associated with ZIKV infection since 2015 (*Zika Cumulative Cases*, 2018).

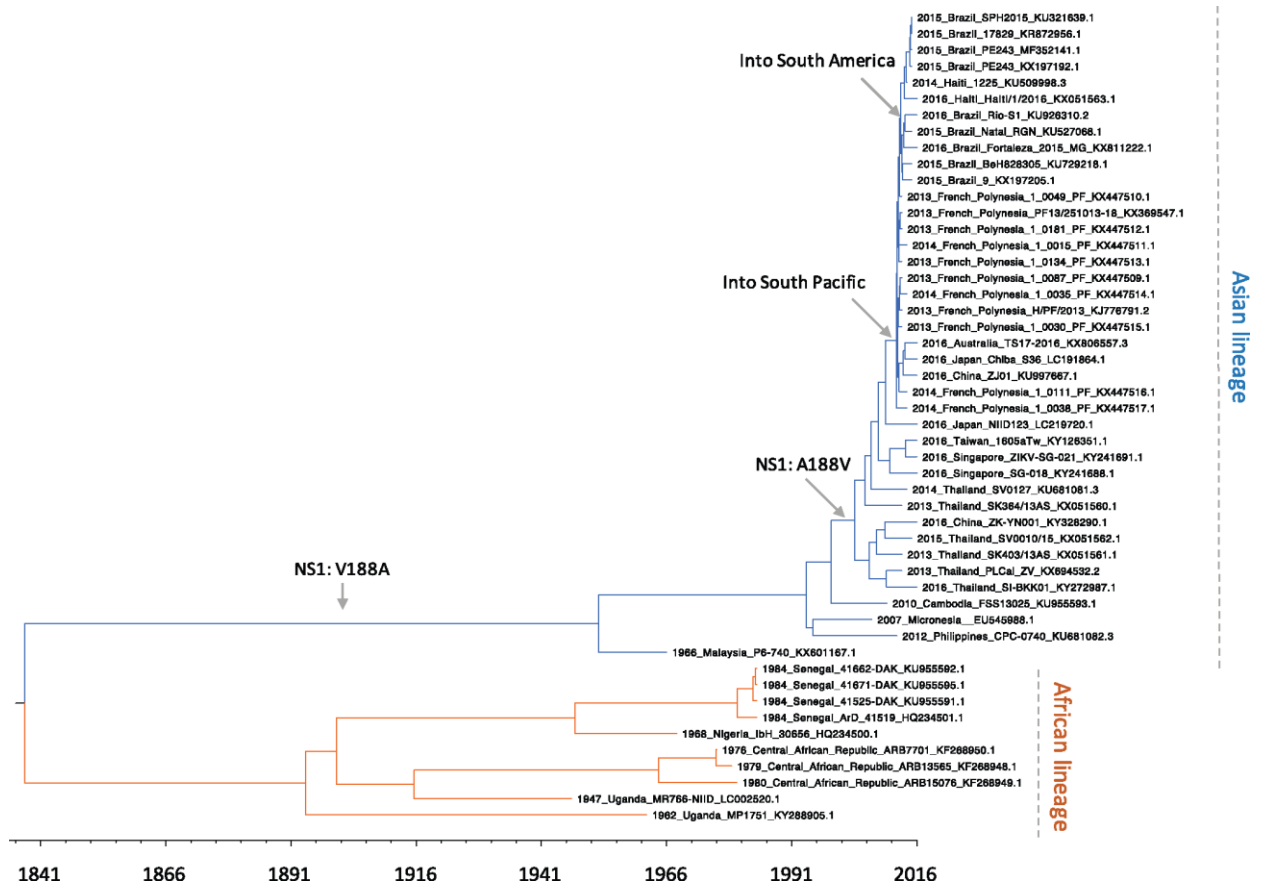


Figure 1.2 Evolutionary timescales of ZIKV

Maximum Clade Credibility (MCC) tree of ZIKV. The Asian and African lineages are highlighted in blue and orange respectively. Source (Gong et al., 2017).

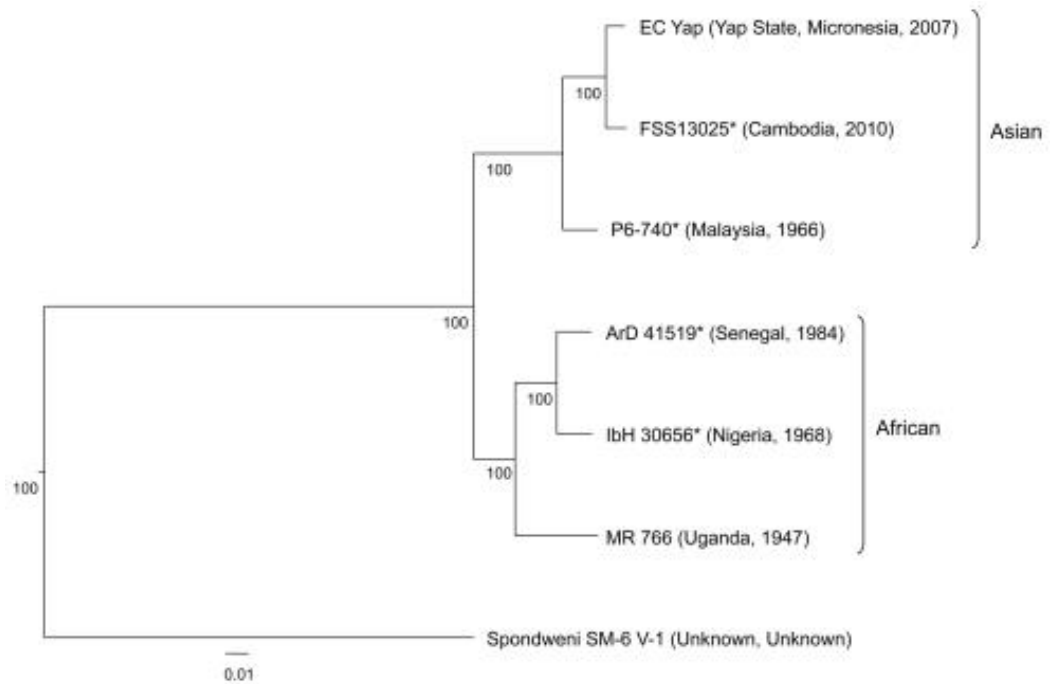


Figure 1.3 ZIKV nucleotide and amino acid alignments

Neighbour-joining phylogeny tree generated from ZIKV strain open reading frames. Tree routes with Spondweni virus. Genetic distance in nucleotide substitutions per site is shown by scale at the bottom. Numbers at the nodes represent percent bootstrap support values based on 1,000 replicates. Source (Haddow et al., 2012).

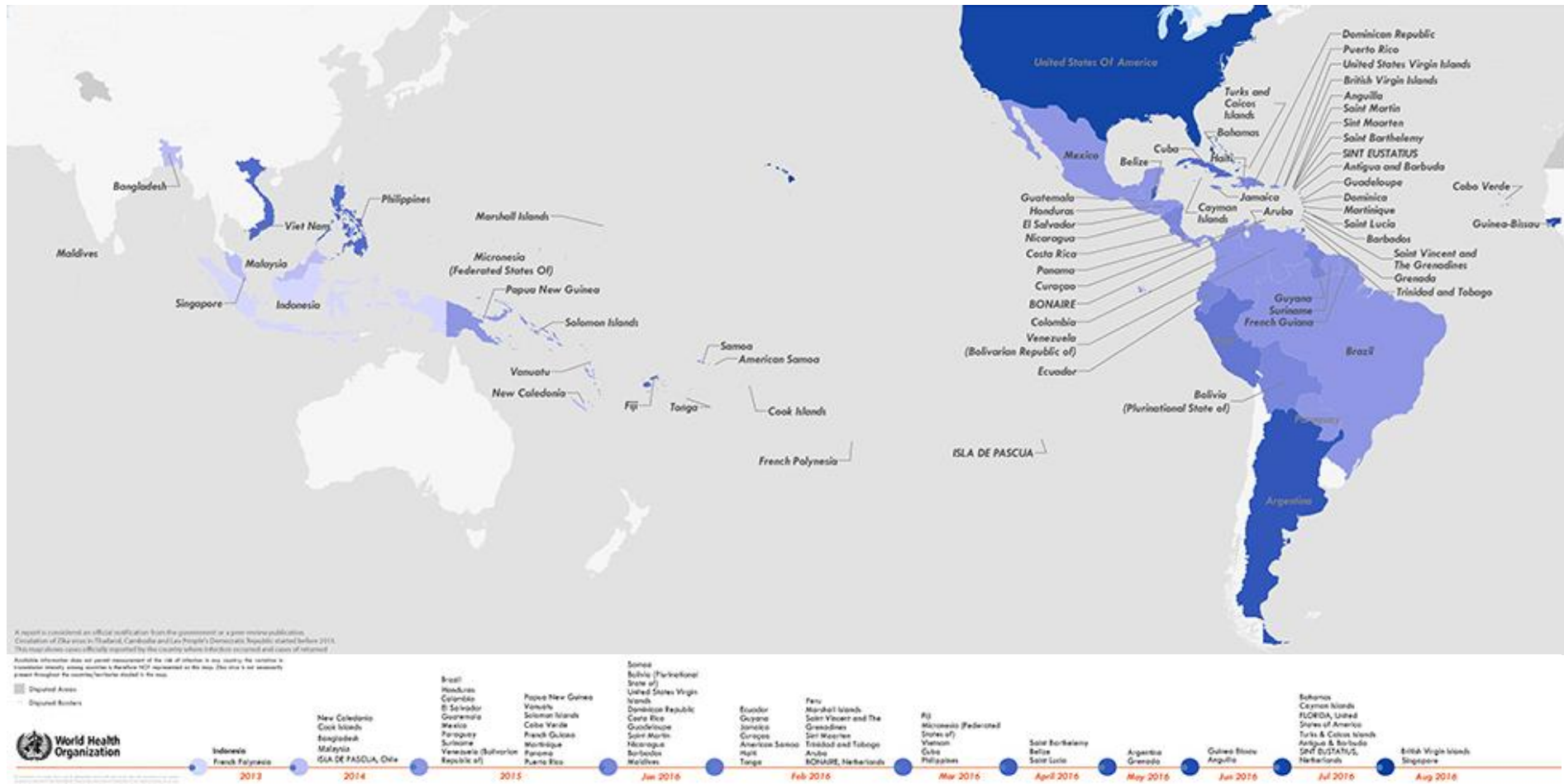


Figure 1.4 Countries and territories showing the spread of ZIKV (2013-2016)

Source (ZIKA VIRUS MICROCEPHALY GUILLAIN-BARRÉ SYNDROME 2016)

1.4 Molecular biology of Zika virus (ZIKV)

1.4.1 Zika virus genome structure

Similar to all *Flaviviruses*, Zika virus has a single-stranded positive-sense RNA genome of around 11kb. The 5'-end of the viral RNA possesses a type I cap (m⁷GpppAmp) and a 5' untranslated region (UTR) of 106 nucleotides (nt). This is followed by a single open reading frame (ORF), then by a 3' UTR of 428 nt. UTRs contain sequence motifs which play multiple roles during translation and replication of the RNA, functioning as positive and negative regulators (Song et al., 2019).

Additionally, the 3' UTR loop structure leads to formation of two subgenomic *Flavivirus* RNA (sfRNA) species, which are likely involved in virus transmission and replication. sfRNA is an extension of the 3' UTR and is produced by incomplete degradation of the viral RNA by host RNA exonuclease protein 5'-3' exoribonuclease 1 (XRN1). Stalling of XRN1 at RNA stem-loops results in sfRNA formation (Pijlman et al., 2008). ZIKV sfRNA is reported to inhibit type 1 IFN responses through antagonism of RIG-I and, to a lesser extent, MDA5 (Donald et al., 2016).

The ZIKV polyprotein is processed co- and post- translationally by both host and viral proteases, including furin and Non-structural protein (NS) 3 respectively (Stadler et al., 1997; Amberg et al., 1994). NS2B – NS3 is known to cleave Capsid (C) – Intracellular capsid protein (Ci), NS2A – NS2B, NS2B – NS3, NS3 – NS4A, NS4A-2K, NS4B – NS5 on the cytoplasmic side of the ER and Ci – precursor membrane (prM), small membrane (M) – Envelope (E), E – NS1, NS1 – NS2, peptide 2K (2K) – NS4B within the ER lumen.

1.4.2 Zika virus structural proteins

Like all members of the *Flaviviridae*, ZIKV proteins are organised spatially with structural elements at the N-terminus and NS proteins at the C-terminus. There are three structural proteins: C, M synthesised as a longer precursor (prM) and E. The functions of these proteins have been studied in ZIKV to a degree, although some are inferred based upon related *Flaviviruses*.

1.4.2.1 Capsid protein

The Capsid (C) protein has many different roles. Its primary role is to associate with viral RNA to form the nucleocapsid during assembly, protecting the RNA genome (Kuhn et al., 2002). However, C also interacts with multiple host proteins including Regulator of nonsense transcripts 1 (UPF1), Zinc Finger CCCH-Type Containing Antiviral 1 (ZC3HAV1) and La-related protein 1 (LARP) involved in evading the immune response through dysregulation or expression of specific transcripts (Fontaine et al., 2018; Scaturro et al., 2018; Scaturro et al., 2019) and interactions with Ly1 Antibody Reactive (LYAR) maintaining embryonic stem cell properties and neuroguidin (NGDN) preventing neuronal development (Scaturro et al., 2018; Scaturro et al., 2019).

DENV C protein has been shown to act as an RNA chaperone, aiding viral RNA structure formation, by forming dimers which are capable of binding RNA (Pong et al., 2011). Moreover, YFV C protein inhibits the mosquito immune system by preventing RNA silencing mediated through binding to long dsRNAs, interfering with the production of virus-derived small interfering RNAs (vsiRNAs) by dicer (Samuel et al., 2016).

Flavivirus C proteins localise in several cellular compartments after translation. C is found accumulated around endoplasmic reticulum (ER) derived organelles called lipid droplets, in parallel with other viruses including hepatitis C virus (HCV) (Samsa et al., 2009; Ogawa et al., 2009), which could help to sequester capsid proteins and allow genome encapsulation. Nuclear localisation of capsid allows interactions with many different host proteins, primarily preventing apoptosis and interactions leading to increased replication. These include interactions of DENV C with Death Domain Associated Protein (DAXX) leading to Fas-mediated apoptotic activity, WNV C interactions with DDX56 after re-locating from nucleolus to cytoplasmic site and phosphorylated WNV C interactions with HDM2 induce p53-dependent apoptosis. (Netsawang et al., 2010; Limjindaporn et al., 2007; Xu, Z. et al., 2011; Yang, M.R. et al., 2008).

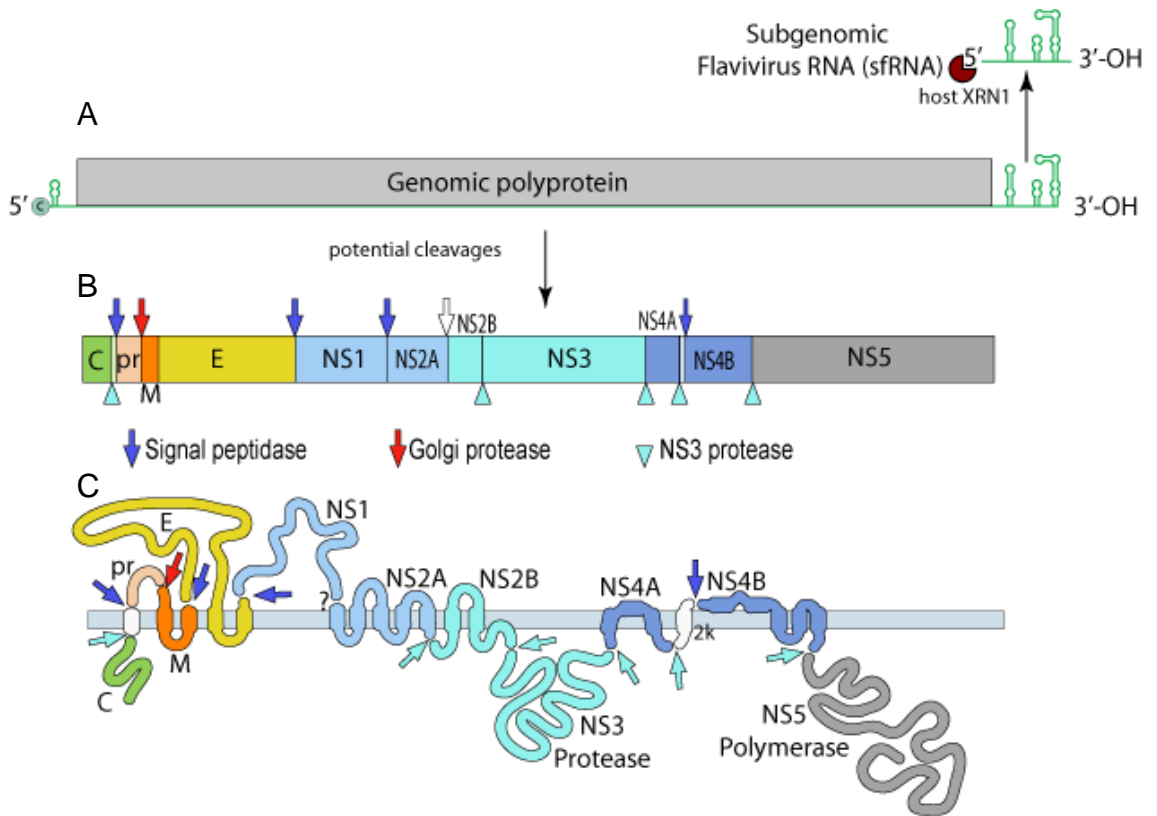


Figure 1.5 ZIKV genome organisation schematics

- A. Polyprotein structure showing 5 and 3 RNA structures. B. Polyprotein schematic of the proteases involved and cleavage products. C. Topology of the polyprotein in membrane. Source (ViralZone).

1.4.2.2 PrM

PrM protein acts as a chaperone protein assisting the folding of E during intracellular virion assembly. Preventing premature fusion of the immature virion prior to release from the host cell by maintaining E in a non-fusogenic state, masking and inactivating the E fusion peptide (Lorenz et al., 2002; Yu et al., 2009; Li, L. et al., 2008).

During the transport of the virion through the *trans*-Golgi network (TGN) the virion encounters a decrease in pH from neutral to around 6. Virion acidification causes the prM-E trimers to reorganise into a herringbone-like arrangement, in which prM molecules cover the fusion loop of E protein. Making the fusion loop of E inaccessible, prevents premature fusion of the virion in the acidic Golgi compartment prior to virion release. Subsequently, host protease furin and furin-like proteases are responsible for cleaving prM to M protein (Yu et al., 2008; Yu et al., 2009; Stadler et al., 1997).

The aforementioned prM cleavage is inefficient, and many virions remain only partially matured. These uncleaved prM proteins may play a role in immune evasion as immature DENV prM-containing particles are more likely to lead to Antibody Dependent Enhancement (ADE) in patients than an infection with fully mature DENV particles (Rodenhuis-Zybert et al., 2011).

Additionally, a prM protein S139N substitution mutation, which first emerged in May 2013, has been shown to significantly increase infectivity of ZIKV when cultured with neural progenitor cells, leading to more pronounced microcephaly in foetal mice of infected mothers (Yuan et al., 2017). The mutation is found within the region of prM which is involved in interactions within trimeric spikes in the immature virus particle (Prasad et al., 2017). Therefore, the mutation may be involved in the transition of ZIKV from immature to mature virions; in turn the maturity heterogeneity of virus may affect “viral fitness” and so neurovirulence. The substitution mutation occurred prior to the French Polynesia outbreak in 2013 and has been maintained in the epidemic strain that spread across the Americas (Yuan et al., 2017).

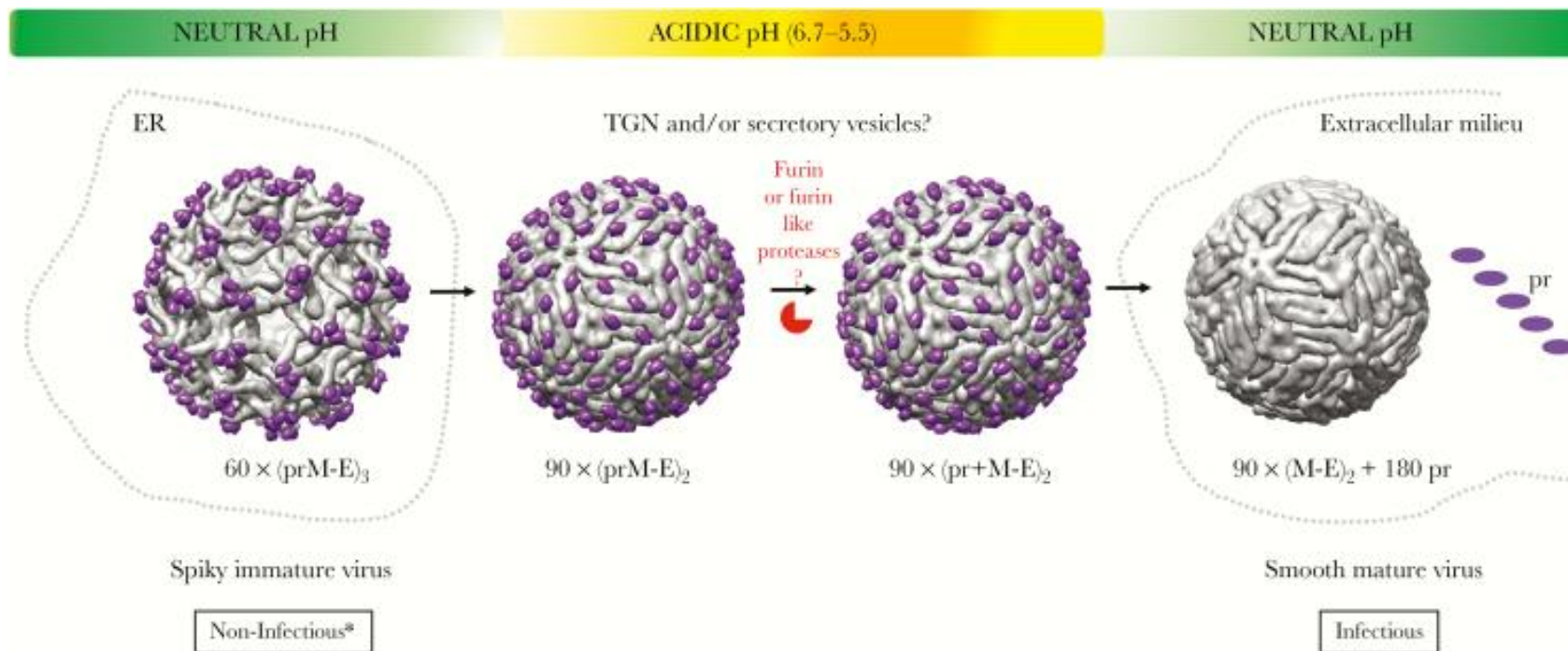


Figure 1.6 Flavivirus maturation

The maturation pathway for Flaviviruses. The conformational changes of surface glycoproteins prM/M and E and the cleavage of prM by host protease furin, converting a spiky immature non-infectious virus to a mature infectious virus. Source (Sirohi and Kuhn, 2017).

1.4.2.3 M

Once pr is cleaved, M remains within the virion membrane as a short hydrophobic protein of 75 amino acids. The role of M within the mature virion membrane is unclear. However, several *Flavivirus* studies have investigated the possibility of M protein exhibiting viroporin activity, playing a role during virus entry and uncoating. It is thought the activity could compare to that of Influenza A virus (IAV) M2. However, there have been conflicting results of channel activity using lipid membranes *in vitro* and *Xenopus* oocytes (Premkumar et al., 2005; Wong et al., 2011).

DENV M protein has been shown to have cytotoxic effects and the ability to induce apoptosis. Through deletion mutagenesis, nine C-terminal amino acids were identified within the ectodomain of M protein that appeared responsible for this phenotype. This region is referred to as "ApoptoM". Further investigation showed ApoptoM transport through the secretory pathway is an essential part of this process, and interactions of ApoptoM with pro-apoptotic protein Bax, of which levels increase during Flaviviral infection, may be required (Catteau et al., 2003).

Cryo-EM structures of mature virus particles reveal that mature M protein comprises two helical transmembrane domains within the mature virus particle membrane, which are present in a dimeric form (Section 1.9) (Sirohi et al., 2016; Sevvana et al., 2018).

1.4.2.4 E

ZIKV E protein is a class II fusion protein with a unique structure of three ectodomains (EDI, II & III) and two transmembrane domains (TMD1 & 2) in a hairpin like structure (Figure 1.7). Upon virus entry via clathrin-mediated endocytosis (section 1.5.1), 90 envelope protein dimers transition from a herringbone-like formation on the virus surface, into 60 E trimers upon low pH conditions within endosomes. All domains of E protein are involved in this irreversible structural rearrangement leading to membrane fusion (Figure 1.8) (Dai et al., 2016; Sirohi et al., 2016).

ZIKV has a broad tropism, mediated through a variety of receptors. The many different cell types include cells of the brain, placenta, skin, testis, kidneys, retina and immune cells. Known ZIKV receptors include: Axl receptor tyrosine

kinase (AXL), Tyrosine-protein kinase receptor TYRO3 (Tyro3), T-cell immunoglobulin and mucin domain 1 (TIM-1), Toll-like receptor 3 (TLR3), Toll-like receptor 8 (TLR8), Melanoma-differentiation-associated gene 5 (MDA5) and Dendritic Cell-Specific Intercellular adhesion molecule-3-Grabbing Non-integrin (DC-SIGN) (section 1.5.1 and Table 1.1) (Meertens et al., 2017; Wang, Z.Y. et al., 2017; Nowakowski et al., 2016; Tabata, T. et al., 2016; Hamel et al., 2015).

The receptor binding promotes virus attachment, followed by clathrin-mediated endocytosis, virion acidification and fusion of the virion membrane with the endosomal membrane during viral entry involving the structural rearrangement of E protein (section 1.5.1 and

Figure 1.12) (Mukhopadhyay et al., 2005; Elshuber et al., 2003; Roby et al., 2015; Saiz et al., 2016).

E protein is translated in the endoplasmic reticulum and forms heterodimers with protein prM. The glycoprotein heterodimers reside within the ER membrane and RNA produced in the replication complexes associates with C protein and buds into the glycoprotein containing ER membrane. The newly formed immature particle is covered with 60 spikes composed of prM-E heterodimers (Figure 1.9). The virion is transported to the TGN where the low pH causes dissociation of the heterodimers and formation of E homodimers (Yu et al., 2008). However, as previously mentioned in section 1.4.2.2, prM-E cleavage is inefficient, and majority of virions are only partially matured, contributing to host immune evasion.

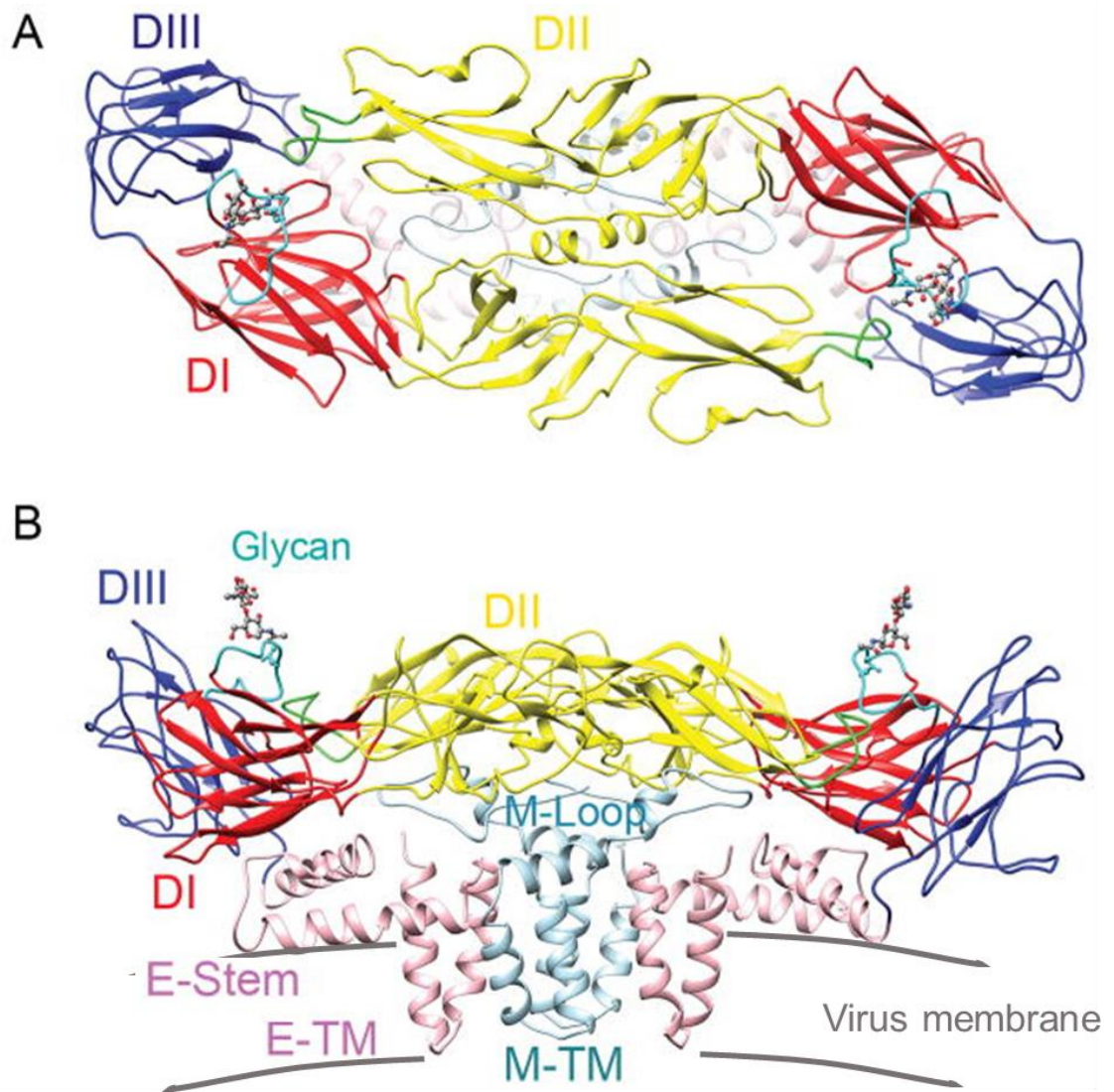


Figure 1.7 E protein

A. The E protein dimer is represented by ribbons, viewed down the two-fold axis. The colour code aligns with the standard labelling of E protein domains I (red), domain II (yellow) and domain III (blue). The stem and transmembrane residues are shown (pink). The fusion loop (green). B. Side view of the E-M dimer showing the three E ectodomains, the E stem/transmembrane domains (pink) and the M protein (light blue), annotated with virus membrane (grey). Source (Sirohi et al., 2016).

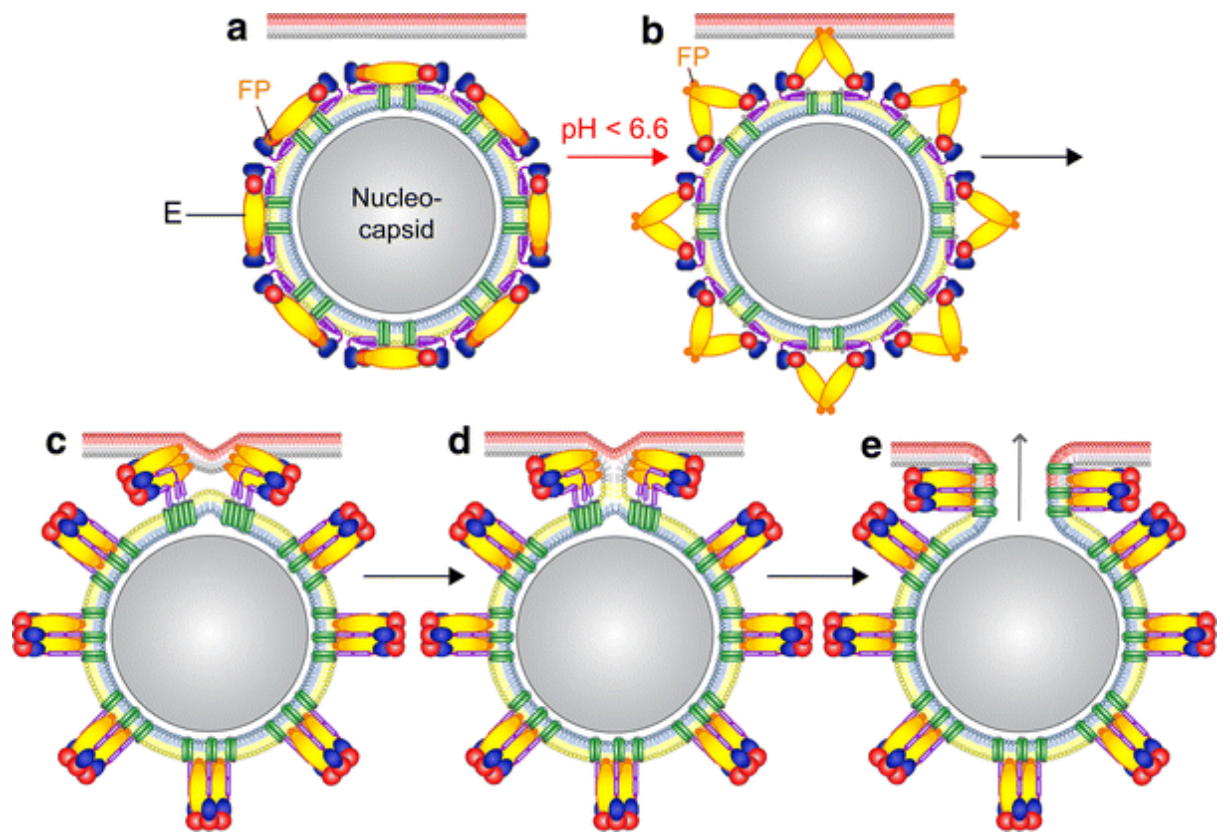


Figure 1.8 Flavivirus membrane fusion schematic

Schematic of the *Flavivirus* membrane fusion process. A. Pre-fusion E dimer in a herringbone pattern on the virus surface. B. Low-pH-induced dissociation of E dimers (\sim pH6.6), E monomers project away from the membrane, and interact with proteins on target membrane. C. Trimer formation and "zippering" of the stem. D. Hemifusion intermediate, the outer leaflets mix. E. Formation of the post-fusion E trimer and pore opens. E protein colour code as in Figure 1.7 (Stiasny et al., 2011)

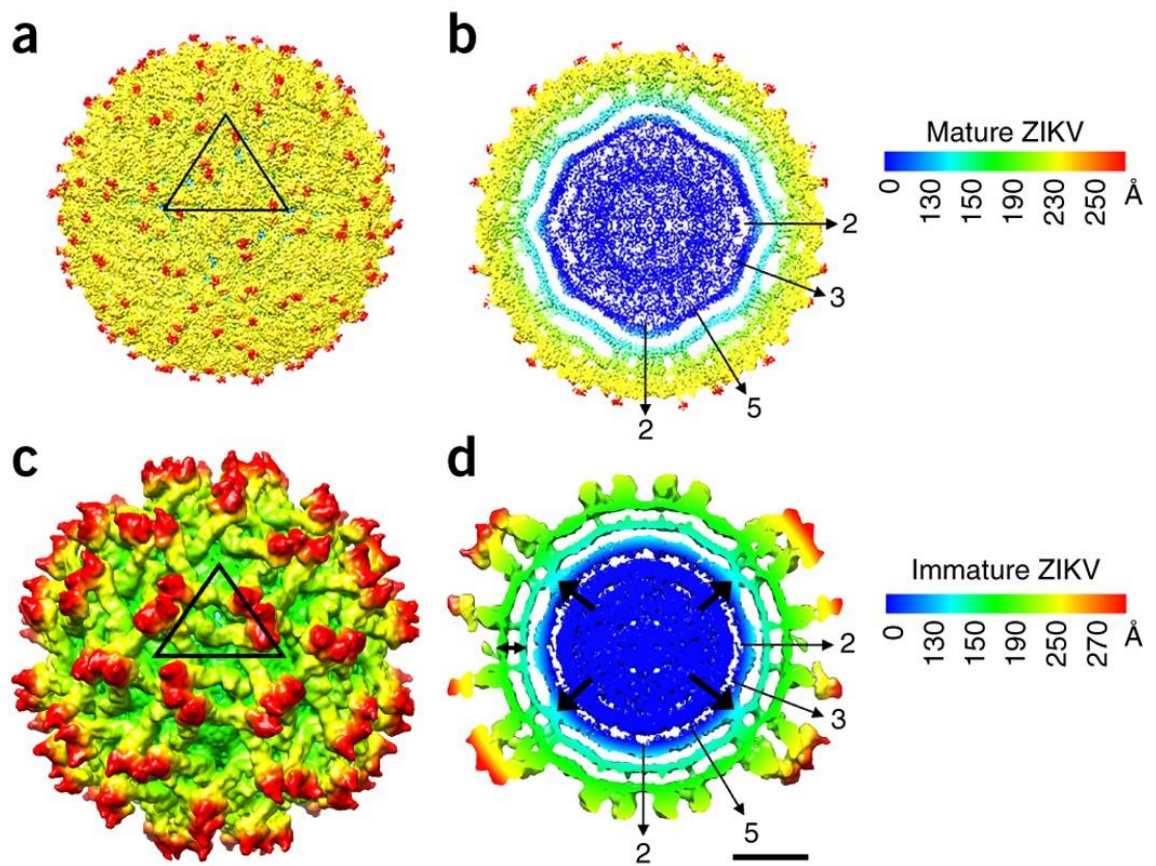


Figure 1.9 Mature and Immature ZIKV structure

A & B. The surface and cross-section view of mature ZIKV. C & D. Immature ZIKV. Both sections coloured corresponding to the adjacent key. The Black triangle in A & C shows the asymmetric unit. Numbered arrows in B & D indicate the icosahedral symmetry axes. Thick arrows in D show the difference in density of the RNA core and viral membrane. Double-ended arrows in D show the distance between the inner and outer layers of the virus membrane. Scale bar is 100 Å. (Prasad et al., 2017)

E proteins form the outer surface of the virion, interacting with M protein forming heterotetramers that arrange into an icosahedral virus surface. E has two transmembrane domains which reside adjacent to M protein, and three ectodomains which are found on the virion surface (Figure 1.7) (Sirohi et al., 2016). The tetrameric E/M protein structure is formed of Envelope and M protein homodimers, however these structures do not remain throughout entry of the virus particle. Upon virion endocytosis, the virus particles are exposed to a drop in pH as the endosomes mature, and the structure of the TBEV and DENV envelope protein has been resolved at this point. The E dimer changes conformation from lying on the surface to protruding away from the virion, additionally the E proteins change from dimeric to trimeric (Figure 1.8) (Bressanelli et al., 2004; Modis et al., 2004).

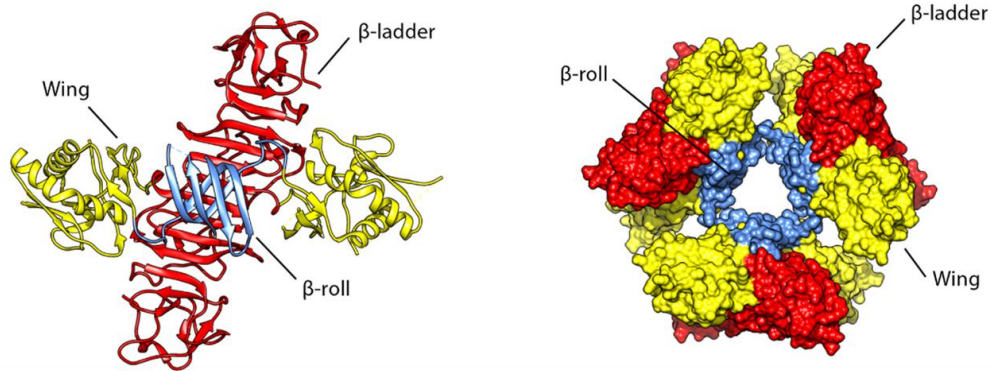
1.4.3 Zika virus Non-structural proteins

1.4.3.1 NS1

NS1 is a highly multi-functional protein, which adopts different tertiary and quaternary forms, each with diverse roles. Dimeric NS1 localises intracellularly, particularly to the ER membrane and lumen (

Figure 1.10) (Akey et al., 2014). By contrast, NS1 also forms a hexamer that is secreted from the infected cell, primarily known for its involvement in immune evasion. A single mutation in NS1 during the ZIKV African to Asian evolution exacerbate its immune evasion capabilities through the A188V substitution which interacts with TBK1 reducing its phosphorylation leading to a reduction in IFN- β production (Xia et al., 2018).

Dimeric NS1 found associated with membranes (mNS1) is reported to be involved in viral genome replication. DENV and WNV mNS1 associate and rearrange liposome membranes *in vitro*, and mNS1 along with NS4A/B play an essential but poorly defined role in virus replication within the ER at replication complexes (Akey et al., 2014; Akey et al., 2015; Welsch et al., 2009). Furthermore, mNS1 interacts with 60S ribosome subunits, retargeting them to replication complexes (Cervantes-Salazar et al., 2015).



Dimeric:
 Intracellular membrane associated (mNS1)
 Rearrange liposome membranes
 Role in virus replication
 Targets 60S to RC's

Hexameric:
 Secreted (sNS1)
 Immune evasion
 TLR4 interactions increasing
 disease severity through
 inflammation



mNS1 localises to TGN
 Removal of carbohydrate moieties by host enzymes
 lead to soluble hexameric NS1 (sNS1)

Figure 1.10 NS1 Structures

A. Dimeric DENV NS1 3D crystal structure shown in ribbon representation (Protein Data Bank accession no. 4O6B) (Akey et al., 2014). The β -roll, Wing and β -ladder domains are highlighted in blue, yellow and red, respectively. B. Hexameric DENV structure shown by surface representation, colour coded in the same manner as A. Source (Scaturro et al., 2015).

Dimeric NS1 also localises to the TGN and interacts with host glycosidases and glycosyltransferases. This results in the removal of NS1 carbohydrate moieties, leading to the formation of a soluble hexameric NS1 complex with an open barrel shaped conformation that is secreted from the infected cell (sNS1) (Flamand et al., 1999; Gutsche et al., 2011; Muller et al., 2012). sNS1 interacts with Toll-like receptor (TLR) 4, leading to activation of macrophages and PBMCs and increased pro-inflammatory cytokine expression. This disrupts endothelial cell integrity, which is linked to increased disease severity during DENV infection (Modhiran et al., 2015). Both dimeric and hexameric NS1 conformations are also thought to form membrane attack complexes (MAC), further increasing the secretion of vasoactive cytokines resulting in deteriorating disease (Avirutnan et al., 2006).

An additional form of NS1 is reported in JEV, WNV & DENV. NS1' results from the presence of a slippery heptanucleotide and pseudoknot structure causing a -1 ribosomal frameshift near the start of the NS1 sequence during translation, at a frameshifting efficiency of 20-50% (Firth et al., 2010). WNV NS1' has a 52 amino acid extension at the C terminus (Melian et al., 2010; Firth and Atkins, 2009). Disrupting the formation of NS1' reduces neuroinvasiveness and NS1' can substitute for NS1 function (Melian et al., 2010; Ye, Q. et al., 2012; Young et al., 2013). Additionally NS1' has been found to co-localise with NS3 and NS5 within the replication complex (Satchidanandam et al., 2006; Takamatsu et al., 2014).

1.4.3.2 NS2A

NS2A is small multifunctional hydrophobic protein and predominantly resides in the viral replication complex playing a role in virus RNA replication and virion assembly. However, ZIKV NS2A has also been shown to antagonise the host immune response (Mackenzie et al., 1998; Chambers et al., 1989; Munoz-Jordan et al., 2003).

The N-terminus of NS2A is cleaved in the ER lumen by an unknown host protease, and the C terminus is produced by NS2B/NS3 viral protease in the cytoplasm (Falgout and Markoff, 1995; Chambers et al., 1990).

Once cleaved, *Flavivirus* NS2A along with NS4A and NS4B provide the scaffolding for the replication complex in the ER (Welsch et al., 2009). Within

this compartment, NS2A is involved with viral RNA synthesis, binding to the viral RNA 3'UTR, NS3 and NS5 (Mackenzie et al., 1998; Xie et al., 2015; Wu, R.H. et al., 2015). The mechanism ZIKV NS2A plays in viral RNA synthesis is not known. However, a single A175V mutation within NS2A was shown to impair ZIKV RNA synthesis *in vivo* (Zhu, X. et al., 2019).

A further replicative role of NS2A is assembly of ZIKV virions. NS2A has been shown to recruit viral RNA, C-prM-E and NS2B/NS3 to assembly sites. The presence of NS2B/NS3 cleaves the C-prM-E polyprotein, leading to RNA encapsidation by C and prM/E envelopment (Zhang, X. et al., 2019).

Additionally, NS2A is involved in modulating the interferon response initiated by the infected host cell as an antiviral response (Munoz-Jordan et al., 2003; Liu, W.J. et al., 2006). NS2A along with NS4A and NS4B inhibits the JAK/STAT signalling pathway in DENV by decreasing STAT1 phosphorylation through “prohibiting its nuclear localisation and preventing IFN- β promoter driven transcription from two ISREs’ (Munoz-Jordan et al., 2003). NS2A downregulates IFN- β promoter, through inhibiting signal activation molecules of IFN- β such as interferon regulatory factors (IRFs). NS2A was also shown to suppress RIG-I (Ngueyen et al., 2019).

NS2A alone has inferred a role in the cause of microcephaly. ZIKV NS2A depletes adherens junction proteins, reducing radial glial cell proliferation and premature differentiation of newborn neurons (Yoon et al., 2017).

NS2A also contributes to the generation of the aforementioned NS1', through a *Flavivirus*-conserved slippery heptanucleotide motif found at the N terminus of NS2A (Melian et al., 2010).

1.4.3.3 NS2B & NS3

NS2B is a small protein of 242 amino acids, with a conserved central hydrophilic region surrounded by three hydrophobic regions, likely to be transmembrane domains. It has been shown the hydrophilic region of NS2B is an essential cofactor for the activation of the viral protease NS3 (Falgout et al., 1991). The NS2B-NS3 protease, alongside host proteases cleaves the viral polypeptide into individual viral proteins at the ER. The N terminal domain of NS3 is a chymotrypsin-like serine protease and can cleave the polyprotein in *cis* and *trans* (Bera et al., 2007; Chambers et al., 1990; Li, J. et al., 2005). The

necessary cofactor for the protease resides in the centre of NS2B between N and C terminal transmembrane domains (Clum et al., 1997).

The vital roles of NS2B-NS3 during the virus life cycle have been explored as targets for inhibitors. However, despite the structural and biochemical information known about the protein no compounds have reached clinical trials. There have been difficulties in finding a peptide capable of competing with RNA binding due to the shallow binding pocket of the protease, and its exposure to the surrounding (Lim et al., 2013b).

Additionally, NS3 also has further enzymatic activity on its own, as a helicase (Fairman-Williams et al., 2010). NS3 has three subdomains, subdomain 1 and 2 contain conserved motifs which have RNA binding and ATP hydrolysis activity (Xu, S. et al., 2019). The third subdomain forms a ssRNA binding tunnel (Tian et al., 2016). NS3 also has RNA 5' triphosphatase activity (RTPase) and triphosphatase hydrolysis is the first step for viral RNA capping (Decroly et al., 2011).

1.4.3.4 NS4A

NS4A is an integral membrane protein found within the ER playing a role in membrane rearrangement for virus replication. NS4A is linked to NS4B by a 23 amino acid signal peptide conserved across *Flaviviruses* with a molecular weight of 2000 Da, named 2K. NS4A and 2K are cleaved by the aforementioned NS2B-NS3 protease, which is required prior to cleavage of NS4B from 2K by a host signalase (Lin, C. et al., 1993).

In DENV and WNV, NS4A expressed alone and NS4A-2K are able to induce rearrangements to the ER membrane similar to that seen in virus infected cells, this is thought to anchor the replication complex to the ER membrane utilising the NS4A TMDs (Kaufusi et al., 2014; Miller et al., 2007; Roosendaal et al., 2006). NS4A is also reported to oligomerise at its N-terminus and bind to host cell protein vimentin. Vimentin binds to NS4A within the replication complexes, providing supportive anchorage for the replication complexes during DENV replication forming a scaffold as well as rearranging the ER membrane (Stern et al., 2013; Teo and Chu, 2014).

However, within the *Flavivirus* genus there are differences in the localisation of these integral membrane proteins. WNV NS4A-2K induces ER membrane

rearrangement, whereas without the 2K peptide, NS4A localises to the Golgi apparatus (Roosendaal et al., 2006). By contrast, DENV-2 NS4A does not require peptide 2K to rearrange the ER membrane and 2K inhibits this rearrangement (Miller et al., 2007), suggesting the mechanisms behind this rearrangement are distinct between *Flaviviruses*.

DENV-2 NS4A keeps infected cells alive by inducing and upregulating autophagy and lipophagy to aid viral replication (McLean et al., 2011; Zhang, J. et al., 2018). To further maintain cells as virus factories, NS4A also plays a role in evading the host immune response. NS4A contributes to the inhibition of interferon signalling and completely blocks IFN signalling when expressed alongside NS2A and NS4B (Munoz-Jordan et al., 2003). It has been shown KUNV NS4A and NS4B induce the unfolded protease response (UPR), a cellular stress response linked to ER stress when unfolded or misfolded proteins accumulate in the ER lumen. UPR is thought to inhibit JAK-STAT signalling when IFN- α is produced (Ambrose and Mackenzie, 2011). Furthermore, NS4A interacts with NS3 helicase as a cofactor allowing it to conserve energy to keep unwinding the viral RNA when ATP levels are low (Shiryayev et al., 2009).

1.4.3.5 NS4B

NS4B is another membrane integral protein and is the largest hydrophobic non-structural protein, consisting of three TMDs. NS4B is translocated into the ER lumen by the 2K signal sequence at the N terminus, after translocation 2K is cleaved off by a host signalase (Miller et al., 2007). Within the ER lumen NS4B is likely to form dimers, as it has been shown to be capable of dimerising when expressed alone and also during virus infection *in vitro* (Zou et al., 2014).

Similarly to NS4A, NS4B interacts with and contributes to forming the replication complex (Miller et al., 2006; Yi, Z. et al., 2012) and evading immune response through ISRE-54 and ISRE-9-27 promoter activation inhibition, therefore leading to decreased STAT1 phosphorylation and IFN suppression, along with NS4A and NS2B (Munoz-Jordan et al., 2005; Munoz-Jordan et al., 2003). The similarity in these functions suggests that NS4A and NS4B may function cooperatively (Zou et al., 2015) and were shown to directly interact in JEV (Li, X.D. et al., 2015). More recently, ZIKV NS4A and NS4B interactions have been reported to induce autophagy to benefit the virus life cycle (Liang et al., 2016).

Additionally, NS4B interacts with NS3 within the replication complex, dissociating the NS3 helicase from ssRNA enhancing helicase activity (Umareddy et al., 2006).

1.4.3.6 NS5

NS5 is responsible for viral genome replication across the *Flavivirus* genus. The N terminus of NS5 contains a methyltransferase (MT) domain, which caps the 5' end of the positive strand viral RNA. The virus cap aids polyprotein translation and helps the virus to evade the host immune response, preventing identification by pattern recognition receptors (Egloff et al., 2002; Ray et al., 2006; Issur et al., 2009; Daffis et al., 2010). The MT domain is followed by a short linker region to the RNA-dependent RNA polymerase (RdRp) domain. The RdRp has two mechanisms of RNA synthesis; *de novo* or primer-dependent initiation (Ackermann and Padmanabhan, 2001; Surana et al., 2014; Lim et al., 2013a; Xu, H.T. et al., 2017; Potisopon et al., 2017; Hercik et al., 2017). The activity of NS5 RdRp is affected by the highly conserved MT domain, which can increase RNA synthesis by altering RdRp conformation (Zhao, B. et al., 2017). The presence of the MT domain is essential for RNA synthesis by either *de novo* or elongation of a primed template, as shown by loss-of-function mutations (Potisopon et al., 2014). The functional ZIKV RdRp forms three different channels, to interact with the template RNA, the nascent RNA and NTPs (Fig 1.10) (Butcher et al., 2001).

Comparative analysis between Ugandan ZIKV strain MR766 NS5 and Brazilian strain PE243 NS5 has identified over 35 amino acid substitutions, yet the NS5 RdRp activities are very similar. Upon identification of these substitutions within the structure, they are found on the protein surface and do not affect the RNA synthesis activity in the RdRp centre. The substitutions could affect other host or viral protein interactions not currently identified (Zhao, B. et al., 2017).

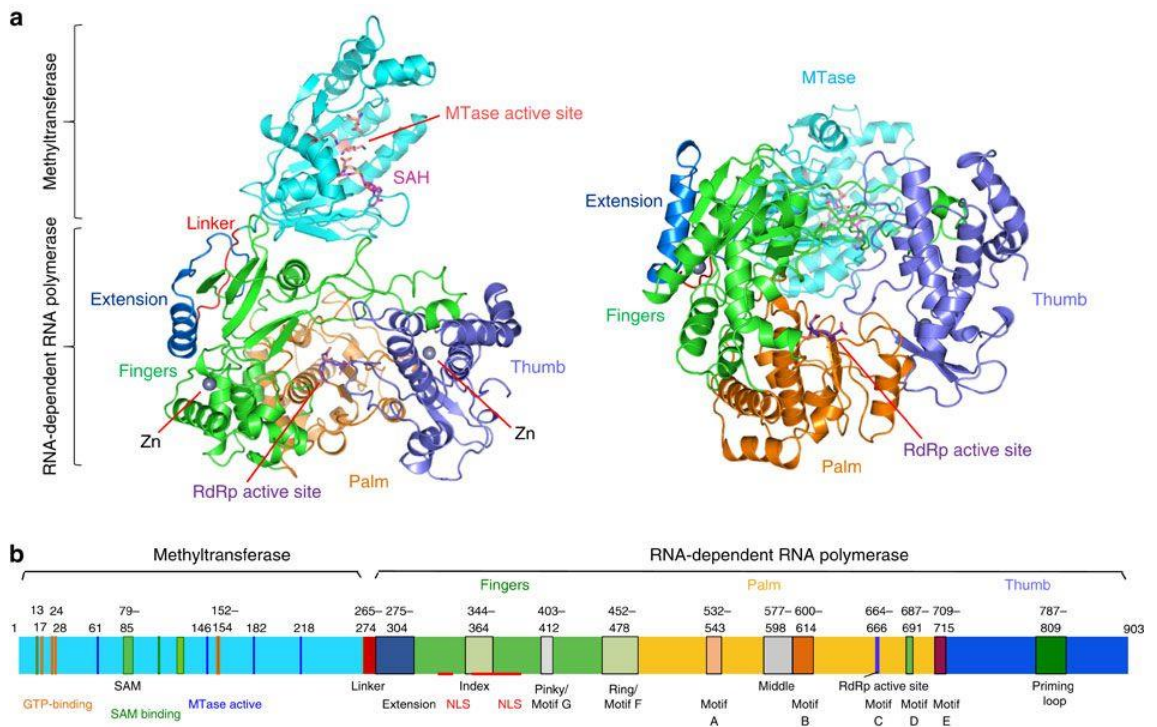


Figure 1.11 ZIKV NS5 Structure

A. Ribbon representation of ZIKV NS5 showing the arrangement of the MT and RdRp domains from top down and side on. B. Schematic of ZIKV NS5 protein showing structural motifs and key residues. Source (Zhao, B. et al., 2017).

1.5 Zika virus life cycle

1.5.1 Entry

ZIKV and other *Flaviviruses* are transmitted by a mosquito bite on the surface of the skin e.g. *A. aegypti*. The arboviral transmission route of a mosquito bite leads to skin cell and immune cell susceptibility. ZIKV particles enter the host cell by the envelope glycoprotein first binding multiple cellular receptors and adhesion factors (Table 1.1). Once engulfed into the cell by clathrin-mediated endocytosis the virus remains within the endosome as it matures until the virus fuses with the endosomal membrane.

1.5.1.1 Receptor binding & susceptible tissues

ZIKV infection utilises cellular receptors AXL, TIM-1 and others to infect dermal fibroblasts and epidermal keratinocytes, and DC-SIGN to enter dendritic cells and CD16+ monocytes (Hamel et al., 2015; Sun, X. et al., 2017; Persaud et al., 2018; Foo et al., 2017; Michlmayr et al., 2017; Lum et al., 2018). ZIKV is also highly infectious within embryonic brains and, to a lesser extent, adult brains, requiring AXL & TLR3 for infection of neural progenitor cells, astroglial and microglial cells (Nowakowski et al., 2016; Wells et al., 2016; Wang, Z.Y. et al., 2017; Meertens et al., 2017; Hamel et al., 2017; Stefanik et al., 2018).

ZIKV can also be transmitted via sexual contact. The human testis is well established to be infectable by ZIKV, with viral RNA detectable up to 100+ days post infection (Eurosurveillance editorial, 2016; Paz-Bailey et al., 2018). Sertoli cells and spermatozoa are also known to require AXL and Tyro3 respectively to become infected (Ma et al., 2017; Sheng et al., 2017; Siemann et al., 2017; Salam and Horby, 2018; Bagasra et al., 2017).

The most severe consequence of ZIKV infection is microcephaly of unborn children due to infection of neural progenitor cells (NPC), leading to restricted brain development (Qian et al., 2017; Li, C. et al., 2016a). Infection of NPC's requires virus to pass through the placenta where ZIKV-susceptible trophoblasts, Hofbauer and endothelial cells reside, rendering the tissue susceptible to virus infection via ZIKV interaction with receptors AXL, tyro3, TIM-1, TLR3 and TLR8 (Bayer et al., 2016; Quicke et al., 2016; Tabata, T. et al., 2016).

Additionally, other tissues have shown to be infected including the retina requiring AXL & tyro3 receptors (Zhao, Z. et al., 2017; Roach and Alcendor, 2017) and kidneys, however the receptors for kidney cell infections are currently unknown (Alcendor, 2017).

Primary Cell	Receptor	References
Brain		
Neural progenitor cells (NPCs)	AXL, TLR3	(Nowakowski et al., 2016; Wells et al., 2016; Wang, Z.Y. et al., 2017)
Astroglial cells	AXL	(Hamel et al., 2017; Stefanik et al., 2018; Chen, J. et al., 2018)
Microglial cells	AXL	(Meertens et al., 2017)
Placenta		
Hofbauer cells	AXL, Tyro3, TIM1	(Bayer et al., 2016; Quicke et al., 2016; Tabata, T. et al., 2016)
Trophoblasts	AXL, Tyro3, TIM1, TLR3, TLR8	(Bayer et al., 2016; Quicke et al., 2016; Tabata, T. et al., 2016)
Endothelial cells	AXL, Tyro3, TIM1	(Tabata, T. et al., 2016; Miner et al., 2016)
Skin		
Dermal fibroblasts	AXL, TIM-1, TYRO3, TLR3, RIG-I, MDA5	(Hamel et al., 2015; Persaud et al., 2018)
Epidermal keratinocytes	AXL, TIM-1, TYRO3, TLR3, RIG-I, MDA5	(Hamel et al., 2015)
Immune cells		
Immature dendritic cells	DC-SIGN	(Hamel et al., 2015; Bowen et al., 2018)
Dendritic cells	DC-SIGN	(Sun, X. et al., 2017)
CD14+ monocytes	Unknown	(Foo et al., 2017; Lum et al., 2018)
CD14+CD16+ monocytes	Unknown	(Foo et al., 2017)
Testis		
Sertoli cell	AXL	(Ma et al., 2017; Sheng et al., 2017; Siemann et al., 2017)
Spermatozoa	Tyro3	(Bagasra et al., 2017; Salam and Horby, 2018)
Kidney		
Renal mesangial cell	Unknown	(Alcendor, 2017)
Glomerular podocytes	Unknown	
Renal Glomerular Endothelial Cell	Unknown	
Retina		
Retinal pericytes	Tyro3, AXL	(Zhao, Z. et al., 2017)
Retinal microvascular endothelial cells	Tyro3, AXL	

Table 1.1 ZIKV Cellular Targets and receptors

1.5.1.2 Clathrin-mediated endocytosis

Clathrin has been reported to associate with the virus-containing vesicles for 80 seconds during DENV entry (van der Schaar et al., 2008), and is thought to be a necessary part of Flaviviruses entering cells, as WNV entry into Vero cells was inhibited with chlorpromazine, preventing clathrin-coated pit formation (Nawa et al., 2003). However DENV-2 can enter cells in the absence of clathrin, insinuating it is cell and virus-type dependent (Acosta et al., 2009).

Following receptor engagement adaptor proteins bind to the receptors cytoplasmic tails, subsequently a clathrin pit then surrounds the invaginating membrane containing the virion, eventually encapsulating it in a clathrin-coated vesicle (Chu and Ng, 2004). This separates from the plasma membrane via dynamin-mediated scission, forming an internalised clathrin-coated vesicle (Cocucci et al., 2014).

Once the virus is encapsulated, clathrin disassociates from the vesicle membrane (van der Schaar et al., 2008) and is transported by lymphocyte antigen 6 locus E (LY6E) tubules through the endocytic pathway (Hackett and Cherry, 2018). Five minutes post-entry of WNV and DENV the vesicles have matured to early endosomes (van der Schaar et al., 2008; Chu and Ng, 2004) which further mature to late endosomes. The endocytic compartment where *Flavivirus* membrane fusion occurs varies dependent upon the virus in question.

1.5.1.3 Membrane Fusion

The low-pH environment inside endosomes triggers conformational changes of the envelope homodimers on the virion surface (Figure 1.8 & Figure 1.12).

Flavivirus envelope proteins are well known for their pre and post fusion conformations. Prior to fusion the low pH environment in the endosomes results in one or more histidine residues on E become protonated (Harrison, 2008). Protonation results in the homodimers disassociating into monomers on the virion surface, releasing the fusion peptide loop previously hidden by interactions with domain I and II within a hydrophobic pocket. E proteins are very similar across the genus and contain three domains on the surface, the monomeric envelope proteins protrude domain II into the outer leaflet of the target membrane, exposing the fusion peptide at the tip of EDII (

Figure 1.12) (Bressanelli et al., 2004; Modis et al., 2005; Nayak et al., 2009; Zhang, Y. et al., 2004). Domain II of envelope mediates interactions between monomers leading to unstable trimerisation, which is then stabilised by domain I interactions (Liao et al., 2010).

Once E protein oligomerises into trimers and is bound to the target membrane, domain III folds back into a hairpin-like conformation forming a hemifusion intermediate where the inner leaflets remain intact and the outer leaflets interact with the target membrane. As the envelope protein continues to fold, the fusion pore forms and enlarges releasing the nucleocapsid (Bressanelli et al., 2004; Modis et al., 2004; Modis et al., 2005; Nayak et al., 2009).

Uncoating of the viral nucleocapsid is one of the least-studied steps in virus life-cycles. After virus envelope fusion with the endosome, the viral nucleocapsid remains intact, enters the host cell cytoplasm and must uncoat to release the viral genome to establish initial translation. However, the capsid protein is bound to the viral RNA with high affinity due to its negative charge, and forms oligomers. It is not known in-depth how the nucleocapsid dissociates.

The DENV capsid protein is degraded by a ubiquitin-proteasome-dependent process. During virus endocytosis, inhibition of host cellular E1 ubiquitin-activating enzyme prevents viral RNA uncoating (Byk et al., 2016). Additionally, inhibition of Hsp70 strongly reduces capsid stability and function, and reduced capsid oligomerisation, therefore suggestive of a role during virus coating and uncoating (Byk et al., 2016). Furthermore, Valosin-Containing Protein (VCP) and p97 are proposed to disassemble ubiquitylated nucleocapsids of YFV (Ramanathan et al., 2019). ST-148 is a novel inhibitor of DENV uncoating and has shown to bind to capsid, however its mechanism is unknown (Byrd et al., 2013).

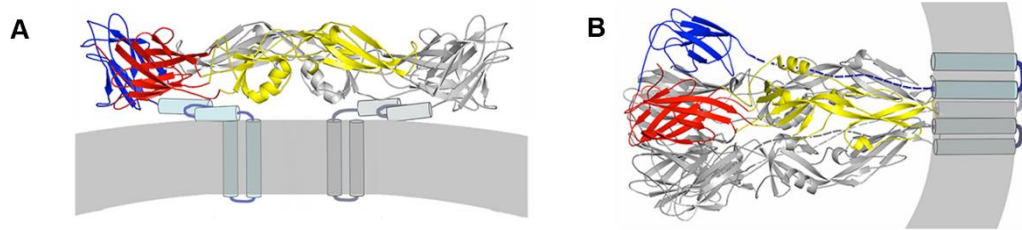


Figure 1.12 Conformational states of the dengue virus E protein

A. Dimeric DENV E protein structure present on the mature virion surface, viewed side on with the viral membrane represented in grey and the protein ectodomain in ribbons, with one monomer coloured coded as in previous figures, domains I, II and III in red, yellow and blue respectively. E stem and TM domains shown as helix-loop-helix. Structure based on (Zhang, W. et al., 2003). B. Trimeric DENV E protein conformation upon virion acidification (Schmidt et al., 2010).

1.5.2 Translation

The *Flavivirus* RNA genome comprises a single open reading frame (ORF), which is translated into a polyprotein. The N-terminus of the nascent polyprotein contains an ER-localisation signal that promotes rapid association of ribosomes translating the viral RNA within the ER membrane. The resulting translated polyprotein remains associated within the membrane and is then co- and post-translationally processed by both host and viral proteases.

Flavivirus RNA similarly to cellular mRNA contains a 5' cap enabling canonical translation initiation (Garcia-Blanco et al., 2016). Conversely, it does not possess a poly-A tail, which is required by cellular mRNA for stability and association with poly-(A) binding protein (PABP) to initiate translation. Although, viral RNA overcomes this, and DENV 3' associates with PABP through binding to the conserved 3' stem-loop adjacent to the two dumb-bell structures. (Polacek et al., 2009).

Additionally, DENV can also translate by cap-independent mechanisms when cap-dependent translation is inhibited, this is likely regulated by both 5' and 3' UTRs (Edgil et al., 2006). More recently, uncapped ZIKV RNA has been shown to initiate infection with a resulting high viral titre, suggesting the use of an internal ribosome entry site (IRES) to control translation. HCV and other

members of the *Flaviviridae* also use an IRES to initiate translation (Song et al., 2019; Hercik et al., 2017).

Furthermore, RNA stem-loop (SL) structures also modulate translation. A conserved 5' UTR SL structure within the capsid-coding region named capsid hairpin (cHP) is also involved in *Flavivirus* translation (Clyde and Harris, 2006; Li, P. et al., 2018). Altering the structure of the cHP decreases initiation of the first AUG start codon, highlighting the role of cHP for correct translation initiation (Mazeaud et al., 2018). Moreover, other RNA structures are also involved in translation including two 3' UTR pseudoknots 5' Ψ and 3' Ψ (Manzano et al., 2011); these have been identified in ZIKV, DENV, JEV and YFV (Olsthoorn and Bol, 2001; Zhu, Z. et al., 2016).

1.5.3 Polyprotein processing

The ZIKV genome encodes fourteen functional subunits. Thus, during and after translation the ZIKV polyprotein needs to be processed and cleaved by viral and host proteases for the individual proteins to carry out their role during the virus life cycle.

Viral protease NS3 and cofactor NS2B cleave seven of the 12 cleavage sites shown in

Figure 1.5 (Assenberg et al., 2009). The viral protease cleaves the junctions between: C/Ci, pr/M, NS2A/NS2B, NS2B/NS3 (self-cleaved), NS3/NS4A, NS4A/2k, and NS4B/NS5. However, the host protease furin, present within the Golgi, is also capable of cleaving pr/M (Stadler et al., 1997). Four of the remaining cleavage sites Capsid/precursor, Membrane/Envelope, Envelope/NS1, and 2k/NS4B are presumed to be targets of one or more host proteases as they have high sequence conservation across the genus. The remaining cleavage site NS1/NS2A is also conserved across the genus, yet it is cleaved by an unknown protease (Sun, G. et al., 2017). It is important to consider that not all cleavage sites and proteases responsible have been tested experimentally, they have been inferred by analysis of ZIKV and related virus sequence alignments.

1.5.4 Virus genome replication

The viral RNA genome is a template for multiple functions: the formation of new replication complexes, production of viral proteins and packaging into new virus particles.

Replication takes place in remodelled ER membranous replication factories, where the concentration of necessary components is increased, and a scaffold is constructed. Vesicle packets are linked to the cytoplasm by a 10 nm pore opening (Paul and Bartenschlager, 2013; Hamel et al., 2015). This pore could lead to release of positive stranded viral genomes to be translated for viral protein production and/or packaging into virus particles, also occurring in the ER (Cortese et al., 2017; Welsch et al., 2009).

NS5 protein is essential for replication to take place due to its RNA-dependent RNA polymerase (RdRp) activity. NS5 binds to stem-loop A at the 5' of the viral genome to initiate synthesis (Filomatori et al., 2006). The first round of synthesis generates a negative stranded viral RNA intermediate, which is subsequently used as a template to generate multiple positive stranded viral genomes. This results in a higher number of positive stranded RNA molecules to negative stranded, in DENV this is observed to be 10 to 100 times greater (Guyatt et al., 2001; Cleaves et al., 1981).

For synthesis of the viral negative strand RNA, the genome must circularise into a panhandle-shaped conformation via 5' and 3' UTR interactions. Circularisation allows NS5 to transfer for the SL A structure on the 5' UTR to the 3' SL at the 3' UTR (Hodge et al., 2016), allowing NS5 to polymerise multiple positive stranded RNA copies from the one negative stranded RNA intermediate.

Similar to translation, RNA secondary structures play a role in RNA genome synthesis. Previously mentioned pseudoknots 5' Ψ and 3' Ψ additionally regulate replication and mutations disrupting the pseudoknots reduce viral genome replication (Olsthoorn and Bol, 2001; Manzano et al., 2011).

Additionally, NS3 is known to be involved in viral replication through direct interactions with NS5 (Takahashi et al., 2012). The mechanism of NS3 helicase within genome replication is not known, however it is thought if viral replication involves dsRNA forming as an intermediate, NS3 helicase may be required to

unwind the strands, thereby allowing for nascent viral RNA to be synthesised (Mazeaud et al., 2018).

1.5.5 Capping

The majority of cellular mRNAs contain a cap structure at their 5' end, which consists of a N-7 methylguanosine (m7G) moiety linked through a 5'-5' inverted triphosphate bridge to the first nucleotide of the nascent mRNA. Cellular mRNA caps are important for splicing, transport, stability and recognition for translation (Banerjee, 1980; Furuichi & Shatkin, 2000; Ghosh & Lima, 2010). Similarly, most virus RNAs contain a similar cap, functioning to evade the host immune response through protecting the 5' triphosphates from the innate immune system (Pichlmair et al., 2006). The cap also mimics cellular mRNA through 2'-O methylation (Daffis et al., 2010; Zust et al., 2011), in addition to aiding viral replication through translation enhancement mediated by N-7 methylation (Ray et al., 2006).

Flavivirus RNAs are capped via the same mechanism as host mRNA, involving RTPase, GTPase and methyltransferase (MTase). However, the process occurs in the cytoplasm rather than the nucleus, so viral proteins carry out capping. RTPase activity is retained by the NS3 C-terminal domain and NS5 domains function as a GTPase and a MTase (Li, K. et al., 2014; Issur et al., 2009). The process of capping involves removing a phosphate from the 5' end of the nascent RNA, generating 5' diphosphate RNA from 5' triphosphate RNA. RTPase, followed by transferring GMP moiety from GTP to the 5' diphosphate RNA forming the core structure of the cap, finally methylation of the guanine at N-7 and ribose at 2'-O forming a type-1 cap structure (Dong et al., 2014).

1.5.6 Virus assembly, budding, maturation and release

The newly synthesised RNA within replication complexes must exit and initiate virus assembly. Assembly begins as the viral RNA genome associates with the basic capsid protein, which has a high affinity to negatively charged viral RNA due to its acidic charge. The nucleoprotein complex must then be packaged one copy per virus particle, however no packaging signal has currently been identified (Pong et al., 2011).

The nucleoprotein complex is then enveloped by an invagination into the ER membrane, which displays E and prM heterodimers on its luminal surface,

anchored through their TMDs, potentially recruited by NS2A (Welsch et al., 2009). The nucleoprotein buds through catalysed by the endosomal sorting complex required for transport (ESCRT) and membrane scission occurs (Tabata, K. et al., 2016), forming an immature virus particle (Welsch et al., 2009; Junjhon et al., 2014). Additionally this area of the ER will display an array of lipids which have been recruited by viral proteins, such as NS4A, to be included in the virus membrane (Leier et al., 2020). The virus particles then bud away from the ER and enter the secretory pathway as immature virions, characterised by the spikey appearance of E trimers on the surface, and the presence of the prM precursor protein within the particle (Sirohi and Kuhn, 2017; Tan et al., 2020; Prasad et al., 2017).

Upon transportation through the secretory pathway the virus particles mature; the acidic environment in the TGN results in major conformational rearrangements of the spikey trimeric E into an antiparallel dimeric E herringbone organisation (Yu et al., 2008). This rearrangement reveals the furin cleavage site within prM, cleavage of which within the TGN matures the virus particle; the characteristic spikes are no longer present (Stadler et al., 1997; Sevvana et al., 2018). However, the cleaved pr peptide remains associated with the E protein, preventing the exposure of the E fusion loop. Once released from the cell, the neutral environment stabilises the E protein resulting in dissociation of pr from the mature particle (Yu et al., 2009).

However, the maturation step is inefficient; ~40 % of particles are not fully mature and undergo varying degrees of pr cleavage, which in turn determines their infectivity (Dowd et al., 2014; Junjhon et al., 2008). Upon maturation, virions are trafficked via multivesicular bodies (MVBs) from the TGN to the cell surface. This section of the virus life cycle is not well studied, yet it is thought the majority of virions are released as individual particles (Burlaud-Gaillard et al., 2014). There is some evidence suggesting the virions present in the ER undergo repackaging into individual membrane bound vesicles (Sager et al., 2018). Though vesicles containing virus particles have been observed enclosed within larger membrane bound structures too (Liu, J. et al., 2018). Once at the cell surface, membrane bound vesicles fuse with the cell membrane, releasing virus particles into the extracellular milieu.

1.6 ZIKV model systems

ZIKV is unable to replicate efficiently within immunocompetent mice. Commonly used model inbred mouse strains such as C57BL/6, CD-1 and BALB/c are not highly permissive hosts of ZIKV and detectable levels of viral RNA and/or infectious virions are very low (Lazear et al., 2016; Rossi et al., 2016).

The resistance of mice becoming an efficient ZIKV host is likely due to the differences between human and mouse STAT2. In humans, the viral NS5 protein degrades human STAT2, thereby inhibiting the type I IFN response (Grant et al., 2016). However, this same process does not occur in mice, as NS5 cannot degrade mouse STAT2, therefore the response to type I IFN is not interfered.

Interferon receptor and STAT knockout mice models have been developed (Morrison and Diamond, 2017), however these models are not reliable for investigating the interactions of ZIKV with the host immune response. An alternative ZIKV mouse model has been developed with a knock-in human STAT2 replacing mouse STAT2, allowing mouse adapted ZIKV strains to replicate in the host and maintain the interferon responses (Gorman et al., 2018).

Non-human primates (NHPs) are an established animal model of disease pathogenesis and therapeutic research due to their relatedness to humans. NHPs are also thought to be part of the ZIKV sylvatic transmission cycle with mosquitos in the wild and are known to be permissive to the virus (Haddow et al., 2012). NHPs rhesus, cynomolgus, and pigtail macaques are infectable subcutaneously with the African MR 766 strain, or more recently adapted Asian ZIKV strains at doses comparable to those derived from infected mosquitos (Li, X.F. et al., 2016; Dudley et al., 2016). Moreover, the effect of ZIKV infection during pregnancy has been investigated utilising both mice and NHPs, with both displaying ZIKV associated pathological effects upon both the placenta and infected foetal brain, consistent with human disease (Mysorekar and Diamond, 2016; Adams Waldorf et al., 2016).

The *in vivo* experiment carried out herein comprised a model established by Marieke Pingen and Clive McKimmie. The model involves C57BL/6 mice injected with an anti-mouse IFNAR-1 antibody prior to virus inoculation, an effective Type I IFN receptor inhibitor (Lazear et al., 2016). Additionally

mosquito bites are included at the virus inoculation site, which is known to enhance virus infection (Pingen et al., 2016).

1.7 Vaccines

Vaccine development against ZIKV began after reports of microcephaly in babies of infected mothers in Brazil in late 2015. In 2017 there were forty ZIKV vaccines in development (Poland, 2018). The large number of vaccines included live-attenuated, inactivated whole viruses, peptide subunit vaccines, DNA and mRNA vaccines and viral vectored vaccines. The majority of these vaccines have been tested using non-human primates and/or immunosuppressed mice (Fragoso et al., 2018).

In 2019 eight of the forty vaccines had reached Phase I studies, of which three are DNA vaccines and have advanced to human testing (Tebas et al., 2017; Gaudinski et al., 2018). Of these three vaccines one has reached phase II studies named ZKADNA085-00-VP, in development by VRC. ZKADNA085-00-VP comprises of a DNA construct of full-length prM-Envelope from ZIKV strain H/PF/2013, with JEV stem and transmembrane regions, to enhance prM-Env protein expression and secretion (Dowd et al., 2016).

As mentioned previously, due to the similarity between DENV and ZIKV, antibodies targeted at one virus may also recognise epitopes of the other. Although virus cross-reactivity could allow cross-protection, it can also cause antibody-mediated enhancement (ADE) of infection, which can prove fatal when patients are sequentially infected by different DENV serotypes. However, researchers designing vaccines investigate this throughout the process. Immunisation of mice with ZIKV E dimers resulted in dimer-specific antibodies protecting the host and its prospective foetus. The dimer lacks prM and contains a triple sulphide bond to keep the fusion loop epitope hidden, both of these features contribute to reducing cross-reactivity and ADE (Slon-Campos et al., 2019).

1.8 Antivirals and pharmacological disease management

The current treatment for patients suffering from ZIKV involves rest, fluid and medication such as paracetamol to relieve symptoms. However, there is a need for targeted antivirals to prevent further spread of infection including across the placenta, and not just treatment of symptoms.

Direct-Acting Antivirals (DAA) directly target circulating virus particles or replicating virus within cells, to repress virus load to a point where the immune system can eliminate the virus-infected cells and prevent spread. Additionally, it is preferential for ZIKV antivirals to cross the blood-brain barrier due to the neurological symptoms associated with the ZIKV infection. Over recent years there have been many high-throughput screens and compound assays to help identify inhibitors of ZIKV infection. These have comprised potential inhibitors derived from small molecules and peptides, including both newly designed compounds and repurposed licenced/generic drugs.

Peptide AH-D was engineered to be a brain penetrating antiviral that acts through disrupting the virus lipid envelope. AH-D is derived from the first 27 amino acids of HCV NS5A, and has been shown to inhibit ZIKV infection in mice, and there is potential to translate this compound to other related enveloped viruses (Jackman et al., 2018).

Another approach is to target host cell proteins involved in virus replication; abrogating infection by this method is less likely to result in resistance mutations. Hsp70 is thought to be required for several different stages of the virus life cycle and inhibiting its activity could therefore prevent virus replication. Additionally, use of the Hsp70 inhibitors including JG18 and JG40 *in vitro* have negligible toxic effects in human cells, although in clinical trials some Hsp inhibitors have shown adverse side effects (Taguwa et al., 2019; Pujhari et al., 2019; Rajan et al., 2011).

A popular route of antiviral identification is repurposing previously approved or identified compounds, due to the availability of clinical and toxicity data. Arbidol is a synthetic drug developed 30 years ago to target influenza A virus (IAV). However, Arbidol has shown potential to target viruses from a variety of families. Recently Arbidol was reported to have a dose dependent effect on ZIKV infection of both African and Asian lineages (Fink et al., 2018). The method by which Arbidol inhibits infection is not known, however it is thought it could target multiple stages of the virus lifecycle (Fink et al., 2018; Belokrinitskaya et al., 2012).

A high throughput screen of almost 500 flavonoid derivatives, naturally found in plants and thought to have low toxicity, identified three hits which gave over 50 % inhibition and positive cell viabilities (Lee, J.L. et al., 2019). Further screening

recognised that compound ST02393, known as pinocembrin, had the strongest inhibition and therefore was selected as the lead compound. Pinocembrin has previously been used for its antibacterial, anti-inflammatory, anti-fungal properties and cancer treatment (Rasul et al., 2013). Additionally, pinocembrin is reported to have neuroprotective effects, relevant due to the GBS and microcephaly symptoms of ZIKV. Phase I clinical trials showed pinocembrin given at 120 mg/day by IV is safe and tolerable in healthy adults (Lee, J.L. et al., 2019). However, its mechanism of action against ZIKV is not known.

Moreover, a popular target for viruses is the polymerase through using nucleoside analogues/derivatives. BCX4430 (Galidesivir) and Sofosbuvir are both previously used analogues that additionally show activity against ZIKV. BCX4430 was originally derived from a HCV drug development programme, however it was developed as a potential treatment for Ebola and Marburg viruses (*Filoviruses*) (Julander et al., 2017). Similarly, Sofosbuvir inhibits HCV and was approved for a combination treatment by the FDA in April 2013 (Ferreira et al., 2017). Other ZIKV targets, such as the methyltransferase activity of NS5 and NS2B/NS3 protease, have been targeted by potential small molecule inhibitors (Wang, L. et al., 2019)

Since 2014 many antiviral candidates have shown to inhibit replication *in vitro* and some *in vivo*. The only therapeutic to have undergone clinical testing is monoclonal antibody Tyzivumab (ClinicalTrials.gov Identifier: NCT03443830, Sponsor: Tychan Pte Ltd). Thus far, no effective ZIKV antiviral has been licenced to date, indicating the difficulty of translating experimental results to the clinic (Saiz and Martin-Acebes, 2017).

1.9 M protein as an antiviral target

1.9.1 M protein structure and function

Within the mature *Flavivirus* virion, M protein resides in the membrane forming heterodimers with E protein in a herringbone-like organisation forming a stable virus surface. Upon virus entry, the E proteins disassociate from M protein, forming E trimers and the M protein structure and stoichiometry is not known. Additionally, the role of M protein in this environment is not known.

However, *Flavivirus* M protein shares characteristics with known viroporins, including small size and hydrophobicity. The C-terminus of DENV M was shown

to form a channel *in vitro* using lipid bilayers, with activity sensitive to hexamethylene amiloride (HMA), an ion channel inhibitor previously used to block HIV-1 Vpu viroporin activity, as well as by somewhat lower concentrations of amantadine, the classical inhibitor of IAV M2 proton channels (Premkumar et al., 2005). Accordingly, in the 1980's it was also shown amantadine and its methylated derivative rimantadine were capable of suppressing DENV replication (Koff et al., 1981; Koff et al., 1980). Conversely, DENV M has been shown to be unable to form a channel when expressed in *Xenopus laevis* oocytes under acidified extracellular conditions (Wong et al., 2011). Our own collaborative studies (Dr Ian Tietjen, Simon Fraser University, CA) showed full length DENV M protein displayed channel activity within a surrogate cell culture model monitoring vesicular acidity using a pH-dependent fluorophore, "LysoTracker Red DND-99" (Invitrogen) (Wozniak et al., 2010). It was shown vesicular pH increased within M-transfected cells, is reversed by the addition of viroporin inhibitor rimantadine (unpublished, personal communication, Ian Tietjen, Wistar Institute, Philadelphia).

1.10 Viroporins

Viroporins are small hydrophobic membrane proteins encoded by numerous viruses, which form oligomeric channels within cellular membranes via hydrophobic interactions, allowing passage of ions and small molecules (Carrasco, 1995; Gonzalez and Carrasco, 2003; Scott and Griffin, 2015). Viroporin monomers are usually shorter than 120 amino acids in length, and play roles during various parts of the virus life cycle, namely virion morphogenesis and release, however others have distinct mechanisms in virus entry and genome replication.

Many clinically relevant RNA and DNA viruses encode viroporins including hepatitis C virus (HCV) p7, Influenza A virus (IAV) M2, Human Immunodeficiency virus 1 (HIV-1) Vpu, Picornavirus VP4, and Human Papilloma virus type 16/18 (HPV) E5 (Clarke et al., 2006; Ewart et al., 1996; Pinto et al., 1992; Holsinger and Lamb, 1991; Sugrue and Hay, 1991; Wetherill et al., 2012; Danthi et al., 2003; Panjwani et al., 2014; Kalko et al., 1992). However, proteins encoded by other viruses also show potential to form viroporins, including *Flavivirus* M protein (Premkumar et al., 2005), Alphavirus

6k (Sanz et al., 1994; Melton et al., 2002) and Coronavirus (CoV) E protein (Wilson et al., 2004).

Although viroporins vary in their structure and functions their simplicity often means they lack the same level of regulatory behaviour as cellular ion channel gating. Furthermore, the compact nature of virus genomes, results in functional redundancy making investigations into these proteins more difficult as they commonly have multiple functions additionally to their role as an ion channel.

Despite their simplicity, many viroporins display weak ion selectivity and specific gating behaviour (Shimbo et al., 1996; Grice et al., 1997). For example, the well-characterised viroporin IAV M2 is a proton channel, which acidifies the virion interior. The M2 channel is gated via HIS37 which when neutral the channel is open to the external environment of the virus but closed to the interior of the virus. Upon diffusion of protons into the channel it becomes open to the virus interior, however closed to the external environment. Indicating a transporter-like mechanism which alternates between the two conformations (Figure 1.13)(Okada et al., 2001; Khurana et al., 2009).

Ion channels are known to be highly effective drug targets. For example, Amlodipine, a calcium channel blocker, is used to treat hypertension and Zolpidem, a GABAA receptor antagonist, is used to treat insomnia. Therefore, channels encoded by viruses could also be an ideal drug target, to stop viral replication and prevent viral infection spreading. M2 was the first viroporin to be targeted by a licensed adamantyl drug, amantadine, in the 1960s (Baker et al., 1969; Davies et al., 1964; Sabin, 1967; Togo et al., 1968; Wingfield et al., 1969). However, the mode of action for amantadine was unknown until the 1980s (Hay et al., 1985). Amantadine and amino-adamantane derivatives including rimantadine not only target M2, they can also inhibit HCV p7, E5 and CoV E and other viroporins, and have shown activity against dengue virus replication (Griffin, S.D. et al., 2003; Torres et al., 2007; Lin, C.C. and Chen, 2016; Wetherill et al., 2012). However, amantadine and Rimantadine are no longer used to treat IAV due to mutations arising within the M2 sequence, rendering them unusable. Due to the failings of amantadine in the treatment of IAV, many viroporins have been disregarded as viable drug targets.

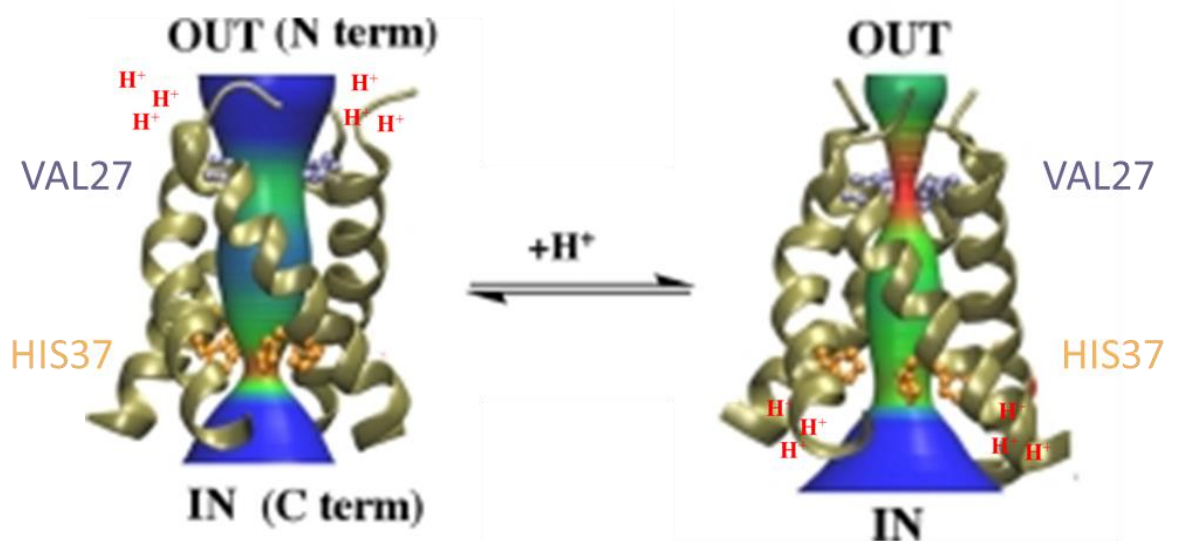


Figure 1.13 IAV M2 as a proton transporter

Schematic of transporter-like mechanism of proton conductance through the IAV M2 channel. M2-TM exists in two conformations. At high pH the VAL27 region opens while the HIS37 region narrows, and the opposite is found at low pH (Khurana et al., 2009).

1.10.1 Influenza A Virus (IAV) M2

IAV encodes M2 a short transmembrane protein of 97 amino acids. M2 is a well-characterised viroporin oligomerising into a tetrameric proton selective channel (Lamb et al., 1985; Sugrue and Hay, 1991; Hay et al., 1985). M2 comprises three domains, the N-terminal domain, a signal anchor TMD and a cytoplasmic domain, each playing roles during the virus life cycle. The M2 ectodomain is necessary for incorporation of M2 into virions (Park et al., 1998). The TMD mediates oligomerisation of four M2 monomers into a proton-selective homotetrameric ion channel (Duff and Ashley, 1992), driven by stabilising disulphide bridges and non-covalent bonds (Holsinger and Lamb, 1991; Castrucci et al., 1997). Lastly, the cytoplasmic tail is reported to be involved in genome packaging, virus budding, membrane scission and undergoes acylation and phosphorylation post-transcriptional modifications of three serine residues (McCown and Pekosz, 2005; Holsinger et al., 1995; Rossman and Lamb, 2013).

In the life cycle of certain strains of IAV, the M2 homotetramer is responsible for modulating pH in the TGN during transport of the HA to the cell surface for virion assembly. IAV virions have two major surface glycoproteins hemagglutinin (HA) and neuraminidase (NA). HA is required to bind sialic acid

on the target cell, however if exposed to a low pH HA undergoes conformational changes preventing this binding, hence M2 must prevent pH lowering to maintain HA conformation (Cross et al., 2001; Ciampor et al., 1992; Grambas and Hay, 1992). Secondly, the M2 homotetramer present in the virion is involved in IAV entry, allowing protons into the virion interior leading to uncoating and dissociating viral ribonucleoproteins (RNPs) from M1 protein (Pinto et al., 1992; Zoueva et al., 2002; Helenius, 1992)

Additionally M2 has minor roles during the life cycle including stabilising virus budding on the cell surface and alters the membrane curvature (Rossman et al., 2010). The C-terminal of M2 contains a highly conserved region of 54 amino acids which had little impact on the M2 proton channel activity (Tobler et al., 1999). It is reported this C-terminal region is vital for vRNPs being incorporated into budding particles (McCown and Pekosz, 2006; Grantham et al., 2010).

The pore lining residues of the M2 homotetramer channel were investigated using cys scanning and oxidative disulphide cross-linking which showed SER22, SER23, VAL27, ALA30, SER31, GLY34, HIS37 and TRP41 lining the pore (Pinto et al., 1997; Bauer et al., 1999; Shuck et al., 2000). VAL27 and HIS37 both cause restrictions in the channel lumen, however HIS37 is a pH sensor, becoming protonated in an acidified environment and TRP41 acts as the gate (Stouffer et al., 2008; Wang, C. et al., 1995).

Early studies investigating the channel activity of M2 involved patch clamping *Xenopus laevis* oocytes confirming M2 channel activity and its sensitivity to amantadine (Pinto et al., 1992). Additionally, TMD M2 peptides showed proton selective channel activity *in vitro* using planar lipid bilayers (Duff & Ashley, 1992). Further studies identified acidic pH activation focussing on the conserved HIS37 residue (Shimbo et al., 1996; Wang, C. et al., 1993; Wang, C. et al., 1994; Wang, C. et al., 1995).

Structural information has been used to investigate the potential of alternative antiviral compounds targeting S31N, identifying compounds to be taken forward to *in vivo* testing (Drakopoulos et al., 2018; Li, F. et al., 2017; Li, F. et al., 2016a; Li, F. et al., 2016b; Musharrafieh et al., 2019; Thomaston and DeGrado, 2016; Wang, J. et al., 2013; Wang, Y. et al., 2018; Wu, Y. et al., 2014; Scott et al., 2020). There are over twenty M2 structures available, however all of these are of truncated proteins, either derived from the transmembrane region or C-

terminally extended conductance domain peptides due to their role in channel formation. However TM and conductance domain (CD) amantadine binding varies from structure to structure (Schnell and Chou, 2008; Stouffer et al., 2008). Structures of the TM region report a single amantadine molecule occluding the lumen, conversely too CD structures showing four rimantadine molecules binding to the channel periphery. This binding controversy has not been resolved due to a lack of comparative studies (Andreas et al., 2010; Cady, S. et al., 2011; Cady et al., 2010; Cady, S.D. et al., 2011; Du et al., 2009; Hu et al., 2011; Kozakov et al., 2010; Ohigashi et al., 2009; Pielak et al., 2011; Pielak et al., 2009; Rosenberg and Casarotto, 2010).

1.10.2 Hepatitis C Virus (HCV) p7

HCV p7 is a small hydrophobic protein of 63 amino acids, predicted to have two TMDs separated by a short cytosolic loop consisting of conserved basic residues (Carrere-Kremer et al., 2002). HCV p7 was discovered during characterisation of HCV polyprotein cleavage, which revealed the cleavage of E2-p7-NS2 and E2-p7 are inefficient processes (Lin, C. et al., 1994; Mizushima et al., 1994; Carrere-Kremer et al., 2004).

HCV p7 is predominantly found in the endoplasmic reticulum membrane (Lin, C. et al., 1994; Griffin, S. et al., 2005; Bentham et al., 2013). Monomeric p7 is reported to form a hairpin structure in membranes (Montserret et al., 2010; Foster et al., 2014; Luik et al., 2009), although this has been debated (OuYang et al., 2013). Two monomeric NMR structures have been published (PDB 2MTS and 3ZD0) (Foster et al., 2014; Cook et al., 2013). However, there are variations potentially due to varying pH (PDB 2MTS, pH 4.0 and PDB 3ZD0, pH 7.0) and varying conditions (detergent or Methanol). Monomeric p7 oligomerises into both hexameric and heptameric higher order structures (Clarke et al., 2006; Griffin, S.D. et al., 2003; Luik et al., 2009). p7 has been shown to exhibit channel activity in various *in vitro* assays including: *Black lipid membranes* (Premkumar et al., 2004; Griffin, S.D. et al., 2003; Pavlovic et al., 2003; Saint et al., 2009; Whitfield et al., 2011; Clarke et al., 2006), patch-clamping (Breitinger et al., 2016; OuYang et al., 2013) and liposome-based assays (Antoine et al., 2007; Madan et al., 2007; Montserret et al., 2010; StGelais et al., 2007).

To further investigate the structure of oligomeric p7, molecular dynamic techniques were used to construct an *in silico* heptameric channel model (Foster et al., 2014). Conversely two hexameric structures have been published, firstly an electron microscopy structure of genotype 2a p7 with similar monomeric conformations to previous structures (Luik et al., 2009), secondly an NMR structure of genotype 5a (PDB 2M6X). However the structure of the monomers in 2M6X differ (OuYang et al., 2013). PDB 2M6X monomers have a staple-like conformation, whereas all other monomers exhibit hairpin like conformations. This dissimilarity could be due to the varying genotypes, however this structure has been queried due to potential artefacts from alkyl-phosphocholine detergents (Oestringer et al., 2018), disputed by the authors (Chen, W. et al., 2018).

Previous NMR studies using synthetic peptides determined the secondary structure elements and along with molecular dynamic simulations identified the pore lining helix and residues (Montserret et al., 2010; Chew et al., 2009). Similarly to M2, acidic pH enhances activity of some p7 proteins, which is hypothesised to be due to HIS17 protonation. However, for M2 this protonation leads to a conformational change in gating residue TRP41, whereas protonation of p7 HIS17 is reported to cause protomers to rotate. This protonation mechanism aligns with data suggesting p7 is stimulated by lower pH and can conduct protons (StGelais et al., 2007; Wozniak et al., 2010). However, HIS17 are not well conserved between p7 proteins. Consequently, HCV genotypes respond to pH with varying levels of sensitivity (Atkins et al., 2014; Li, H. et al., 2012). Mutation of HIS17 had little effect on HCV virion production of genotype 2a isolate JFH-1 (StGelais et al., 2009). Additionally PHE25 is hypothesised to act as a gate of heptameric p7 channels, mutation resulted in a hyperactive channel in liposome assays (Foster et al., 2011).

The HCV p7 channel is selective for positively charged ions *in vitro* (Griffin, S.D. et al., 2003; Premkumar et al., 2004; Pavlovic et al., 2003) and proton channel activity is seen within HCV infected cells (Wozniak et al., 2010). Thus, p7 can be substituted by IAV M2 in a cell-based assay transporting aforementioned pH sensitive HA (Griffin, S.D. et al., 2004). Additionally viral genomes containing mutant p7 cannot support infectious virus production, however can be restored

by *trans*-complementing with IAV M2 (Wozniak et al., 2010; Bentham et al., 2013).

Although p7 is not essential for viral replication, it is critical for efficient egress of virus particles, leading to identification as a HCV drug target (Steinmann et al., 2007a; Yi, M. et al., 2007; Jones et al., 2007). Previously studied M2 inhibitors such as adamantanes and imino sugars can block some p7 genotypes channel function and virion production in cell culture (Griffin, S. et al., 2008; Steinmann et al., 2007b) however resistance mutations to rimantadine and imino sugars have been identified (Foster et al., 2011; Mihm et al., 2006).

pH maturation happens at a late stage in HCV particle production either before or during particle release, directly influenced by p7 (Atkins et al., 2014; Wozniak et al., 2010). The majority of HCV particles reside in the ER at neutral pH (Gastaminza et al., 2008), p7 may play a role controlling and restricting secretion of the HCV particle, by increasing the pH of the secretory pathway. However, HCV cell-cell spread is less sensitive to p7 inhibitors (Meredith et al., 2013) suggesting the pathway is less dependent upon channel activity (genotype dependent).

Additionally p7 is suggested to have channel activity during the virus entry stage of the virus life cycle due to improved hepatocyte uptake of p7 containing HCV like-particles (Saunier et al., 2003) and infectious HCV was inhibited by p7 channel inhibitors during entry (Griffin, S. et al., 2008), however p7 has not been detected in infectious particles (Vieyres et al., 2013; Catanese et al., 2013).

Furthermore, p7 interacts with both non-structural protein 2 (NS2) and NS5A and P7-NS5A co-localisation is required for virus assembly. Targeted mutations of p7, NS2 and E2 has suggested they contain signals, which act synergistically to direct NS2 towards an interaction with NS5A positive membrane lipid droplets (Jirasko et al., 2008; Jirasko et al., 2010; Boson et al., 2011).

1.10.3 Human immunodeficiency Virus type-1 (HIV-1) Vpu

HIV-1 Vpu protein is 81 amino acids long and contains three domains, a short endoplasmic domain and a TMD followed by a longer cytoplasmic domain. Unlike some other viroporins, Vpu is not found within HIV-1 virions and is translated late in the viral replication cycle along with Env from the same mRNA

(Cohen et al., 1988; Strebel et al., 1988). Vpu exhibits multiple roles including inducing CD4 degradation, preventing detection by the immune system (Willey et al., 1992a; Willey et al., 1992b), antagonising tetherin, promoting virion budding from the cell surface (Neil et al., 2008) and ability to form a viroporin (Schubert et al., 1996; Ewart et al., 1996)

Vpu has shown channel activity when present in *Xenopus* oocytes (Schubert et al., 1996), planar lipid bilayers permeable to sodium and potassium ions and sodium-permeable *E.coli* membranes (Ewart et al., 1996).

Inhibition studies of Vpu channels have reported amiloride derivatives can successfully inhibit Vpu peptide channels *in vitro*, and inhibit budding of HIV-1 VLP in cell culture (Ewart et al., 2002). Mutagenesis studies show an Ala18His substitution generates an amantadine-sensitive HIV-1, further supporting its role as a channel protein (Hout et al., 2006). The mechanism behind this sensitivity is the formation of a HxxxW tetrad in the Vpu sequence, which is present in the IAV M2 sequence (Sharma et al., 2011).

Conversely Vpu is proposed to not exhibit channel activity itself, but by interfering with cellular channel Twik-related acid sensitive K⁺ (TASK) channel TMDs (Coady et al., 1998). Vpu is suggested to degrade the aforementioned channels, therefore preventing the flow of potassium ions (Hsu et al., 2004).

1.10.4 Human Respiratory Syncytial Virus (hRSV) SH

The SH protein encoded by hRSV is a small hydrophobic protein of 64-65 amino acids predicted to have only one TMD and form higher order oligomeric channels (Gan et al., 2012; Perez et al., 1997; Carter et al., 2010). SH protein forms part of the virion, although in cell culture deletant viruses have shown RSV can replicate without SH. However, levels of IL-1B significantly increased suggesting a role of SH in immune evasion similarly to other viroporins (Russell et al., 2015). *In vivo* studies have shown using chimpanzees and small animals hRSV can replicate in the absence of SH, however leading to 40 and 10-fold lower virus titres respectively (Bukreyev et al., 1997; Jin et al., 2000; Whitehead et al., 1999). SH is therefore an important virulence factor. Furthermore, SH is thought to have roles in preventing infected cell death by preventing TNF- α signalling which leads to apoptosis (Fuentes et al., 2007).

SH has been shown to form pentameric and hexameric complexes with a predicted single TMD. Sedimenting SH protein using sucrose gradients, cross-linking SH and using PFO-PAGE have all shown SH in a pentameric conformation (Collins and Mottet, 1993; Gan et al., 2008). Additionally using electron microscopy SH showed both five-fold and six-fold symmetry suggestive of pentameric and hexameric pores formed in detergent (Carter et al., 2010).

SH channel activity has been shown in liposome-based assays used to study activity of many viroporins (Carter et al., 2010), as well as bacterial membrane permeability assays (Perez et al., 1997). Surprisingly, cation selectivity *in vitro* and cation transport is reduced when pH drops, conversely to the reaction of other viroporins including M2 (Carter et al., 2010; Gan et al., 2012). However deletion of conserved gating residues HIS22 and HIS51 results in non-functional SH by patch clamping (Gan et al., 2012). Additionally, residues ARG 59 and 61 in the C-terminal domain potentially play a role stabilising the oligomeric channel through protein-membrane interactions.

Inhibition of SH has been reported using Pyronin B, which was identified using liposome-based assays. Upon further testing in cell culture the 250 nM of Pyronin B prevented RSV infection of Vero cells, however there have been no reports of other inhibitors since (Li, Y. et al., 2014)

1.10.5 Human Papillomavirus type 16 (HPV-16) E5

HPV's are small dsDNA viruses and a subgroup of these including HPV-16 and 18 are known to be oncogenic. HPV-16 E5 is an 83 amino acid protein and is highly hydrophobic (Halbert and Galloway, 1988). E5 monomers consist of three TMDs and are known to oligomerise (Gieswein et al., 2003), however the only published structure model was constructed *in silico* and there is no confirmed structure of the monomer or oligomer (Wetherill et al., 2012). Moreover, expression of recombinant E5 formed an oligomeric species in a membrane-like environment, thought to be hexameric and showed channel activity of a defined lumen diameter (Wetherill et al., 2012).

Additionally, E5 exhibited further viroporin characteristics. Channel activity was enhanced at lower pH when recombinant protein was expressed in a liposome-based channel activity assay (Wetherill et al., 2012). Similarly channel activity was inhibited by the presence of rimantadine (Wetherill et al., 2012).

Furthermore, the *in silico* oligomeric model led to drug screening which highlighted compound MV006 as a potential compound. MV006 was found to inhibit E5 in the liposome based assay and reduced the E5-mediated EGFR signalling effects in cell culture (Wetherill et al., 2012; Supryniewicz et al., 2010; Pim et al., 1992). This implies that MV006 targets E5 oncogenic function. More recently further oncogenic properties of E5 channel activity within the HPV life cycle have been determined, increased ERK-MAPK activation and cyclin B1 expression (Wetherill et al., 2018).

1.10.6 Enterovirus VP4

VP4 protein along with VP1, VP2 and VP3 comprise the icosahedral virus capsid. VP4 is found internally, however the capsid is dynamic and 'breathes', exposing internal components of the capsid on the surface of the non-enveloped virus. During this process the N-terminus of VP4 is transiently present at the surface (Lin, J. et al., 2012; Li, Q. et al., 1994). Upon virus entry into the host cell VP4 is irreversibly externalised triggered by receptor binding or endosomal acidification (Tuthill et al., 2010). Localisation of VP4 on the virus surface has been shown to interact with cellular membranes, leading to viral RNA release (Davis et al., 2008; Fricks and Hogle, 1990; Panjwani et al., 2014; Strauss et al., 2013; Tuthill et al., 2006). However, VP4 does not arbitrarily disrupt membranes, it has been shown to induce discreet channel formation *in vitro* (Danthi et al., 2003). Similarly to many other viroporins, recombinant VP4 protein also displays activity in liposome dye-release assays (Davis et al., 2008). Furthermore, pentameric and hexameric complexes have been observed in DHPC and liposome membranes, and activity enhanced by reduced pH and myristoylation, consistent with the environment during virus endocytosis (Panjwani et al., 2014). VP4 N-terminus can form multimeric structures in a lipid bilayer (Panjwani et al., 2016), however VP1 is also thought to be involved in the release of viral genome into the host cell, forming an 'umbilicus', linking the virus particle to the membrane (Strauss et al., 2013). VP4 is thought to be suitable antiviral target for enteroviruses and the wider picornavirus family. Anti-VP4 antibodies have shown to neutralise the virus in addition to antiviral compound WIN 52084, thought to lock VP4 inside the capsid, preventing virus attachment to the cell surface (Goncalves et al., 2007; Katpally et al., 2009).

1.11 Aims

We hypothesise that ZIKV M protein (as well as M from other *Flaviviruses*) is able to form an ion channel within the acid-exposed mature virion that serves to promote virion uncoating during virus entry. This activity should be sensitive to inhibition using small molecules, providing not only an opportunity to target this process for therapy but also tools with which to further examine M protein function.

Our approach combines medicinal chemistry, molecular dynamics and structure modelling with molecular virology and techniques for examining ion channel activity. First using computer modelling to assess the potential structure of a channel and its response to altered pH, followed by *in vitro* laboratory work investigating the oligomerisation of M through cryo-EM, and its role during the virus life cycle in cell culture and its potential as a drug target *in vitro*.

1. Use Molecular Dynamics to understand the potential formation of an M protein viroporin
2. To investigate whether M forms channels *in vitro*, in cell culture, and their potential function during the virus life cycle
3. To identify M protein inhibitors utilising a Molecular Dynamic model with *in silico* high-throughput screening.

Chapter 2 Materials and Methods

Vero and baby hamster kidney (BHK-21) cells were kindly provided by Dr Victoria Jennings and Dr Clive McKimmie, respectively. Both were originally sourced from ATCC and checked regularly for mycoplasma infection.

2.1.1 Zika Virus

ZIKV/H. sapiens/Brazil/PE243/2015 (PE243) Zika virus was kindly provided by Prof Alain Kohl, MRC Centre for Virus Research and University of Glasgow as a frozen viral stock derived from C6/36 cells at 6×10^6 PFU/mL. A new stock was generated in house at 1.6×10^6 PFU/mL (section 2.3.1).

2.2 Mammalian Cell Culture

2.2.1 Recovery of frozen cells

Vero and BHK-21 cells were taken from liquid nitrogen and quickly thawed in a water bath at 37 °C. Cells were then diluted in 10 mL cell culture media (Appendix A.1 and A.2) in a 15 mL falcon tube. Cells were centrifuged at 1500 x g for 5 min at RT, separating the cells from the freezing media (Appendix). Cells were resuspended in 10 mL of cell culture media, prior to transferring to a T75 tissue culture flask (Corning). Cells were cultured at 37 °C in 5 % CO₂.

2.2.2 Maintenance and Passage of Cells

Vero and BHK-21 cells were cultured in complete Dulbecco's modified essential cell culture media (Appendix A.1 and A.2) at 37 °C in 5 % CO₂ in a humidified culture incubator. Every 2-3 days cells were passaged by washing in phosphate buffered saline (PBS) (Sigma), followed by incubation with trypsin (Sigma) to detach cells from the flask surface for 2-5 min at RT. Trypsin was then inactivated using an equal volume of serum-containing complete cell culture media. Vero and BHK-21 cells were sub-divided using ratios between 1:5 and 1:10.

2.2.3 Freezing cells

Vero & BHK-21 cells were centrifuged at 1500 x g for 5 min. The cell pellet was resuspended in freezing media (Appendix A.3) at a density of 1×10^6 cells/mL.

Cells were frozen slowly, wrapped in tissue and placed in polystyrene box at -80 °C, after 24 hr cells were transferred to liquid nitrogen for long-term storage.

2.2.4 MTT Assay

Vero cells were seeded at 3×10^3 cells/well into 96 well plates and left to adhere overnight. Cells were incubated with increasing concentrations of compounds (0-220 μ M), or a DMSO solvent control, for 24 hr. Following incubation 20 μ L of MTT (3-(4,5-dimethylthiazol-2-yl)-2,5-diphenyltetrazolium bromide) 5 mg/mL was added to each well and incubated at 37 °C for 4 hr. Post-incubation the MTT & media was removed from the wells, washed with PBS twice and 150 μ L DMSO was added and shaken for 10 min at RT. The OD₅₅₀ absorbance was measured using a plate reader (Multiskan Ex, Thermo Scientific). Data was normalised to the appropriate DMSO solvent control.

2.2.5 EGF Uptake Assay

Vero cells were seeded at 1×10^6 per well in 6-well plates (Corning). After 4 hr Rimantadine was added to the cell culture media (Appendix A.1) and incubated overnight at 37 °C and 5 % CO₂. Cells were then washed and treated with Epidermal growth factor complexed with Alexa Fluor™ 488 (ThermoFischer) for 20 min. Fluorescence was quantified using flow cytometry, using the 488 laser and FITC channel (Cytoflex S), FITC positive cells were calculated as a percentage of total cells.

2.2.6 Immunofluorescence

Cells were plated onto sterile glass cover slips in a 12 well plate or directly in to a 96-well plate and cultured under normal cell culture conditions for 4 hr. Cells were infected with ZIKV for 1 hr, after which virus containing supernatant was replaced with fresh media. Cells were fixed with 4 % v/v paraformaldehyde for 10 min and permeabilised using 0.1 % v/v Triton X-100 in PBS. Cells were washed with PBS and probed for Zika Envelope protein (1:500, mouse monoclonal, Aalto Bio Reagents #AZ1176), prM/M protein (1:200, rabbit polyclonal, Genetex #GTX133305), NS3 (1:500, rabbit polyclonal, Andres Merits) and NS5 (1:500, rabbit polyclonal, Andres Merits) in 10 % v/v FCS in PBS overnight at 4 °C. Cells were washed with PBS three times prior to adding the secondary Alexa Fluor-labelled antibody (Invitrogen) in 10 % v/v FCS in PBS. Cells were incubated in the secondary antibody for one hr at RT.

ProLong Gold (ThermoFisher) was placed on microscope slides and the coverslips mounted on top facing the solution. The edges of the coverslip were sealed using transparent nail varnish. Cells in 96 well plates were stored in PBS. Stained cells on coverslips were viewed on an Eclipse Ti-E widefield microscope (Nikon) at 40x magnification. Cells in 96 well plates were imaged and quantified using an IncuCyte Zoom (Essen Bioscience) microscope using 10x objective. Four images per well were taken to calculate the number of total cells and infected cells per well. Parameters for optimal detection of cells and fluorescent cells were setup using an image collection of positive and negative control wells allowing for alteration of the processing definition (Stewart et al., 2015).

2.3 Virus production and storage

2.3.1 Virus stock propagation

Vero cells were seeded at $4-6 \times 10^6$ per T75 flask and left to adhere for over 4 hr. Cells were washed once in PBS, prior to addition of PE243 virus in complete DMEM media + 10mM HEPES (Gibco), at a multiplicity of infection (MOI) of 0.001 PFU/cell. After infection for 1 hr at 37 °C, 5 % CO₂, media was replaced with fresh complete DMEM. Once cytopathic effect (CPE) was observed for ~60% of the cells, virus containing media was clarified and stored

2.3.2 Freezing virus

Virus-containing supernatants were clarified by centrifugation (3184 x g, 20 min, 4 °C) in an Eppendorf 5810 R centrifuge, supernatants were transferred to 0.5 mL eppendorf tubes, and 1.0 mL cryovial tubes. Virus was snap frozen using liquid nitrogen. Once frozen virus was either kept at -80 °C for shorter term storage or liquid nitrogen for long term storage.

2.3.3 Determination of Virus Titre

For quantification of virus titre, both plaque assays and focus forming assays were performed. For plaque assays both Vero and BHK-21 cells were used at a confluency of 80 % in a 12-well plate with 10-fold virus serial dilutions in 0.75 % PBSA (PBS containing 0.75 % bovine serum albumin). 200 µL of serial dilutions was added to each well for 1 hr with rocking every 15 min. After 1 hr 2 mL overlay media of 2X MEM medium (Gibco) containing 4 % FCS (Gibco), 200

units/mL penicillin and 0.2 mg/ mL streptomycin, mixed with viscous 1.2 % Avicell (FMC Biopolymer). Vero and BHK-21 cells were incubated for 5 and 3 days respectively at 5 % CO₂ and 37 °C. After incubation, supernatant was removed and cells were fixed in 10 % PFA for one hr at 4 °C prior to staining with 0.1 % Toluidine Blue (Sigma) for 30 min. Virus PFU titre was calculated using the following equation:

$$\frac{\text{PFU}}{\text{mL}} = \frac{\text{average number of plaques}}{\text{amount of inoculum} \times \text{dilution factor}}$$

2.3.4 Virus assays

2.3.4.1 Focus Forming assay

Vero cells were seeded at 2000 cells per well in a 96 wells cell culture dish (Greiner Bio-one), after 4 hr cells were incubated with virus at an MOI of 1 PFU/cell for one hour. Following a 1 hr infection, virus containing media was removed, cells were washed with PBS and replaced with fresh cell culture media (Appendix A.1). Cells were incubated at 37 °C and 5 % CO₂ for 48 hr.

Cells were fixed using 4 % PFA for 10 min at RT and permeabilised with 0.1 % Triton X-100. For quantification, cells were stained using a primary ZIKV E antibody and a secondary AlexaFluor 488 anti-mouse antibody (section 2.2.6). IncuCyte Zoom was used to quantify infected cells.

2.3.4.2 Plaque reduction assay

Effectivity of compounds against ZIKV infection was determined using plaque assays (section 2.3.3). The number of plaques was compared between duplicate compound treated cells and DMSO negative control treated cells. Cells were incubated with the compound throughout the assay, or for combinations of the experiment as described in time of addition assays (section 4.5.3).

2.4 Preclinical *in vivo* models of ZIKV replication

In vivo experiments, up to the point of sacrifice, were kindly carried out by Daniella Lefteri and Clive McKimmie (Leeds). Mice were dosed with 1.5 mg InVivoMAb anti-mouse IFNAR-1, a day prior to virus inoculation. The mice were

then anaesthetized using 0.1mL/10g of Sedator/Ketavet via intraperitoneal (I.P.) injection. Once anesthetized the mice were placed on top of mosquito cages using foil to expose only the dorsal side of one hind foot to the mosquitos. No more than 5 mosquitoes were allowed to feed on each mouse. 2000 PFU of C6/36 derived ZIKV was injected directly to the bite site using a 5 μ L 75N syringe, 26ga (Hamilton) using small RN ga33/25mm needles (Hamilton).

Mice were observed 4 times throughout the 24-hr experiment and weighed once. Mice were culled 24 hr post infection. Skin from the bitten foot and the spleen were dissected and placed in 0.5mL RNAlater (Sigma Aldrich, USA) in 1.5mL tubes. I then took over the experiment and stored the tissues in RNAlater at 4 °C for a minimum of 16 hr preventing RNA degradation. Blood samples were also collected from the ventricles and centrifuged to isolate serum which was stored at -80 °C until used.

2.5 Protein Biochemistry

2.5.1 Western blot

To analyse cellular protein levels, lysates were made using an appropriate volume of Enriched Broth Culture(EBC) lysis buffer (Appendix A.4). To lyse the cells growth media was removed, and cells were washed three times using PBS. After washing, cells were scraped off into PBS and the cells were pelleted by centrifugation at 2000 x g then resuspended in EBC lysis buffer (Appendix A.4) and kept on ice for 20 min. Lysates were normalised for protein concentration using a Pierce BCA Protein Assay Kit (Thermo Fisher Scientific). Then diluted with an equal volume of 2x Laemmli Buffer (Appendix A.5). Lysates were denatured by heating for 5 to 10 min at 95 °C. Lysates were normalised for concentration and run on hand-cast Tris-Glycine polyacrylamide gels with 5-15 μ L of lysate per well; the polyacrylamide percentage of the gel depended on the protein of interest, either 8, 10, 12 or 15 %. Proteins were resolved by SDS-PAGE (sodium dodecyl sulfate-polyacrylamide gel electrophoresis) at 120-160 V for 1-2 hr using Tris glycine running buffer (Appendix A.6).

Proteins were transferred from the polyacrylamide gels to PVDF (Polyvinylidene fluoride- Immunoblot-FL Merck Millipore) membrane by semi-dry blot transfer

(Hoefer). PVDF membrane was activated with methanol for 30 s and placed along with the gel between thick blotting paper soaked in Towbin buffer (Appendix A.7). Transfer of proteins was performed at a constant current of 120-240 mA for 1-2 hr depending on the number of gels and the molecular weight of the protein of interest. Membranes were blocked for non-specific binding using 5 % w/v fat-free milk in TBS-T (Tris buffered saline (Appendix A.9) with 0.1 % v/v Tween 20, Sigma-Aldrich) for 1 hr at RT. Membranes were probed with primary antibody for protein of interest (Zika Envelope protein (1:10000, mouse monoclonal, Aalto Bio Reagents #AZ1176), prM/M protein (1:5000, rabbit polyclonal, Genetex #GTX133305), NS3 (1:10000, rabbit polyclonal, Andres Merits) and NS5 (1:10000, rabbit polyclonal, Andres Merits) in either 5 % w/v fat-free milk in TBS-T or 5 % w/v BSA (Bovine Serum Antibody, Fisher Scientific) in TBS-T shaking at 4 °C overnight. Secondary antibodies (Goat anti-mouse IgG-Horseradish peroxidase (HRP) conjugate, #A4416, Sigma and Goat anti-rabbit IgG-HRP, #A6154, Sigma) were diluted 1:5000 in either 5 % fat-free milk in TBS-T or 5 % BSA in TBS-T were incubated with the membranes shaking at RT for 1-2 hr. Membranes were washed for 3 x 10 min in TBS-T, with shaking, between each step. Immunoblots were visualised using either prepared Enhanced ChemiLuminescence (ECL) substrate solution (A.9) or ECL prime western blotting detection reagent (GE Healthcare Life Sciences) on X-ray film using a Medical fil processor (SRX-101A, Konica Minolta Medical & Graphic, Inc.). Protein sample sizes were compared with prestained molecular weight markers (prestained Seebblue® Plus2, Invitrogen).

2.5.2 Native PAGE

Protein was solubilised at 37 °C for 10 min in 300 mM detergent (1,2-dihexanoyl-sn-glycero-3-phosphocholine (DH(6)PC), 1,2-diheptanoyl-sn-glycero-3-phosphocholine (DH(7)PC), 1-palmitoyl-2-hydroxy-sn-glycero-3-phospho-(1'-rac-glycerol) (LPPG) and 1-myristoyl-2-hydroxy-sn-glycero-3-phospho-(1'-rac-glycerol) (LMPG)) in Liposome Assay Buffer (Appendix A.11). Native-PAGE loading dye (Appendix A.12) was added to samples, which were loaded onto gradient precast gels (4-20%) (Bio-Rad) and run using Native-PAGE running buffer (Appendix A.13) at 140 V for 1 hr. Gels were stained with

Coomassie Brilliant Blue as described in section 2.5.3. Unstained SDS-free molecular weight marker (Sigma-Aldrich) was used to estimate protein size.

2.5.3 Coomassie-blue staining

Polyacrylamide gels were incubated in Coomassie Brilliant Blue stain (Appendix A.14) overnight at RT with continuous rocking. Gels were destained to visualise protein using Coomassie Blue destain solution (Appendix A.15).

2.5.4 M peptide

M peptide was purchased from Alta Bioscience and was provided lyophilised (Appendix). The peptide comprised the two TMDs and a truncated N-terminal helix. Details of the sequence are noted below:

Ac –

ESREYTKHLIKVENWIFRNPGFALVAVAIAWLLGSSTSQKVIYLV MILLIAPAYS

2.6 *In vitro* liposome assay

2.6.1 Liposome preparation

Lipids (Avanti Polar Lipids) were kept on ice, combined in a glass tube and handled under non-oxygen gas (Nitrogen). 50 μ L PA, 50 μ L PC & 5 μ L PE were mixed together to give 1 mg of lipid. The PE lipid head groups were labelled with lissamine rhodamine, giving a final concentration of 0.5 % w/w. Lipids were stored in chloroform, this was evaporated from the mixture overnight using a vacuum at room temperature (RT). Lipids were rehydrated to 2 mg/mL, at a self-quenching concentration of carboxyfluorescein (CF) buffer (Appendix A.16) and vigorously shaken overnight at RT.

A 3 μ L pre-extrusion sample was taken, followed by 15 passes through an Avanti extruder containing a 0.4 μ M filter (Whatmann), at 37 °C. Unilamellar liposomes were washed three times with liposome assay buffer (Appendix A.11) to remove the remaining CF and purified via centrifugation at 35,000 rpm (100,000 x g) for 15 min at RT, using a MLS-50 rotor in a Beckman Coulter TLX ultracentrifuge. The last liposome pellet was resuspended in liposome assay buffer (500 μ l).

Liposome concentration was determined by measuring the rhodamine absorbance (OD_{570}) using a spectrophotometer (Jenway) of the pre-extrusion sample (3 μ L diluted 1:20) and the post-extrusion samples (3 μ L neat liposomes). The absorbance values were then entered into the following equation:

$$\text{Liposome concentration (mM)} = \frac{2.75 \text{ mM (average lipid molarity)}}{OD_{570 \text{ pre extrusion}} \times \text{dilution factor (20)}} \times OD_{570 \text{ post extrusion}}$$

2.6.2 End-point *in vitro* M protein liposome dye release assay

M peptides were reconstituted to 1 mM in Dimethyl Sulfoxide (DMSO). Further stock dilutions were made in DMSO; which was added to a maximum of 5 % w/w DMSO per well.

End-point dye release assays were carried out using flat-bottomed, black 96 well plates (Greiner Bio One). Each reaction comprised 50 μ M liposomes and up to 800 nM peptide (780 nM for normal use) in liposome assay buffer (Appendix A.11) to 100 μ l. FLUOstar Optima plate-reader (BMG Labtech) was used to measure CF release every after 30 min at 37 °C. All reactions were repeated in triplicate alongside 50 μ M liposomes plus 5% (v/v) DMSO to calculate background fluorescence and 0.5 % v/v Triton X-100 to set gain adjustment of 90 % fluorescence.

An increase of CF release and fluorescence indicated permeabilisation of liposomes induced by the addition of peptide. Assays were carried out at RT and kept on ice until inserted into the machine. End-point values were used to measure the level of permeability induced by the peptide.

2.6.3 Inhibitor assays

Inhibitors were added to reaction wells maintaining the 5 % v/v DMSO as mentioned in 1.8.2. Compounds were incubated with peptides for 5 min at RT prior to the addition of chilled liposomes and assay buffer. End point values were taken and negative control (DMSO only) values were subtracted for each condition. Each biological replicate contained three technical repeats.

2.6.4 pH Liposome assay

Determining the effect of pH on M peptide activity in liposomes was carried out using end-point measurement due to the quenching effect of acidic pH on CF fluorescence. Liposomes containing 50 μ M CF were resuspended in Liposome assay buffer at different pH (6.2, 6.7 and 7.4). Liposome reactions were made as previously described (section 2.6.1), however after 30 min at 37 °C the samples were centrifuged at 100,000 $\times g$ for 15 min using a TLA45 rotor (Beckman) and a TL Ultracentrifuge (Beckman). The liposome-free supernatant was transferred to a 96-well plate and adjusted to pH 7.4 by the addition the same volume of 1M Tris-HCl pH 8.0. The endpoint CF fluorescence was then measured using a FLUOstar Optima plate-reader (BMG Labtech) at ex 485/ em 520 nm.

2.6.5 Lipids

L- α -phosphatidic acid (α -PA), L- α -phosphatidyl choline (α -PC) and L- α -phosphatidyl ethanolamine with lissamine rhodamine b labelled head groups (α -PE), were purchased from Avanti Polar Lipids. All were derived from chicken eggs and supplied in chloroform as 10 mg/ml stock solutions, these were aliquoted using Hamilton glass syringes into glass vials, stored at -80 °C.

2.6.6 Transmission Electron Microscopy

5 μ g of M peptide was incubated in 10 mM HEPES, 107 mM NaCl and varying concentrations of DHPC for 10 min at RT, this was added to copper grids, before washing with water and negatively stained with 2 % uranyl acetate and examined using a Tecnai F20 at 120 kV on a FEI CETA camera at a nominal magnification of 125000 providing a pixel sampling of 4.18 Å per pixel. Particle picking and 2D class averaging was carried out using RELION software, 2D class averaging was carried out with 25 iterations.

2.7 Molecular Dynamics

2.7.1 Coarse-grained simulations

Coarse-grained (CG) Molecular Dynamic simulations of Monomeric and Dimeric M proteins were performed using Martini v2.2 force field (de Jong et al., 2013) and GROMACS (Abraham et al., 2015). The cryo-EM structure of ZIKV M protein structure (PDB: 5IRE) (Sirohi et al., 2016) was converted to coarse-grain resolution. An elastic network was only used in the monomer and dimer

simulations to maintain the secondary structure, however not the tertiary structure. Additionally, an elastic network was used when restraining the C α during dimirising simulations as this would maintain the secondary and tertiary structure. The cryo-EM structure was used to simulate Model-1, however Modeller was used to generate Model-2 straightening the linker region between the two TMDs into a longer TMD (Fiser and Sali, 2003).

A POPC bilayer or WNV emulated bilayer (POPC(57%): POPS(25%): POPE(3%): SM (15%) was built using INSANE (INSert membrANE) CG tool (Wassenaar et al., 2015). Systems were solvated with CG water particles and ions were added to neutralize the system to a final concentration of 150 nM NaCl.

Prior to simulation, systems were energy minimised using the steepest descent algorithm for 500 steps in GROMACS and equilibrated for 10 ns with the protein backbone restrained.

The temperature was set at 323 K and controlled by V-rescale thermostat (coupling constant of 1.0) (Bussi et al., 2007). Pressure was controlled by Parrinello-Rahman barostat (coupling constant of 1.0 and a reference pressure of 1 bar) (Parrinello and Rahman, 1981). Integration step in 20 fs Lennard-Jones interactions were shifted to zero between 9 and 12 Å and Coulombic interactions between 0 and 12 Å respectively.

2.7.2 Atomistic Simulations

The all-atom hexameric and heptameric M protein oligomers were first energy minimised prior to conversion into CG using Martini and as above inserted into the bilayer system using INSANE, the systems were then equilibrated in CG restraining the protein. The systems were then converted back into atomistic resolution using the martini backward tool (Wassenaar et al., 2014). Simulations were then energy minimised, equilibrated for 20 ns with the protein C α atoms restrained and run in CHARMM36 force field (Huang and MacKerell, 2013). Simulations ran for 200 ns. Temperature and pressure were controlled using the v-rescale thermostat (Bussi et al., 2007) and Parrinello-Rahman barostat (Parrinello and Rahman, 1981) respectively. Bond lengths were kept constant using the LINCS algorithm (Hess et al., 1997). The time-step was 2 fs and the temperature set to 323 K.

2.7.3 Design of Hexamer and Heptamers

A python script was used to calculate the co-ordinates of each monomer within the oligomeric structure, a radii of 1.3 nm was used for hexamer.

```
import math

n = 6          # Number of sides
x = 0          # Origin on x axis
y = 0          # Origin on y axis
r = 1.3        # Radius of Circle polygon is in

for i in range (0, n):
    posx = x + (r * math.cos (2 * math.pi * i / n))
    posy = y + (r * math.sin (2 * math.pi * i / n))

    print ("% 2d : %2.4f : %2.4f" % (i, posx, posy))
```

Chapter 3 *In silico* modelling of M protein

3.1 Introduction

Flavivirus M proteins are 75 amino acids in length, regions of which are highly conserved throughout the genus (Figure 3.1). M protein, known to play a role during assembly as a chaperone for the virus envelope protein, is first produced as part of the pr-M-E fusion peptide. However, after cleavage by furin or other *trans*-Golgi resident proteases (Stadler et al., 1997), the mature form of M resides within the virus membrane (Sirohi et al., 2016), where its role remains unknown.

The function of mature M protein is poorly understood amongst the entire *Flavivirus* genus. All M proteins are highly hydrophobic, making them difficult to synthesise, express as recombinant proteins and purify; however, its presence within the virion is suggestive of a role during virus entry.

The structure of M protein inside the virion has been resolved as dimeric across multiple examples within the genus by cryo-EM (Figure 3.2 and Figure 3.3) (Nieva et al., 2003; Melton et al., 2002; Raghava et al., 2011; Clarke et al., 2006; Carter et al., 2010). However, as the virus enters the cell via clathrin-mediated endocytosis (Persaud et al., 2018), the endosome containing the virion matures from early to late and acidifies, resulting in a harsh environment of around pH 5 (van der Schaar et al., 2008; Chu and Ng, 2004). At this stage, envelope glycoproteins re-arrange their conformation from dimeric to trimeric, providing dimeric M, which resides beneath envelope, a similar opportunity to change conformation. However, the structure of M protein in this environment is partially disordered, therefore has not been resolved, and so remains unknown (Zhang, W. et al., 2003; Klein et al., 2013; Zhang, X. et al., 2015).

We hypothesised that M protein within this dynamic acidified environment may behave similarly to IAV M2 by playing a role during virus uncoating (Pinto et al., 1992). As M is capable of dimerising, it could further oligomerise into a virus-encoded channel, or “viroporin”. An M protein viroporin allowing H⁺ into the virus capsid may destabilise the interactions between these proteins and the viral genome, expediting the release of RNA into the host cell cytoplasm. Previous work with DENV-2 M protein C-terminal peptides has supported cation channel activity *in vitro* that was sensitive to the prototypic viroporin inhibitors,

amantadine and hexamethylene amiloride. Additionally, amantadine and its methylated derivative, rimantadine, inhibited DENV infection *in vitro* (Koff et al., 1980; Koff et al., 1981). Conversely, the ability of M to act as a proton channel has been disputed in electrophysiology studies using *Xenopus* oocytes (Premkumar et al., 2005; Wong et al., 2011).

Expression of viroporins by classic overexpression systems is challenging due to their hydrophobicity and small size. Previously, viroporins have been expressed using prokaryotic expression systems, either by targeting them to inclusion bodies, or in a soluble form with the addition of a tag (Nieva et al., 2003; Melton et al., 2002; Raghava et al., 2011; Clarke et al., 2006; Carter et al., 2010) However, this requires large amounts of optimisation and yields are generally low. Once expressed, the proteins require extraction using detergents, which can be problematic following subsequent purification, and when introduced into membrane-containing systems. Accordingly, our own attempts at expressing M in bacteria using previously successful viroporin strategies yielded only minimal amounts of soluble protein with poor purity. Thus, we moved on from expressing M protein in the laboratory and instead undertook the modelling of M protein *in silico* using molecular dynamics (MD) simulations.

MD simulations have been used previously with many other viroporins to complement wet laboratory techniques and provide molecular insights into structures, including generating models for monomeric and oligomeric p7 (Chandler et al., 2012; Montserret et al., 2010; Saint et al., 2009) and highlighting the protonation states of HIS37 as a conductance mechanism of the M2 viroporin, (Khurana et al., 2009). This chapter describes the study of M protein structure and oligomeric interactions in different membrane environments using MD simulations



Figure 3.1 Amino acid sequence alignment of *Flavivirus* M proteins

Flavivirus M proteins are 75 amino acids in length and contain highly conserved residues and regions, shown aligned here. Residues 35-44, indicated above by parentheses, are particularly well conserved. This region contains the last 3 residues of the N-terminal helix (helix 1) and the first residues of the N-terminal TMD helix (helix 2). The alignment was produced using Clustal Omega (<https://www.ebi.ac.uk/Tools/msa/clustalo/>) and output using BOXSHADE 3.21 (https://embnet.vital-it.ch/software/BOX_form.html)

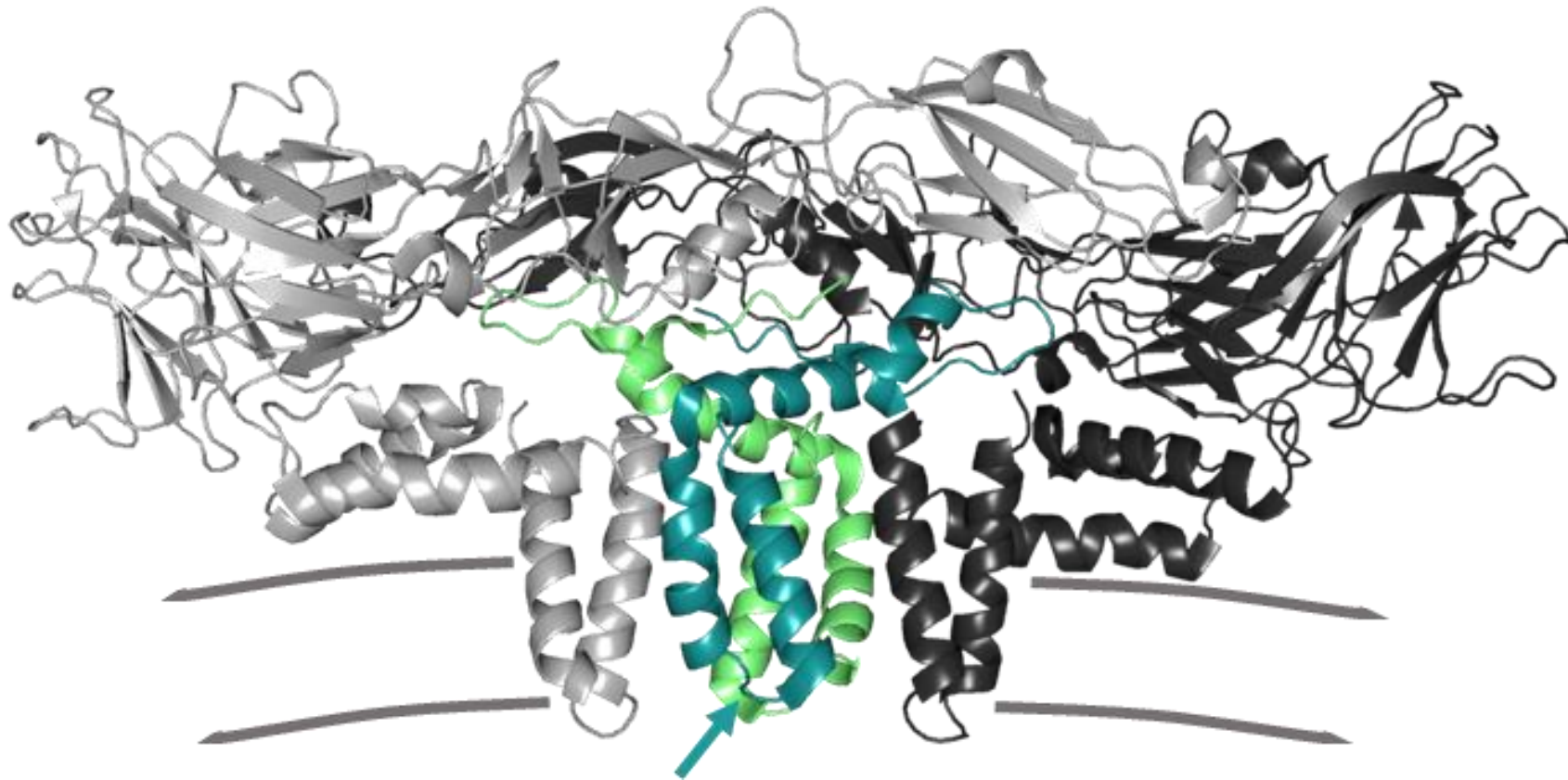


Figure 3.2 Cryo-EM structure of ZIKV E and M protein within the virion membrane

Side view of E-M dimer. E proteins shown in black and white with the E ectodomains on the surface of the virion and the E transmembrane. M protein loop and transmembrane domains shown in green and blue with the linker region indicated by the arrow. The E and M TMDs are found within the lipid bilayer as indicated in grey. Protein PDB: 5IRE (Sirohi et al., 2016)

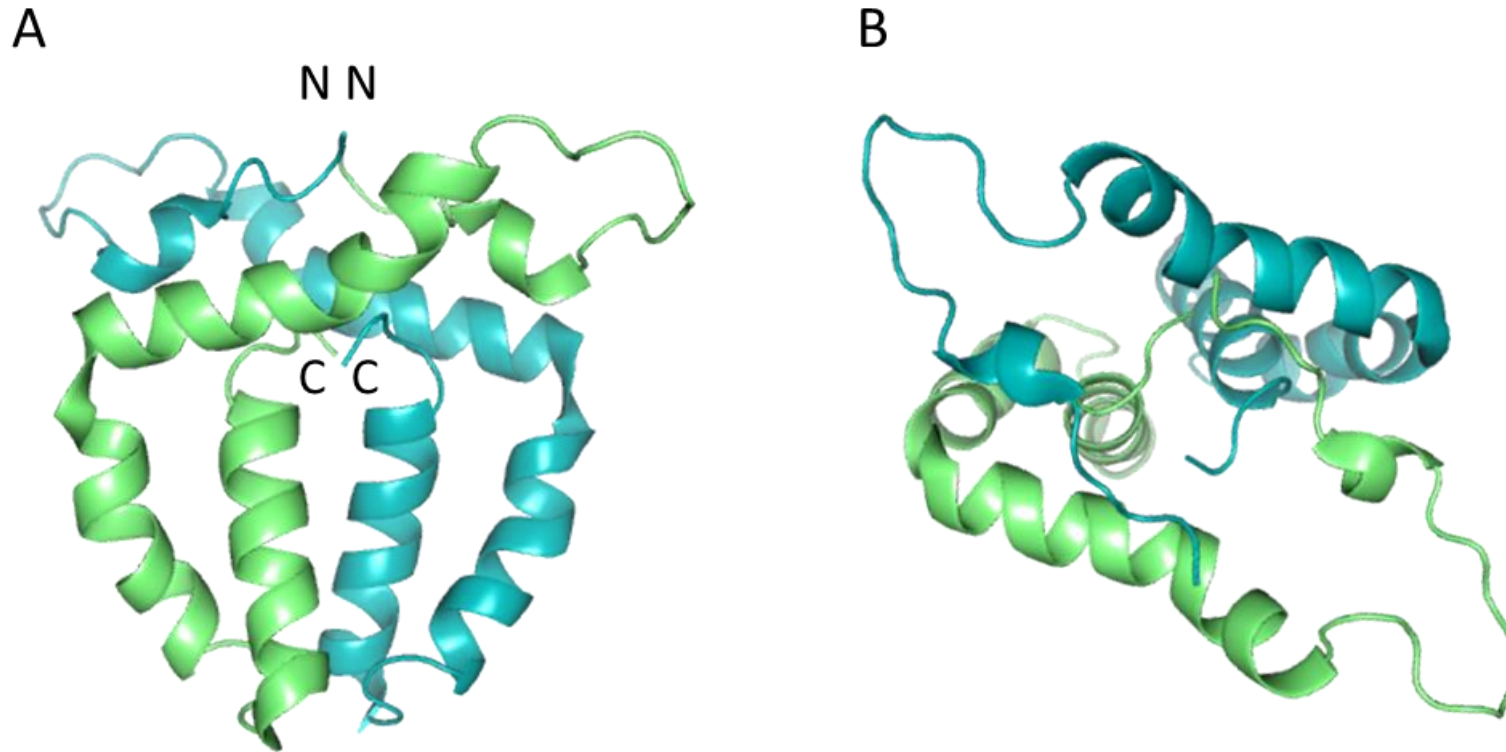


Figure 3.3 M protein dimer structure

M protein dimeric structure taken from cryo-EM ZIKV E-M heterodimer, one monomer shown in green, one shown in blue. **A.** Side view of dimeric M. **B.** Top down view of dimeric M.

3.2 *In silico* predictions of M protein secondary structure

Flavivirus M protein within the mature virion cryo-EM structure has very short transmembrane domains of 13-14 amino acids, ~2.4 nm in length, whereas a typical lipid bilayer spans 3 nm (Ding et al., 2015). Therefore, we postulated the M linker region between the two TMDs highlighted in Figure 3.2 may be under high conformational stress and could change conformation upon virus acidification. When the virus arrives in the acidic endosome environment the E proteins change from dimeric to trimeric, potentially releasing M protein from underneath (Bressanelli et al., 2004).

Using computational protein secondary structure prediction tools, we obtained conflicting results for the TM domains of monomeric M protein. The 'TMHMM' server uses a hidden Markov model (HMM) to predict the likelihood for each residue to be part of a TMD, incorporating hydrophobicity, charge bias and helix length. TMHMM inferred a strong probability for M protein to have a single TMD (Figure 3.4A). It predicted residues 1-34 to be cytoplasmic (probability of ~0.65, blue line), followed by one TMD from residue 35-54 (probability of ~0.7, red lines) and residues 55-75 to be non-cytoplasmic (probability of ~0.6, pink line) (Moller et al., 2001). Additionally we used two other computational tools that predicted M protein to have one TMD, Phobius and TOPCONS (Figure 3.4) (Bernsel et al., 2009; Kall et al., 2007). Phobius, similarly to TMHMM, uses a HMM but is more reliable for proteins containing both a signal peptide as well as TMDs (Kall et al., 2004; Zhang, Xiaohui et al., 2009). Phobius (Figure 3.4C) predicted residues 1-41 to be non-cytoplasmic, (probability of ~0.6, blue line), followed by a single TMD spanning residues 42-71, (probability of ~0.8, grey lines), and residues 72-75 were predicted to be cytoplasmic (probability of ~0.55, displayed by the green line).

TOPCONS server uses a fundamental algorithm utilising BLAST and a consensus prediction to predict topology and measures this in reliability. TOPCONS (Figure 3.4B) predicted residues 1-40 to be cytoplasmic as displayed by the red line, followed by a TM-helix (in → out) from residue 41-62 as displayed by the grey box, and residues 63-75 to be non-cytoplasmic as displayed by the blue line all with a reliability of over 0.9.

Conversely, we also used MEMSAT and SPLIT, which predicted the presence of two TMDs (Figure 3.5). SPLIT (Figure 3.5A) predicts the two TMDs to be 39-

56 and 58 to 75 by using method of preference functions. MEMSAT-SVM (Figure 3.5B) predicts the two TMDs to be from 37-52 and 56-72. MEMSAT-SVM uses multiple support vector machines (SVM) to identify the many residue presences before combining these into a probability output (Nugent and Jones, 2009),

Thus, upon release from dimeric E it may be possible for the two TMD helices of M to flip, forming a single TMD spanning the membrane prior to oligomerising into a channel.

The disparate results from TMD predictions led us to construct models based on both one TMD and two TMD conformations for analysis by MD. We also considered the composition of the virion membrane (Martin-Acebes et al., 2014), and how this might influence the M protein properties; phospholipids with shorter chains may allow the linker region between the two TMDs to interact and maintain its position within the inner leaflet.

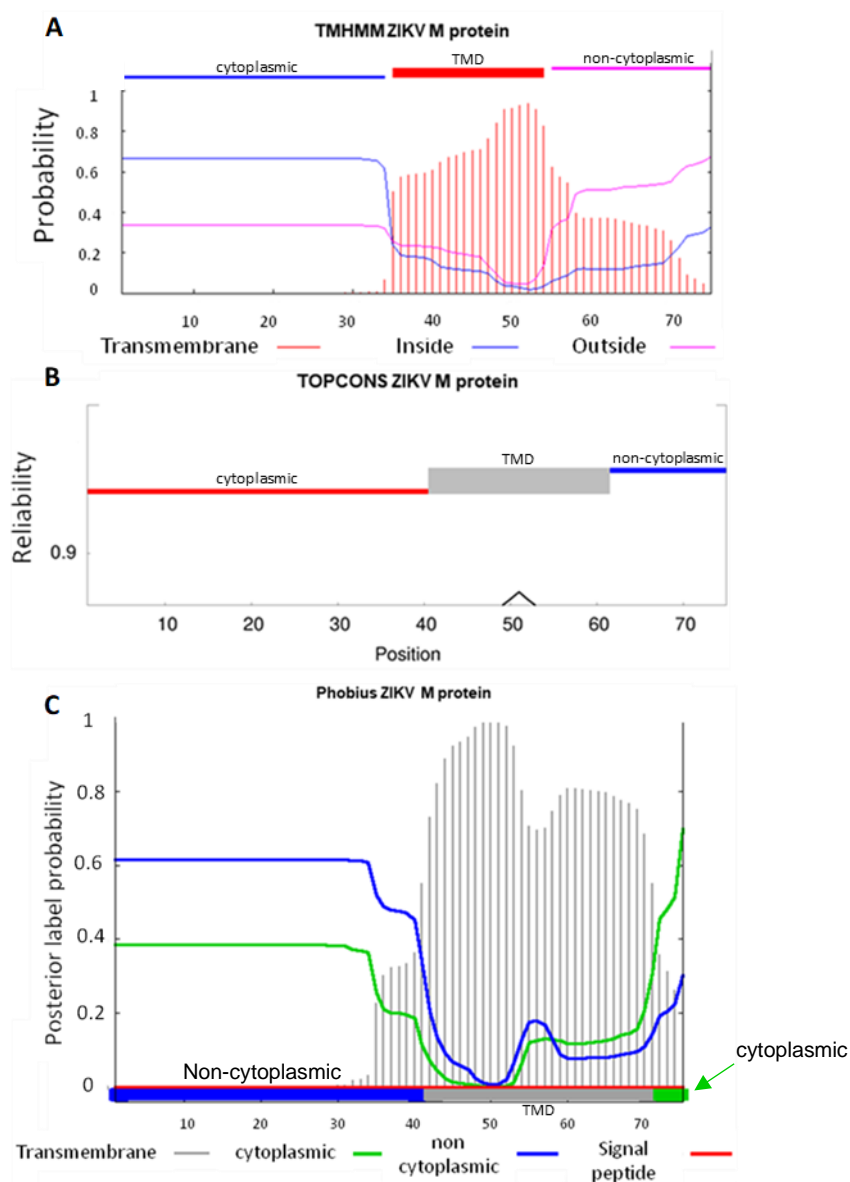


Figure 3.4 Single TMD predictions of the ZIKV M protein structure from TMHMM, TOPCONS and Phobius servers.

A. TMHMM predicts ZIKV M residues 1-34 to be cytoplasmic with a probability of ~0.65 as displayed as a blue line, followed by one TMD from residue 35-54 with a probability of ~0.7 as displayed by the red vertical lines and residues 55-75 to be non-cytoplasmic with a probability of ~0.6 as displayed by the pink line. **B.** TOPCONS tool predicts ZIKV M residues 1-40 to be cytoplasmic as displayed by the red line, followed by a TM-helix (in→out) from residue 41-62 as displayed by the grey box, and residues 63-75 to be non-cytoplasmic as displayed by the blue line all with a reliability of over 0.9. **C.** Phobius tool predicts ZIKV M residues 1-41 to be non-cytoplasmic with a probability of ~0.6 as displayed by the blue line, followed by one TMD from residue 42-71 with a probability of ~0.8 as displayed by the grey vertical lines and residues 72-75 to be cytoplasmic with a probability of ~0.55 as displayed by the green line.

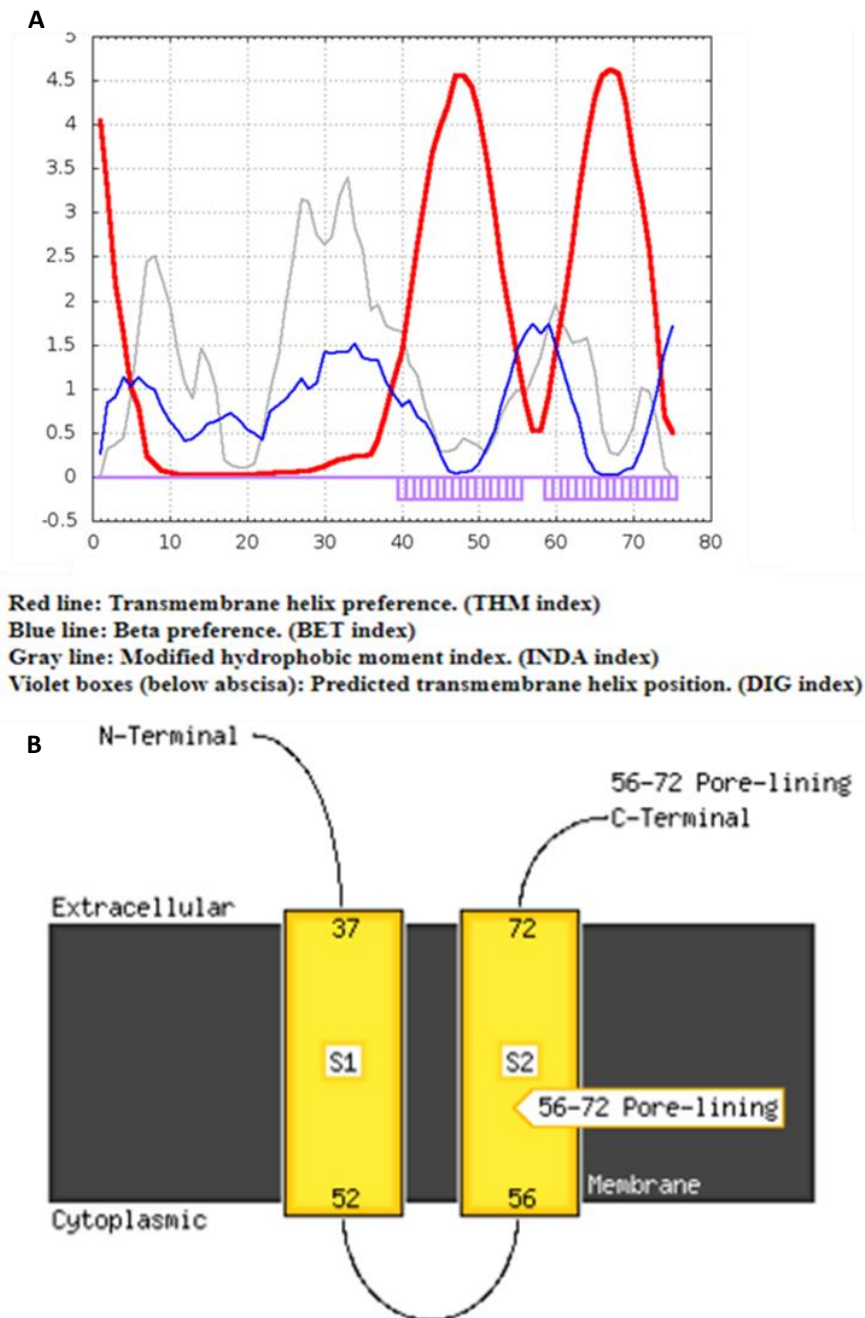


Figure 3.5 Two TMD predictions of the ZIKV M protein structure from SPLIT and MEMSAT-SVM servers.

A. SPLIT v4.0 tool predicts ZIKV M to have two TMD from residue 39-56 and 58-75 as displayed by the violet boxes, the red line indicates the transmembrane helix preference, which aligns with the prediction shown in the violet boxes. The beta preference shown in blue indicates a low probability of beta sheet presence. **B.** MEMSAT-SVM predicts ZIKV M to have two TMDs from residue 37 to 52 and 56 to 75 indicated by the yellow boxes.

3.3 Modelling M protein monomers *in silico*

M protein is dimeric in the mature virion, yet if the protein is capable of forming higher order oligomers then it is likely to be stable, maintaining its' secondary and tertiary structure within a bilayer in its monomeric form. Additionally, as E-M heterotetramers dissociate during entry into E trimers, some M dimers are likely to also rearrange from dimers to monomers. All simulations conducted throughout this chapter use an amino-terminally truncated M protein. The native 75 amino acid protein was truncated to 58 amino acids for computational efficiency, removing a region of the N-terminal domain that was predicted to be unstructured, as seen in the cryo-EM structure (Figure 3.2) (Sirohi et al., 2016) and the TMD predictions (Figure 3.4 and Figure 3.5). The structure of the truncated protein is shown in Figure 3.6.

The monomeric simulations described in this section assessed whether M protein may change conformation and membrane topology after dimer release from E during endosome acidification, based upon the stability of either single or double TMD M conformers. Initially, we generated a long single TMD protein comprising both helices present within the cryoEM structure, reflecting the prediction results of TMHMM, TOPCONS and Phobius shown in Figure 3.4. Secondly, M was simulated as a two TMD protein to assess whether the two M protein helices are long enough to span a membrane bilayer individually, reflecting the cryo-EM structure (Sirohi et al., 2016) and prediction results from SPLIT and MEMSAT shown in Figure 3.5. Finally, we generated a further truncated protein with the C-terminal TMD absent to determine whether the linker region between the two proposed TMDs can interact sufficiently with the inner leaflet to remain stably anchored or if the second TMD is required (Appendix B.1). Table 3.2 lists coarse-grained MD simulations performed for this chapter and atomistic MD simulations are listed in Table 3.3. Coarse-grained MD simulations were run for 3 or 6 μ s using martini 2.2 force field (de Jong et al., 2013) and atomistic MD simulations were run for 200 ns using CHARMM36 force field (Huang and MacKerell, 2013). A simulation snapshot of the coarse-grained MD simulation system containing protein, lipids, water and ions is shown in Figure 3.7.

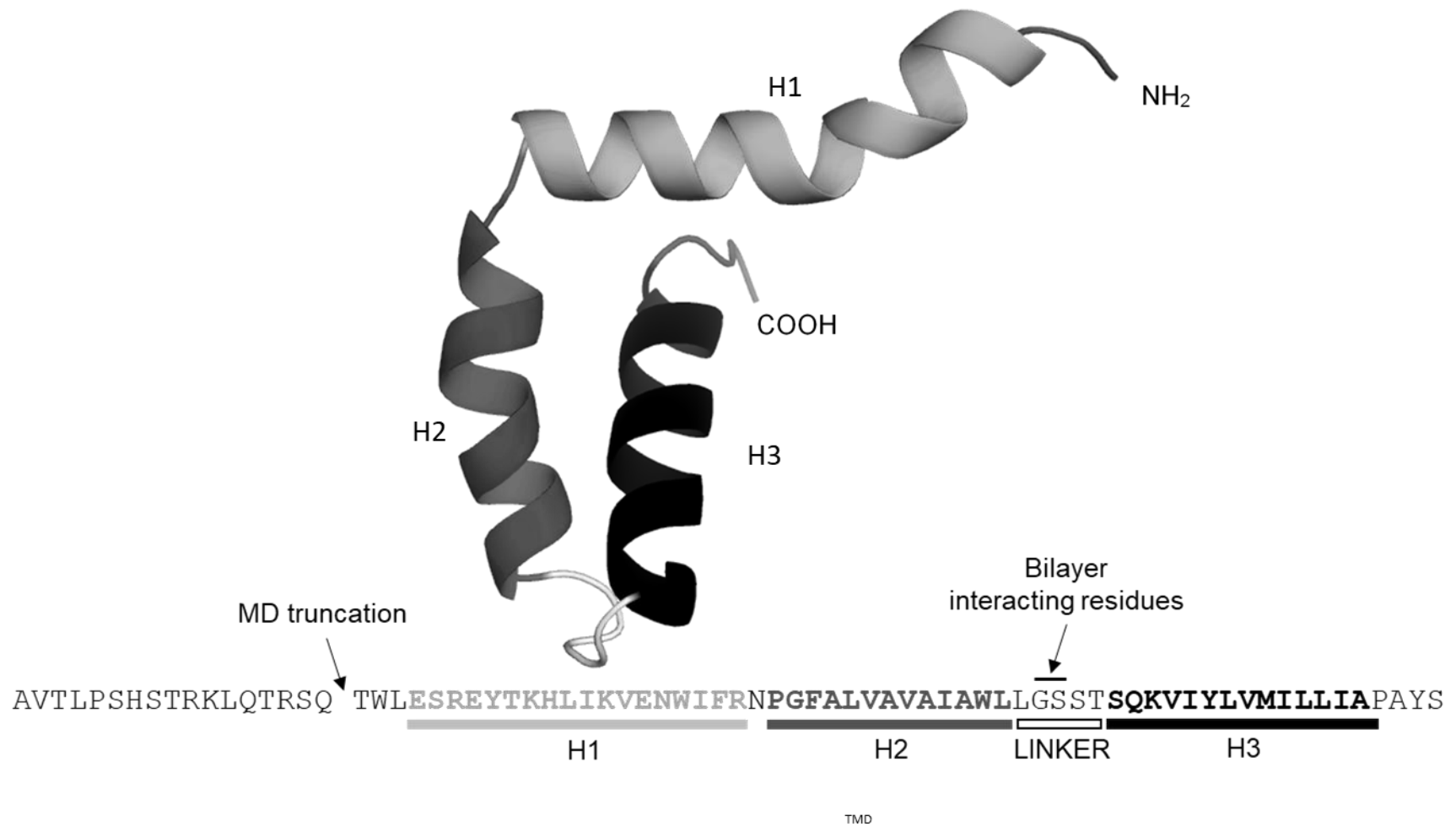


Figure 3.6 Structure and protein sequence of ZIKV M protein truncation

M protein monomeric structure is shown in shades of grey, which correspond to the protein sequence shown below, highlighting structural regions.

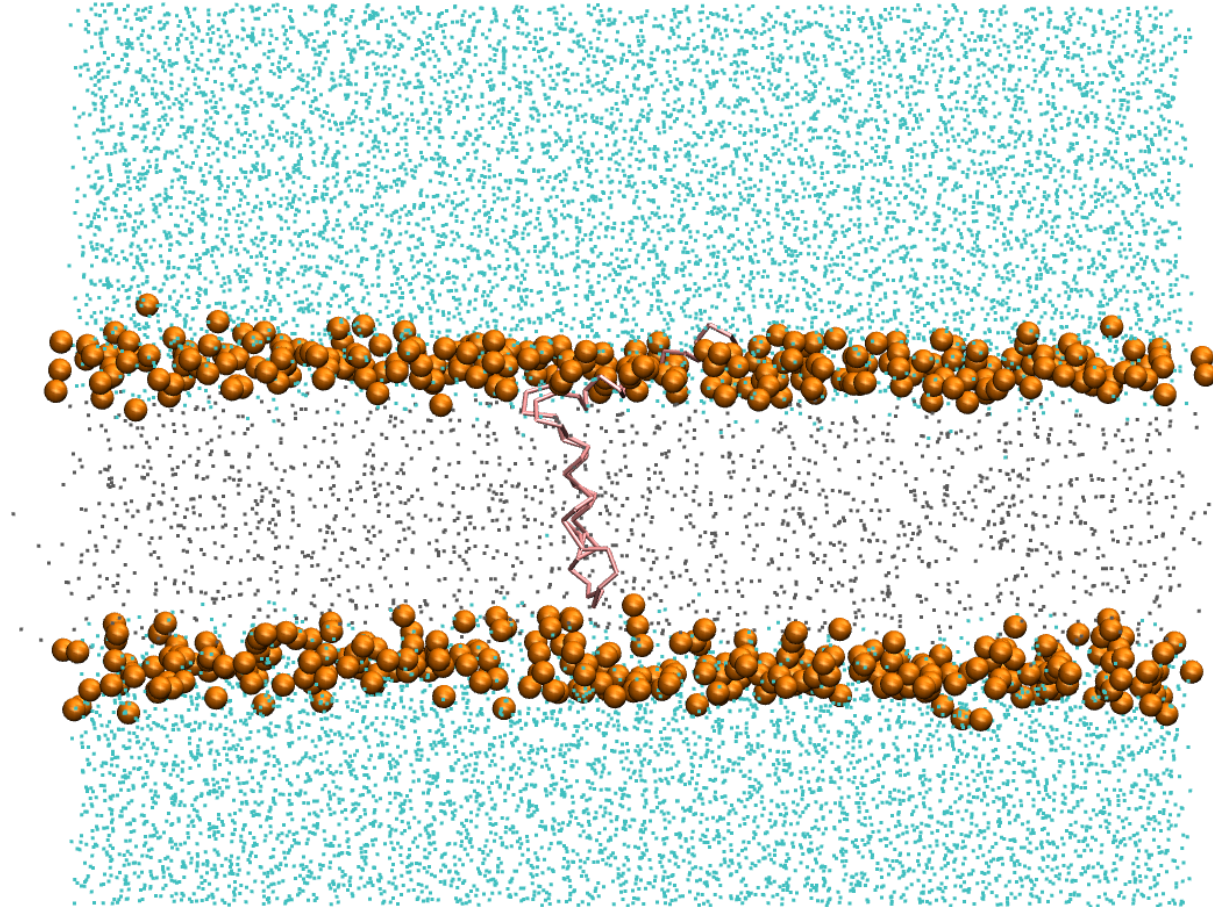


Figure 3.7 Simulation system of coarse-grained MD simulations of the M protein monomer

Simulation system showing M protein backbone in pink, phospholipid heads in orange, lipid tails represented by grey dots and water and ions represented by blue dots.

3.3.1 Is M protein stable as a one or two transmembrane domain M protein in a POPC bilayer?

To simulate monomeric M, the structure of the protein in the mature ZIKV particle cryo-EM was taken from PDB: 5IRE (Sirohi et al., 2016). However, to convert the two TMD protein with short helices into a single TMD protein with one long helix, the structure of the hairpin linker region highlighted in Figure 3.6 between the TMDs was straightened using Modeller software (Webb and Sali, 2016). The protein was then inserted into a POPC model membrane with the N-terminal helix outside the membrane bilayer as shown in

Figure 3.8A. After simulating for 3 μ s, the single TMD protein had surprisingly markedly changed conformation (

Figure 3.8B), partially reverting to a structure comparable to that of the mature virion two TMD cryo-EM structure and the same region can be seen forming the linker region, indicated by the blue arrow (

Figure 3.8C). During repeated simulations, it took 2 ns on average for the protein to adopt this revertant conformation. The conversion of the 1 TMD protein back into a 2 TMD protein results in the linker region between the two TMD helices interacting with the inner leaflet of the bilayer (

Figure 3.8B), thereby narrowing the membrane due to the short TMDs, and the second TMD (H3) residing within the bilayer, although without outer leaflet interaction. Root mean square deviation (RMSD) analysis of the simulation shows the structure changed a lot over the first few ns as the RMSD rapidly increased from 0 to 1 nm (

Figure 3.8D & E), where it became more stable in the altered TMD structure and stayed similar throughout the simulation.

We then carried out a set of double TMD M protein simulations to compare with results for single TMD simulations. The input conformation for these comprised a double TMD protomer derived from the dimeric structure reported in the ZIKV virion cryo-EM structure (PDB: 5IRE), (Sirohi et al., 2016) with TMDs from residue 40-52 and 58-72 as this approximately reflected predictions from SPLIT (residues 39-56 and 58-75) and MEMSAT-SVM (residues 37-52 and 56-72). The two TMD species was inserted into a POPC membrane with the N-terminal helix outside the membrane bilayer, with the two TMDs resident within the

membrane. However, the helices were not long enough to span the POPC bilayer at the start of the simulation (Figure 3.9A).

After the 3 μ s of coarse-grained MD simulation, unexpectedly both TMDs remained within the membrane and were largely structurally unchanged throughout the simulation, although the bilayer had rearranged allowing for the shorter TMDs (Figure 3.9A and B). However, the N-terminal helix appeared very flexible throughout. Subsequent analysis of the distance between the tip of the N-terminal helix and the tip of C-terminal TMD (blue arrows) shows the N-terminal helix was very flexible and often faced in the opposite direction to the starting conformation (Figure 3.9C). Additionally, the root mean square deviation (RMSD) plot (Figure 3.9D) shows an increase from 0 to 0.5 nm at the start of the simulation, as the monomer becomes established within the membrane. The RMSD then increases, aligning with the altered positioning of the N-terminal helix seen in Figure 3.9B. Overall the two TMD monomers remain stable throughout the 3 μ s simulation, with a flexible N-terminal helix.

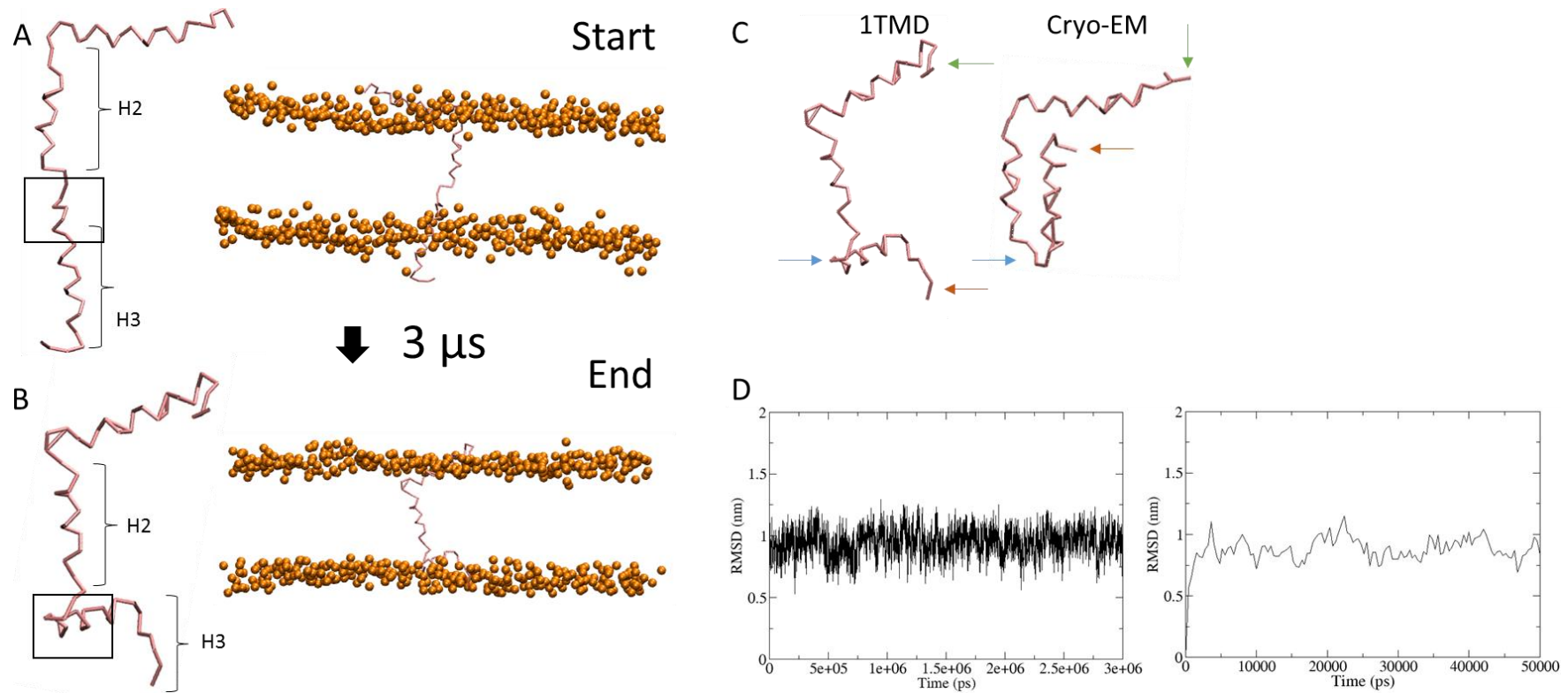


Figure 3.8 Monomeric M protein is not stable as a single TMD protein in a POPC lipid bilayer

Conformations of M protein before and after 3 μ s of simulation. Protein backbone shown in pink and phospholipid bilayer heads shown in orange. **A.** Monomeric single TMD M protein simulation starting conformation, shown side on with and without phospholipid bilayer heads, with the linker region position indicated. **B.** Monomeric single TMD M protein simulation after 3 μ s, shown side on with and without phospholipid bilayer heads, with the linker region position indicated. **C.** Alignment of M 1TMD simulation next to the cryo-EM 2TMD structure with corresponding regions highlighted with arrows. **D.** Root mean square deviation over time (RMSD) of one representative simulation and RMSD for the first 50 ns of the same simulation.

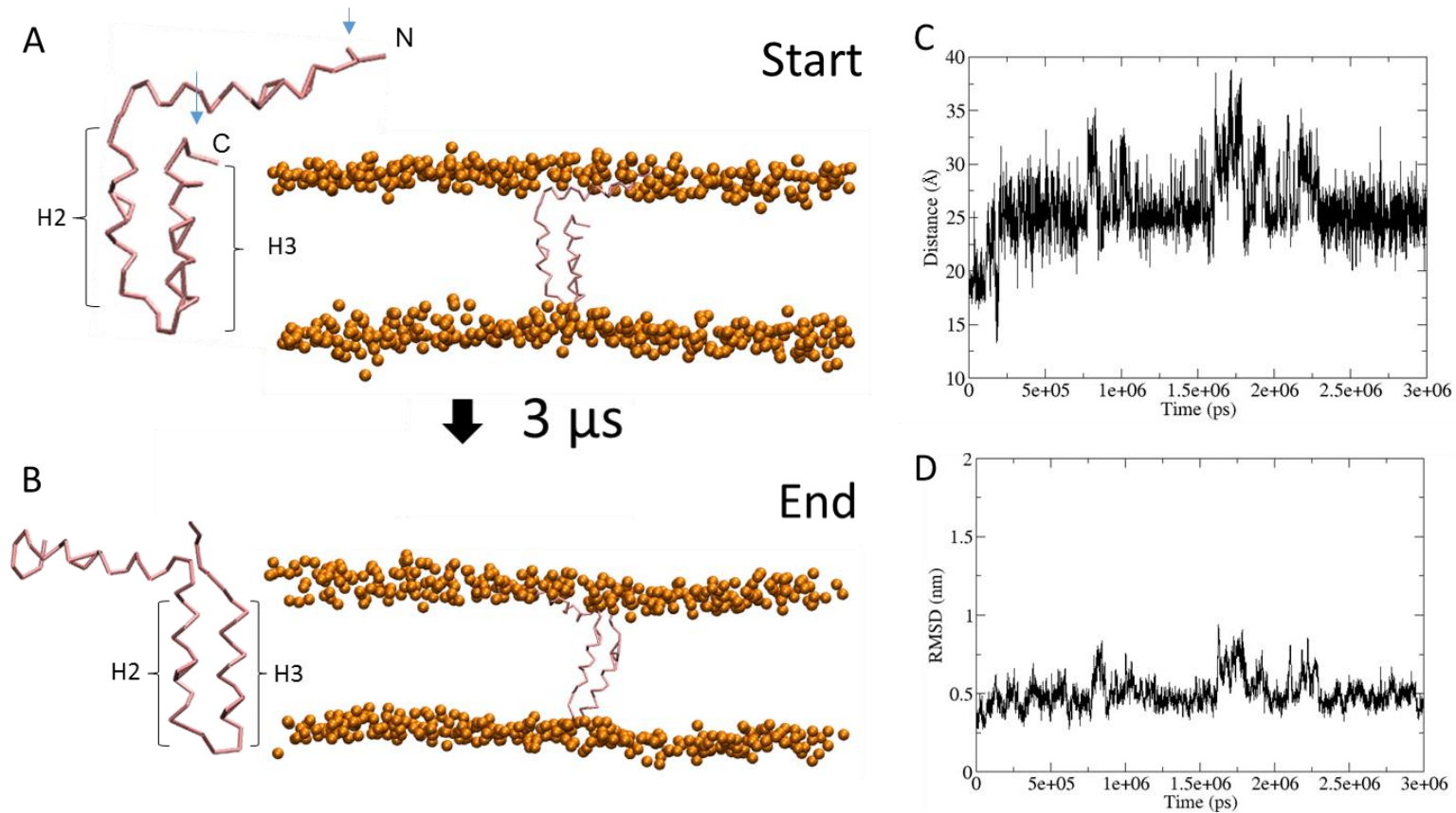


Figure 3.9 Monomeric M protein with two TMDs is stable in a POPC bilayer

A & B Conformations of M protein before and after the 3 μs simulation. Protein backbone shown in pink and phospholipid bilayer heads shown in orange. Shown side on with and without phospholipid bilayer heads. **C.** The distance between the two blue arrows in A, throughout the simulation. Showing the N-terminal helix is flexible and moves to face the opposite direction during the simulation. **D.** Root mean square deviation over time (RMSD) of one representative simulation.

3.3.2 Is M protein stable as a two transmembrane domain protein (Model-1) in a representative *Flavivirus* virion bilayer?

In previous simulations the lipid bilayer simulated surrounding M protein has been entirely composed of POPC phospholipids. Although the majority of *Flavivirus* membranes contain a high proportion of POPC lipids (Martin-Acebes et al., 2014; de Oliveira Dos Santos Soares et al., 2017; Zhang, Q. et al., 2012), bilayers solely comprised of this fatty acid are neither representative of cellular membranes, nor, more importantly, a virus particle (Mackenzie et al., 2007; Welsch et al., 2009). Virion membranes are derived from the host cell lipid bilayers, yet their composition varies due to the recruitment of different lipids at varying compositions by non-structural proteins or the glycoproteins themselves (Aktepe and Mackenzie, 2018; Wewer and Khandelia, 2018).

Thus, to determine whether lipid composition affects M protein behaviour the model membrane was altered to that of WNV, due to the absence of related data for ZIKV; specifically: POPC(57%): POPS(25%): POPE(3%): SM (15%) (Martin-Acebes et al., 2014).

After 3 μ s simulations of the two TMD M conformer (PDB: 5IRE) within a WNV composed membrane, the structure was the same as those when simulating M protein within a POPC membrane (Figure 3.9 and Figure 3.10). The change in lipids surprisingly appears to have little effect on the flexibility or final conformations of M protein as a monomer within the *Flavivirus* lipid bilayer in comparison to a 100 % POPC bilayer.

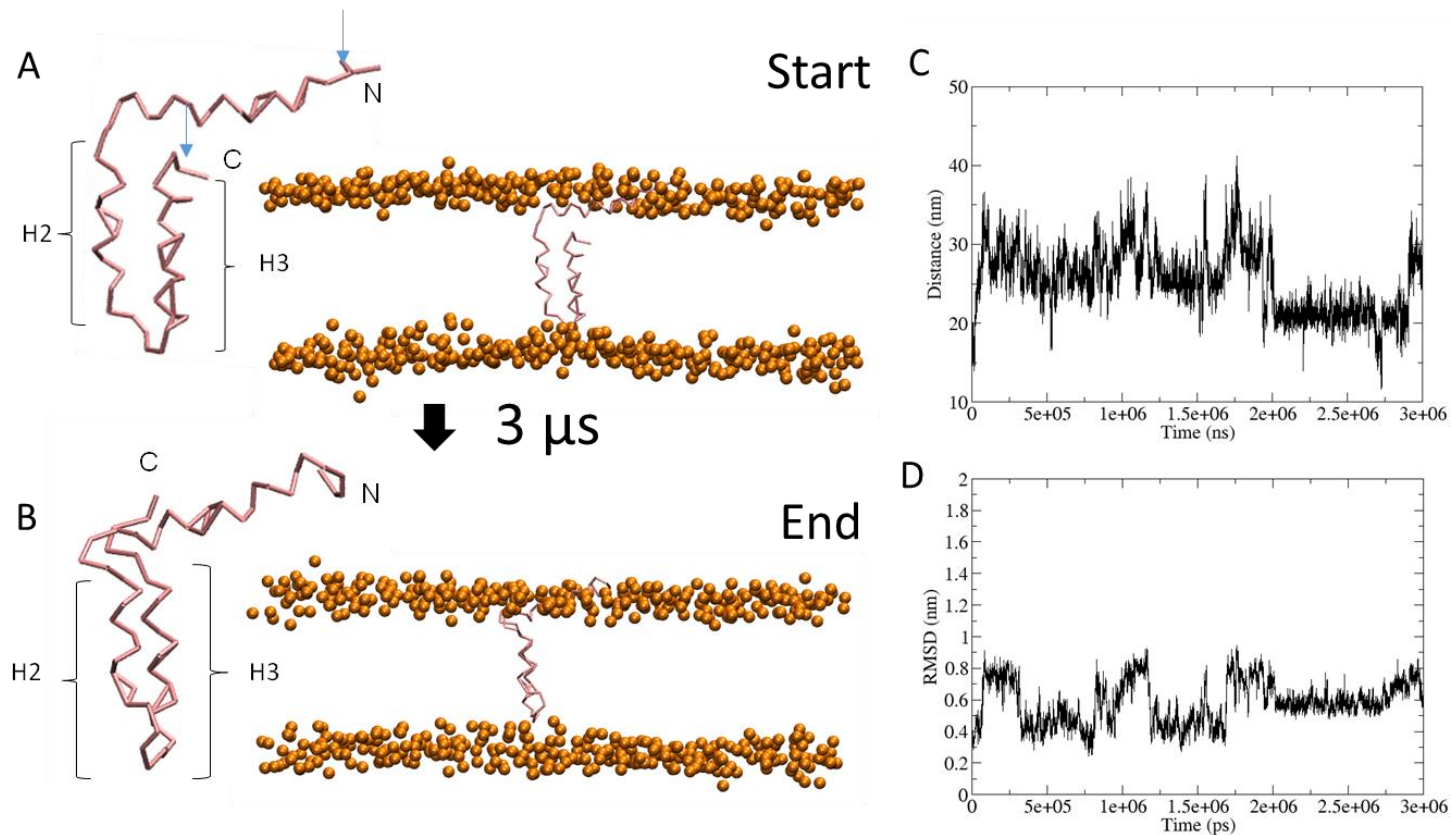


Figure 3.10 Monomeric M protein with two TMDs is stable in a WNV derived lipid bilayer

A + B Conformations of M protein before and after the 3 μ s simulation. Protein backbone shown in pink and phospholipid bilayer heads shown in orange. Shown side on with and without phospholipid bilayer heads. **C.** The distance between the two blue arrows in A, throughout the simulation. Showing the N-terminal helix is flexible and moves to face the opposite direction during the simulation. **D.** Root mean square deviation over time (RMSD) of one representative simulation.

3.4 Dimerisation of M protein *in silico*

Section 0 supports that M protein is stable as a two TMD monomer within membranes *in silico*, yet the protein is known to be stable as a dimer within mature virions as seen by cryo-EM (Figure 3.2 and Figure 3.3) (Sirohi et al., 2016). Within the virion, M protomers appear to interact through the two C-terminal TMD helices (H3) with the N-terminal TMD helices (H2) on the periphery, adjacent to the E TMD anchors (Figure 3.3). Additionally, E subunits I-III reside on the surface of the virion and interact with M protein H1 and the unstructured region from above (Figure 3.2). Therefore, dimerisation of M may require the presence of E for stabilisation, or M dimers may form alone but may be less stable in the absence of E.

If M protein is to oligomerise into a higher order structure, monomers and dimers of M protein must interact intermediately during the formation of the oligomer from dimers. M protein may oligomerise similarly to M2, which forms a tetramer starting from a dimeric conformation, creating a 'dimer of dimers' (Sharma et al., 2010), or the rearrangement of E dimers to trimers during acidification may result in the dissociation and rearrangement of M dimers into higher order oligomers.

This section investigates whether two M protein monomers can interact to form dimers and the subsequent conformations thereof. All the coarse-grained simulations in section 3.4 were run for 6 μ s each and 10 repeats were carried out. M proteins were situated 6 nm apart within the described lipid bilayer, using coarse-grained force field martini v2.2.

3.4.1 M protein forms stable dimers in standard POPC bilayers

Two M proteins were simulated at distance in a 100 % POPC bilayer to determine whether they could interact and dimerise. Ten simulations were run under the same conditions and dimerisation did indeed occur during each simulation. However, interestingly, dimeric interactions were not identical in each case (Figure 3.11). Dimers formed as one of four different classes; Class I: as per ZIKV virion cryo-EM dimers (Sirohi et al., 2016), where interactions occur between H3, and H2 is present upon the periphery; Class II: interactions occurring at H2 with H3 on the periphery; Class III: interactions occurring at both H2 and H3; Class IV: interactions at both H2 and H3 regions, yet

alternating in direction. In this set of ten simulations only one formed a Class I conformation, two formed Class II conformations, five formed Class III conformations and two formed Class IV conformations. Interestingly, class III adopted a conformation that might enable orientation of further protomers into a circular channel-like structure with H3 lining an aqueous pore based on the MEMSAT-SVM prediction (Figure 3.5) (see section 3.5). Representative graphs of which residues form the most interactions during simulations are shown under the corresponding classes. The residues forming the highest number of interactions for class III dimers are SER58, ILE49, ALA46, ALA45, ALA43, ASN34, VAL32, ARG31, HIS28, TYR25, GLU24, ARG23 and SER22. Moreover, classes did not correlate with the time taken for the dimers to come together; the average time taken was 1.46 μ s, although times varied from 320 ns to 4.64 μ s due to randomisation of the simulation and the absence of structural viral proteins (Figure 3.12).

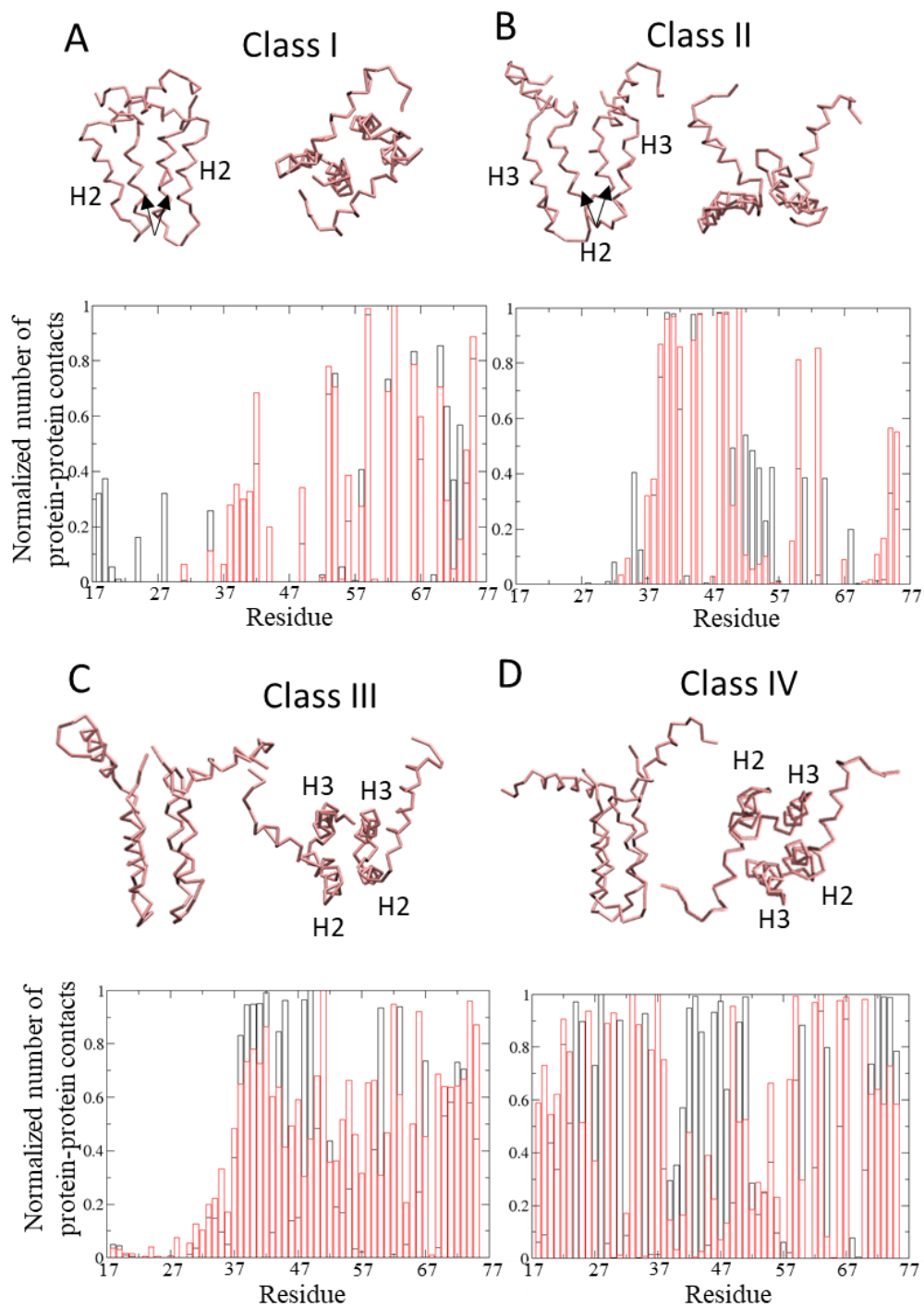


Figure 3.11. M protein dimerises in a POPC bilayer

Dimerisation conformations of M protein monomers within a POPC bilayer after a 6 μ s coarse-grained simulation. M protein shown in pink, side on and above. Representative protein-protein interaction graphs show one monomer in black and the other in red. Interactions are normalised to the largest number of contacts of a residue, with 1 equating to maximum interactions and 0 being no interactions. **A.** Dimeric M protein in a Class I conformation, with H3s forming interactions. **C.** Dimeric M protein in a Class II conformation with H2s interacting. **D.** Dimeric M protein in a Class III conformation with H3s interacting and H2s interacting. **E.** Dimeric M protein in a Class IV conformation with H3-H2 interactions.

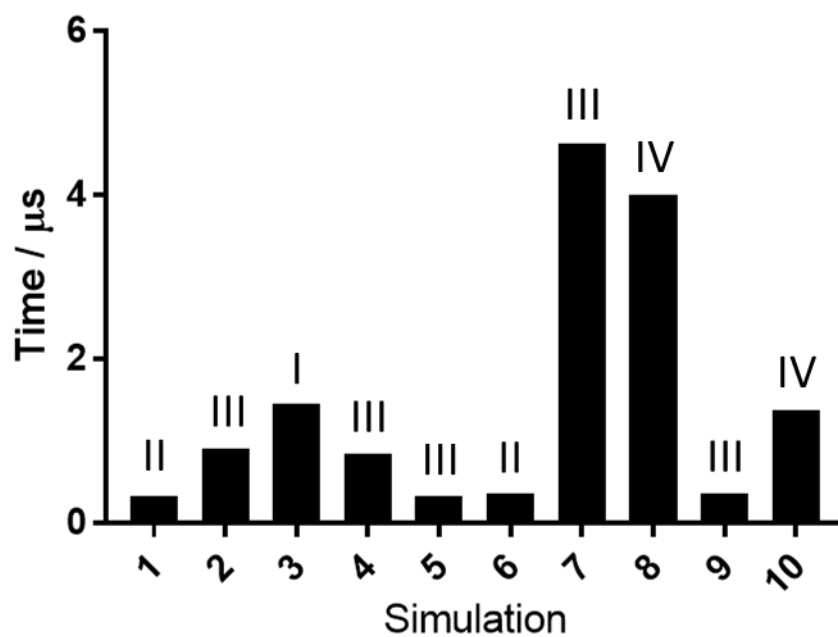


Figure 3.12 Dimerisation analysis of monomers in a POPC bilayer

Time taken for monomers to dimerise in the ten repeat 3 μs simulations carried out in a POPC composed membrane.

3.4.2 Dimerisation of M protein in WNV virion composition bilayer differs to a POPC bilayer

Flavivirus virion membrane phospholipid composition, as described in section 0, is distinct from cellular organelles, although the precise composition of the ZIKV particle membrane has not yet been defined. Virion membranes are primarily formed from the ER membrane at the site of virus assembly, where viral proteins recruit and attract certain lipids for composition into the virus membrane (Mukhopadhyay et al., 2005; Gillespie et al., 2010). After this work was undertaken a study using MD techniques was published showing Zika E and M proteins specifically enrich the surrounding membrane with PS lipids (Wewer and Khandelia, 2018). The activity and interactions of M protein may therefore vary based on the surrounding lipids. The lipid bilayer composition for these simulations are the same as used in simulations in section 0, which recapitulated a *Flavivirus* WNV virion membrane (Martin-Acebes et al., 2014).

Dimerisation of M proteins in a WNV lipid derived bilayer occurred within a similar timeframe, on average 1.49 μ s compared to 1.46 μ s in POPC bilayers, and time taken for dimerisation ranged from 140 ns to 3.34 μ s (Figure 3.13). However, surprisingly two simulations did not result in M protein dimerization.

Again, dimers formed were categorised into the aforementioned classes, however with an addition (Figure 3.14). Two dimers were classified as class I, similar to cryo-EM, four were class II and one class III. Additionally, one dimer class did not resemble the four previous POPC derived conformations as one H3 interacted with H2 from the other protomer, whilst the other TMD helices were adjacent (Figure 3.14). Furthermore, the classifications did not correlate with time taken to dimerise (Figure 3.13). The reduced number of dimer interactions demonstrated the WNV lipid derived bilayer as less favourable.

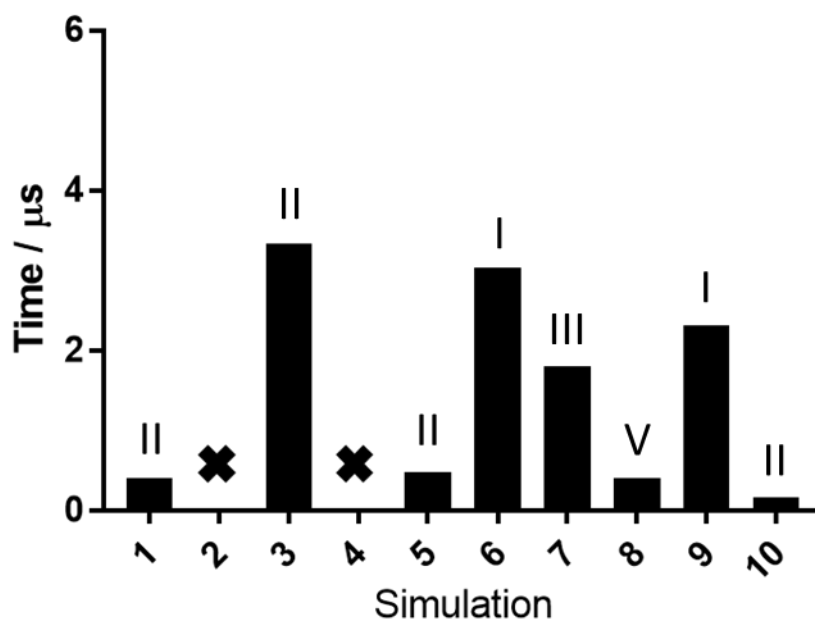


Figure 3.13 Dimerisation analysis of monomers in a *Flavivirus* derived lipid bilayer

A. Time taken for monomers to dimerise in ten repeat 3 μs simulations, in a WNV composed membrane, x denotes a simulation where monomers did not dimerise.

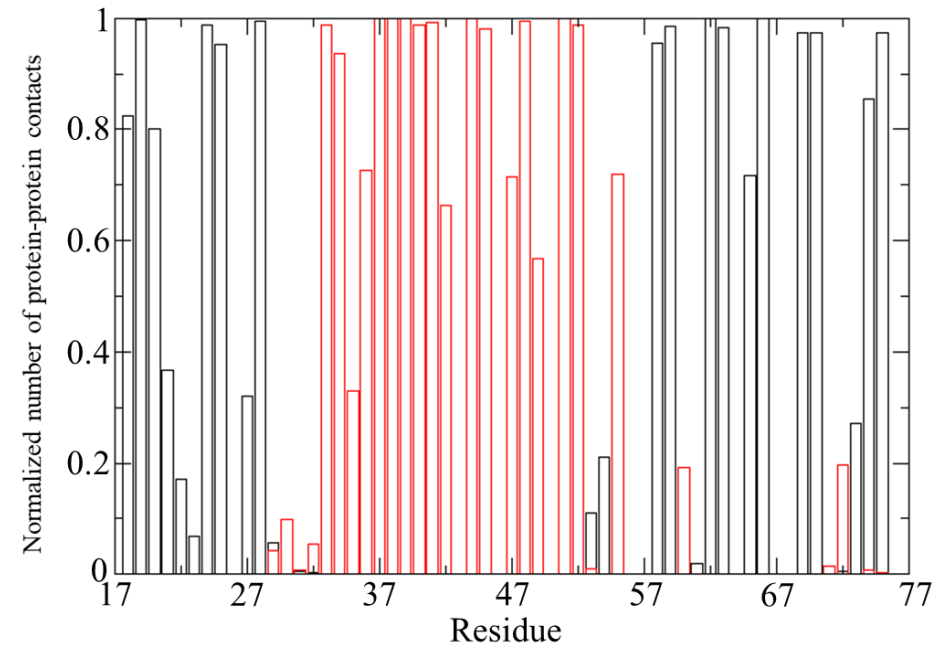
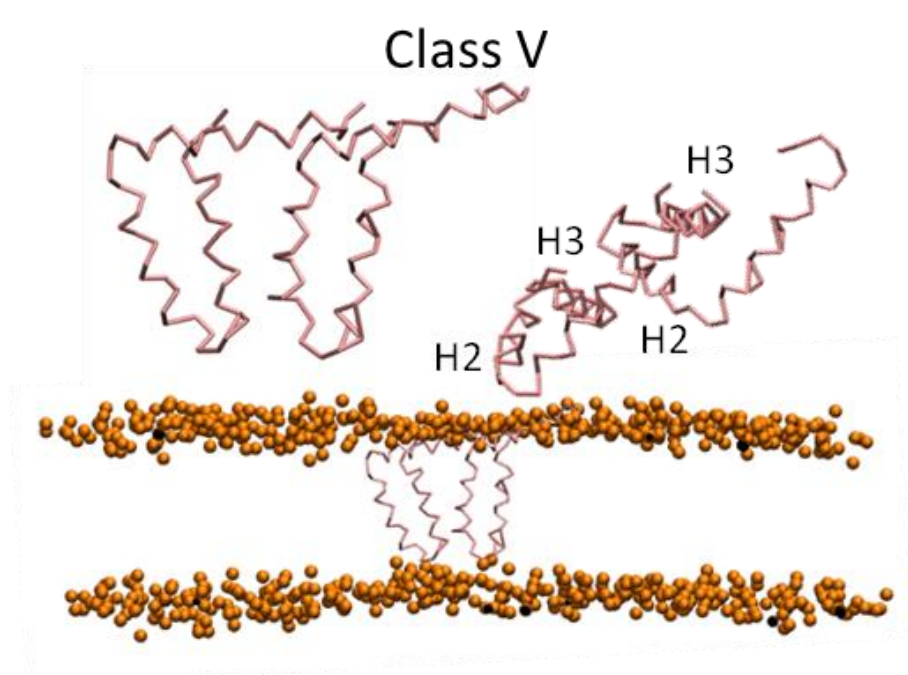


Figure 3.14 M protein dimerises in a *Flavivirus* composed lipid bilayer

Additional dimerisation conformation of M protein monomers within a WNV derived lipid bilayer after a 6 μ s coarse-grained simulation. **A.** M protein shown in pink and phospholipid heads shown in orange, protein shown with and without bilayer side on. Dimeric M protein in a Class V conformation with a H3-H2 interaction. **B.** Graph displaying the residues with the normalised highest number of interactions. Monomers coloured black and dimers red.

3.4.3 Restraining M protein conformation during dimerisation alters dimer class preferences

MD allows experimentation with protein dynamics not currently possible in the laboratory. We can simulate proteins with conformational restraints to observe the resulting difference of their interactions. In previous simulations (section 3.4.1 and 3.4.2) it was noticed the N-terminal hydrophilic helix (H1) was very flexible and sometimes was the first point of interaction between dimers. Therefore, we questioned whether this H1 flexibility was required for M protomers to come together. In addition, the presence of E protein within the immature and mature virion prior to acidification may restrain M, favouring the formation of specific dimer conformations (Bressanelli et al., 2004; Sirohi et al., 2016). To assess these factors we restrained the movement of all C-alpha atoms within M protein during the simulation, effectively preventing the dynamic structural variations observed in other systems by rigidifying the protein backbone.

When M protein C-alpha ($C\alpha$) atoms were restrained and simulated within a POPC bilayer, dimerisation occurred on average within 2.74 μ s (Figure 3.15), compared to 1.46 μ s for unrestrained dynamic protein. However, one of the 10 simulations did not dimerise within the 6 μ s timeframe. Although the $C\alpha$ restraints resulted in a slower dimerisation, the frequency of conformations also differed. Unlike the unrestrained protein forming class III conformations, the class I dimer which has a conformation similar to that found in the virion occurred most frequently, with four of the ten simulations adopting this H2-H2 H3-H3 interacting conformation compared to just one when M was not restrained. Logically, this might therefore reflect the influence E protein has on M protein dimers forming within the virion, whereby the glycoprotein exerts structural restraints upon M, favouring the formation of class I dimers, as seen in the cryo-EM structure. No dimers formed a class II conformation, suggesting flexibility is required for this conformation to form. Only two dimers formed the class III conformation, which could form a higher order oligomer with a predicted aqueous channel due to the adjacently aligned protomers, in comparison to five dimers when not restrained. Additionally, no dimers formed the class IV conformation and three dimers formed the class V conformation in comparison to two and zero respectively when the $C\alpha$ atoms were not restrained.

Similar results were seen when dimerization simulations were run with a WNV lipid composed bilayer and the C α atoms of M proteins were restrained. The results of these ten simulations showed dimerisation happened in every simulation and occurred on average after 1.64 μ s (Figure 3.16), which is quicker than when C α atoms were restrained in a POPC bilayer (2.74 μ s), however somewhat slower than when M was not restrained and simulated in a WNV virion derived membrane (1.49 μ s). Moreover, the mean time to dimerization for each of the scenarios ranges from 1.46-2.74 μ s, in this course-grained simulation the difference in time does not lend itself to any conclusions, except, the addition of C α restraints appears to increase the time taken.

The restrained dimers simulated in a WNV composed bilayer see similar proportions of classes to the restrained dimer in POPC bilayer and the patterns from not restrained to restrained are also comparable. The dimers formed five class I conformations, an increase from two when not restrained, again potentially reflecting the influence of E proteins on the dimers formed. One class II, one class III, no class IV and three class V conformations were also formed, compared to three class II, one class III, one class IV and one class V when not restrained.

These changes in dimeric conformations do not seem to be influenced by the lipid membrane composition, however the changes may be due to the reduction of H1 structural flexibility. The dimers formed may provide an insight into the interactions that occur when E protein is acidified, oligomerises and no longer restricted M dimers.

Simulation set	Dimeric classes as a % of all simulations					
	I	II	III	IV	V	N/A
POPC membrane	10	20	50	20	0	0
WNV membrane	20	40	10	0	10	20
POPC membrane restrained	40	0	20	0	30	10
WNV membrane restrained	30	10	10	0	30	20

Table 3.1 Dimeric classes formed across simulation sets

The number of dimers which formed the differing class conformations across the simulations carried out in POPC membranes and WNV comprised membrane with and without C α restraints.

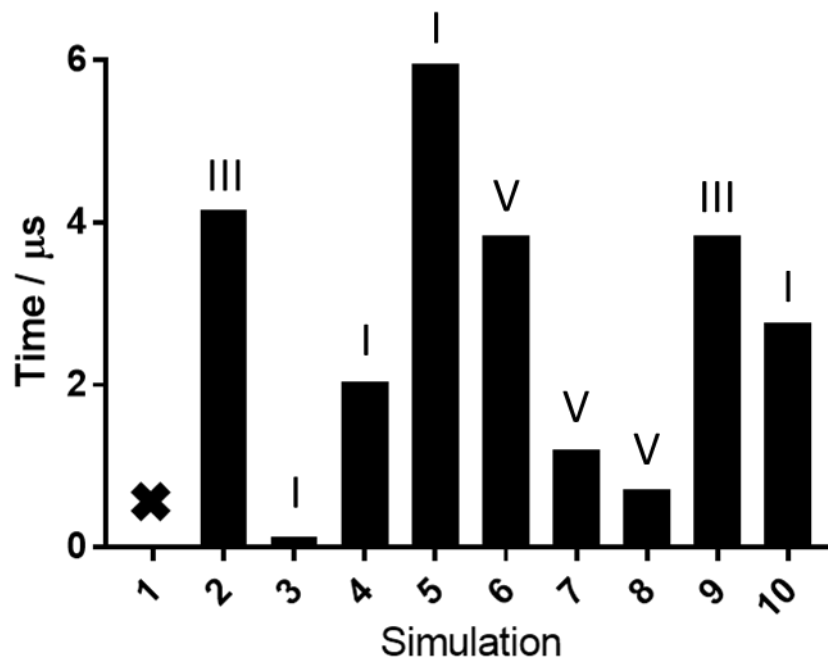


Figure 3.15 Dimerisation analysis of restrained monomers in a POPC lipid bilayer

A. Time taken for monomers to dimerise, in ten repeat 3 μs simulations, with a POPC membrane and the Ca atoms of the protein restrained. X denotes a simulation where monomers did not dimerise.

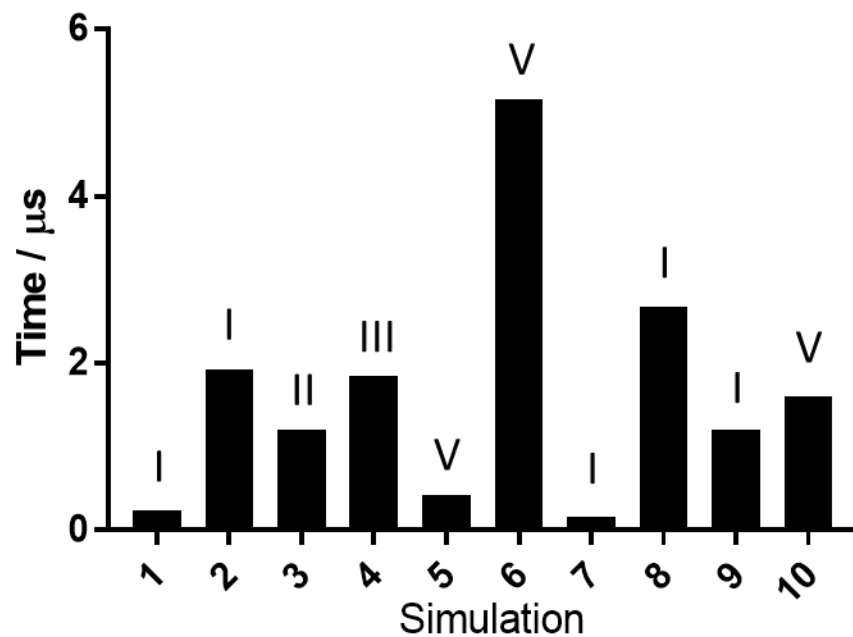


Figure 3.16 Dimerisation analysis of restrained monomers in a *Flavivirus* derived lipid bilayer

Time taken for monomers to dimerise, in a WNV composed membrane with Ca atoms of the protein restrained. X denotes a simulation where monomers did not dimerise. B. RMSF plot of dimers forming class III and IV conformations and those not dimerised. C. RMSF plot of dimers forming class I and II conformations.

3.5 Simulating M protein channels *in silico*

We hypothesised that M protein is capable of forming a higher order oligomeric channel during virus entry once acidic pH promotes E protein conformational changes from dimeric to trimeric (Dai et al., 2016). This change in conformation would no longer restrain M protein in proximity to dimeric E, potentially allowing M protein to oligomerise further. Applying the data from section 3.4 we sought to identify possible prior interactions between monomers that might promote channel formation.

Applying C α restraints to M protein monomers during simulations in section 3.4.3, caused an increase in the formation of class I dimers, reflecting the mature M protein dimeric structure, therefore these are potentially similar to the restraints applied by the presence of E dimers. However, M protein monomers simulated without restraints formed a higher percentage of dimers in orientations that favour forming an oligomeric channel, i.e. where helix 3 is in close apposition and aligned (class III), favouring the pore lining helix predicted by MEM-SAT SVM (Figure 3.5).

Viroporins are typically small membrane proteins of 100 residues or less, comprising up to three TMDs, which subsequently oligomerise into a membranous pore, ranging from tetrameric, IAV M2 (Sakaguchi et al., 1997) to heptameric, HCV p7 (Clarke et al., 2006) with a single helix lining the pore. The aforementioned viroporin properties led to the generation of the schematic in Figure 3.17. As previously mentioned, known viroporins range from being tetrameric to heptameric, however when generating M protein oligomeric models, it became apparent the pore is lined by a minimum of five helices to ensure the radius for a water permeable channel to form, as pentameric channels had a narrow pore diameter of less than 3 Å (data not shown). Additionally, the presence of dimeric M within the virion, and the stable dimers formed in section 3.4 indicate that it is more likely for M protein monomers to remain closely associated in pairs. Consequently, we assumed M protein channels would form from a minimum of six pore-lining helices, in line with the stoichiometry of other viroporins such as p7, E5 and SH. In addition, ZIKV virions contain 180 M proteins and the presence of M at the point of 3-fold symmetry, where six M proteins are present, is suggestive of hexameric

channels. Therefore, we hypothesise M protein oligomers are unlikely to form channels from class I, II or V dimers, which require 12 monomers and are unlikely to form from class IV dimers due to both helix 2 and 3 lining the pore, which has not been seen with any previously identified viroporins.

This highlights class III dimers may comprise the starting conformation of higher order oligomers leading to the formation of a channel. However, this would require the class I (cryo-EM) dimers to alter their interacting surface, to change to a class III dimeric conformation, the class III conformation may be more favourable once the restraints from envelope protein dimers have been released as discussed in section 3.4.3. If time had allowed, removing C α restraints from class I cryo-EM dimers at a defined point during simulations, then observing whether dimers altered conformation, would have investigated this possibility.

We began modelling hexameric channels using MD software GROMACS. GROMACS, as mentioned in chapter 1, is widely used and allows use of many different force fields and water models. Additionally, GROMACS has been used to successfully study ion channels or viroporins previously (Ulmschneider et al., 2013; Bagneris et al., 2014; Shukla et al., 2015; Araujo et al., 2016; Shaw et al., 2019). Hexamers were constructed using class III dimers in different orientations with either helix 2 or helix 3 lining the pore. In addition, for both hexamer structures, monomers were further rotated from a 'radial' structure to a 'compact' structure to increase inter-monomer interactions and investigate how this influenced the channel stability and activity, creating four different structures to simulate. Furthermore, structures were simulated at neutral pH, either with or without protonated HIS28 residues, reflecting the acidified endosome environment, which is known to activate or enhance activity of other viroporins (Wang, C. et al., 1995; Chizhnikov et al., 1996; Wetherill et al., 2012; StGelais et al., 2007; Wozniak et al., 2010; Atkins et al., 2014).

Due to the complexity of the predicted interactions between monomers in channel conformations, atomistic simulations were carried out, allowing us to study the proteins' conformational dynamics. Simulations were run three times for 200 ns using the all-atom CHARMM36 force field (Huang and MacKerell, 2013) An example simulation system is shown in Figure 3.18.

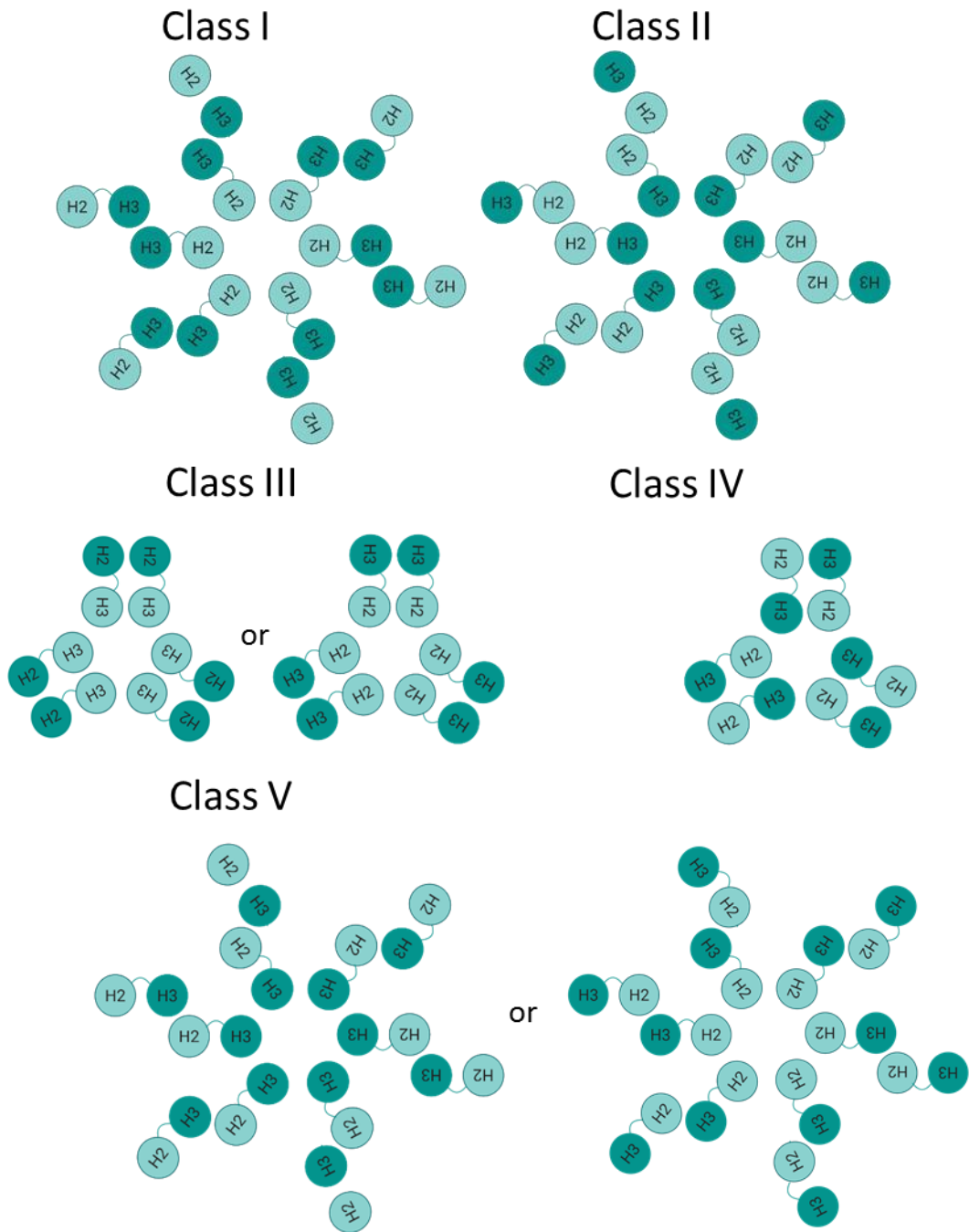


Figure 3.17 Hexameric channel conformations based on dimeric classes

Schematic displaying how dimeric classes I-V would fit together in a hexameric channel conformation, N-terminal TMD (H2) shown in light blue, C-terminal TMD (H3) shown in dark blue, helix 1 is not shown.

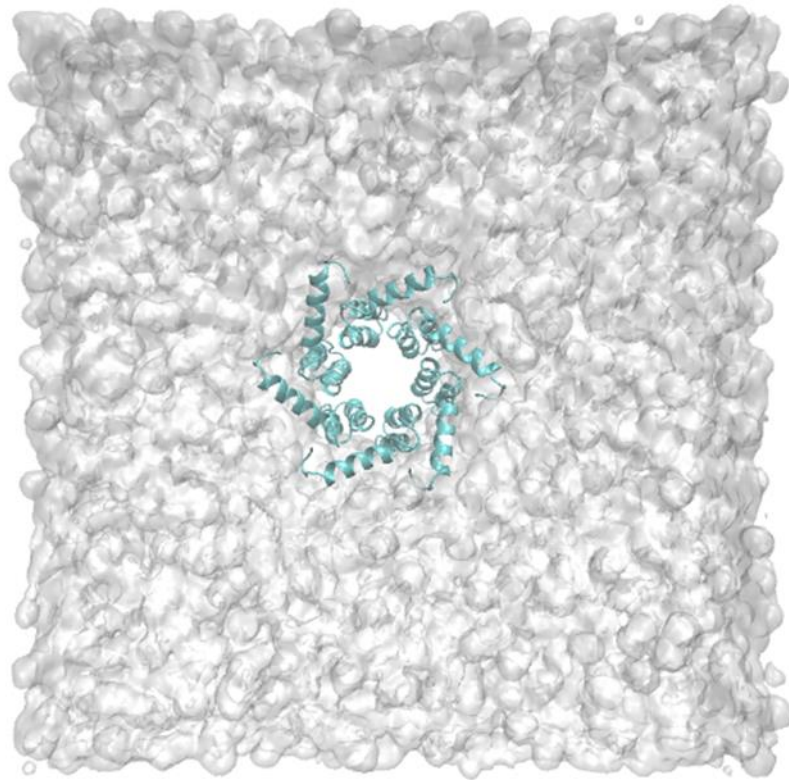
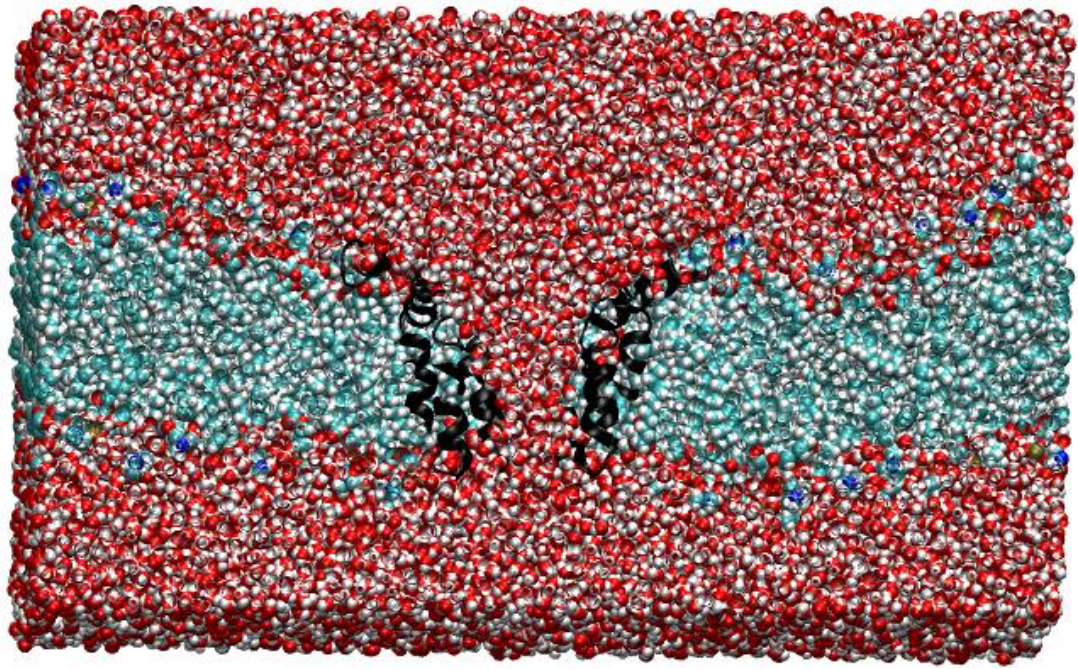


Figure 3.18 Simulation system visualisation of M protein channel

Simulation system of an all-atom simulation. A. Cut away system side view showing protein as ribbons in black, water shown in red and lipids shown in blue as van der waals, Cl^- and Na^+ ions are not shown. B. System from above showing lipids present in white by a surface representation, and protein represented as ribbons in blue.

3.5.1 Which TMD helix lines the M protein pore?

Pore-lining helices do not have readily definable characteristics. However, they usually contain a mixture of hydrophobic and polar residues compared with lipid facing helices. Helix 2 is comprised wholly of non-polar residues (Figure 3.19). In this regard, helix 3 contains one polar and charged residue (Figure 3.19) and was predicted by MEMSAT-SVM to be the pore-lining helix of M protein viroporin channels (Figure 3.5).

3.5.2 Are hexameric channels with pores lined by Helix 3 stable?

MD simulations of M protein channels were run with helix 3 pore-lining in two different conformations, named 'radial' and 'compact'. Channels were constructed with hexameric stoichiometry. Six monomers were packed and each rotated 60 or 80 degrees for the radial and compact conformations respectively (see section 2.7.3 for coordinates), producing two structures with different inter-monomer interactions without steric clashes. Next, all-atom simulations of the two conformations were run in a neutral pH environment, with and without protonation of the six HIS28 residues. This protonation imitates placing the protein in an acidic endosomal environment, where we hypothesise M protein channels are likely to form during virus entry.

3.5.2.1 Simulating channels with pores lined by helix 3, within a neutral pH environment.

The 'radial' conformation with helix 3 lining the pore was constructed with the N-terminal helix protruding away perpendicular to the channel pore (Figure 3.20). The starting conformation of the channel exhibited a lumen radius of 4.137 Å with pore lining residues LYS60, TYR63, LEU64, ILE67 and LEU69 (Figure 3.21). These residues are predominantly hydrophobic with the exception of the positively charged lysine residue, often found within Na⁺ channel lumens (Li, Y. et al., 2016). Lysine is regarded as an amphipathic residue, with its long hydrophobic carbon tail and a positively charged residue both found on its side chain. Due to the charge of the lysine, it may repel and destabilise the oligomer, although the lysine residue is found at the channel base, allowing it to interact with the lipids phosphate atoms, potentially neutralising its charge, stabilising the channel complex.

The start 'radial' conformation of the 200 ns atomistic simulations is shown in Figure 3.20. Helix 1 does not interact with the adjacent monomers, so the only interacting residues are found in the TMDs. Figure 3.22 shows a representative channel conformation at the end of one of the simulations, including a surface plot of pore radius generated using the HOLE programme. Out of three 200 ns simulations, all oligomers maintained their association to adjacent protomers, one channel retained a pore radius of 3.342 Å (Figure 3.22D), whereas the others closed after 6 and 40 ns, respectively (Figure 3.22A, C).

In Figure 3.22B the orientation of the channels that closed during simulation is shown in more detail, with hydrophobic residues LEU64, ILE67 and LEU68 playing major roles during channel closure. ILE67 occludes both channels with the addition of LEU68 in simulation one. However, LEU64 also restricts both channels. An overlay of the start and end conformations is shown in Figure 3.23.

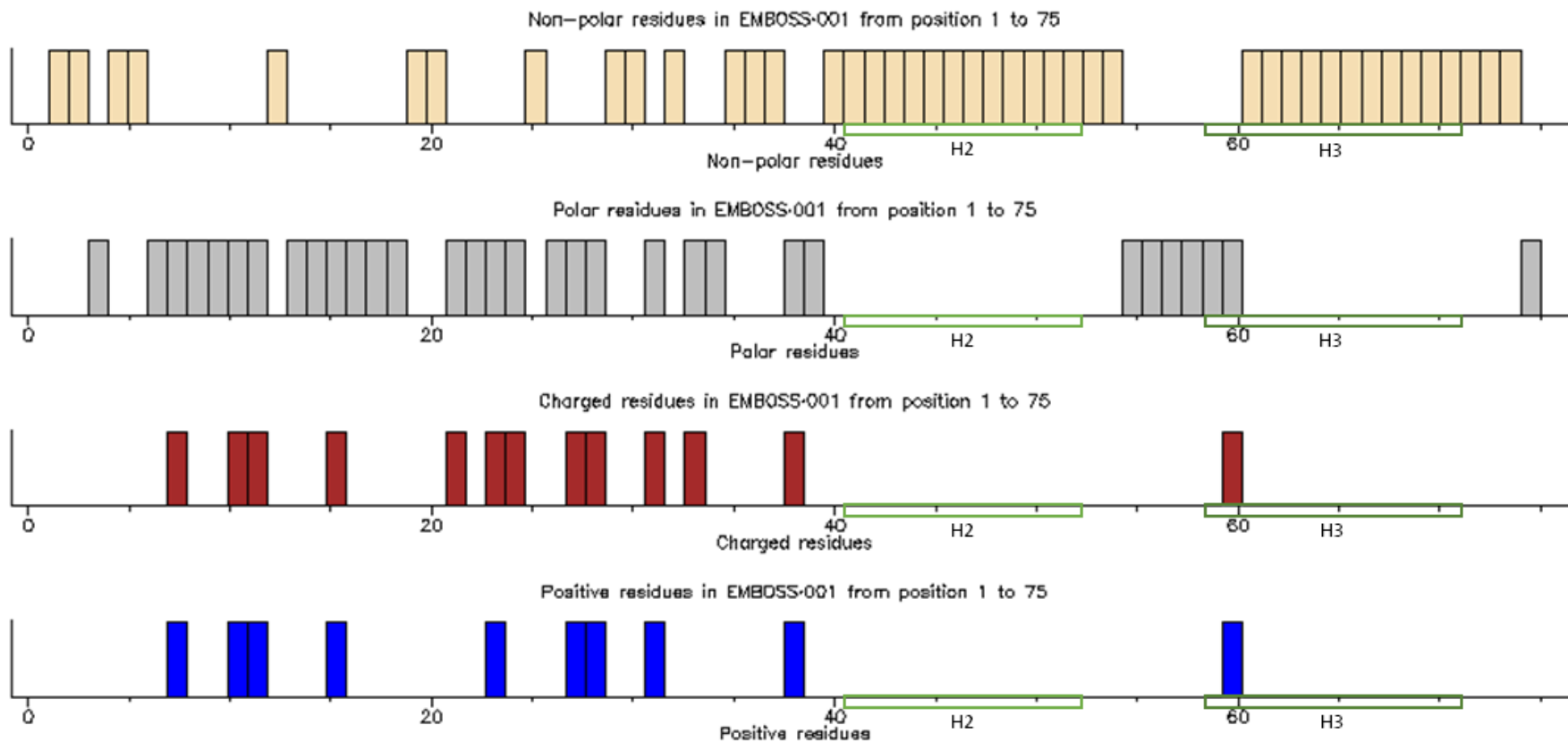


Figure 3.19 M protein amino acid properties determined by EMBOSS Pepinfo

Properties of the 75 residues of M protein, aligned to the two TMDs helix 2 (H2) and 3 (H3). Properties shown are non-polarity, polarity, charge and positive charge.

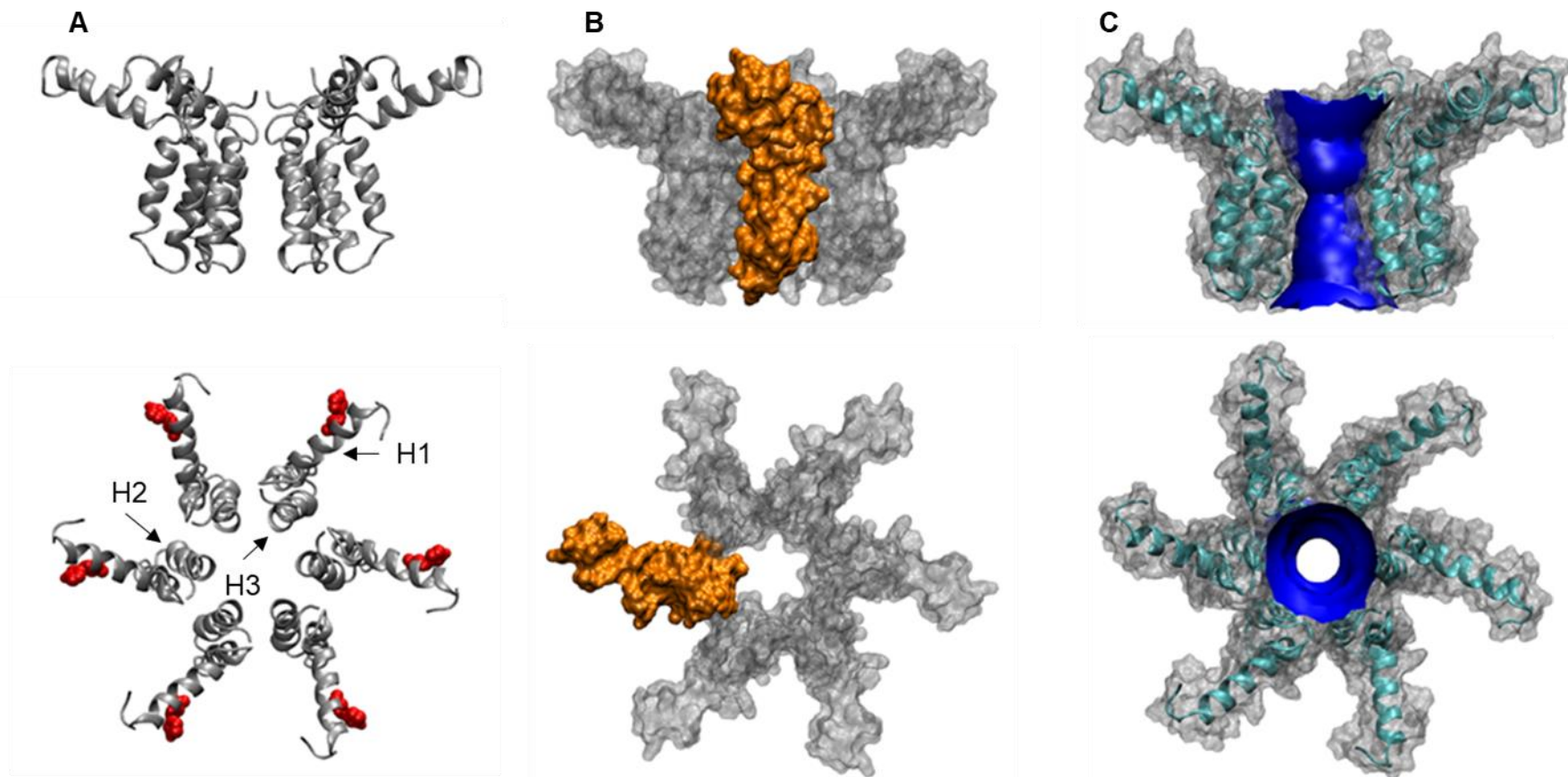


Figure 3.20 Starting conformations of hexameric 'radial' channel with pore lined by Helix 3

A. Ribbon representation side on and from above with HIS28 residues highlighted in red with helices indicated. B. Surface representation side on and from above with one protomer highlighted in orange. C. Ribbon and Surface overlay representation with HOLE profile through the centre displaying the space inside the pore.

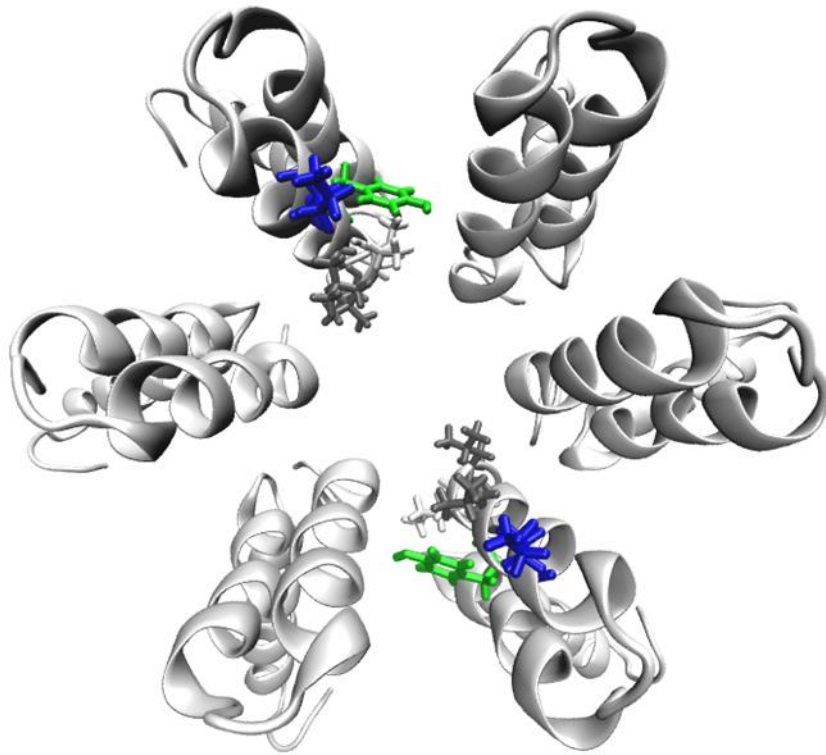
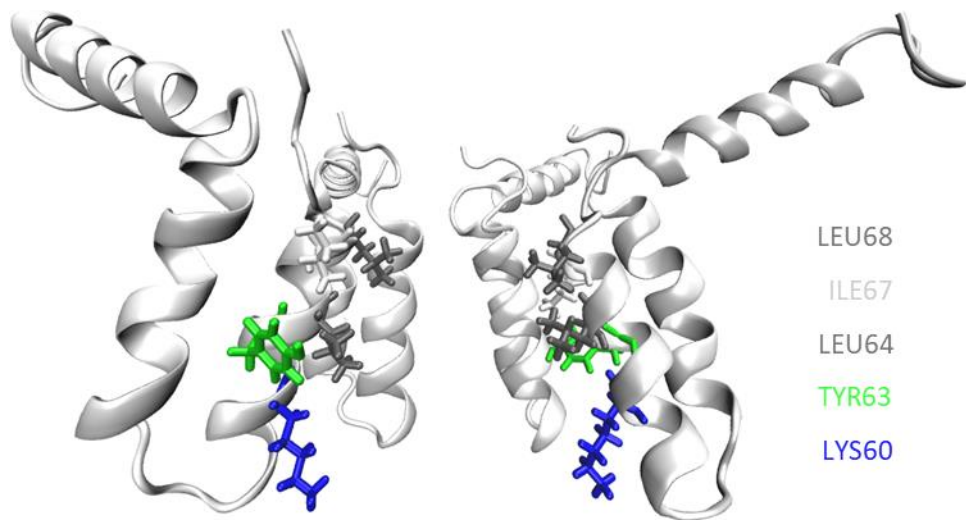


Figure 3.21 Hexameric helix 3 pore-lining ‘radial’ channel luminal residues

Pore lining residues of a Hexameric M protein channel in a ‘radial’ conformation with the C-terminal TMD (helix 3) lining the pore. Pore lining residues LEU68 in grey, ILE67 in white, LEU64 in grey, TYR63 green and LYS60 in blue.

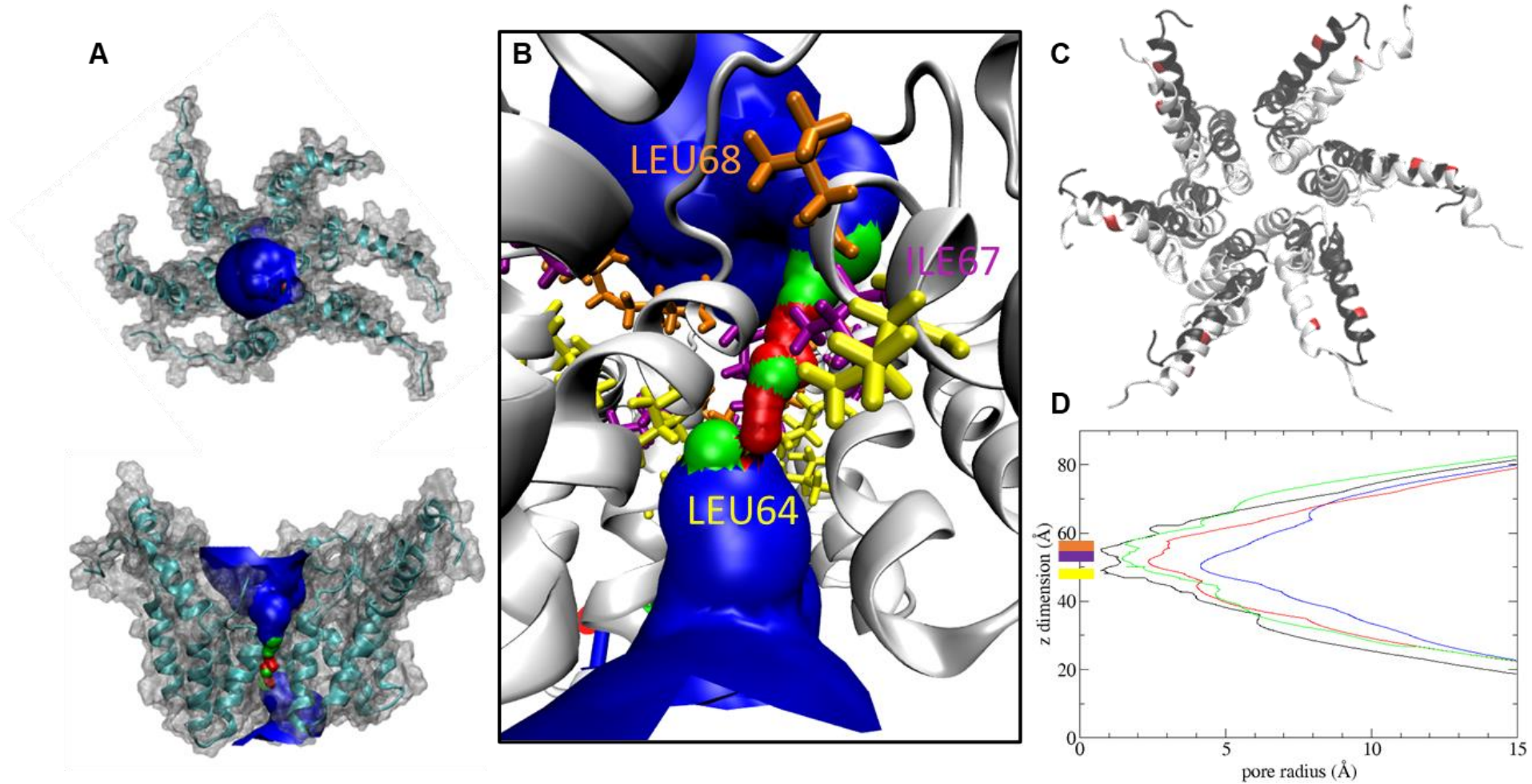


Figure 3.22 200 ns conformation of hexameric 'radial' channel with pore lined by helix 3

A. Surface and Ribbon representation of simulation three at 200ns from above and side with one helix cut away and HOLE surface plot displayed. Areas inaccessible to water with a pore radius $< 1.15 \text{ \AA}$ in red, referred to as a closed channel, areas that will allow passage of one water molecule $1.15 \text{ \AA} > \text{pore radius} < 2.30 \text{ \AA}$ in green, and areas accessible to greater than one water molecule pore radius $> 2.30 \text{ \AA}$ in blue. **B.** Simulation three channel zoomed in with HOLE surface plot displayed and residues closing the channel shown with sticks. LEU64 in yellow, ILE67 in purple and LEU68 in orange. **C.** Overlay of starting conformation in black and representative end conformation in white, with HIS28 in red. **D.** HOLE profile plot of pore radius, starting conformation shown in blue, simulation one, two and three in black, red and green respectively, with positions of residues LEU64 in yellow, ILE67 in purple and LEU68 in orange.

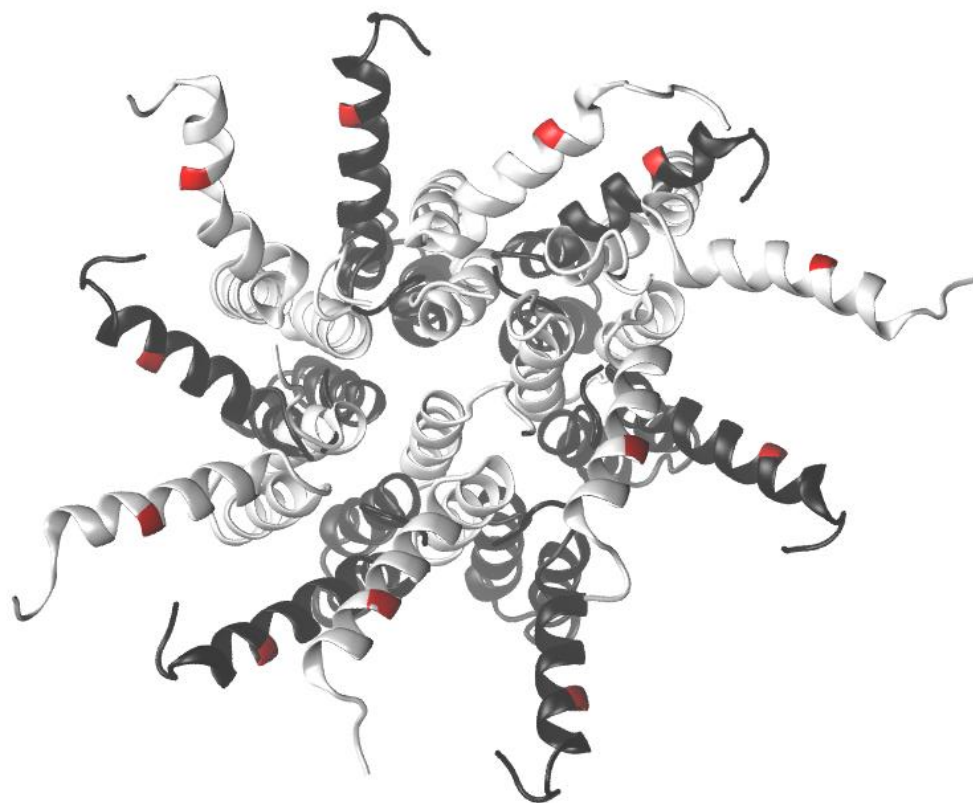


Figure 3.23 Helix 3 pore lining radial start and end conformation overlay

Overlay from above of helix 3 pore lining radial start and representative end conformations in black and white respectively with HIS28 shown in red.

'Radial' structures, whilst remaining intact through the simulations, retained poor packing between protomers resulting in a low number of potentially stabilising interactions. However, rotation of the protomers by an additional 20 degrees in a clockwise direction, observed from the top of the channel complex, greatly increased the proportion of surface interactions between protomers (Figure 3.25C). The more 'compact' hexameric structure (Figure 3.24) in comparison with the 'radial' structure (Figure 3.20), has a visibly increased number of interactions between monomers, including interactions of the N terminal helix with adjacent protomers similarly to those seen in class III dimers. We therefore hypothesised the N-terminal helices (helix 1) interactions would reduce the overall flexibility of the channel complex. In addition, this region contains a HIS at position 28 on helix 1 (Figure 3.24), which is likely to become protonated in the acidifying endosomes, and therefore could influence the overall structure. These interactions may influence the activity of the channel, especially due to the presence of HIS28 on helix 1, which would be protonated in an acidic environment, such as within an internalised endosome. HPV E5 also possesses a peripheral HIS residue, using a liposome-based assay, indirect E5 channel activity is enhanced at acidic pH (Wetherill et al., 2012). Moreover, DENV M HIS39 present on the N terminal helix was shown to be important for particle production (Pryor et al., 2004).

The helix 3 pore-lining compact channel lumen has a radius of 5.233 Å at the start of the simulation compared to 4.137 Å when 'radial' due to protruding side chains, with pore lining residues THR57, VAL61, ILE62, VAL65, MET66, LEU68 and LEU69 (Figure 3.25), very different from the 'radial' pore lining residues (Figure 3.21) with only LEU68 present in both channels. However, both channel lumens contain a high percentage of residues with hydrophobic side chains, the exceptions being positively charged amino acid lysine for radial channels and polar amino acid threonine for compact channels.

Helix 3 pore lining compact oligomers also all maintained their interactions between protomers, not becoming dissociated. The compact channels closed in 70, 80 and 176 ns, compared to 6, 40 and >200 ns for helix 3 pore lining radial channels. Therefore, compact channels are open for a greater time period on average, irrespective of a single radial channel remaining open for >200 ns, due

to the short periods of time the remaining channels were open for. Thus the helix 3 pore lining compact oligomer is more likely to be representative of those found in the virion as it remains open for a greater period of time.

A representative closed conformation is shown in Figure 3.26A with the lower part of the channel closed, as seen across all three final channel conformations. However, upon closer inspection of the simulation one channel also closes in the middle and the closure of simulation two channel extends upwards to the middle of the channel. These closures involve LEU64 and LEU68 similarly to the radial conformations, despite LEU64 not being a pore-lining residue in the compact conformation at the start of simulations. Additionally, pore-lining residues VAL61 and VAL65 also cause channel closure in these conformations (Figure 3.26B, C).

These differences in closures may be a consequence of the compact conformation, which retains a greater number of pore-lining residues compared to radial models. However, interestingly LEU64, a residue not pore-lining at the start, was involved in the closure and restriction of the channels. An overlay of the start and end conformations is shown in Figure 3.27.

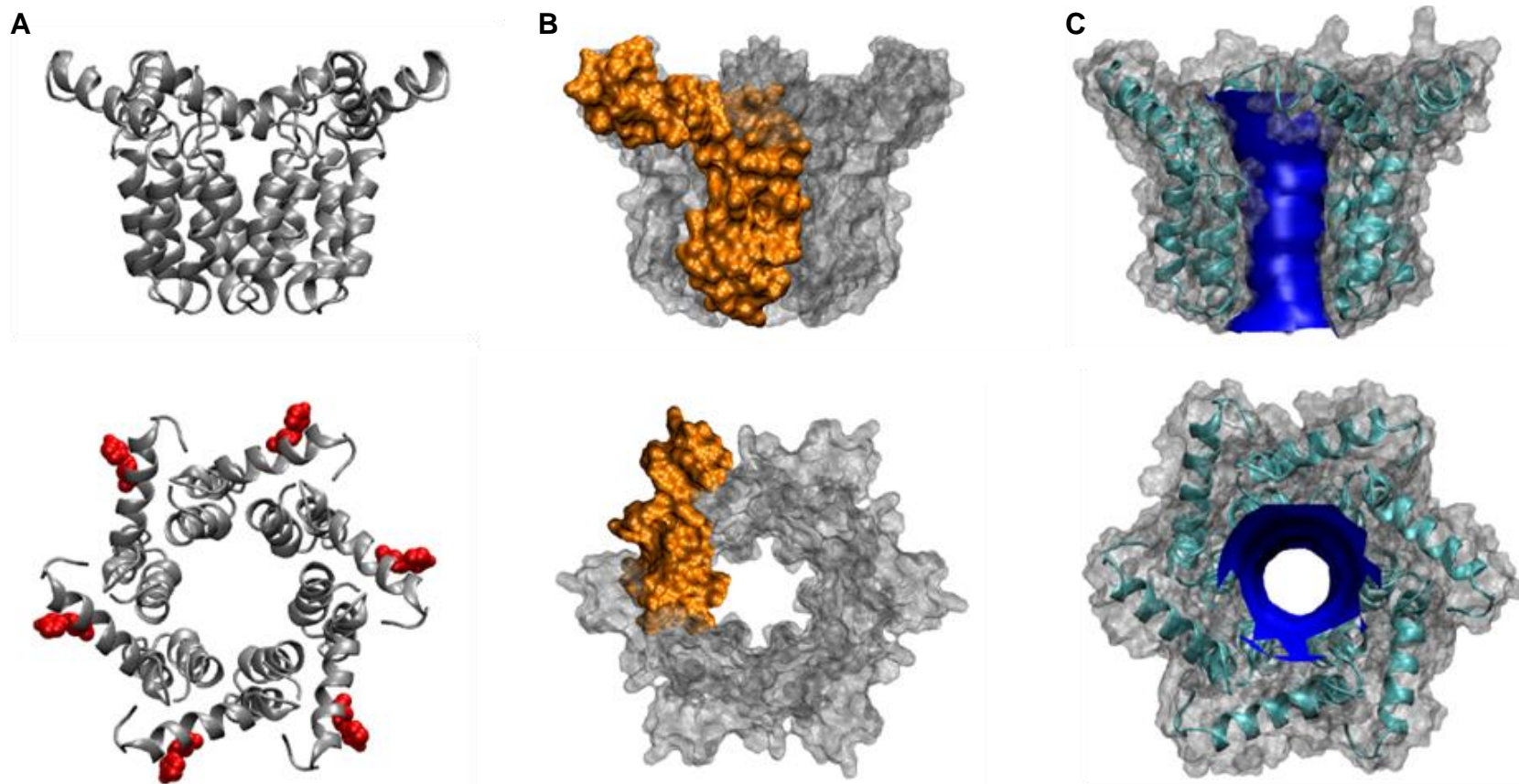


Figure 3.24 Hexameric Helix 3 pore-lining 'compact' channel, starting conformations

A. Ribbon representation side on and from above with HIS28 residues highlighted in red. B. Surface representation side on and from above with one protomer highlighted in orange. C. Ribbon and Surface representation overlay with HOLE profile through the centre displaying the space inside the pore.

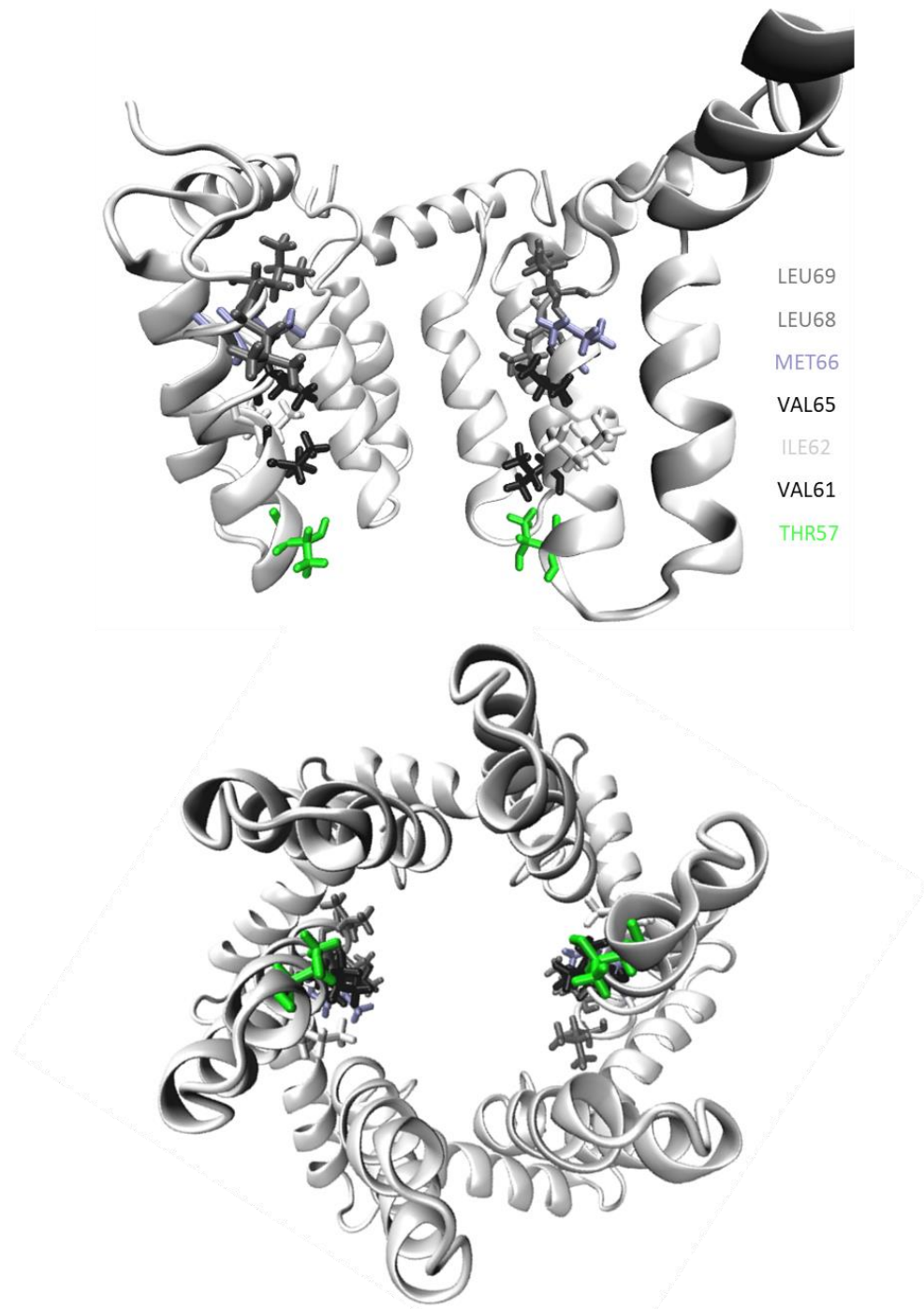


Figure 3.25 Hexameric helix 3 pore-lining 'compact' channel luminal residues

Pore lining residues of a Hexameric M protein channel in a 'compact' conformation with the C-terminal TMD (helix 3) lining the pore. Pore lining residues LEU69 in grey, LEU68 in grey, MET66 in purple, VAL65 in black, ILE62 in white, VAL61 in black and THR57 in green are shown from side on with two protomers hidden and from below.

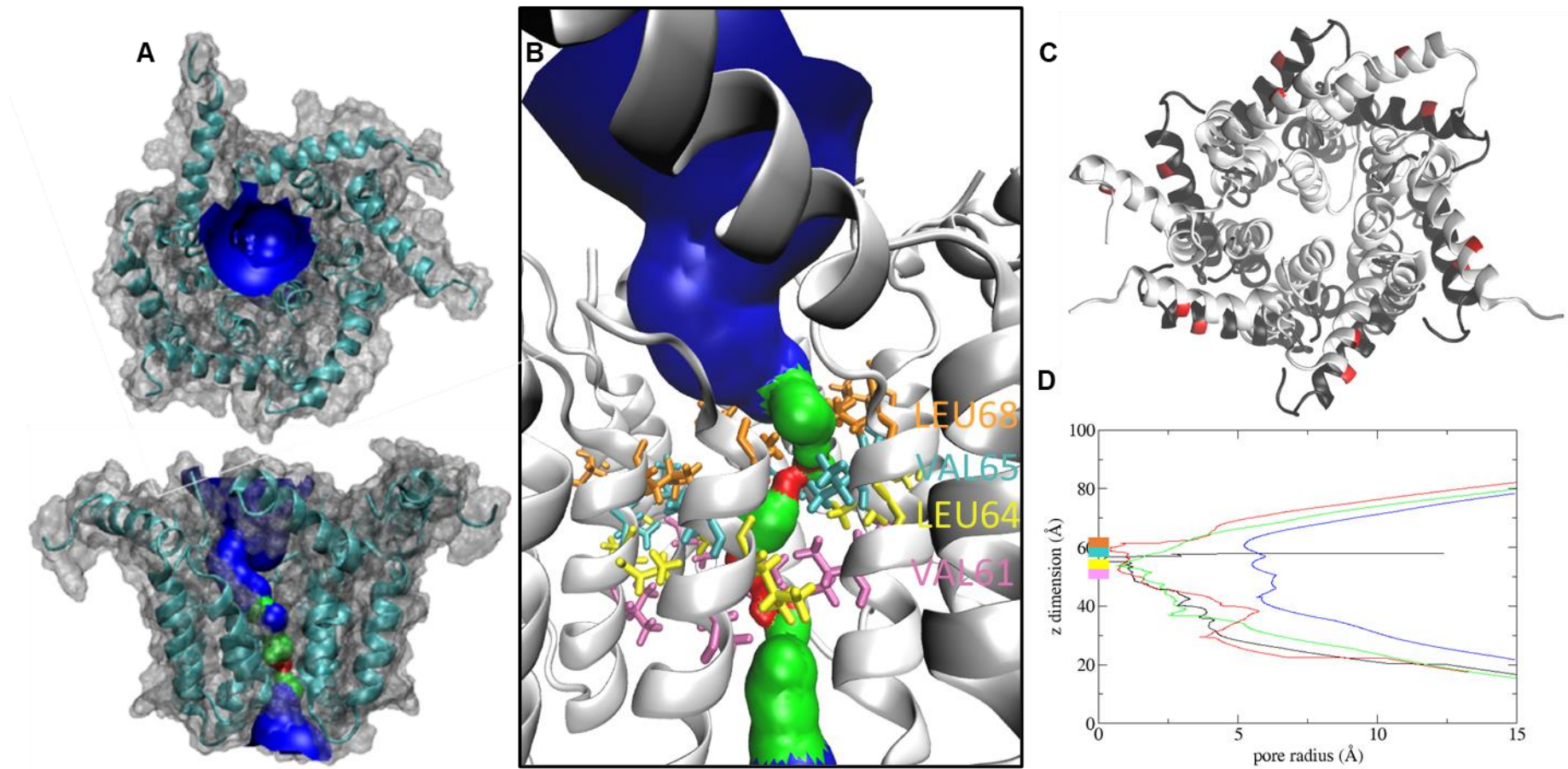


Figure 3.26 Hexameric Helix 3 pore-lining 'compact' channel conformations after 200 ns simulation

A. Surface and Ribbon representation of simulation three at 200ns from above and side with one helix cut away and HOLE surface plot displayed. Areas inaccessible to water with a pore radius $< 1.15 \text{ \AA}$ in red, referred to as a closed channel, areas that will allow passage of one water molecule $1.15 \text{ \AA} > \text{pore radius} < 2.30 \text{ \AA}$ in green, and areas accessible to greater than one water molecule pore radius $> 2.30 \text{ \AA}$ in blue. **B.** Simulation two channel zoomed in with HOLE surface plot displayed and residues closing the channel shown with sticks. LEU64 in yellow, LEU68 in orange, VAL61 in mauve and VAL65 in cyan. **C.** Overlay of starting conformation in black and representative end conformation in white, with HIS28 in red. **D.** HOLE profile plot of pore radius, starting conformation shown in blue, simulation one, two and three in black, red and green respectively, with residues LEU64 in yellow, LEU68 in orange, VAL61 in mauve and VAL65 in cyan.

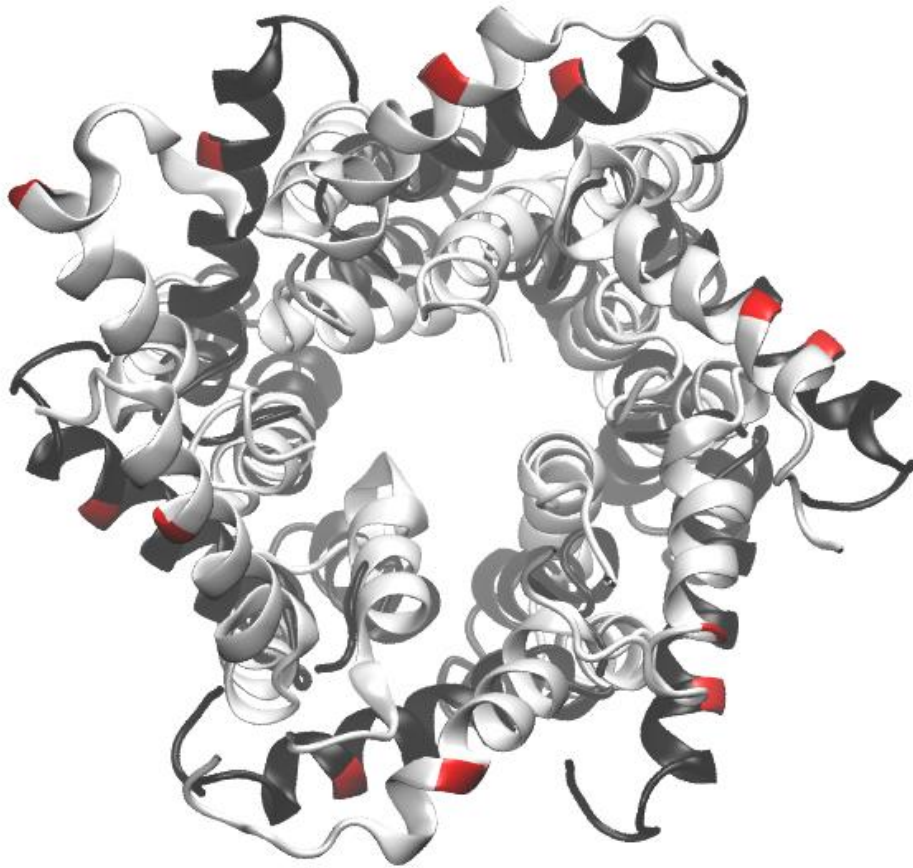


Figure 3.27 Helix 3 pore lining compact start and end conformation overlay

Overlay from above of helix 3 pore lining compact start and representative end conformations in black and white respectively with HIS28 shown in red.

3.5.2.2 Does protonation of HIS28 change the structure of the hexameric helix 3 pore lining channels and their rate of closure?

Simulations of hexameric M protein channels with helix 3 pore-lining in neutral pH showed stability by not disassociating upon equilibration, and have shown potential for channel activity by staying open for over 200 ns in one simulation. However, M protein channels are expected to form in an acidic environment within an endosome. Thus, we chose to mimic this environment by protonation of HIS28, located within the N-terminal helix 1, and to examine ensuing effects upon predicted channel structure and resultant switching between open and closed conformations.

Interestingly, protonation of the 'radial' structure reduced the pore radius from 4.137 to 3.8 Å (Figure 3.29 and Figure 3.22). However, protonated complexes displayed a similar propensity to close as did non-protonated radial structures during simulations (25, 27 and 172 ns), although direct comparison is challenging given that one of the non-protonated channels remained open for the duration (6, 40 and >200 ns) (Figure 3.22 and Figure 3.29). Had time permitted, an extended series of simulations may have yielded a more definitive measure of how HIS28 protonation affected the helical bundle. Similarly to non-protonated simulations, channel closure involved LEU64, ILE67 and LEU68, with the addition of SER58 in one simulation (Figure 3.29). Despite the reduction in pore radius, the differences between protonated and non-protonated HIS28 radial simulations are minimal, potentially due to the greater molecular distances separating HIS28 from the remainder of the channel in comparison to compact channels, resulting in the diminished influence of the associated positive charge. Measurement of the distance between the pore centre and HIS28 was found to be 31.28 Å.

Conversely, protonation of the histidines on 'compact' helix 3 pore-lining channels had a greater impact upon channel behaviour. HIS28 protonation had minimal effect upon the channel radius, the narrowest point which remained virtually identical to non-protonated complexes: 5.233 compared with 5.207 Å (Figure 3.26D and Figure 3.31D). However, compared to non-protonated complexes, the presence of positive charge upon HIS28 led to an increase in the time taken for channels to close during three 200 ns simulations: 100, 130

and >200 ns compared with 70, 80 and 176 ns. Whilst again the lack of closure during one of the simulations makes it difficult to compare directly, the extended channel opening supports that M protein channels in this conformation are capable of responding to acidified environments. In comparison to radial channels, the distance between HIS28 and the pore centre in compact channels was reduced considerably to 16.8 Å, as opposed to 31.28 Å. This proximity may influence channel activity when HIS is protonated in an acidified environment.

Furthermore, the remaining open channel exhibited a lumen radius of 2.533 Å at 200 ns, reducing by around half from 5.233 Å, yet still retaining a water column, providing an insight into the potential structure of an M protein viroporin (Figure 3.31). The conformation of a representative channel after 200 ns can be seen in Figure 3.31A, and in detail in Figure 3.23B, showing similarities between the protonated and not-protonated channels (Figure 3.26). Both sets of channels close similarly with residues VAL61, LEU64, VAL65 and LEU68 occluding the pore, with the addition of residue ILE62 when channels are protonated.

It is apparent from analysing the helix 3 pore-lining simulation sets that compact protonated channels remain open for the longest time periods, demonstrating that the compact channels respond as we would expect a channel to in a protonated environment, opening favourably in the acidic environment, mimicking the acidified endosome. Whereas the 'radial' structures did not respond to the protonation change.

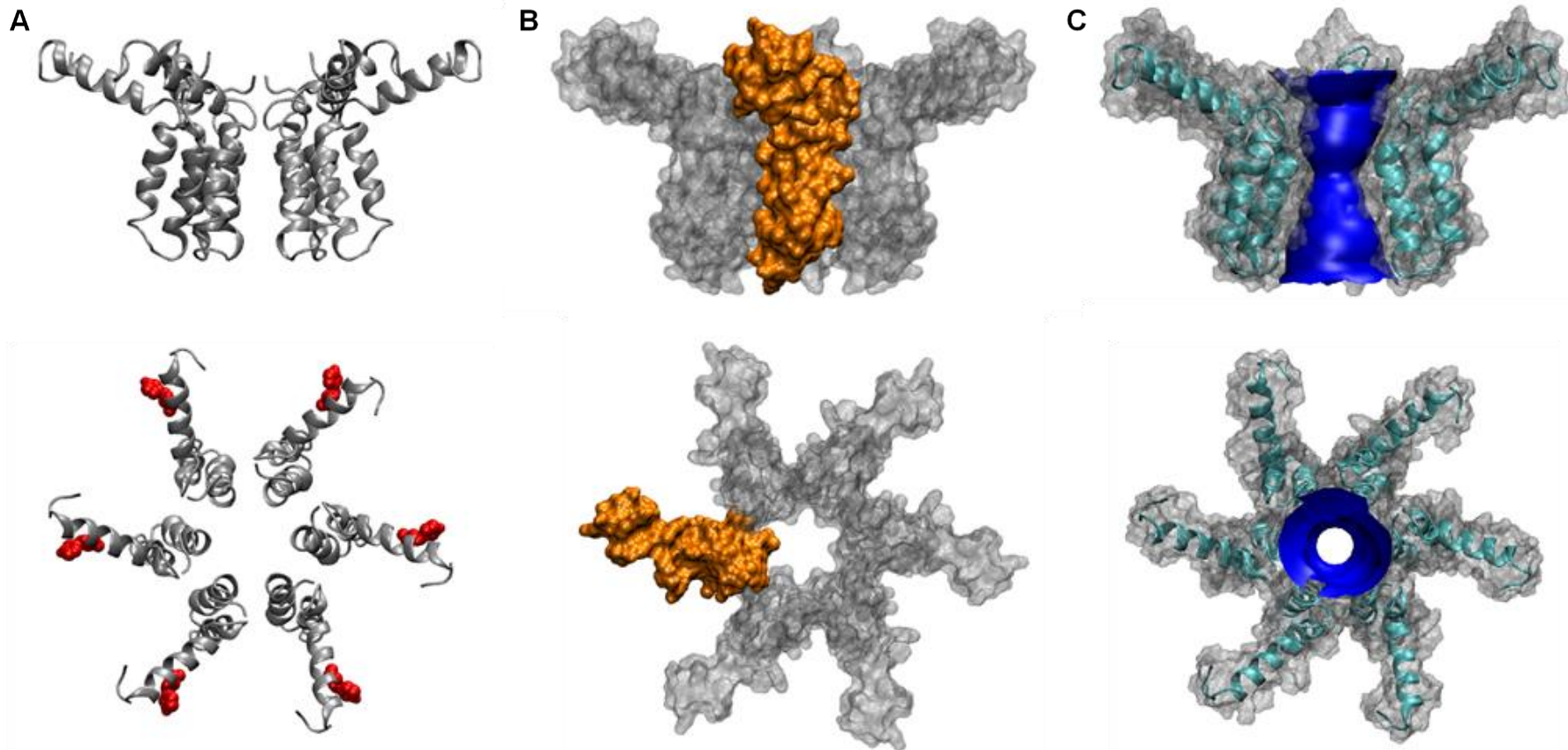


Figure 3.28 Hexameric Helix 3 pore-lining 'radial' protonated channel starting conformations

A. Ribbon representation side on and from above with histidine residues highlighted in red. B. Surface representation side on and from above with one protomer highlighted in orange. C. Ribbon and Surface overlay representation with HOLE profile through the centre displaying the space inside the pore.

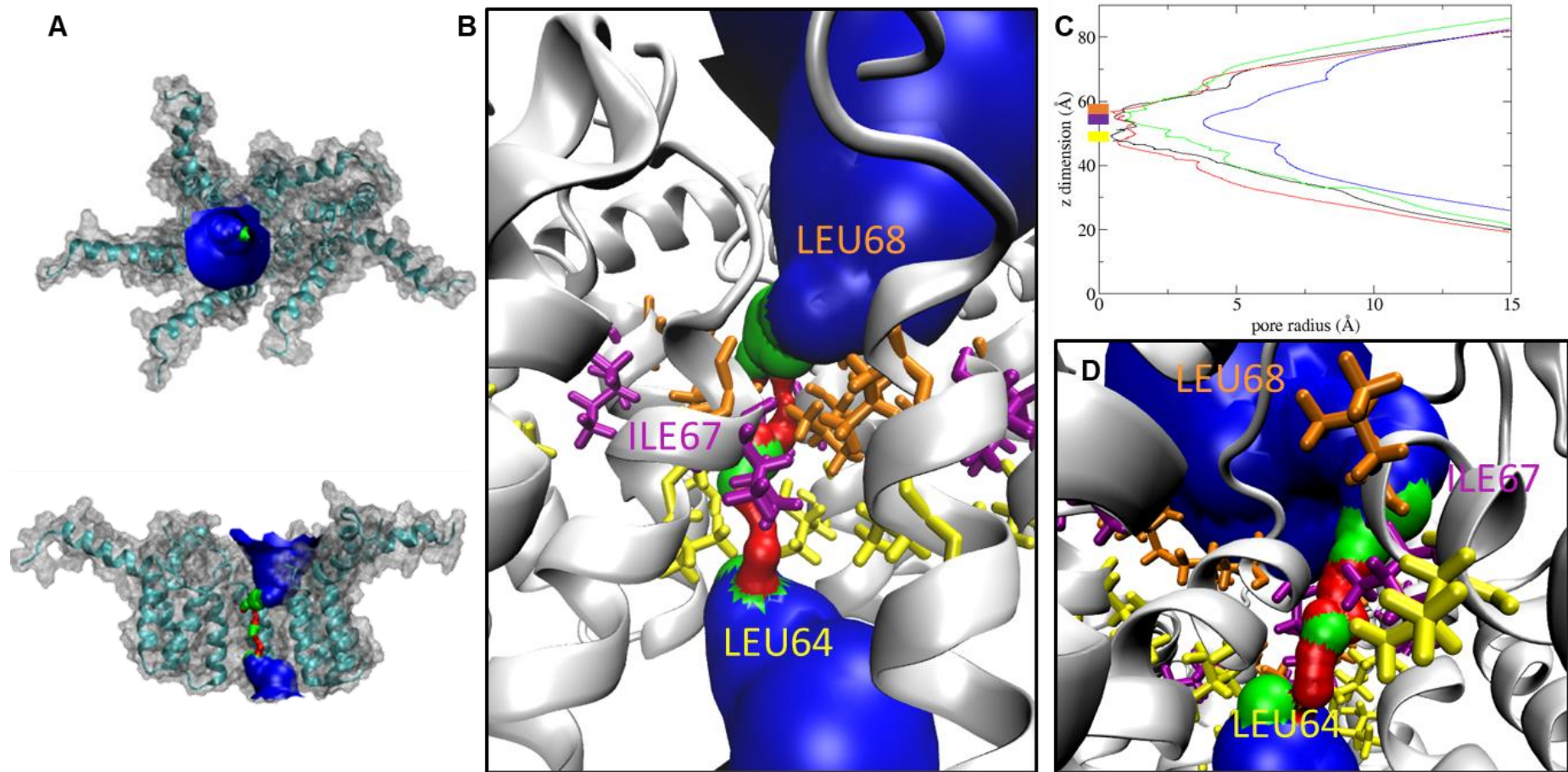


Figure 3.29 Hexameric Helix 3 pore-lining 'radial' protonated channel conformation after 200 ns simulation

A. Surface and Ribbon representation of simulation three at 200ns from above and side with one helix cut away and HOLE surface plot displayed. Areas inaccessible to water with a pore radius $< 1.15 \text{ \AA}$ in red, referred to as a closed channel, areas that will allow passage of one water molecule $1.15 \text{ \AA} > \text{pore radius} < 2.30 \text{ \AA}$ in green, and areas accessible to greater than one water molecule pore radius $> 2.30 \text{ \AA}$ in blue. **B.** Representative channel zoomed in with HOLE surface plot displayed and residues closing the channel shown with sticks. LEU64 in yellow, ILE67 in purple and LEU68 in orange. **C.** HOLE profile plot of pore radius, starting conformation shown in blue, simulation one, two and three in black, red and green respectively. **D.** Representative final conformation of the helix 3 pore lining radial simulation previously shown in Figure 3.22.

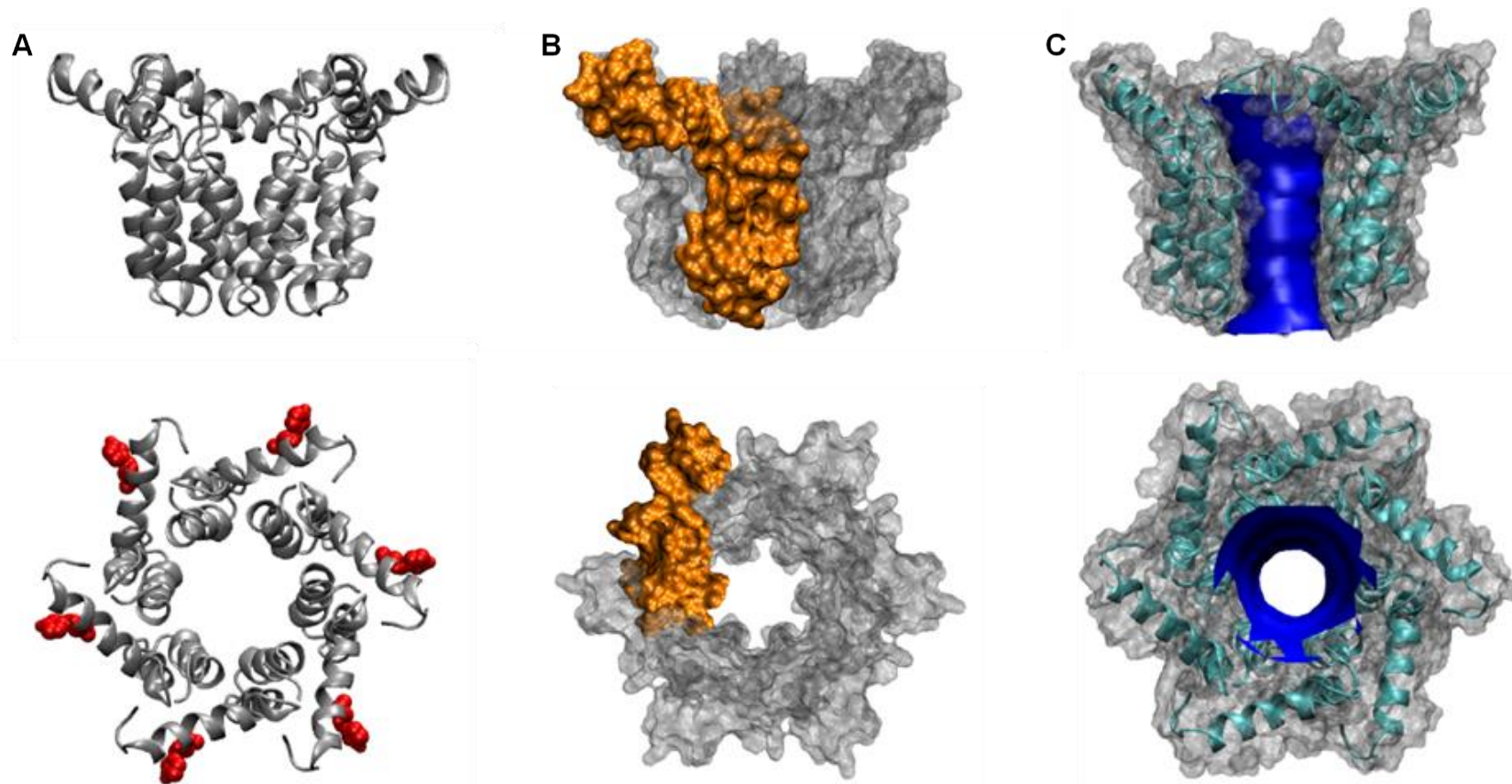


Figure 3.30 Hexameric Helix 3 pore-lining 'compact' protonated channel starting conformations

A. Ribbon representation side on and from above with histidine residues highlighted in red. B. Surface representation side on and from above with one protomer highlighted in orange. C. Ribbon and Surface overlay representation with HOLE profile through the centre displaying the space inside the pore

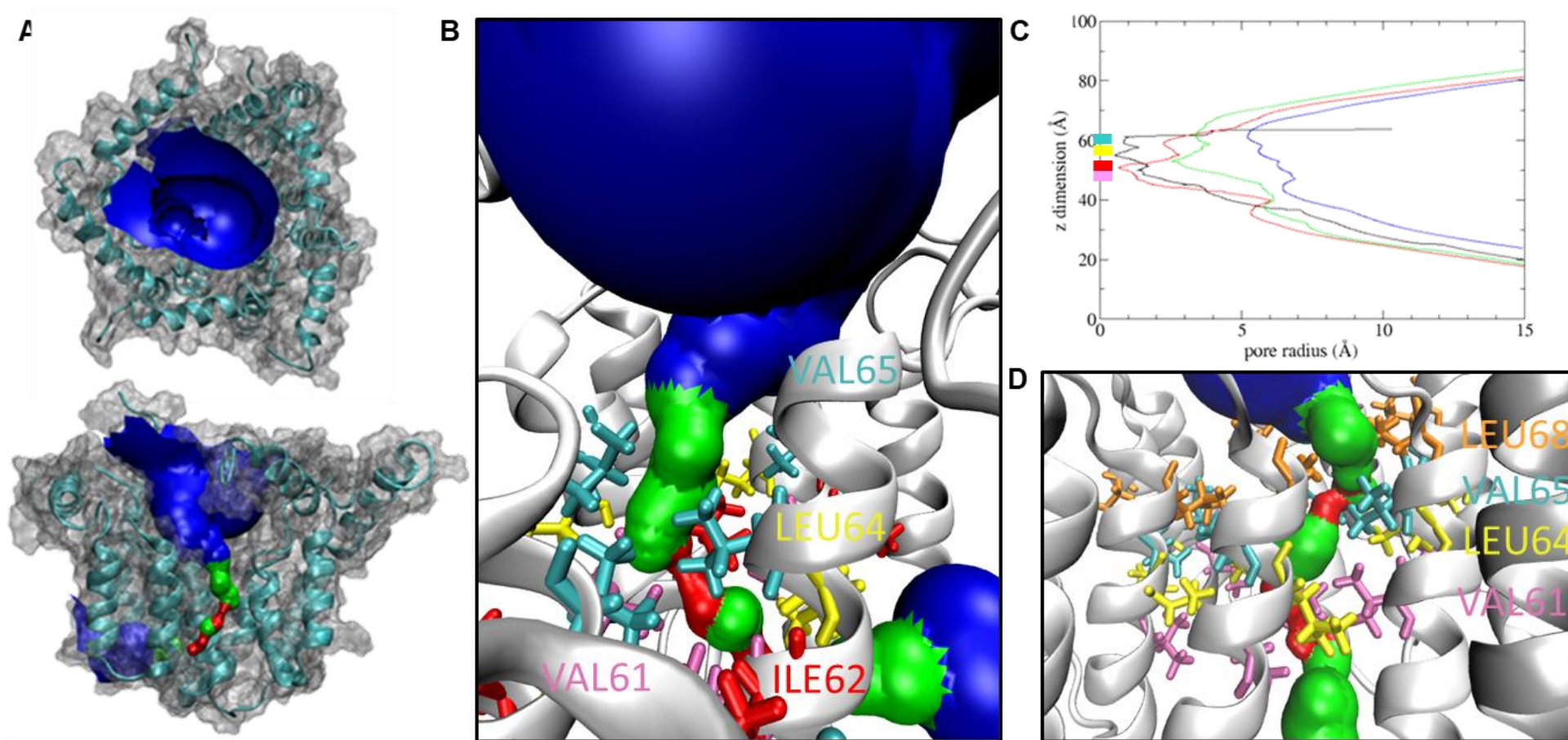


Figure 3.31 Hexameric Helix 3 pore-lining 'compact' protonated channel conformation after 200 ns simulation

A. Surface and Ribbon representation of simulation three at 200ns from above and side with one helix cut away and HOLE surface plot displayed. Areas inaccessible to water with a pore radius $< 1.15 \text{ \AA}$ in red, referred to as a closed channel, areas that will allow passage of one water molecule $1.15 \text{ \AA} > \text{pore radius} < 2.30 \text{ \AA}$ in green, and areas accessible to greater than one water molecule pore radius $> 2.30 \text{ \AA}$ in blue. **B.** Simulation two channel zoomed in with HOLE surface plot displayed and residues closing the channel shown with sticks. LEU64 in yellow, VAL61 in mauve and VAL65 in cyan and ILE62 in red. **C.** HOLE profile plot of pore radius, starting conformation shown in blue, simulation one, two and three in black, red and green respectively. **D.** Representative final conformation of the compact not protonated simulation previously shown in Figure 3.25.

3.5.2.3 Helix 1 truncation destabilises M protein channels

M protein oligomers have shown stability with either Helix 2 or 3 pore lining, however Helix 3 channels retain a water permeable pore for extended periods of time in comparison. The role of Helix 1 in M protein channel stability has not been investigated. Through simulations of M protein channels with Helix 3 pore lining and a truncated Helix 1 we observed channels do not retain their pore. Of three repeat simulations, channels closed within 50 ns in each occurrence, suggesting Helix 1 plays a role in stabilising the open pore. Helix 1 may make vital interactions between monomers forming a more stable structure, or its residues may respond to the acidifying endosomal environment due to the presence of a HIS residue.

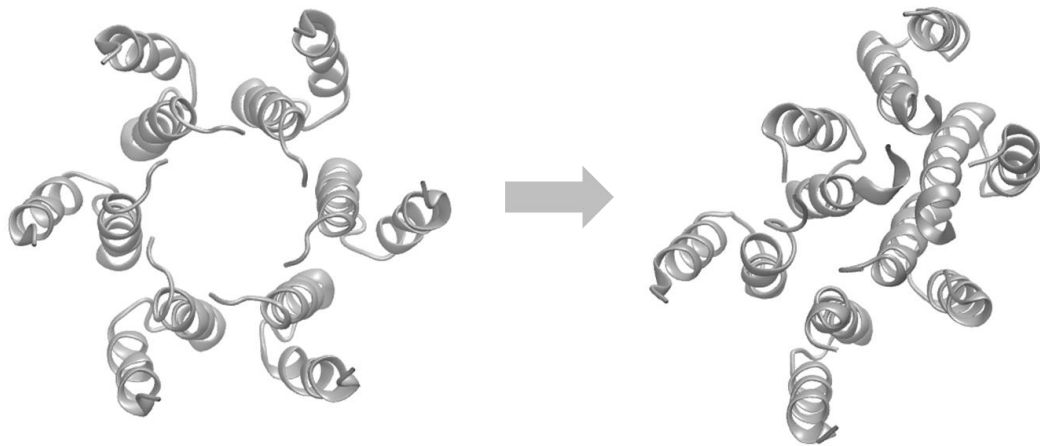


Figure 3.32 Hexameric helix 3 pore lining channel simulations with truncated helix 1

Ribbon representations of M protein channels with helix 3 pore lining and helix 1 truncated before and after a 50 ns simulation.

3.5.3 Are channels with Helix 2 lining the pore stable?

Helix 2 was not predicted to be a channel pore-lining helix using MEM-SAT SVM software (Figure 3.5). However, to control for whether these predictions would apply during simulations, additional experiments were performed using radial and compact models where helix 2 lines the pore, including the simulation of HIS28 protonation. MD simulations were run with either helix 3 (section 3.5.2) or helix 2 in the centre of the pore for comparison. Similarly to the helix 3 pore lining channels, simulations were run in differing conformations, either 'radial' or 'compact' and both were simulated in a neutral and a protonated environment, as previously run for helix 3 pore-lining to determine activity in an acidic environment.

3.5.3.1 Simulating channels with helix 2 lining the pore, in a neutral pH

The radial conformation of M protein hexamer with the helix 2 lining the pore was constructed with the N-terminal helix protruding away from the channel, resulting in helix 3 wrapping around the outside of the channel (Figure 3.33). The channel has a pore radius of 3.2 Å at its narrowest point, wider than the radius of a water molecule at 1.375 Å, the residues lining the pore start with PRO40 at the neck followed by LEU44, ALA47 and TRP51 prior to simulation (Figure 3.34).

Channels were simulated for 200 ns using atomistic resolution. The channels remained open for just 6 ns in each of the three simulations. In Figure 3.33 the channel formed through the hexamer is obvious at the start of the simulation, after 200 ns the conformation of the closed channels can be seen in Figure 3.35A, B. The channels closed in different ways, however all channels were occluded at the bottom by TRP51.

As seen in section 0 rotation of individual protomers of the helix 3 pore-lining channels into the compact conformation results in more interactions between them, potentially stabilising the channel in comparison to the 'radial' conformation. The same rotation was applied to helix 2 pore-lining radial channel protomers. However, due to the position of the connecting helix 3, clockwise rotation of M protomers was not possible, as this would lead to steric clashes over

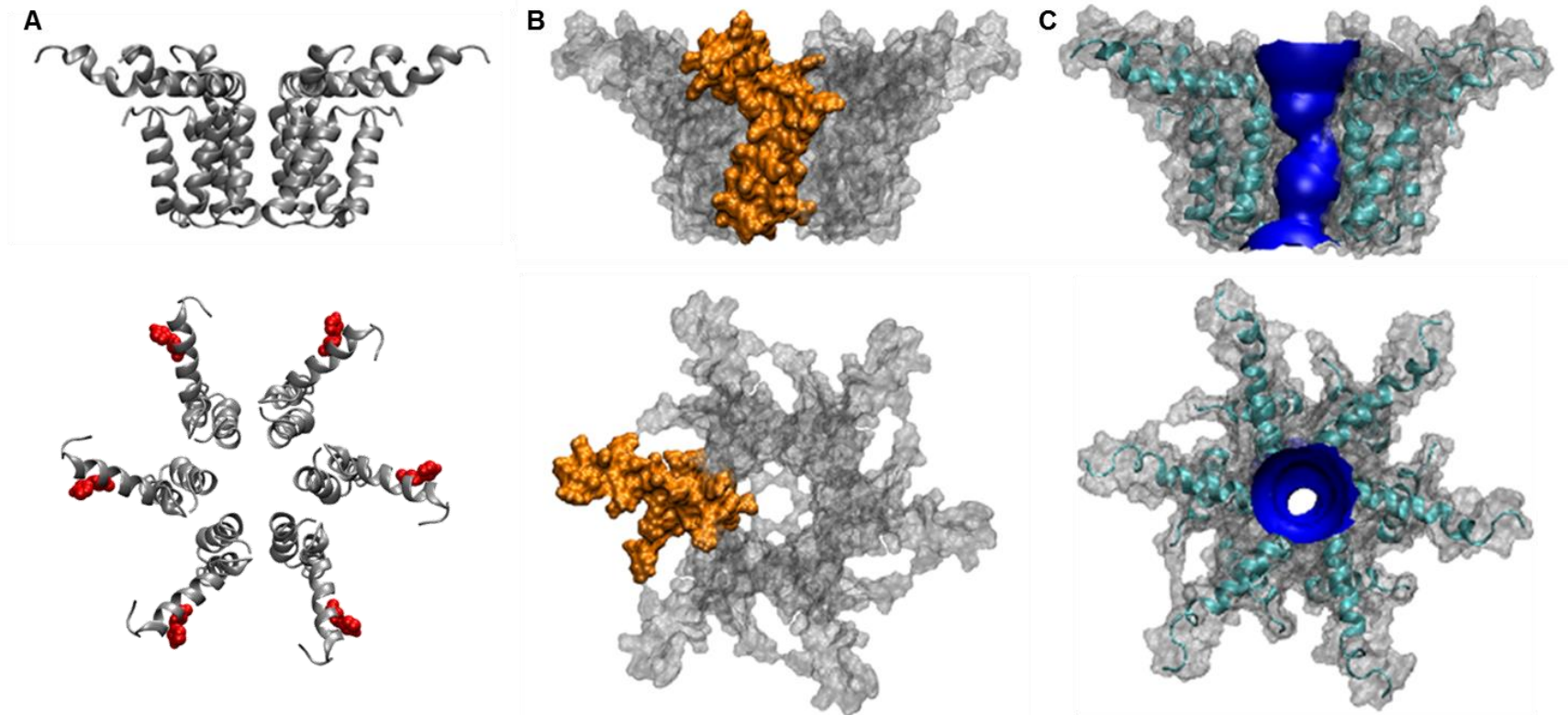


Figure 3.33 Hexameric Helix 2 pore-lining 'radial' channel starting conformations

A. Ribbon representation side on and from above with histidine residues highlighted in red. B. Surface representation side on and from above with one protomer highlighted in orange. C. Ribbon and Surface overlay representation with HOLE profile through the centre displaying the space inside the pore.

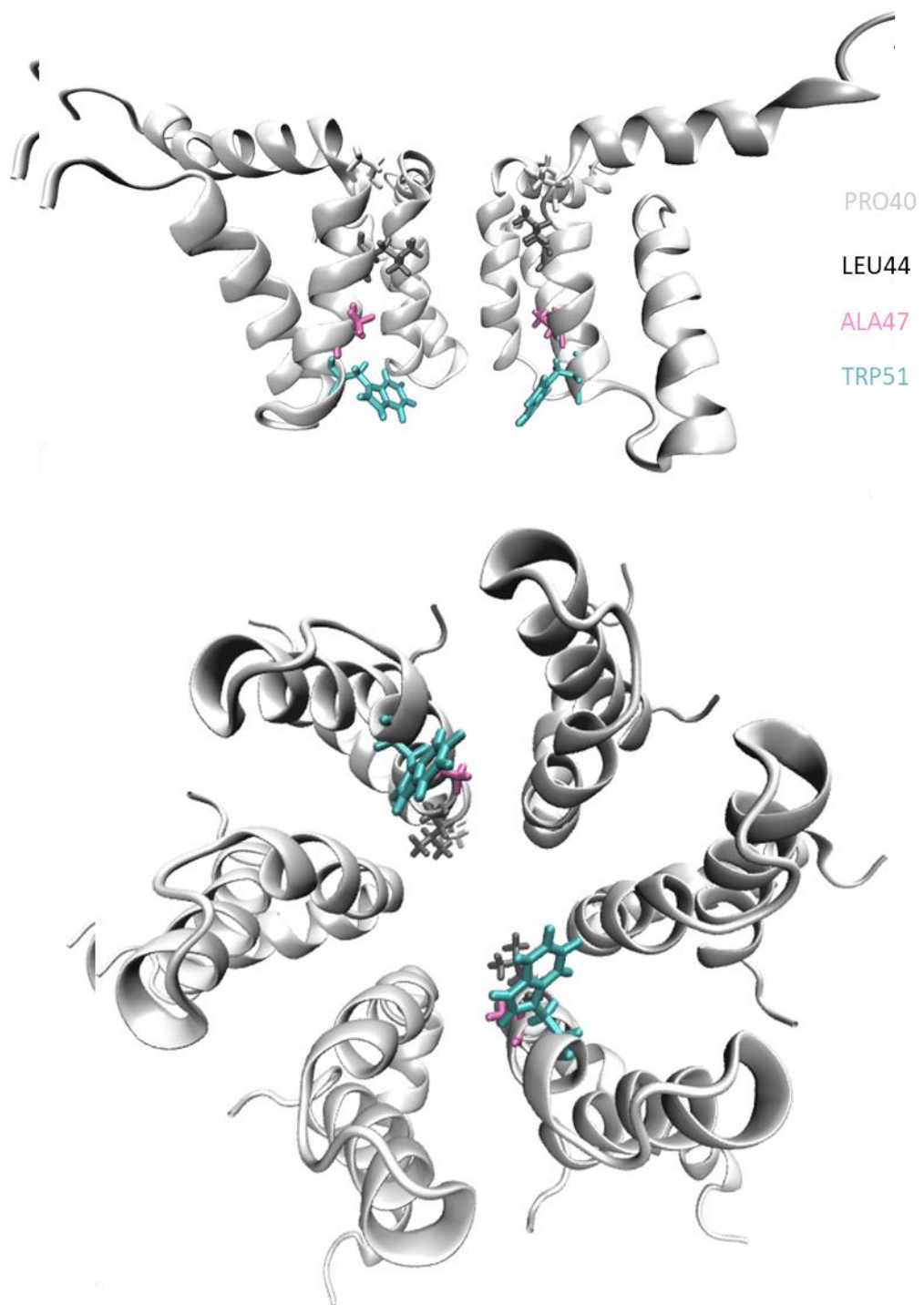


Figure 3.34 Hexameric helix 2 pore-lining 'radial' channel luminal residues and comparison of radial and compact conformations.

Pore lining residues of a hexameric M protein channel in a 'radial' conformation with the N-terminal TMD (helix 2) lining the pore. Pore lining residues PRO40 in white, LEU44 in black, ALA47 in pink and TRP51 in blue are shown from side on with two protomers hidden and from below. B. Comparison of radial and compact conformations in black and white respectively with HIS28 highlighted in red.

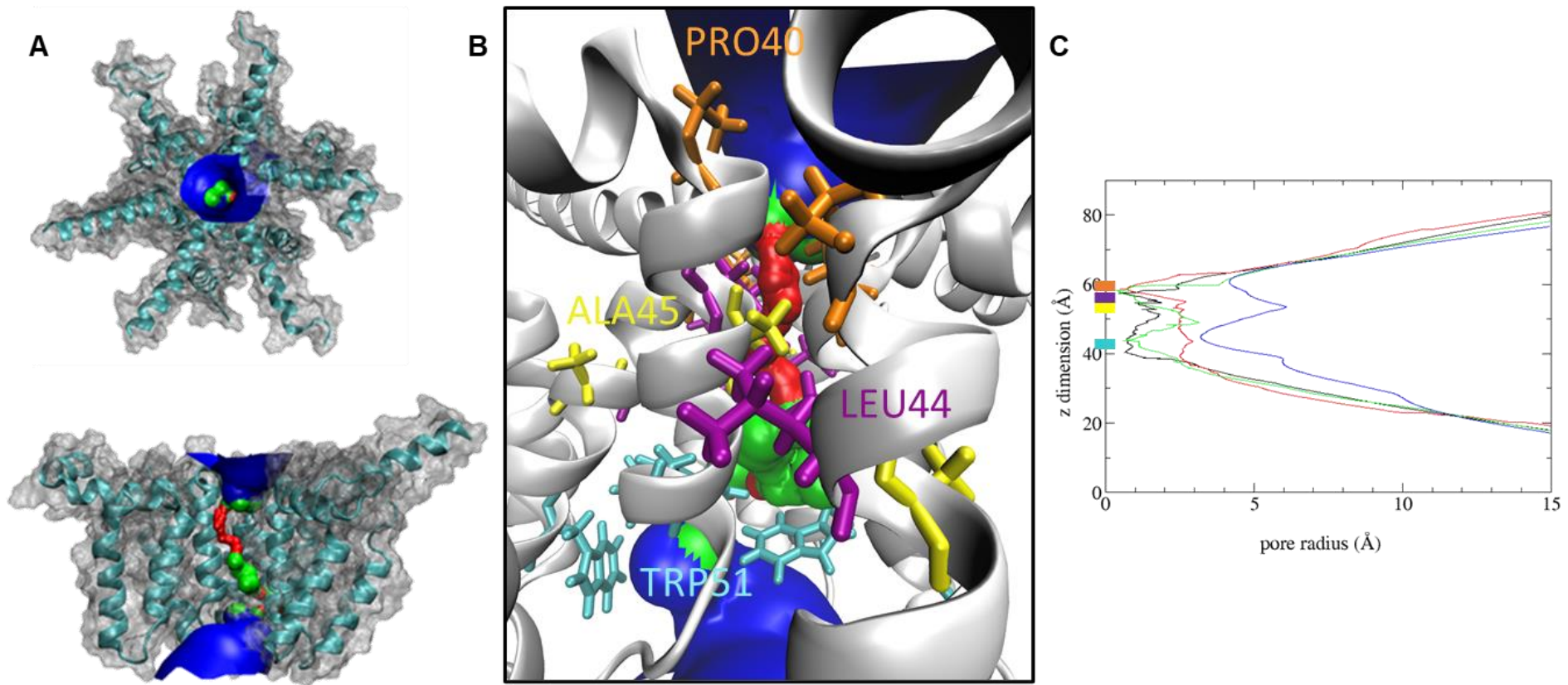


Figure 3.35 Hexameric Helix 2 pore-lining 'radial' channel conformation after 200 ns simulation

A. Surface and Ribbon representation of simulation three at 200ns from above and side with one helix cut away and HOLE surface plot displayed. Areas inaccessible to water with a pore radius $< 1.15 \text{ \AA}$ in red, referred to as a closed channel, areas that will allow passage of one water molecule $1.15 \text{ \AA} > \text{pore radius} < 2.30 \text{ \AA}$ in green, and areas accessible to greater than one water molecule pore radius $> 2.30 \text{ \AA}$ in blue. **B.** Representative channel zoomed in with HOLE surface plot displayed and residues closing the channel shown with sticks. PRO40 in orange, LEU44 in purple, ALA45 in yellow close the channel at the top and TRP51 in cyan at the bottom. **C.** HOLE profile plot of pore radius, starting conformation shown in blue, simulation one, two and three in black, red and green respectively.

the monomers overlapping. Therefore, the protomers were rotated anti-clockwise for maximum interactions between protomers (Figure 3.33C).

Starting conformations of the compact channels shown in Figure 3.36 had a radius of 4.236 Å, compared to the 3.2 Å of the radial conformation, explained by the different pore lining residues of PHE42, ALA45, ILE49 and LEU52 (Figure 3.37). These compact channels also closed very quickly after 12 ns compared to 6 ns when radial, suggesting these channels are not a physiological representation of channel structure formed by M protein.

A closed representative structure is shown in Figure 3.38A, and the pore-lining residues closing the structures are highlighted in Figure 3.38B. As seen with radial structures, all simulations close at the lower end of the channel by residue TRP51, for the compact structures the residues closing this region are TRP51, LEU52 and LEU53. Additionally, all channels are occluded at the top by residues GLY41, PHE42 and LEU44 (Figure 3.38B) in comparison to residues PRO40, LEU44 and ALA45 of the radial channels (Figure 3.35) These minor changes in pore closures demonstrate the change in structure due to rotation.

3.5.3.2 Does protonation change the activity and structure of the hexameric helix 2 pore lining channels?

Previously helix 2 pore-lining channels remained open for a very short period of time, 6 ns for 'radial' and 12 ns for 'compact' on average. However, upon protonation of HIS28 on the 'radial' structures the pore radius reduces to 3.0 from 3.2 Å and the channels remain open longer, for 33 ns on average. By contrast, the same effect was not observed for 'compact' channels, where the pore radius reduced from 4.236 to 4.040 Å, but the channels only remained open for 5 ns on average. Determining protonation of HIS28 only improved the channel stability of 'radial' channels, potentially due to the direction of protomer rotation. The HIS28 residue is found on helix 1, which when highlighted on the radial structure (Figure 3.39A) is shown to be close to the adjacent protomer in a clockwise direction, however the location of HIS28 on the helix 1 on 'compact' channels this is found close to the adjacent protomer in an anti-clockwise direction (Figure 3.41A).

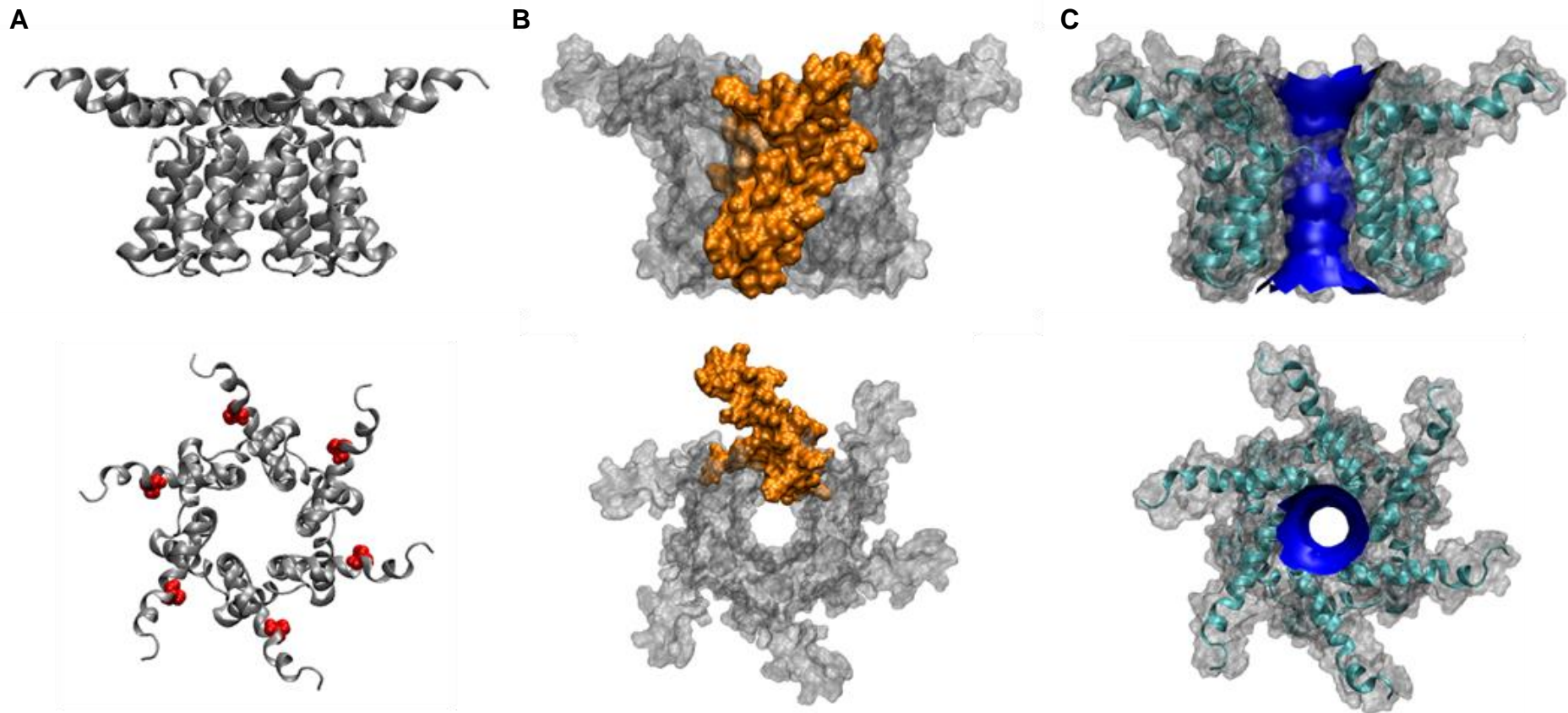


Figure 3.36 Hexameric Helix 2 pore-lining 'compact' channel starting conformations

A. Ribbon representation side on and from above with histidine residues highlighted in red. B. Surface representation side on and from above with one protomer highlighted in orange. C. Ribbon and Surface overlay representation with HOLE profile through the centre displaying the space inside the pore

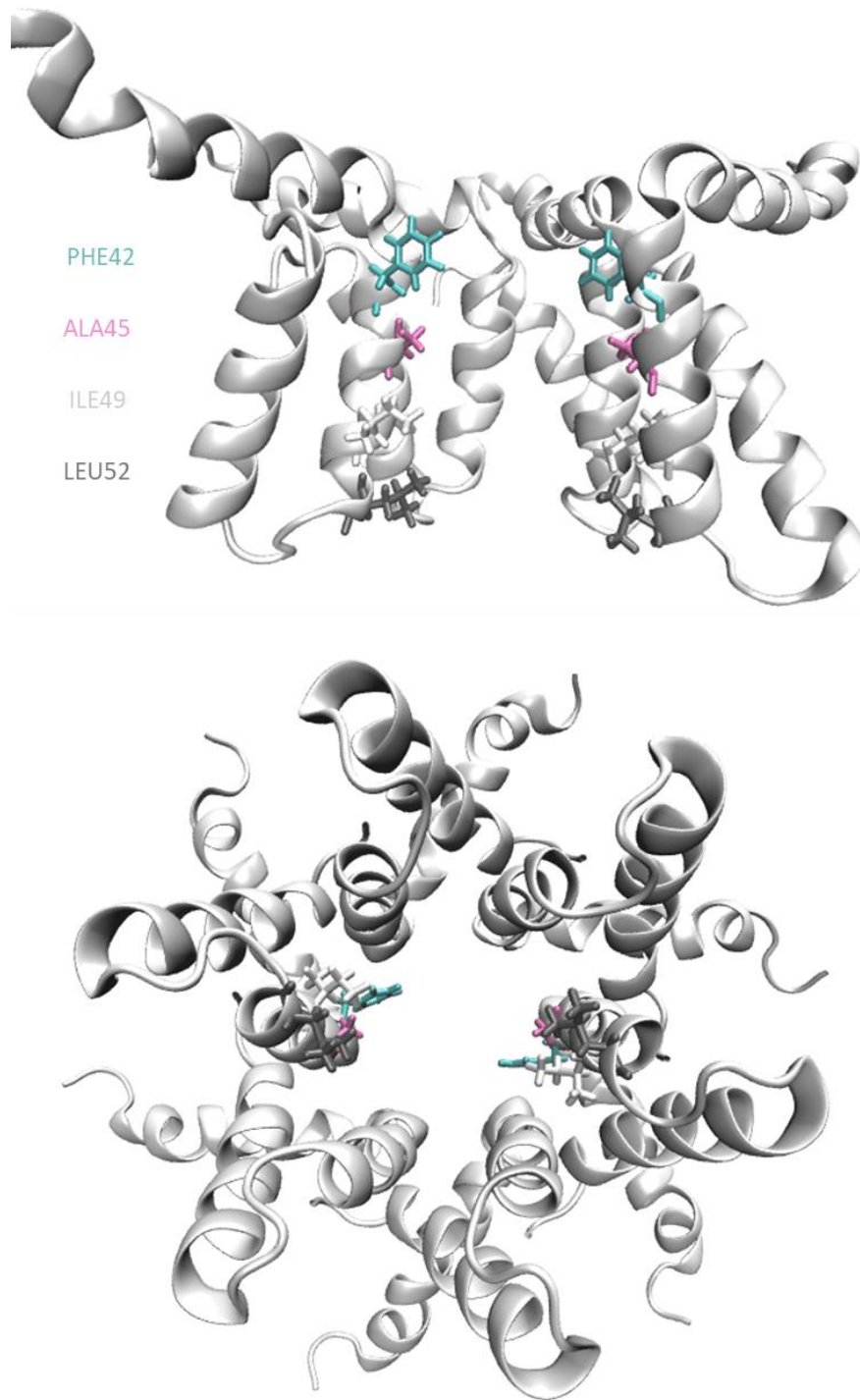


Figure 3.37 Hexameric helix 2 pore-lining 'compact' channel luminal residues.

A. Pore lining residues of a Hexameric M protein channel in a 'compact' conformation with the C-terminal TMD (H3) lining the pore. Pore lining residues PHE42 in blue, ALA45 in pink, ILE49 in white and LEU52 in grey are shown from side on with two protomers hidden and from below.

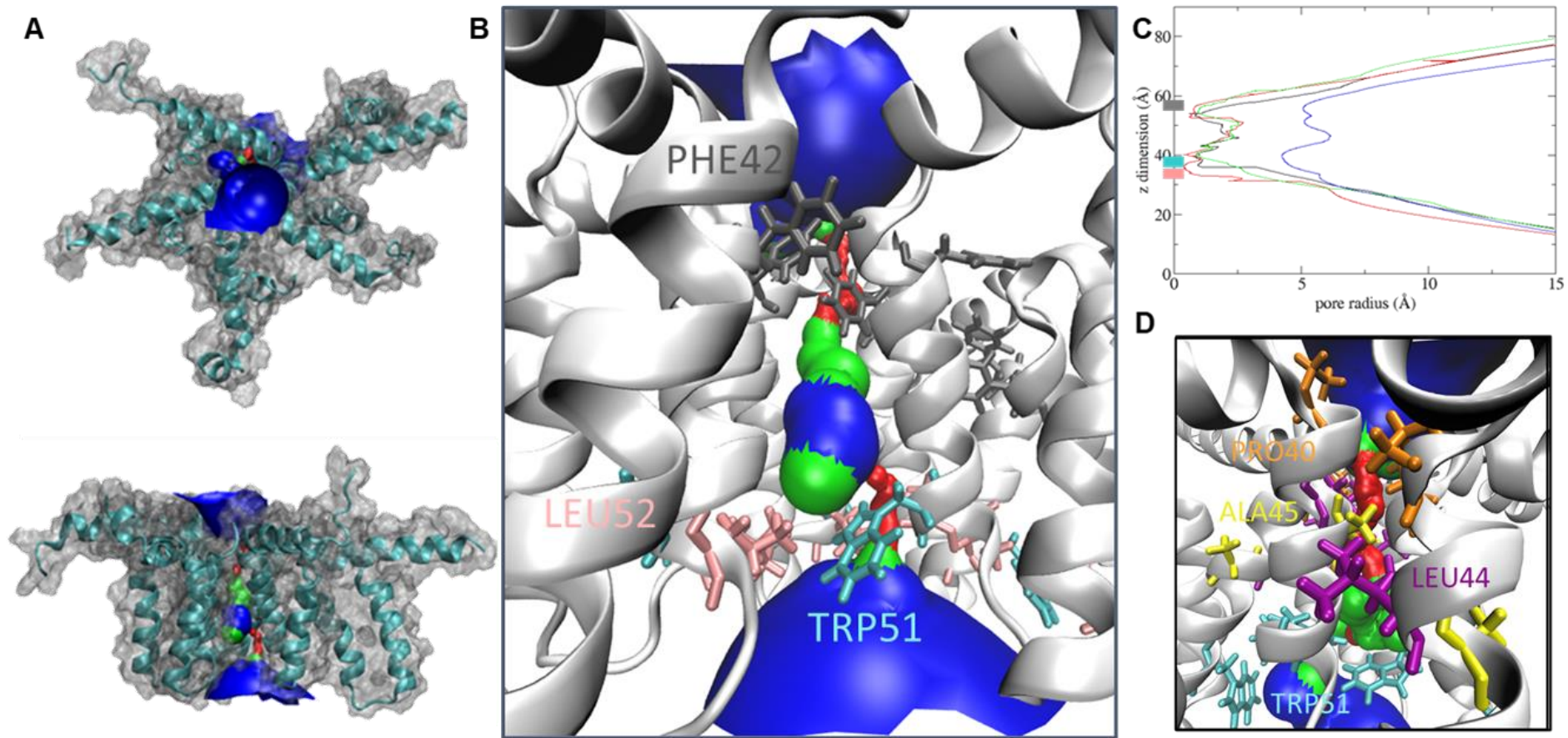


Figure 3.38 Hexameric Helix 2 pore-lining 'compact' channel conformation after 200 ns simulation

A. Surface and Ribbon representation of simulation three at 200 ns from above and side with one helix cut away and HOLE surface plot displayed. Areas inaccessible to water with a pore radius $< 1.15 \text{ \AA}$ in red, referred to as a closed channel, areas that will allow passage of one water molecule $1.15 \text{ \AA} > \text{pore radius} < 2.30 \text{ \AA}$ in green, and areas accessible to greater than one water molecule pore radius $> 2.30 \text{ \AA}$ in blue. **B.** Simulation two channel zoomed in with HOLE surface plot displayed and residues closing the channel shown with sticks. PHE42 closes the top, TRP51 and LEU52 close the bottom. **C.** HOLE profile plot of pore radius, starting conformation shown in blue, simulation one, two and three in black, red and green respectively. **D.** Simulation one of helix 2 pore lining radial conformation, previously shown in Figure 3.35.

Additionally, the pore-lining residues involved with channel closures are altered in the radial structures. Residue TRP51 still plays a role in closing channels, however this appears more of a restriction which leads to combinations of residues PRO40, GLY41, LEU44, ALA48 and LEU53 to close the channels (Figure 3.40). Residues PRO40, LEU44 also close the non-protonated channels with the addition of residue ALA45. Compact channels also observe similar closings, prior to protonation all channels were obstructed at both the top and bottom by combinations of GLY41, PHE42, LEU44 and TRP51, LEU52, LEU53 respectively (Figure 3.38). However, after protonation only two channels were obstructed at the top, involving combinations of residues ASN39, GLY41 and PHE42 and only two channels were closed lower down by residues TRP51 and LEU52 (Figure 3.42).

The subtle differences of residues involved in channel closure likely reflect the interactions induced by HIS28 protonation, the increase in time the helix 2 pore lining 'radial' protonated channels remained open could highlight the importance of the location of the HIS28 in relation to the channel. Furthermore the helix two pore-lining channel remained open for a much shorter average time than the helix 3 pore lining channels, and did not respond as positively to protonation, demonstrating they are unlikely to represent the structure of M protein viroporins within the acidified virion during entry and uncoating. Conversely helix 3 pore-lining channels remained open for over 100 ns on average, and the compact conformations responded positively to being protonated, taking the channels longer to close, or in some cases not close within the 200 ns simulations. The simulation data shown in this section indicates helix 2 is not likely to line the pore of the channel, in comparison to helix 3 simulation data shown in section 3.5.3.1.

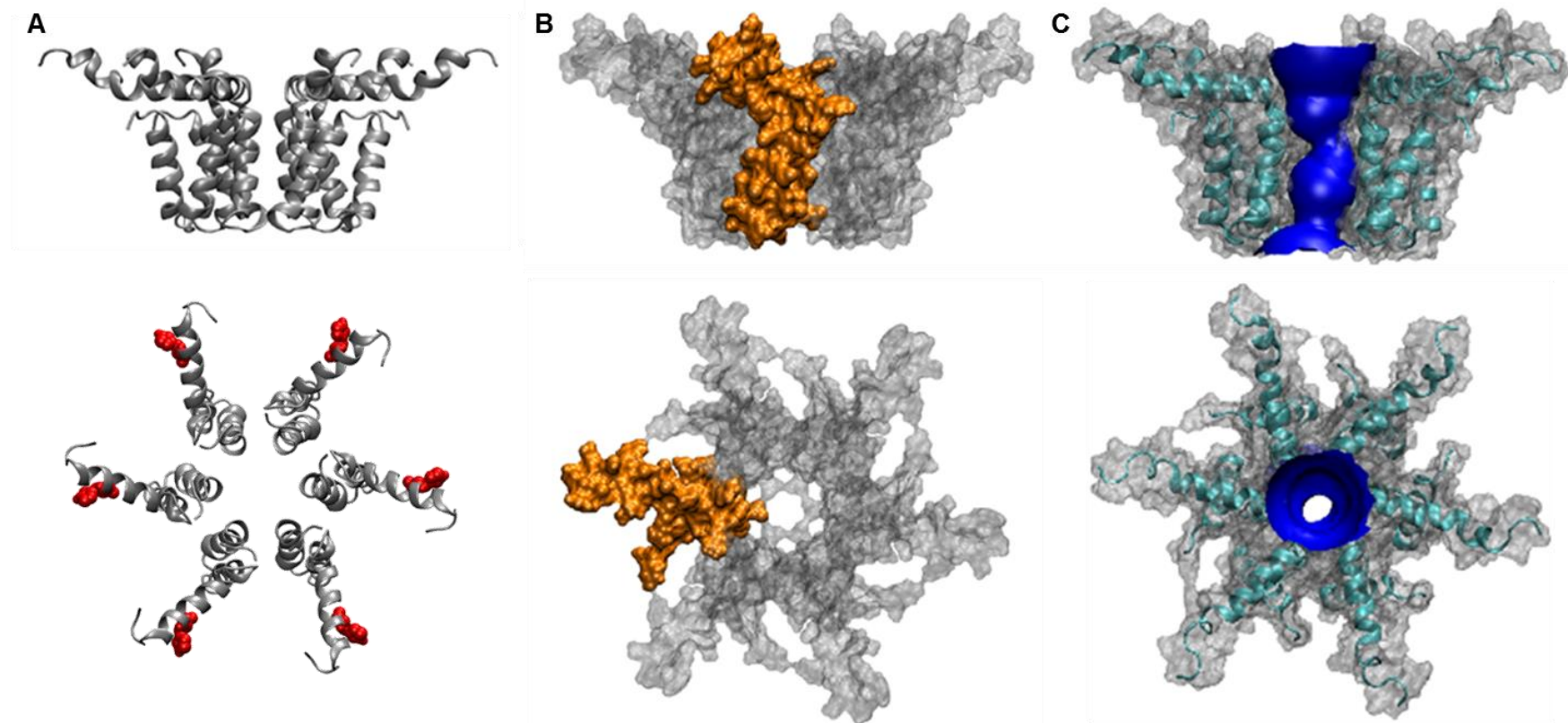


Figure 3.39 Hexameric Helix 2 pore-lining 'radial' protonated channel starting conformations

A. Ribbon representation side on and from above with histidine residues highlighted in red. B. Surface representation side on and from above with one protomer highlighted in orange. C. Ribbon and Surface overlay representation with HOLE profile through the centre displaying the space inside the pore

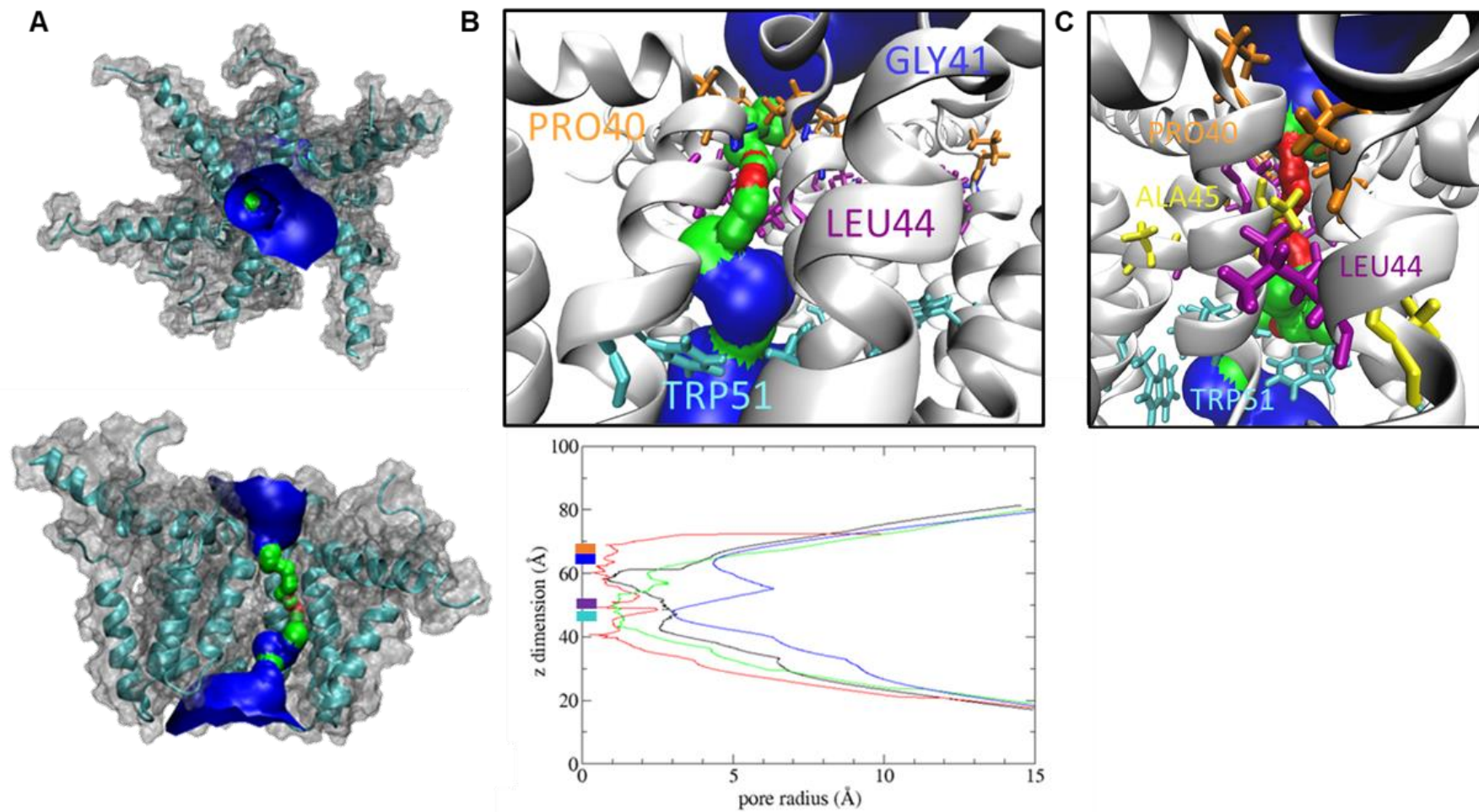


Figure 3.40 Hexameric Helix 2 pore-lining 'radial' protonated channel conformation after 200 ns simulation

A. Surface and Ribbon representation of simulation three at 200ns from above and side with one helix cut away and HOLE surface plot displayed. Areas inaccessible to water with a pore radius $< 1.15 \text{ \AA}$ in red, referred to as a closed channel, areas that will allow passage of one water molecule $1.15 \text{ \AA} > \text{pore radius} < 2.30 \text{ \AA}$ in green, and areas accessible to greater than one water molecule pore radius $> 2.30 \text{ \AA}$ in blue. **B.** Simulation three channel zoomed in with HOLE surface plot displayed and residues closing the channel shown with sticks. PHE42 closes the top, TRP51 and LEU52 close the bottom. **C.** HOLE profile plot of pore radius, starting conformation shown in blue, simulation one, two and three in black, red and green respectively. **D.** Simulation one of helix 2 pore lining radial conformation, previously shown in Figure 3.27.

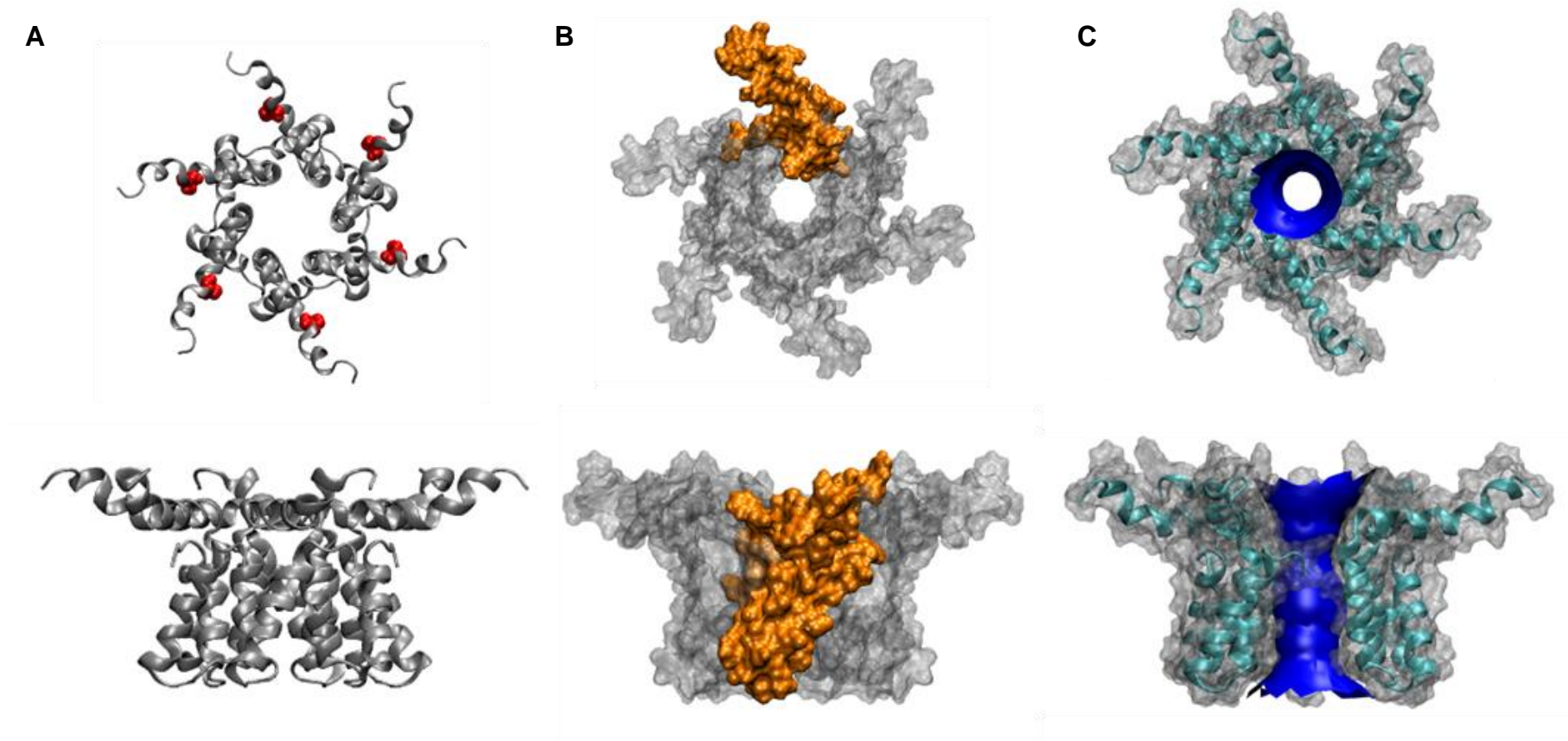


Figure 3.41 Hexameric Helix 2 pore-lining 'compact' protonated channel starting conformations

A. Ribbon representation side on and from above with histidine residues highlighted in red. B. Surface representation side on and from above with one protomer highlighted in orange. C. Ribbon and Surface overlay representation with HOLE profile through the centre displaying the space inside the pore

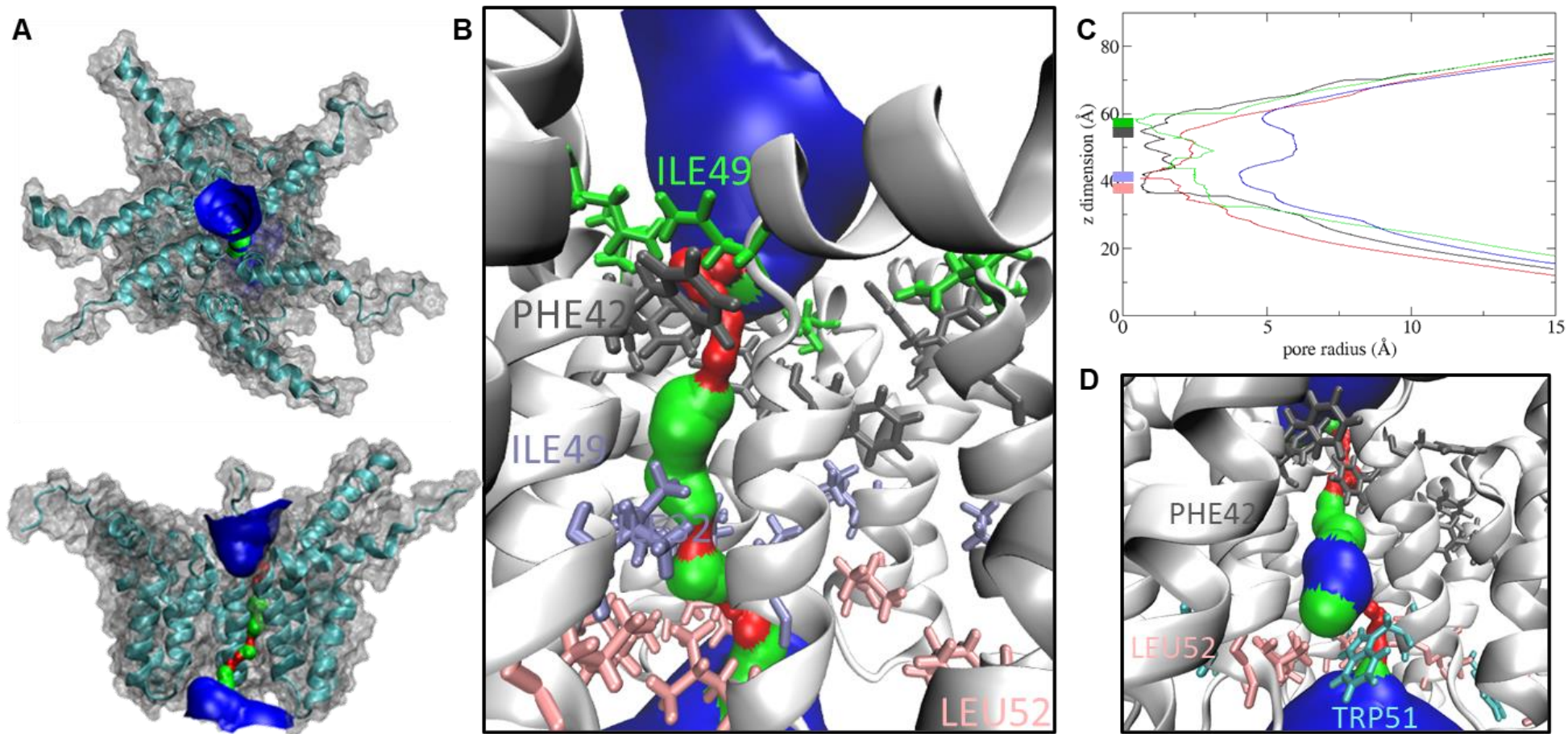


Figure 3.42 Hexameric Helix 2 pore-lining 'compact' protonated channel conformation after 200 ns simulation

A. Surface and Ribbon representation of representative channel at 200ns from above and side with one helix cut away and HOLE surface plot displayed. Areas inaccessible to water with a pore radius $< 1.15 \text{ \AA}$ in red, referred to as a closed channel, areas that will allow passage of one water molecule $1.15 \text{ \AA} > \text{pore radius} < 2.30 \text{ \AA}$ in green, and areas accessible to greater than one water molecule pore radius $> 2.30 \text{ \AA}$ in blue. **B.** Representative channel zoomed in with HOLE surface plot displayed and residues closing the channel shown with sticks. ILE49 in green and PHE42 in grey close the top, ILE49 in purple occludes the middle and LEU52 in pink restricts the bottom. **C.** HOLE profile plot of pore radius, starting conformation shown in blue, simulation one, two and three in black, red and green respectively. **D.** Representative helix 2 pore lining compact conformation, previously shown in Figure 3.34.

3.6 Discussion

Using MD simulation, we have predicted that M is capable of forming a stable two TMD monomer within a POPC lipid bilayer, as well as in a more complex membrane present within WNV virions (Figure 3.9 and Figure 3.10). The short TMD's of the cryo-EM M protein structure raised questions regarding its capability to span a lipid bilayer, and potentially the need for a variety of lipids with different length hydrophobic tails for the protein to remain within the membrane. However, as a one TMD M protein, E would reside on the incorrect side of the virion membrane. Furthermore, our simulations in Figure 3.9, have shown M protein is stable within a more simple POPC bilayer. Although during simulations phospholipid heads of the lipid bilayer are seen pinching into the leaflets to meet the short TMDs maintaining the protein within the membrane.

This feature is known as hydrophobic mismatching, a result of the difference in thickness of the lipid membrane and the proteins' hydrophobic domain (Jensen and Mouritsen, 2004). Hydrophobic mismatching is seen with other viral and non-viral proteins, where hydrophobic TMDs are shorter (negative hydrophobic mismatch) or longer (positive hydrophobic mismatch) than the lipid bilayer. Appropriately hydrophobic mismatching is observed during MD simulations of HCV p7 viroporin channels, causing membrane pinching and straightening of the TMDs, reducing their tilt angle (Chandler et al., 2012). Conversely, HIV-1 Vpu monomers undergo tilting of TMD helices due to a positive hydrophobic mismatch (Yeagle et al., 2007). M protein helices do not appear to change their tilt angle, however the mismatching is maintained by phospholipid tails tilting instead.

The overall morphology of *Flavivirus* particles is stabilised by the icosahedral surface of E/M in the mature virions and through their anchoring into the virus membrane (Figure 3.2). The membrane underneath each region of the icosahedral surface exhibits either a concave, planar, convex or saddle shape, which together result in spherical membrane formation (Zhang, W. et al., 2013). The herringbone arrangement of E/M proteins on the surface of the ZIKV virion (Sirohi et al., 2016), is formed by units of three Envelope dimers and three M protein dimers. MD coarse-grained simulations of each of these hexamers has a visible effect on the membrane curvature, particularly M protein which results

in a positive curvature of the lower leaflet, thought to be important in assembly of the virus particle into the icosahedral shape (Wewer and Khandelia, 2018).

Additionally, we consistently observed the inner leaflet of the lipid bilayer where the linker region resides to be the area with most pronounced lipid rearrangements, in line with virion membrane curvature for vesicle formation. Furthermore, the M protein TMDs diverge from the linker region, resulting in a gap between them at the outer bilayer leaflet. This structure forms a wedge-like conformation, which along with hair-pin regions lends themselves to membrane curvature and ultimately vesicle formation (Jarsch et al., 2016).

More recently, a variety of coarse-grained and all atom MD simulations of a DENV E/M homotetramer resulted in the same membrane pinching indentation on the lower leaflet as seen in the dimers in section 1.4, reducing membrane thickness (Wewer and Khandelia, 2018). Further simulations of 5 homotetramers were arranged as seen at the five-fold axis however on a planar DENV derived lipid membrane, similar in shape to a square wafer. After 440 ns of simulation the E/M homotetramers caused the membrane to curve extensively resulting in a complete vesicle formed of 17.3 nm (de Oliveira Dos Santos Soares et al., 2017).

Our monomeric and dimeric simulations were conducted in more simplistic POPC bilayers and bilayers emulating the composition of a WNV virion. However, the differences in stability observed for monomers and interactions between dimers were not obviously different between these lipid bilayers. Thus, we simulated higher order oligomeric structures in simple POPC bilayers, due to time restraints. However, a recent study simulating ZIKV and DENV E & M glycoproteins reported differential interactions between glycoproteins and certain phospholipids (Wewer and Khandelia, 2018). The simulated membranes consisted of PC : PS : PE : SM at the respective ratios of 57 : 25 : 3 : 15. ZIKV and DENV both enriched the surrounding membranes with PS and PE lipids in comparison to PC and SM, however PE localised closer to DENV proteins and conversely PS lipids localised closer to ZIKV proteins, hotspots on these proteins for the lipids were identified (Wewer and Khandelia, 2018). If time allowed, it would be interesting to analyse the lipid-protein interactions of the previously run simulations, to observe if similar interactions are seen with our

minimally different PC : PS : PE : SM lipid bilayer composition of 57 : 21 : 5 : 17 (Martin-Acebes et al., 2014).

As mentioned previously the class proportions of final dimer conformations did not vary widely between the lipid environments, however restraining C α atoms resulted in a shift of the classes seen. Restraints saw an increase of the cyro-EM dimeric M conformation (Sirohi et al., 2016) from 1 and 2 instances for POPC and WNV membranes to 4 and 3 when restrained. This dimeric conformation occurs in viruses due to the bringing together of two prM-E heterodimers, which upon pr cleavage by furin go on to form two E and M homodimers, therefore forming in a restrained environment. C α restraints may partially mimic this physiological restraint on M protein held by E protein in the virion. Additionally, reductions in class II, III and IV dimers were observed upon restraining; this change in dimer class formation may reflect the need for helix 1 flexibility for these dimer classes II, III and IV to form. As observed in Figure 3.17 we expect dimers of Class III conformation to form higher order oligomers, these form more frequently when restraints are not applied. We hypothesise M channels form once the virion is acidified and dimeric M is released from underneath dimeric E; at this point, the restraints upon the dimers would be released. Therefore, future work could focus on simulating unrestrained M protein class I dimers in an acidic environment, or by histidine protonation observing if there are conformational changes from class I to class III dimers.

M protein channel simulations uncovered a potential insight into the structure and activity of an M protein viroporin. Hexameric M channels closed within varying timeframes dependent on the pore-lining helix and the protonation state of the channels. M protein appears capable of functioning as a hexameric ion channel, however radial conformations with helix 2 lining the pore did not result in a stable open channel in a neutral environment, all channels closed their pores after only 5 or 6 ns. On the other hand, helix 3 lining the pore resulted in a water column remaining intact for much longer (6, 40 and over 200 ns) with one channel not closing within the 200 ns. These results align with the pore-lining helix prediction results mentioned in section 3.2 from MEMSAT SVM. The prediction software used in Figure 3.4 and Figure 3.5 were all the currently available online prediction tools, and MEMSAT-SVM was the only pore-lining helix predictor. Furthermore, the prediction of DENV M to be a single TMD

protein from the Phobius prediction tool was published (Tomar et al., 2019). However, the research suggests DENV M may also be a viroporin.

Moreover, rotation of protomers results in both helix 2 and helix 3 pore-lining channels remaining open for longer, helix 2 pore-lining channels increased slightly from an average of 6 to 12 ns of channel activity and helix 3 pore-lining channels increased from an average of 82 to 108 ns. Rotation of the individual protomers increases the interactions between adjacent protomers, particularly with the N-terminal helix for helix 3 pore-lining channels (Figure 3.21 and Figure 3.24) Furthermore, comparison of Figure 3.23 and Figure 3.27 shows the changes in structure are greater for the radial structure than the compact, possibly due to the more favourable conformation and the increase in inter-monomer interactions. However, rotation also changed the pore-lining residues, which largely influences the stability of the water column. Helix 2 pore lining channel 'radial' conformation has a pore containing a proline, leucine, alanine and tryptophan (Figure 3.34). After rotation, the pore changes slightly to contain a phenylalanine, alanine, isoleucine and leucine (Figure 3.37). Both of these pores contain residues with similar properties of hydrophobic side chains.

Helix 3 pore lining 'radial' conformation starts simulations with two leucines, an isoleucine, tyrosine and lysine lining the pore (Figure 3.21), however with rotation of protomers the channel is lined with two leucines, a methionine, two valines, an isoleucine and threonine (Figure 3.25). Both the 'radial' and 'compact' helix 3 pore-lining channels are lined predominantly by hydrophobic amino acids with the addition of one or two polar or charged residues. The addition of an amphipathic or hydrophilic residue may increase the stability of the pore in comparison to helix 2, which does not have a hydrophilic residue in the pore lining.

In comparison to other viroporin lumens, M2 contains a valine, alanine, glycine (Pinto et al., 1997) and the multiple computational p7 structures contain alanines, valines, leucines and isoleucines (Chandler et al., 2012). Comparatively M protein is also largely lined with hydrophobic residues, however the radial channel conformation contains a polar tyrosine and a positively charged lysine, or in a compact channel conformation a polar threonine, capable of being charged.

Moreover, protonation of the N-terminal histidine affected the closing of the channel lumens as well. Helix 2 'radial' channels stayed open for 33 ns when protonated as opposed to 6 ns when not protonated, however their final HOLE conformations are comparable. Protonated helix 2 'compact' channels remained open for 5 ns on average and 12 ns when not. Repeatedly the final conformations of the channel closures appear comparable. The opposing nature of these results could be due to the location of the protonated histidine and its proximity to the channel lumen.

In contrast, helix 3 pore-lining 'radial' channel conformations remained open for 72 ns with protonation and 82 ns without, with one non-protonated channel remaining open for the whole simulation. Helix 3 compact channels take 108 ns on average to close and this is lengthened to 137 ns when protonated. As mentioned previously the change in time taken for the channels to close is likely due to the location of the histidine, its proximity to the channel and which residues it interacts with. In Figure 3.29 the histidine is highlighted and can be seen much closer to the channel lumen at 16.8 Å and potentially interacting with adjacent protomers comparatively to Figure 3.32, showing the 'radial' conformation with the highlighted histidine much further away from adjacent protomers and the channel lumen than seen in the compact conformation at 31.28 Å. Acid sensitive viroporin M2 and some genotypes of p7, both have a HIS residue present within the channel lumen (Ito et al., 1991; Oestriinger et al., 2019). However, viroporin E5 has two HIS residues present at the C-terminal tail of each monomer, similarly to the presence of the two M protein HIS residues found at the N-terminus leading to pH activation (DiMaio and Petti, 2013), moreover both HIS residues of E5 are present in the unstructured C terminal region, whereas M protein contains one in both the structured and unstructured N terminal regions. Simulations of M2, compared to protonated M2 showed differences in structure, comparable to the previously resolved structures in both environments (Khurana et al., 2009).

As noted earlier, M protein channels are only likely to form within the endocytic pathway during virus entry. Endosomal pH is less than 6.5, and so will cause protonation of histidines present on the exposed N-terminal region of M, including helix 1 from our simulation that contains HIS28. MD simulations in this protonated environment contribute to simulating a more physiologically relevant

environment. Additionally, other viroporins contain conserved histidines, including IAV M2 and some HCV p7 genotypes. Protonation of M2 histidine 37 causes channel activation and proton-selective conductance of the channel (Pinto et al., 1997; Betakova and Kollerova, 2006), p7 pore-lining HIS17 is conserved and is important for genotype 1b p7 channel activity (StGelais et al., 2009; Chew et al., 2009).

Evidence supporting that helix 3 may represent a pore-lining helix was first obtained through the MEMSAT-SVM prediction. However, its longer channel opening and positive reaction to protonation further supports that helix 3 comprises the lining of the pore. Two channels simulated with helix 3 pore-lining remain open after 200 ns. However, upon closure of the remaining channels it appears ILE64 is involved in closure of all channel simulations regardless of protomer rotation and LEU68 is also involved in the majority of these. LEU68 as seen in Figure 3.1 is conserved in YFV and WNV however not in DENV, although ILE64 is not a conserved residue. Compact channels also are closed by VAL61 and 65 and again these are not conserved residues. As ILE64 and LEU68 cause the closure of most of these channels, they may be identified as gating residues.

Conversely helix 2 pore-lining channels all close relatively quickly, indicative of an unfavourable channel. In radial channel simulations a non-conserved TRP51, and a conserved PRO40 and LEU44 are responsible for channels closing. Upon protonation an additional residue GLY41, found to be highly conserved throughout the *Flavivirus* genus, closes all channels alongside previously mentioned TRP51, PRO40 and GLY41. When helix 2 pore-lining channels are compact the residues lining the pore and closing the channels change, a conserved PHE42 closes all channels run in the absence of protonation alongside previously mentioned TRP51 and an additional LEU52. When protonated these channels remain closing by PHE42 and LEU52. The involvement of highly conserved residues in closure of channels is likely due to these channels being highly involved in maintaining the structure of the channel, however from a membrane-facing role as a peripheral helix, as opposed to a pore-lining helix.

The four hexameric structures simulated suggest that helix 3 pore-lining compact oligomers are the most representative of those found in the virion, as

they remain open for the longest period of time. However, it is not clear how long channels would remain open during infection. p7 channels in DOPC rich bilayers remain open for ~500 ms by patch clamping, far longer than our simulations (Hyser, 2015), however Rotavirus non-structural protein 4 (NSP4) channels formed in planar lipid membranes remained open for just 65 ps (Pham et al., 2017). Additionally, compact helix 3 pore-lining channels do respond positively to being HIS-protonated indicating the model is the most accurate in a physiologically relevant environment.

Heptameric M protein channels also formed stable oligomers which remained interacting throughout simulations. Helix 2 pore lining radial and compact conformations remained open for far longer than corresponding hexameric channels. However, upon protonation helix 2 pore lining heptamers closed more quickly, whereas protonated hexameric channels remained open for longer.

With helix 3 pore lining, the majority of heptameric channels remained open throughout the simulation with many 'compact' conformations retaining a water column for almost 200 ns regardless of protonation. These channels take longer to close due to the high number of interactions between adjacent protomers, forming a highly stable structure. When protomers with pores lined by helix 3 are radial, channels show an increased propensity to close, however both these averages reflect two out of three channels remaining open with one channel closing sooner.

Although we are able to simulate heptameric channels, it is unlikely channels of seven would form due to the virion stoichiometry. Additionally, M protein is present within the virion as a dimer, and simulations of two M protein monomers (section 3.4) consistently show dimerisation in the vast majority. Disassociation of dimers has not been observed in the MD simulations, however, when the E-M heterotetramers dissociate during entry, allowing E trimers to form, it could be possible for M dimers to also dissociate.

Our MD simulations and analysis suggest hexameric channels with helix 3 pore-lining are the most likely viroporin structure, due to these channels remaining open for longer periods of time and when protonated this time is extended. Conversely, heptameric channels remain open for long time periods regardless of the helix lining the pore, this lack of specificity highlights heptameric channels

exhibit a high level of inter-monomer interactions which are hard to interrupt (Appendix B2).

CG-simulation	Membrane Composition	Duration
Monomer		
1 TMD POPC	POPC (100)	3 μ s
2 TMD POPC	POPC (100)	3 μ s
2 TMD WNV	POPC:POPS:POPE:SM (57:25:3:15)	3 μ s
1 TMD truncated POPC	POPC (100)	3 μ s
Dimer		
POPC	POPC (100)	6 μ s
WNV	POPC:POPS:POPE:SM (57:25:3:15)	6 μ s
Restrained - POPC	POPC (100)	6 μ s
Restrained - WNV	POPC:POPS:POPE:SM (57:25:3:15)	6 μ s

Table 3.2 Coarse-grained Simulation Overview

AA-simulation	Membrane Composition	Duration
Hexamer		
H2 Radial	POPC (100)	200 ns
H2 Radial protonated	POPC (100)	200 ns
H2 Compact	POPC (100)	200 ns
H2 Compact Protonated	POPC (100)	200 ns
H3 Radial	POPC (100)	200 ns
H3 Radial protonated	POPC (100)	200 ns
H3 Compact	POPC (100)	200 ns
H3 Compact Protonated	POPC (100)	200 ns
Heptamer		
H2 Radial	POPC (100)	200 ns
H2 Radial protonated	POPC (100)	200 ns
H2 Compact	POPC (100)	200 ns
H2 Compact Protonated	POPC (100)	200 ns
H3 Radial	POPC (100)	200 ns
H3 Radial protonated	POPC (100)	200 ns
H3 Compact	POPC (100)	200 ns
H3 Compact Protonated	POPC (100)	200 ns

Table 3.3 All-atom simulation overview

Chapter 4 M protein displays pH activated, rimantadine-sensitive, channel activity with a role during ZIKV entry

4.1 Introduction

Increasing numbers of small (60-100 amino acids), hydrophobic viral membrane proteins are being recognised to form oligomeric complexes that exert channel activity. Such proteins, termed “viroporins”, play often-essential roles during virus life cycles, with many of them acting to expedite virus egress and/or entry (Scott and Griffin, 2015). Hence, based upon molecular dynamics simulations (Chapter 3) combined with its primary structure and studies on related M proteins (Premkumar et al., 2005), we hypothesised that ZIKV M bore the characteristic hallmarks of a viroporin and so should both oligomerise and display channel activity *in vitro*.

Formation of higher-order viroporin structures can be induced using non-ionic, membrane-mimetic detergents (e.g. 1,2-dihexanoyl-sn-glycero-3-phosphocholine (DH(6)PC) or 1,2-diheptanoyl-sn-glycero-3-phosphocholine (DH(7)PC)) at concentrations above the critical micellar concentration (CMC). These micelles stabilise membrane protein complexes (Wetherill et al., 2012; StGelais et al., 2009; Schnell and Chou, 2008; Luik et al., 2009; OuYang et al., 2013; Panjwani et al., 2014), substituting for lipids such as POPC, which form vesicles and are more technically challenging for structural studies (Figure 4.1). Biochemical analysis of viroporin oligomerisation has previously comprised multiple techniques, including visualisation using native-PAGE and transmission electron microscopy (TEM).

However, visualisation of oligomers is not sufficient to ascribe viroporin function to a given protein. We required an assay adaptable to the use of a truncated M protein peptide (section 2.5.4), to provide evidence of channel activity and to enable screening of potential inhibitors. Thus, we adapted a previously used, liposome-based, dye release assay as a robust indirect method (StGelais et al., 2007; Tuthill et al., 2006; Davis et al., 2008) for assessing viroporin activity.

This liposome-based assay is most suitable for observing channel activity and identifying potential inhibitors, as other systems struggle with scaling up, including BLMs and single cell patch clamping. We have shown the assay works routinely in a 96 well plate, furthermore, the liposome-based assay has

been used to screen compounds against HCV p7 channels, in a 384 well plate format, achieving a satisfactory z score (Gervais et al., 2011).

Liposome-based systems have previously been used to investigate channel activity of viroporins including M2, alphavirus 6k, poliovirus 2B and HCV p7 (Scott and Griffin, 2015; Antoine et al., 2007; Madan et al., 2007; Montserret et al., 2010; StGelais et al., 2007). Use of this assay has been disputed on one occasion (Gan et al., 2014), however many reports mentioned above support its indirect measurement of channel activity. Dye release assays can also identify other properties, including the use of fluorescent dextrans to determine pore size, the effect of pH on channel activity and viroporin inhibitors such as Rimantadine (Wetherill et al., 2012; Panjwani et al., 2014; Shukla et al., 2015; StGelais et al., 2007). The effect of pH was of considerable interest as we hypothesised that M protein forms channels during virion endocytosis. However, identification of inhibitors can also support proof of M protein oligomerisation, in addition to development of a potential antiviral compound.

In vitro methods have been used successfully to identify inhibitors previously, however evidence of their activity in cell culture is further convincing. Incubating host cells and virus with potential antivirals throughout infection can show their effect of reducing virus titre. Furthermore, time of addition (TOA) assays determine the virus life cycle stage at which a virus inhibitor is active. TOA assays are carried out by adding an antiviral compound to the virus and host cells at different times in the virus life cycle. The distinct stages are: pre-treating host cells or the virus prior to inoculation, co-treatment of cell and virus during inoculation and treatment of virus-infected cells during the post-inoculation period. The stages can also be combined to see the effects of the compound when present in multiple stages of the virus life cycle (Pauwels et al., 1990; Kato et al., 2016; Daelemans et al., 2011; Chen, M. et al., 2017). Observing the lifecycle stage where a previously screened inhibitor has the greatest effect is of great interest to help identify the viral target.

Additionally, successful inhibitors in cell culture can be translated into an *in vivo* model system to further investigate the effect an identified compound may have on a whole organism when infected, and whether the effects of the compound are comparable to those seen in cell culture.

This chapter presents evidence for M protein oligomerisation in a membrane mimetic environment and channel activity is demonstrated using liposome dye release assays. Additionally, M protein channels are found to be sensitive to the channel-blocking compound, rimantadine, *in vitro*, and the corresponding antiviral activity of this compound in cell culture supports a role for M protein channels during virus entry. Lastly, we demonstrate that rimantadine prevents ZIKV spread *in vivo*, supporting that M might be exploited as an effective therapeutic target.

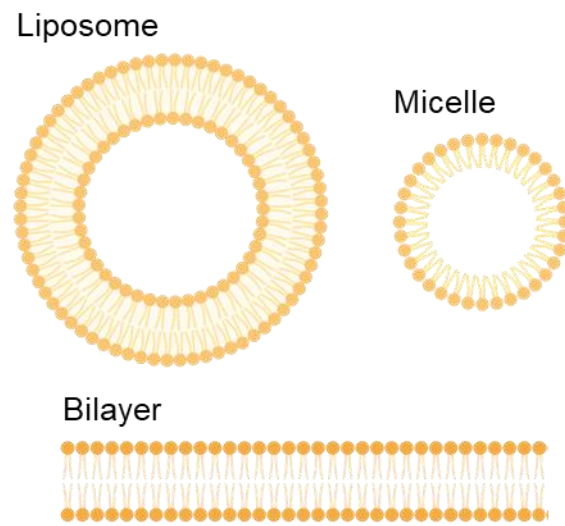


Figure 4.1 Schematic comparing phospholipid structures
Comparison of liposomes, micelles and membrane bilayers

4.2 ZIKV M protein forms oligomers in detergent micelles

4.2.1 M protein oligomerises in DHPC detergent

To explore whether M protein can oligomerise in a membrane mimetic environment, a truncated M peptide of 55 amino acids, lacking 20 N-terminal residues (Figure 4.2), was diluted in various non-ionic detergents which have previously been used in viroporin studies: 1,2-dihexanoyl-sn-glycero-3-phosphocholine DH(6)PC, DH(7)PC, 1-palmitoyl-2-hydroxy-sn-glycero-3-phospho-(1'-rac-glycerol) (LPPG) and 1-myristoyl-2-hydroxy-sn-glycero-3-phospho-(1'-rac-glycerol) (LMPG). Other viroporins including p7, SH and E5 have previously been shown to form higher order structures in detergent environments by both native PAGE and transmission electron microscopy (TEM) (StGelais et al., 2007; Carter et al., 2010; Wetherill et al., 2012; Li, Y. et al., 2014; Luik et al., 2009).

M was insoluble in aqueous solution, therefore dissolved in DMSO prior to dilution in detergent. DH(6)PC, DH(7)PC, LMPG and LPPG were selected to stabilise M protein and characterise its oligomerising capabilities based on previous viroporin studies (Griffin, S.D. et al., 2003; Clarke et al., 2006; Carter et al., 2010; Luik et al., 2009). All detergents were used above their respective CMC's and protein was diluted into each at 500 ng/ μ L. After 10 min at 37 °C, samples were separated by native PAGE and stained with Coomassie brilliant blue reagent (section 2.5.2 and 2.5.3) (Figure 4.3A).

M peptide oligomerisation occurred in the presence of DH(6)PC, but not for the other detergents. Monomeric truncated M peptide is 6.3 kDa in molecular weight and the M-DH(6)PC detergent complexes migrated at a similar rate to the ~45 and ~66 kDa molecular weight markers. However, native PAGE separates proteins by net charge, molecular weight, and conformation; thus, protein migration cannot be accurately related to molecular weight using this technique.

To gain an insight of the tertiary arrangements of oligomeric M protein in the detergent environment we chose to employ negative TEM to investigate whether this oligomer represents a channel-like structure, based upon previous studies of viroporins including, HCV p7, RSV SH, HPV E5.

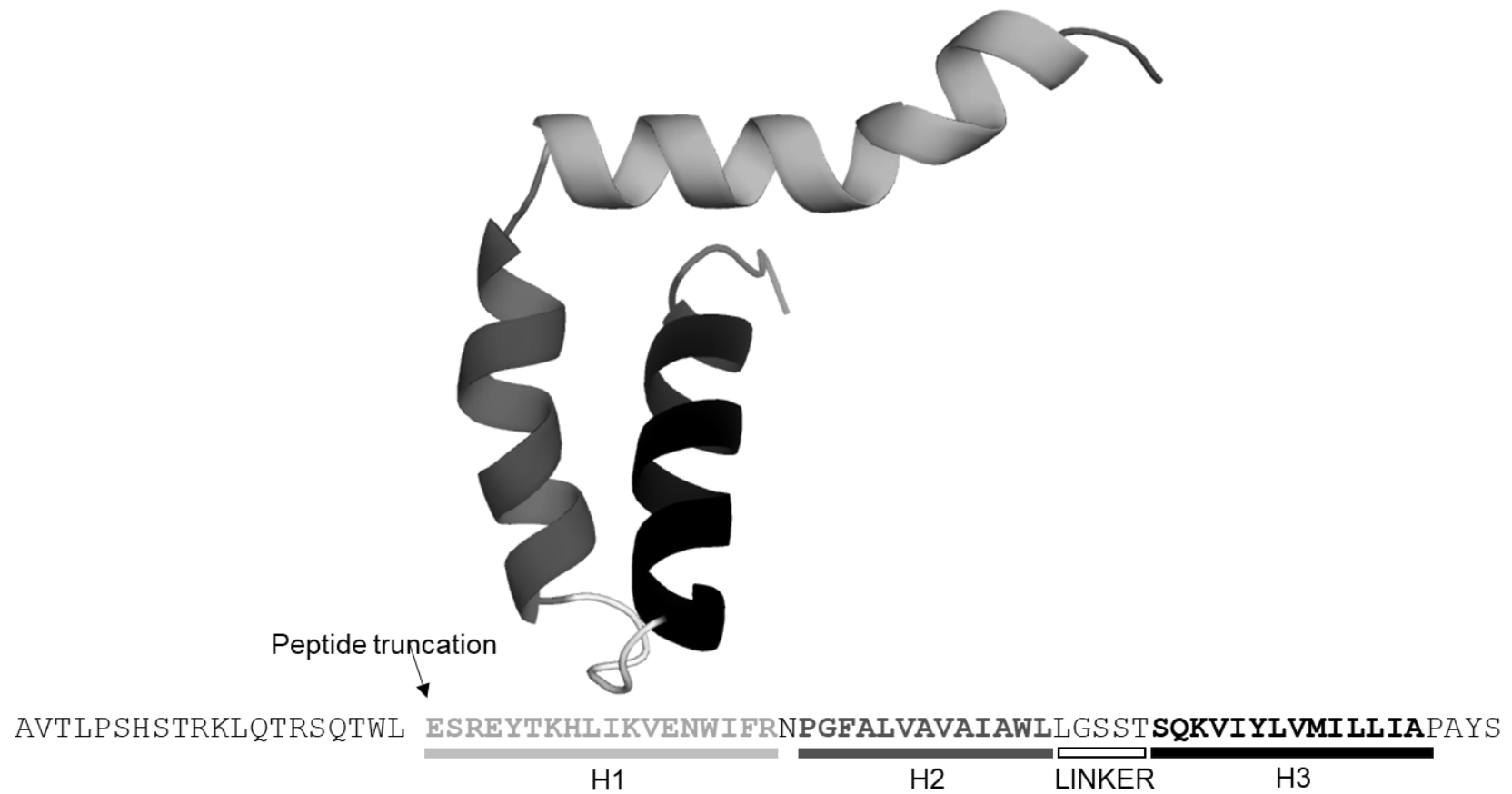


Figure 4.2 M peptide of 55 amino acids with an N terminal truncation

Protein shaded with sections corresponding to the structural regions of the protein sequence shown below. The site of the peptide truncation from the full-length M also indicated.

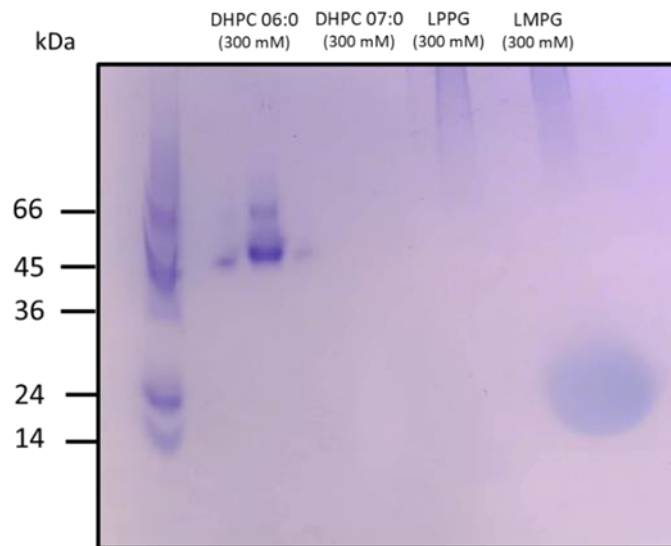


Figure 4.3 Oligomerisation of M protein in detergent environment by native PAGE

Native PAGE analysis of M protein 5 μ g in differing membrane mimetic detergents (300 mM), DH(6)PC, DH(7)PC, LPPG and LMPG. Gel stained using Coomassie Blue.

4.2.2 Visualisation of ZIKV M peptide oligomers by Transmission Electron Microscopy (TEM)

Structural information for ZIKV M protein hails from the mature virion cryo-EM structures, where it resides as a dimer within the virion membrane (Sirohi et al., 2016; Sevvana et al., 2018). M protein has not been visualised in isolation, or in the context of an acidified virus particle mimicking the entry process. Hence, the structure of M in the absence of adjacent E protein TM regions remains unknown (section 3.2). In section 3.4.3 M protein simulations gave insight into the potential influence of the presence of E protein on M protein dimers through N-terminal restraints, potentially causing preferential formation of 'class III' dimers which may represent a dimeric structure which leads to the formation of oligomers.

Based upon native PAGE data (section 4.2.1), truncated M peptide was reconstituted across a range of DH(6)PC concentrations, deposited onto carbon coated grids and analysed using negative stain TEM. Ring-like structures with an electron-dense central pore were readily observable at all DH(6)PC concentrations (125-175 mM) (section 2.6.6 & Figure 4.4). Additionally, channels were seen at 300 mM, the concentration used in the native PAGE, but at far lower frequency. These structures resembled those observed for other viroporins under similar conditions, including HCV p7 (Clarke et al., 2006; Luik et al., 2009).

Consistent with the presence of M protein oligomers, many channel structures with an average oligomer diameter of 8.6 nm were present at 150 mM DH(6)PC, which was the optimal in terms of the lowest signal noise ratio and particle heterogeneity (Figure 4.4B). Particles seemingly aligned in a single plane relative to the grid surface displaying the presence of the electron-dense pore.

The favourably aligned orientations of M protein channels appeared ideal for two-dimensional class averaging to determine channel stoichiometry. 9907 particles were picked at 150 mM DH(6)PC (Figure 4.6B), yet the resolution of the images did not allow the stoichiometry to be determined. The issues with resolution may be due to the thickness of 2 % uranyl acetate stain and/or potential heterogeneity of the oligomers.

Additionally, the 125, 150 and 175 mM concentrations of DH(6)PC displayed seemingly different channel configurations (Figure 4.4). Channels observed in 150 mM DH(6)PC were chosen for further analysis due to their high levels of homogeneity and frequency. The average diameter of oligomers was determined by measuring all channels from two fields of view. Channels present in 150 mM DH(6)PC averaged 8.8 nm, comparatively oligomers in 125 mM DH(6)PC had an average diameter of 7.6 nm, with more smaller oligomers and an electron dense pore not being present (Figure 4.4A), furthermore at 175 mM DH(6)PC channels averaged 10.5 nm and the background noise had increased (Figure 4.5).

This analysis represents the first visualisation of oligomeric channels for any Flavivirus M protein. The ZIKV M protein oligomers exhibiting electron dense pores, reminiscent of other viroporins is highly supportive of our ZIKV M viroporin hypothesis. To determine whether the channels seen by TEM can form membrane-permeabilising pores, we introduced the M peptide into a dye-release assay.

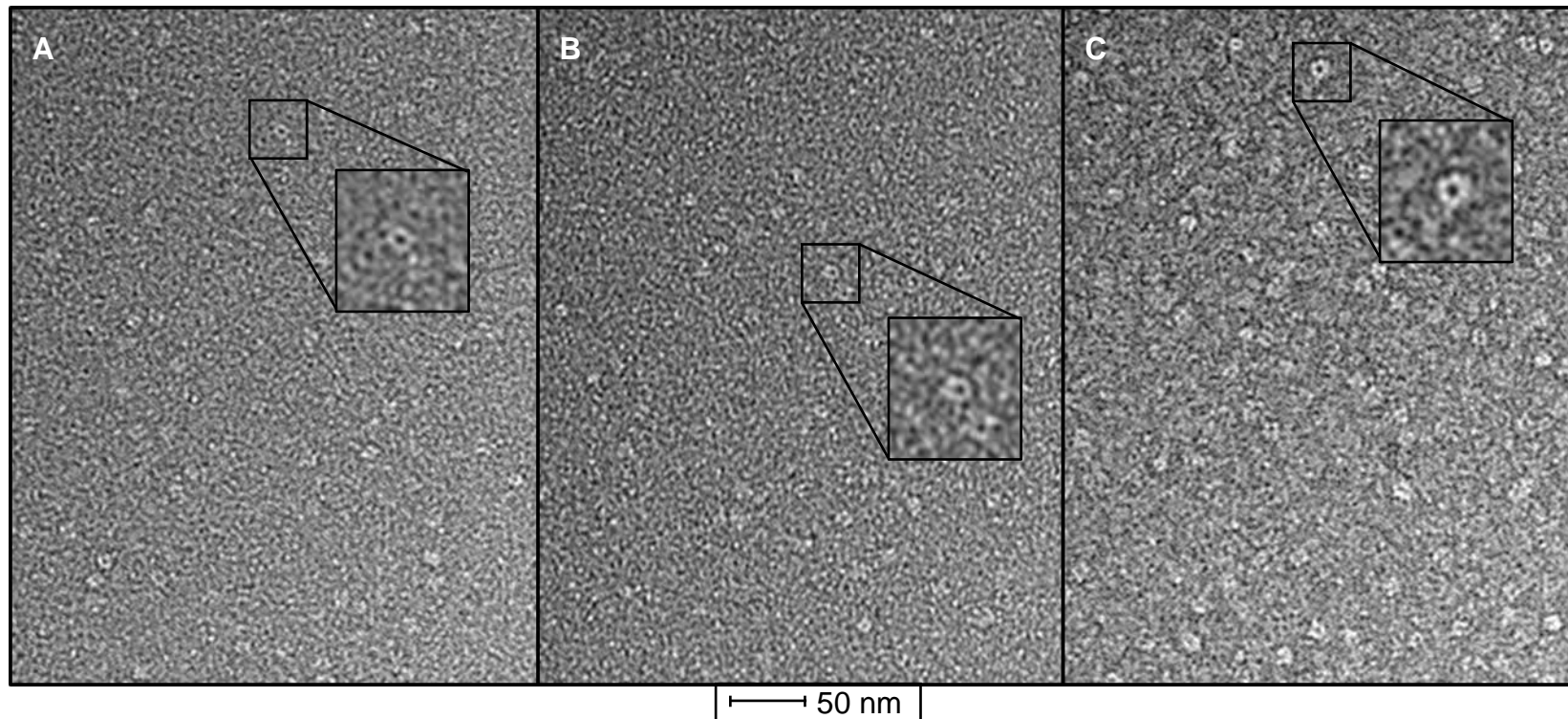


Figure 4.4 M oligomerisation at varying DH(6)PC concentrations, visualised by TEM

M protein diluted in DH(6)PC prior to staining with 2 % uranyl acetate and visualisation at 125 000 x magnification by transmission electron microscopy. **A.** M protein added to 125 mM DH(6)PC **B.** M protein added to 150 mM DH(6)PC **C.** M protein added to 175 mM DH(6)PC. TEM images kindly generated by Dr Daniel Maskell and Dr Rebecca Thompson.

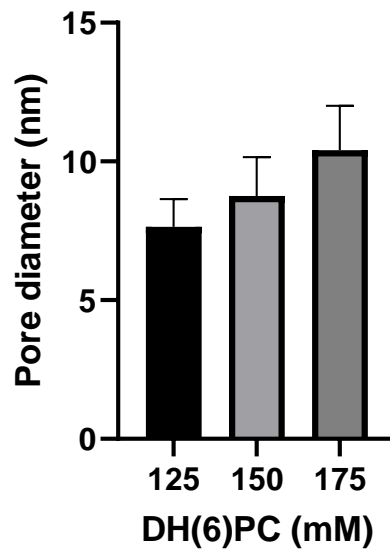


Figure 4.5 Pore diameter of M protein oligomers in a detergent environment

M protein channels in the presence of 125, 150 and 175 mM DH(6)PC were imaged using transmission electron microscopy and the channels formed were quantified for two fields of view. For 125, 150 and 175 n = 107, 68 and 222 respectively

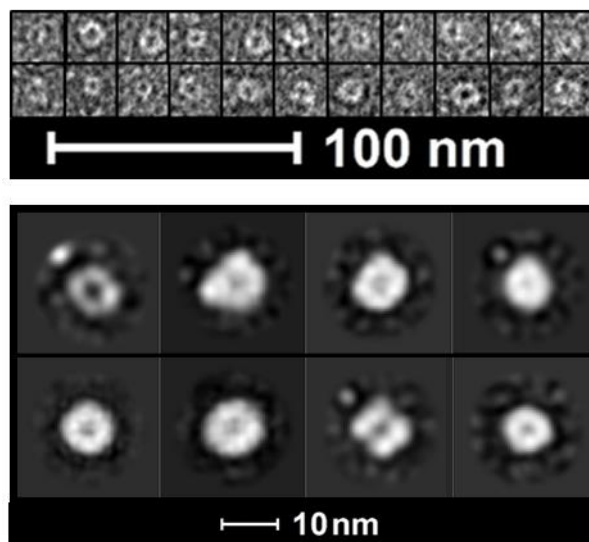


Figure 4.6 Oligomerisation of M protein in detergent environment by Transmission Electron Microscopy

A. A selection of M protein channels in the presence of 150 mM DH(6)PC stained with 2 % uranyl acetate, on average ~8.6 nm in diameter. **B.** 2D class averaging of 9907 channels with 25 iterations in 150mM DH(6)PC. TEM images kindly generated by Dr Daniel Maskell and Dr Rebecca Thompson.

4.3 M peptides mediate dose-dependent release of carboxyfluorescein from liposomes

Visualisation of M protein by TEM in a detergent environment showed M peptide oligomerised to form a ring-like structure indicative of a channel. To determine whether this channel is functional *in vitro*, a published liposome-based dye release assay was optimised for use with M peptides (StGelais et al., 2007; Tuthill et al., 2006; Davis et al., 2008).

Liposomes were made by extrusion using commercially available phospholipids: l- α -phosphatidic acid (PA), l- α -phosphatidylcholine acid (PC) and N-lissamine rhodamine labelled l- α -phosphatidylethanolamine (PE), and contain carboxyfluorescein (CF) at a self-quenching concentration (section 2.6.1).

Positive controls comprising rimantadine resistant M2 derived peptides (channel activity) or Triton X-100 (maximal dye release) (Atkins et al., 2014; Scott et al., 2020) (Figure 4.6A and B) were added to the liposomes releasing CF, diluting CF from its self-quenching concentration within the liposomes and into the surrounding buffer. The resulting fluorescence was monitored by fluorimetry over a 30 min period. Baseline levels were calculated from solvent controls (5 % DMSO or 5 % MeOH) (section 2.6.2).

Increasing concentrations of M protein resuspended in DMSO were added to CF containing liposomes, resulting in a concentration-dependent increase in total CF released from liposomes (Figure 4.7C). However, reconstitution of M protein up to 50 nM in MeOH showed no activity (Figure 4.7B), and this applied up to 250 nM (data not shown). Therefore, M protein was resuspended in DMSO at a concentration of 780 nM in subsequent experiments.

The indirect measurement of ZIKV M channel activity described in this section is the first case of *in vitro* quantified activity for ZIKV M protein, and results are comparable with those of well-characterised IAV M2, HCV p7 and HPV E5 in the same assay (Carter et al., 2010; Wetherill et al., 2012; StGelais et al., 2007; Atkins et al., 2014; Scott et al., 2020).

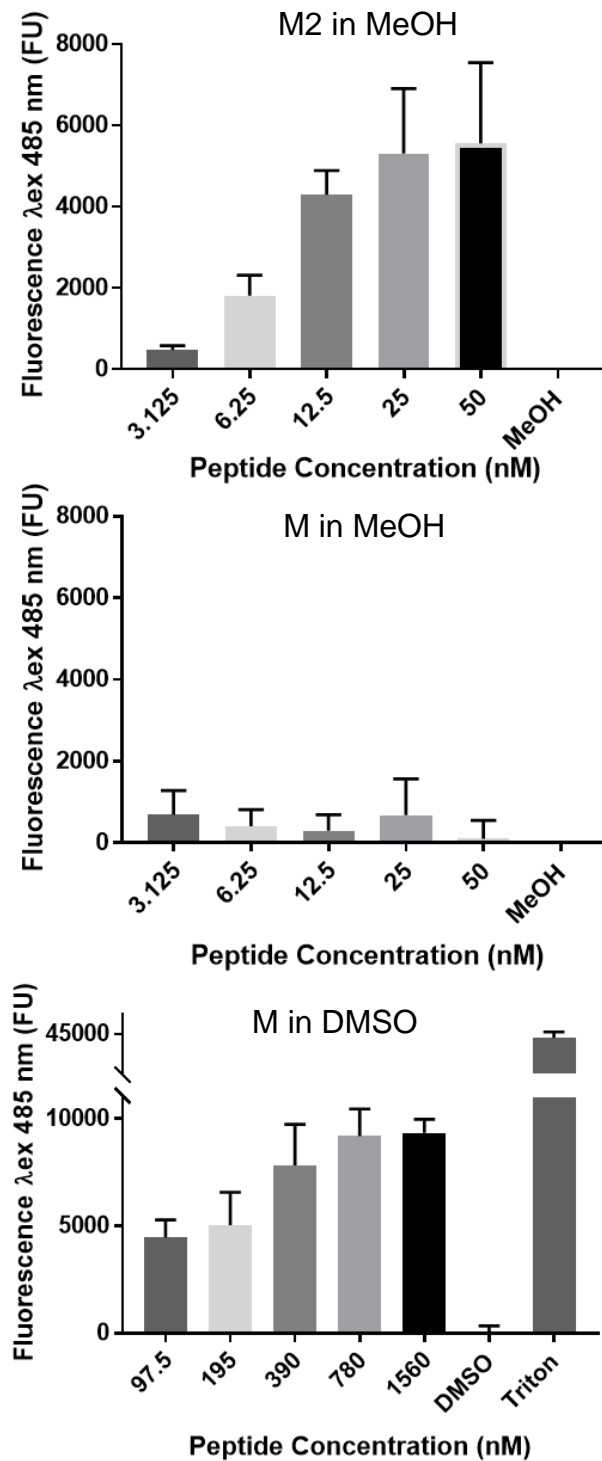


Figure 4.7 M peptide displays channel activity in the liposome-based assay when reconstituted in DMSO.

M2 shows a concentration-dependent effect of CF released from liposomes when reconstituted in methanol (MeOH). B. ZIKV M protein does not show activity when reconstituted in DMSO. C. ZIKV M protein displays concentration-dependent channel activity when titrated in the liposome assay between 97.5 and 1590 nM. Released CF fluorescence was analysed by fluorimetry (λ_{ex} 485 nm/ λ_{em} 520 nm). All data shown, n=3 biological repeats, Error bars represent standard deviation of the mean

4.3.1 ZIKV M protein channel activity is enhanced at acidic pH

We hypothesise that M protein will oligomerise within endosomal compartments. During endosomal maturation pH decreases from 6.8-5.9 in early endosomes to 6.0-4.9 in late endosomes (Maxfield and Yamashiro, 1987; Huotari and Helenius, 2011), therefore it was important to determine whether pH affected the activity of M protein channels.

The archetypical M2 viroporin is pH gated via HIS37 protonation (Wang, C. et al., 1995; Chizhnikov et al., 1996). M2 activity aids the entry and uncoating of IAV by allowing protons from the acidified endosome into the virus core, resulting in virion destabilisation. Additionally, other viroporins have displayed pH-dependent activity including E5 and p7, although p7 pH sensitivity is genotype specific (Wetherill et al., 2012; StGelais et al., 2007; Wozniak et al., 2010; Atkins et al., 2014).

The liposome-based assay was adapted to assess the effect of pH on M channel activity, as performed for p7 and E5 (StGelais et al., 2007; Wetherill et al., 2012). This published endpoint assay employed external buffers at differing pH, with liposome-depleted supernatants re-buffered prior to measurement of fluorescence due to acid quenching of CF. Additionally, Triton-X100 and DMSO controls were included to validate the reliability of the liposomes in each pH buffer (section 2.6.4).

Figure 4.8 shows a statistically significant increase in levels of M-mediated CF release corresponding to decreasing pH between 6.2 and 7.4. Thus, these experiments suggest that M protein channel activity increases in response to acidic pH *in vitro*. The acidic buffer pH in this assay reflects the pH found within the endosomal pathway environment, corresponding to early endosomes (pH 6.5-6.0). This suggests that M protein channels are potentially activated in endosomal compartments, consistent with studies on DENV entry (Cruz-Oliveira et al., 2015). Further acidification to pH 6.0-5.5 would be reflective of late endosomes.

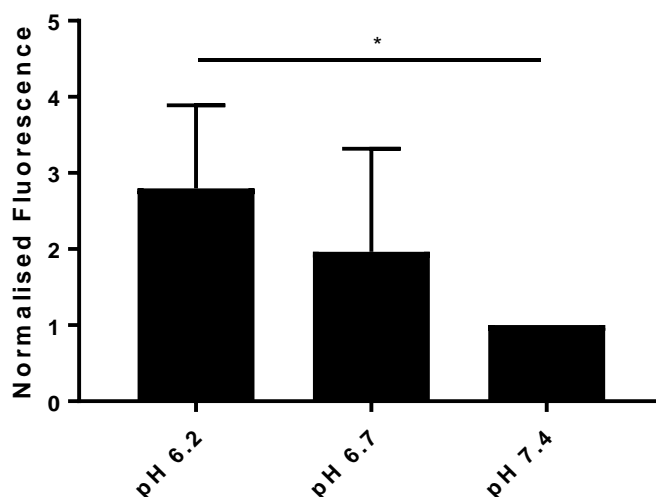


Figure 4.8 The effect of pH titration on M protein channel activity

Levels of CF release mediated by M protein was enhanced by acidic pH. M peptide (1 μM) and Triton x-100 were added to CF liposomes resuspended in liposome assay buffer adjusted to pH 6.2, 6.7 and 7.4. Liposome-free supernatants were quantified by fluorimetry and the pH was adjusted to pH 7.4 by the addition of 20 μL 1 M Tris-HCl pH 8.0 per 100 μL of supernatant. Triton X-100 (T) lysed controls were used to determine maximum fluorescence. Error bars represent standard deviation of three repeat experiments individually background subtracted. Data was normalised to pH 7.4. Statistical significance was determined using an unpaired t test, p value pH 7.4 to 6.8 = 0.14, *p value pH 7.4 to 6.2 = 0.023 n=3 biological repeats.

4.4 M peptide channel activity displays sensitivity to Rimantadine *in vitro*

Rimantadine (Rimantadine hydrochloride ((RS)-1-(1-adamantyl)ethanamine) Maybridge), was originally licensed in the 1980s to treat influenza A virus (IAV) infection, along with its related compound, amantadine, which was licensed in the 1960s. Whilst originally targeted against the prototypic IAV viroporin M2 (Hay et al., 1985; Schnell and Chou, 2008), Rimantadine is now also known to block HCV p7 (Clarke et al., 2006; Griffin, S.D. et al., 2003; Griffin, S.D. et al., 2004; Hay et al., 1985; Schnell and Chou, 2008; StGelais et al., 2007), HPV E5 (Wetherill et al., 2012), and evidence also suggests that it blocks channels formed by C-terminal peptides from DENV M protein (Koff et al., 1981; Koff et al., 1980; Premkumar et al., 2005). Rimantadine and its derivatives are promiscuous compounds due to their small size, 3-dimensional hydrophobic adamantyl-cage and polar amine group, which help it occupy a wide variety of diverse binding cavities with greater or lesser avidity. Previously, rimantadine has been used in our lab to identify druggable binding sites via low potency interactions, which can be further explored via rational drug discovery methods (Foster et al., 2011; Foster et al., 2014; Griffin, S. et al., 2008).

M peptide was used in liposomes at a final concentration of 780 nM, as determined by previous M peptide titrations (Figure 4.7). Rimantadine was titrated from 1.95 μ M to 4 mM. Inhibition of M protein channel activity was classified by a decrease in the endpoint fluorescence when compared to vehicle-only control (section 2.6.3).

Rimantadine concentrations at or lower than 500 μ M inhibited M protein activity (Figure 4.9). However, at higher concentrations rimantadine caused artefactual higher levels of CF release from liposomes. At the lowest concentration tested, 390 nM of rimantadine displayed inhibition levels of around 40 % (Figure 4.9), moreover 1 μ M gave the most consistent inhibition (Figure 4.10). Although rimantadine has previously shown inhibitory effects on DENV M peptide channels *in vitro* and DENV in cell culture, the drug has not been tested against ZIKV or ZIKV M protein. Inhibition of ZIKV M channels by rimantadine *in vitro* highlights the possibility of therapeutically targeting M protein channels. If

rimantadine consistently inhibits ZIKV in cell culture and *in vivo*, the compound and its respective binding site could be used for drug development.

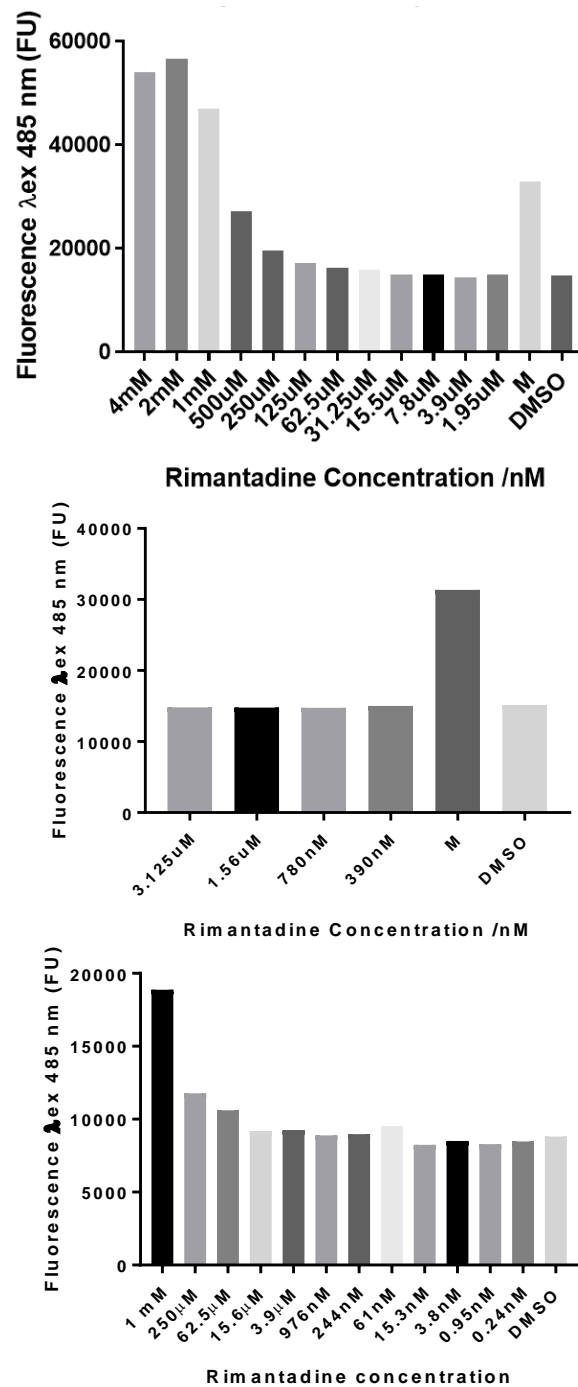


Figure 4.9 Rimantadine has a dose-dependent effect on M protein-mediated CF release

A. Titration of rimantadine from 4 mM to 1.95 μM and in the presence of M protein, rimantadine was added to 780 nM of M protein 5 min prior to addition to CF containing liposomes. B. Titration of rimantadine from 3.125 μM to 390 nM in the presence of 7.6 μM M protein. C. Titration of rimantadine in the absence of M protein. Released CF fluorescence was analysed by fluorimetry (λ_{ex} 485 nm/ λ_{em} 520 nm). N=1

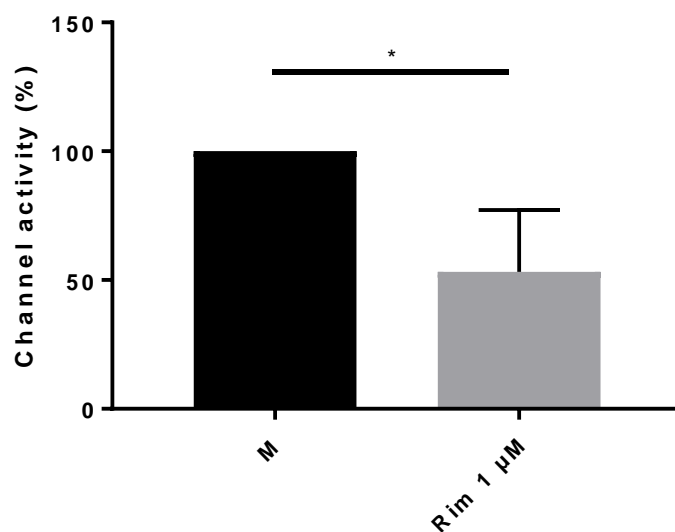


Figure 4.10 Rimantadine at 1 μ M reproducibly reduces M protein-mediated CF release

Addition of rimantadine at 1 μ M in the presence of M protein (780 nM) was added to CF containing liposomes. Background fluorescence was subtracted from final values and channel activity was calculated relative to M alone. Rimantadine reduced the fluorescence released from 100 % to 52 % on average from 3 biological repeats of a single well. Error bars represent standard deviation of the mean and statistical significance of channel activity was assessed by unpaired t-test (* $p=0.0278$).

4.5 Rimantadine mediates dose-dependent inhibition of ZIKV in cell culture

Previous identification of rimantadine inhibition of viroporins in dye release assays has been translatable to virus inhibition in cell culture (StGelais et al., 2007; Griffin, S. et al., 2008). Therefore, if rimantadine could inhibit ZIKV replication in cell culture, it could suggest the presence of M protein channel formation. It has previously been published rimantadine has a dose-dependent effect on the replication of closely related DENV in cell culture (Koff et al., 1981). However, its activity against ZIKV has not previously been reported.

Vero cells were infected with ZIKV at a multiplicity of infection (MOI) of 0.1 plaque forming units per cell (pfu/cell). Ensuing virus replication was assessed using immunofluorescence and western blotting 48 hours post infection, using α NS3, α NS5, α E and α M antibodies with Hoechst co-staining for α NS3 and α NS5 antibodies (Figure 4.12) (section 2.2.6, 2.5.1, α NS3, α NS5 gifted from Andres Merits, Tartu). However due to the lack of Hoechst staining, non-infected stained cells and primary-only and secondary-only antibody staining, there are limitations of the staining, in particular the specificity of the antibodies. Optimisation of Immunofluorescence (Figure 4.11) revealed the likely localisation of NS3 and E to be cytoplasmic, whereas NS5 appeared to localise to the nucleus. Of note ZIKV M shown in the bottom panel, stained for using AlexaFluor 594 suggests M co-localises with Envelope in AlexaFluor 488. However, further controls would be needed to confirm the aforementioned findings.

Western blot data in Figure 4.12 shows the sizes of probed ZIKV proteins, interestingly the blot probed the using α M antibody shows two bands at ~10 and 25 kDa, suggesting both mature M and prM were present in the infected cell lysate. Downstream analysis for cell imaging and automated cell counting was carried out using the IncucyteZOOM determining titre represented as the number of infectious units per μ L at 48 hpi, adapted from protocols developed for HCV (Stewart et al., 2015).

MOI 0.1

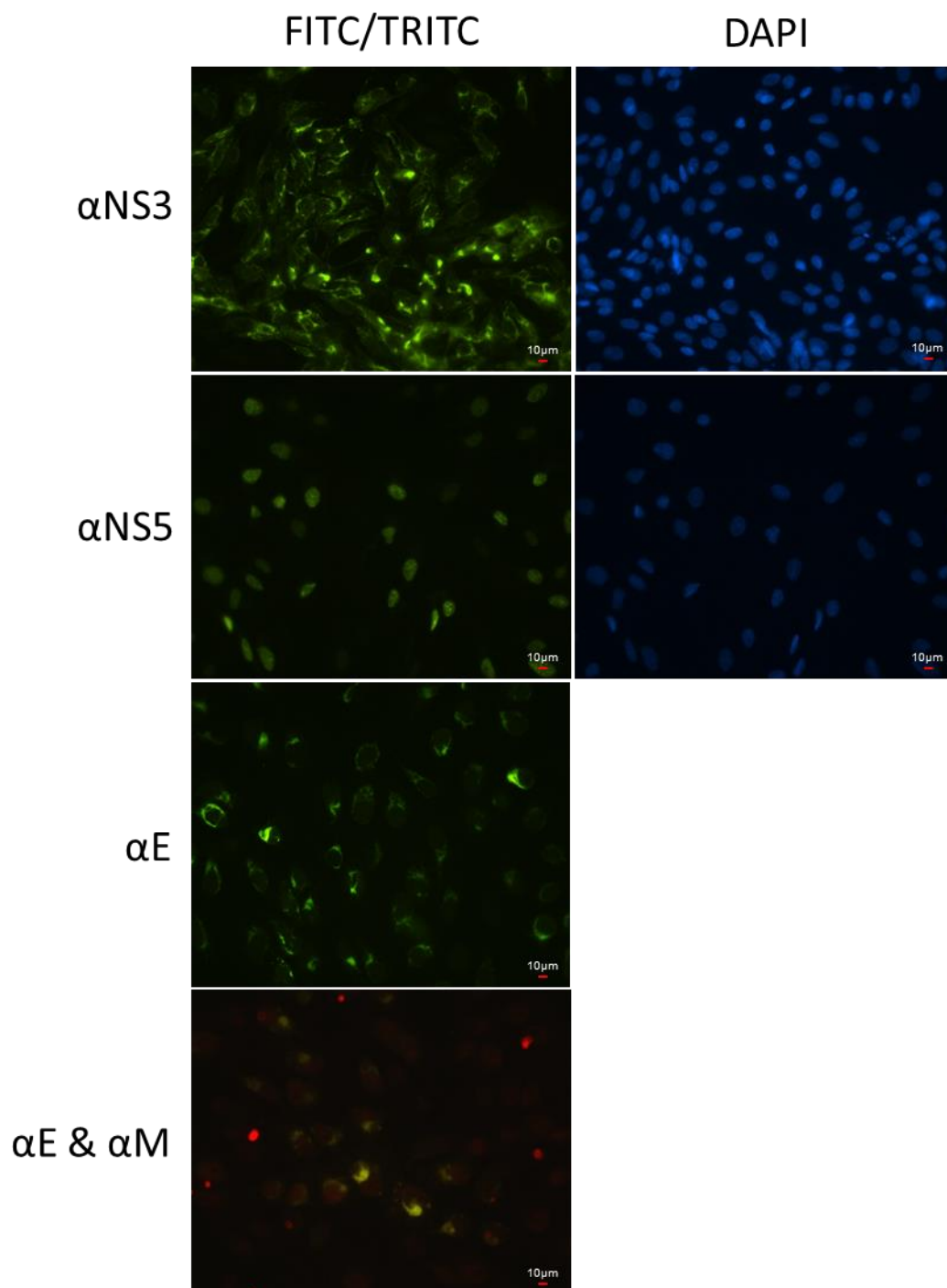


Figure 4.11 Optimisation of ZIKV specific antibodies for we/stern blot and immunofluorescence

A. Immunofluorescence staining of cells treated with ZIKV at an MOI of 0.1 PFU/cell. Cells were fixed and stained with anti-NS3 antibody, anti-NS5 antibody or anti-E antibody with AlexaFluor 488 and Hoecsht, or anti-E and anti-M antibody with AlexaFluor 488 and 594 respectively, then imaged at 40x magnification using a Ti-E widefield microscope.

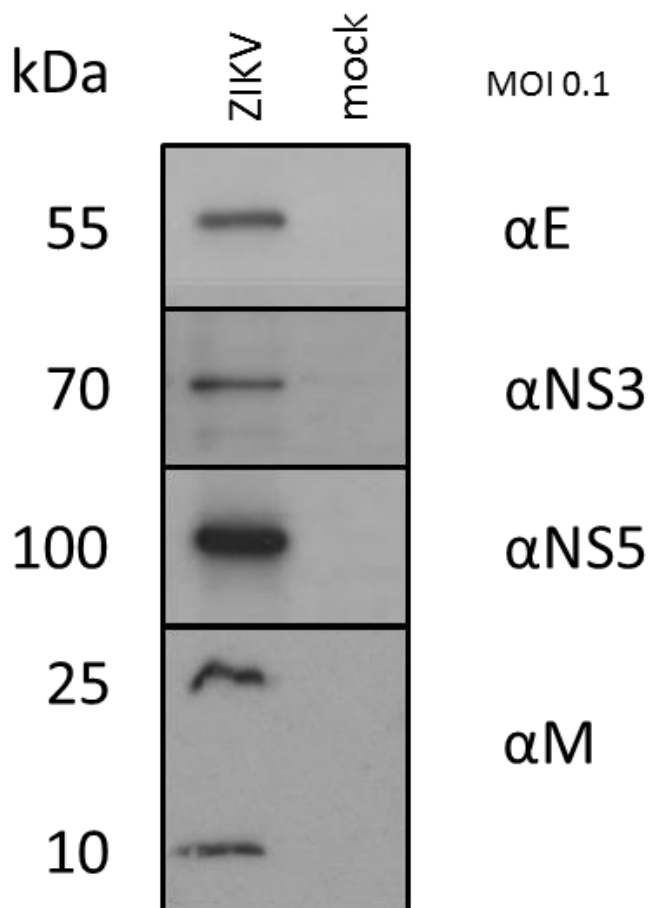


Figure 4.12 Optimisation of ZIKV antibodies by western blot

Detection of ZIKV positive cell lysate, by anti-E antibody, anti-NS3 antibody, anti-NS5 antibody and anti-M antibody.

4.5.1 Rimantadine does not affect cell cytotoxicity or endocytic uptake of EGF

Prior to testing rimantadine in virus culture, we conducted a cell viability assay using a proxy measure of metabolic activity to determine the range of rimantadine concentrations to use for experiments upon vero cells. We tested the effect of rimantadine using MTT (3-(4,5-Dimethylthiazol-2-yl)-2,5-diphenyltetrazolium bromide) for assays. Previous use of rimantadine in cell culture has been widely reported over a range of concentrations (Koff et al., 1981; Black et al., 1993; Govorkova et al., 2004; Koff and Knight, 1979).

Rimantadine was tested between 5 and 120 μM for cell toxicity effects over a 48 hr incubation period using MTT assays, results show rimantadine does not induce cell toxicity when added at concentrations below 100 μM . MTT levels were quantified by absorbance at 590 nm (Figure 4.13) (section 2.2.4).

Additionally, the effect of rimantadine on the clathrin-dependent endocytic pathway, used by Flaviviruses for cell entry (Chu and Ng, 2004; Sorkin and Waters, 1993), was investigated using uptake of fluorescently labelled EGF (section 2.2.5). Rimantadine at 80 μM and below had no effect upon clathrin dependent endocytic uptake of fluorescent EGF, when measured and quantified by flow cytometry. Moreover, Bafilomycin A1, which is known to inhibit endocytosis through targeting the V-ATPASE proton pump, was used as a positive control (Figure 4.14). There are no error bars in Figure 4.14 as this was not repeated due to time constraints, however 25000 cells were counted for each condition.

4.5.2 Rimantadine suppresses ZIKV replication in cell culture

To investigate the effects of rimantadine on ZIKV replication, cells were incubated with rimantadine at non-cytotoxic concentrations (section 4.5.1). Rimantadine and ZIKV at an MOI of 0.1 pfu/cell were added to cells in standard cell culture medium. After 1 hr of incubation allowing for uptake of the virus, the media was removed and replaced by rimantadine containing media (Figure 4.15A) (section 2.3.4.1). Multicycle virus replication was measured 48 hours post-infection, by both western blot and quantification of infected cells using IncuCyte Zoom analysis of E-specific immunofluorescence.

Rimantadine exerted a concentration-dependent inhibition of ZIKV infection, evidenced by both reduced numbers of infected cells by IF (IncucyteZOOM) and diminished levels of ZIKV E protein by western blot. The presence of 10 μM rimantadine or above had a significant effect on ZIKV infection (Figure 4.15).

Translating inhibition of ZIKV M protein channels *in vitro* to inhibition of ZIKV infection in cell culture, is a significant step in proving M protein forms oligomeric channels which can be targeted by therapeutics and subsequently reduce virus infection. Furthermore, rimantadine has the potential to inhibit ZIKV *in vivo* and if successful, indicates ZIKV M can be therapeutically targeted *in vivo*.

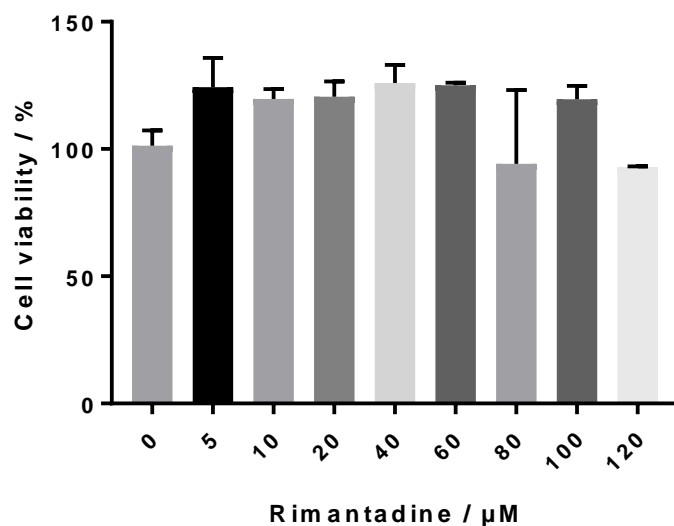


Figure 4.13 The effect of Rimantadine on cell viability

Vero cells were treated for 48 hr with increasing concentrations of rimantadine and were compared to DMSO treated cells. The cell viability was measured using an MTT assay, the output of this was read using a plate reader at an absorbance of 590 nm. n=3 technical repeats. Error bars represent standard deviation.

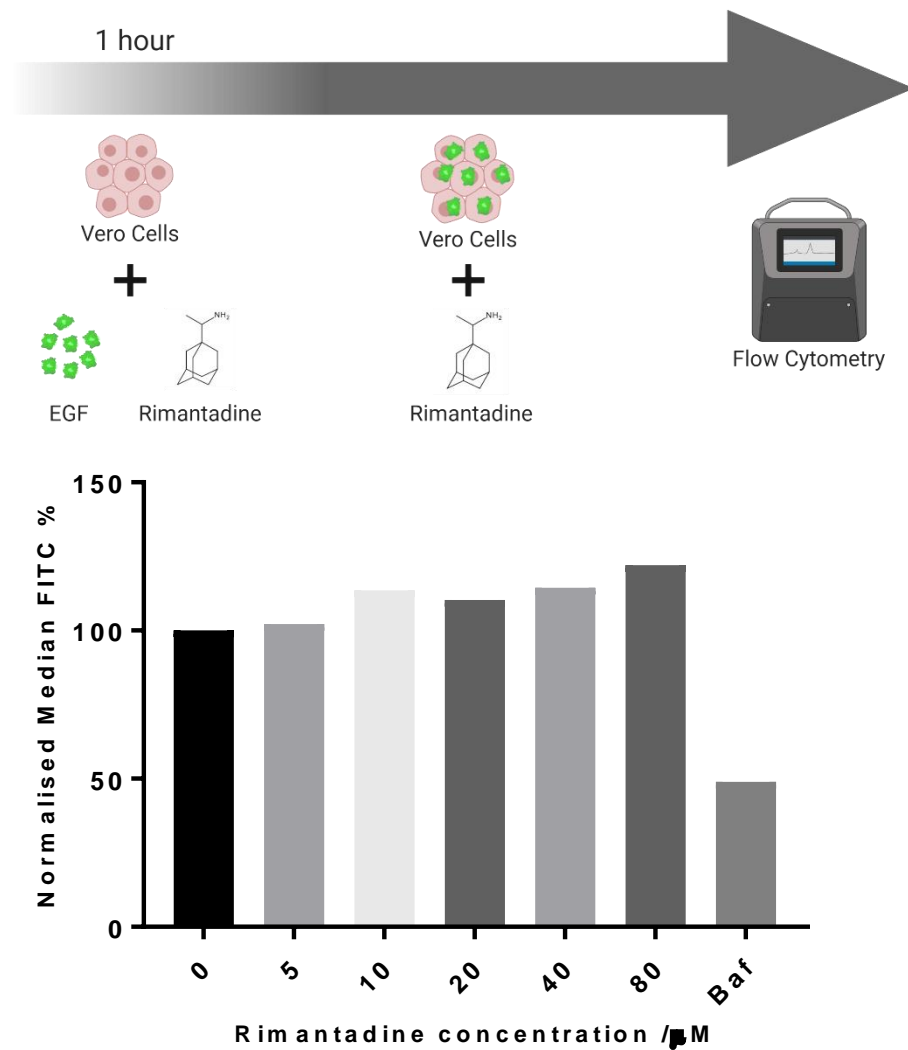


Figure 4.14 Rimantadine does not effect the uptake of fluorescently labelled EGF

A. Schematic of experiment used to determine if rimantadine effects uptake of fluorescently labelled EGF by endocytosis. **B.** Rimantadine pre-treated cells endocytosed fluorescently labelled EGF, independent of the rimantadine concentration between 5 and 80 μ M. The fluorescent EGF uptake of cells was measured using flow cytometry and quantified using median FITC, displayed as a % of maximum fluorescent EGF uptake at 0 μ M rimantadine. Bafilomycin A1 was used at 1 μ M. Single technical repeat, 25000 cells counted per condition.

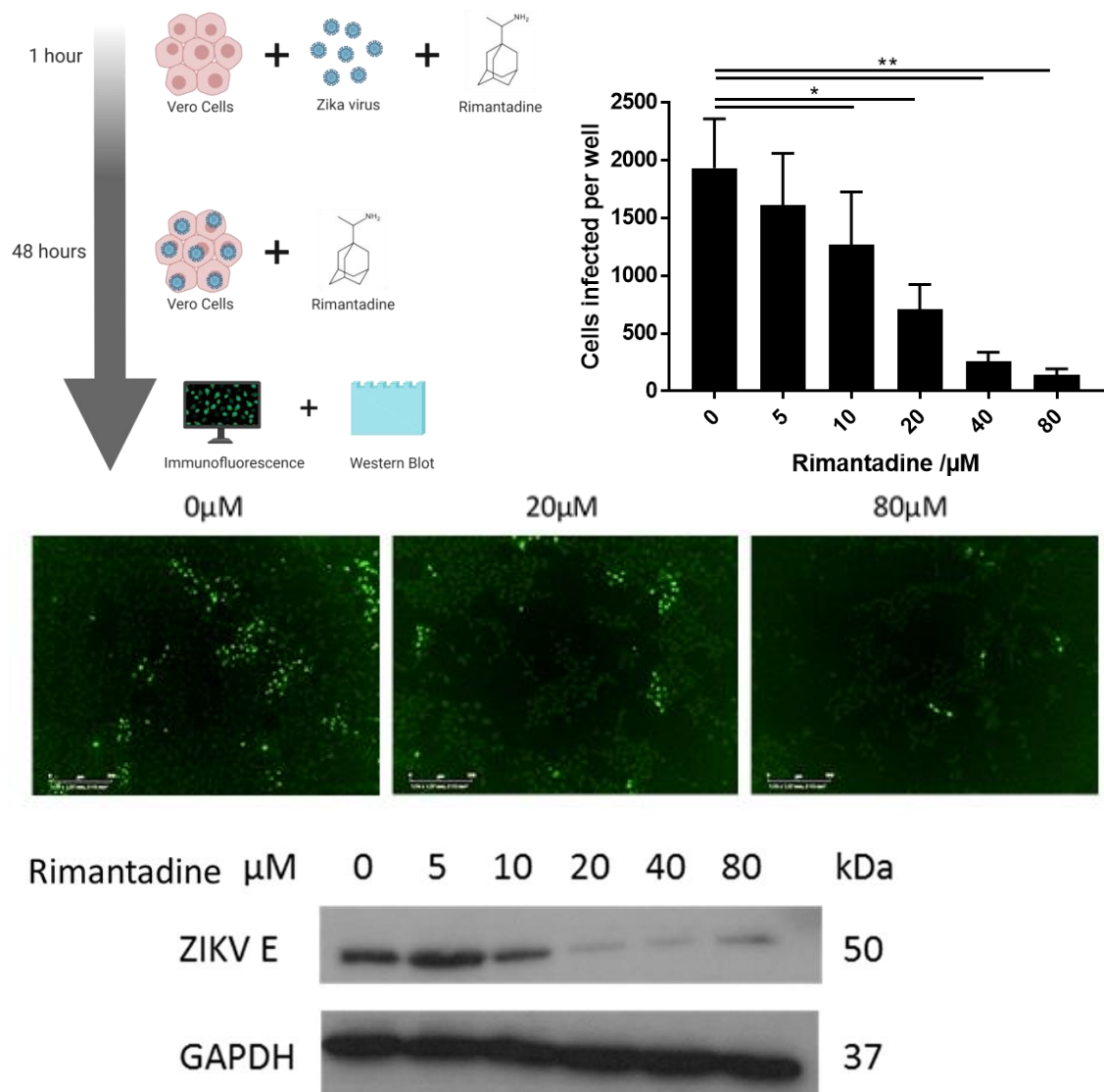


Figure 4.15 Rimantadine has a dose-dependent effect on ZIKV infection in cell culture

Rimantadine has a dose-dependent effect on ZIKV replication at an MOI of 0.1 between 0 and 80 μM . **A.** Schematic showing experiment protocol. **B.** Quantified immunofluorescence staining for ZIKV E protein. **C.** Representative images of the immunofluorescence staining for ZIKV E protein at 0, 20 and 80 μM . **D.** Western blot micrographs probing for ZIKV E protein alongside housekeeping gene GAPDH at 0, 5, 10, 20, 40 and 80 μM . N=3 biological repeats for immunofluorescence and western blot experiments. Error bars represent standard deviation of the mean and statistical significance of ZIKV infected cells was assessed by unpaired t-test comparing rimantadine treated cells with untreated cells (* $p < 0.01$, ** $p < 0.001$).

4.5.3 Rimantadine targets an early stage of the ZIKV life cycle

Rimantadine was added over a time course corresponding to the early stages of infection to investigate at what stage of the virus life cycle rimantadine inhibits ZIKV replication; specifically we asked whether rimantadine targets ZIKV entry, when we believe M protein channels will form. The effects upon infectivity were determined via a plaque reduction assay (section 2.3.4.2).

Rimantadine was pre-incubated with BHK-21 cells for 4 hr, or added at the same time as the virus inoculum or post inoculation for a 48 hour period, Rimantadine was also added at a combination of these stages for further analysis (Figure 4.16 A). Rimantadine was added to cells prior to infection to investigate whether it blocked virus uptake into the cells. Pre-incubation presumably causes rimantadine to be taken up and stored in endocytic vesicles for a short time after its removal from cell culture media during virus entry. While addition of rimantadine during virus inoculation examines the effect of it on virus entry. Finally, the treatment of virus-infected cells post-inoculation examines the effect of rimantadine on the later stages of the virus life cycle. Figure 4.16 shows rimantadine has the most pronounced effect on inhibiting ZIKV prior to and during virus inoculation, therefore indicating rimantadine is likely to be inhibiting ZIKV replication via disruption of virus entry, further supporting our hypothesis of M protein forming channels during endocytosis and playing a role in virus entry, which has not been shown previously.

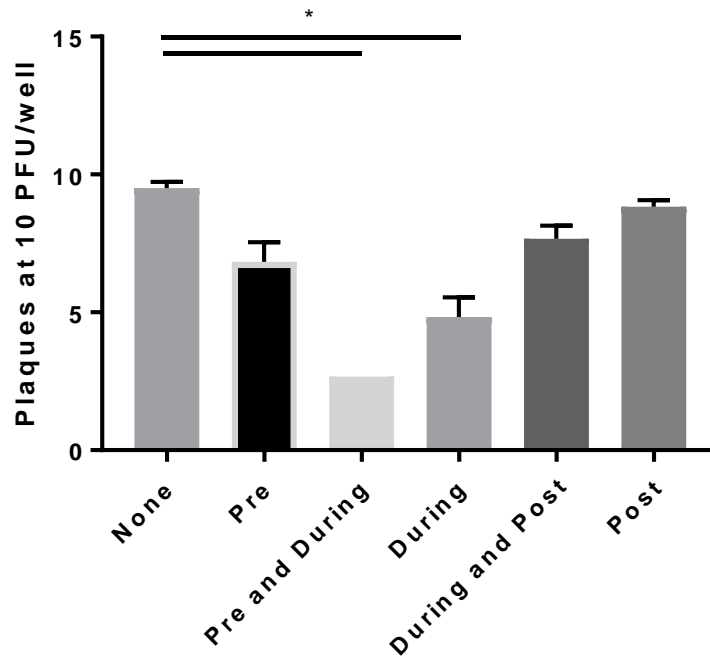
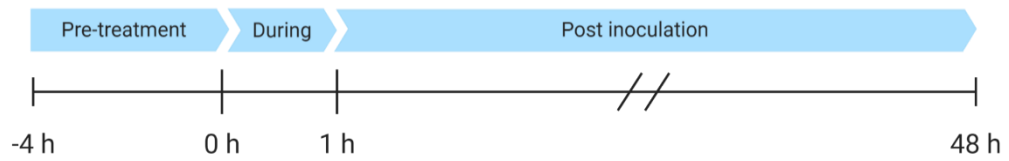


Figure 4.16 Rimantadine targets entry step of virus life cycle shown by time of addition plaque assay

Rimantadine was added at 80 μ M at various stages of the plaque assay protocol (section 2.3.4.2). Rimantadine was either added prior to inoculation for 4 hr, during the 1 hr inoculation period, for the 48 hr post inoculation period or combinations of these. Error bars represent standard deviation of the mean and statistical significance of ZIKV titre was assessed by t-test comparing rimantadine pre-treated cells or cells treated pre and during inoculation to untreated cells (* $p < 0.01$). Single biological repeat with two technical repeats per condition.

4.6 Rimantadine inhibits ZIKV infection *in vivo*

Rimantadine reduced levels of ZIKV infection *in vitro* and in cell culture, yet it was unclear whether this would translate into an *in vivo* system. Murine models are popular ways of recapitulating viral infections, although ZIKV does not usually establish an infection in immunocompetent mice, due to its inability to antagonise the murine STAT2-dependent interferon (IFN) response (Grant et al., 2016). For this reason, ZIKV murine models either use IFN/IFNAR knock-out (KO) mice, or mice treated with an anti-IFNAR1 antibody (Rossi et al., Lazear et al., 2016). Therefore, we decided upon IP treatment of mice with 1.5 mg anti-IFNAR1 antibody allowing transient inhibition of the receptor, retaining the remaining immune response and preventing intracranial infection and subsequent encephalitis (Hayashida et al., 2019). The ZIKV infection was then given at the same site as up to five mosquito bites from an *Aedes aegypti* mosquito, the principal vector of ZIKV, which is reported to enhance transmission (Pingen et al., 2016).

Ten C57BL/6 received a dose of 20 mg/kg rimantadine subcutaneously 30 min prior to ZIKV infection. The mice were then infected with ZIKV (1000 pfu) by injection into the sole of one hind foot and up to five female *Aedes aegypti* mosquitoes subsequently bit the foot once at the same site. Five hr post infection, a second dose of rimantadine in PBS at 20 mg/kg was administered. 24 hr post infection the mice were sacrificed and tissue samples from the skin of the foot, spleen and the serum were taken from the ten treated mice and ten infected control mice. These chosen organs were chosen due to previous investigative experiments, where ZIKV was detected (McKimmie, unpublished) (section 2.4).

This experiment was repeated, although the data from the first experiment was discounted due to use of incorrect needles for ZIKV injection, causing bleeding in some mice at the site of injection, therefore enhancing infection.

The serum taken from the mice was titred by plaque assay on Vero cells due to issues with previously used focus forming assay (Figure 4.16) (section 2.3.3 and 2.3.4.1). Rimantadine treated mice had significantly lower levels of ZIKV present in their serum. Conversely, the RNA was extracted from the skin and spleen, which are known to be sites of ZIKV replication and using the same

protocol in the absence of rimantadine ZIKV has been detected in these organs. The RNA was analysed by reverse transcription qPCR. However, the levels of ZIKV RNA in both skin and spleen samples of control and rimantadine treated mice were below the detection threshold for this experiment.

The reduction of ZIKV titres measured in rimantadine treated mice compared to control mice show rimantadine acts systemically, inhibiting virus infection. From *in vitro* research reported in this chapter, rimantadine inhibits ZIKV through targeting M protein during virus entry.

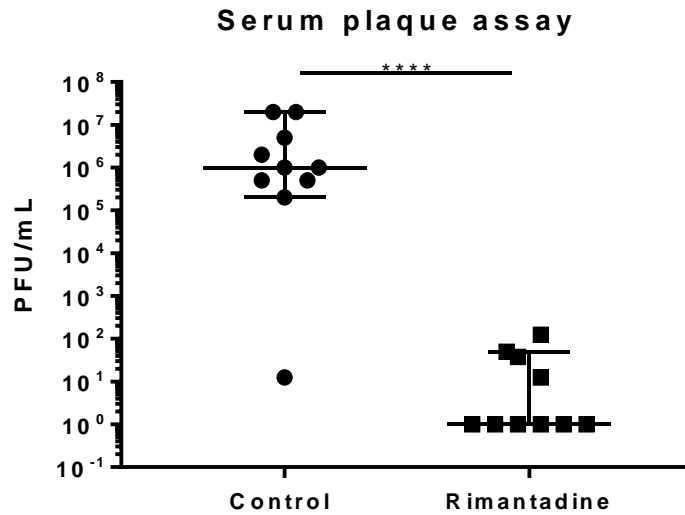


Figure 4.17 Rimantadine reduces viral titres of ZIKV infected mice

Mice were given 20 mg/kg rimantadine half an hr prior to infection with 2000 PFU ZIKV and up to five *A. aegypti* mosquito bites, followed by a second dose of 20 mg/kg rimantadine post infection prior to taking samples 24 hr post infection. Serum from the 10 control infected mice and 10 rimantadine treated mice was titred for ZIKV on Vero cells. The graph shows individual data points with the mean value and SD shown. Statistical significance of ZIKV titre was assessed by t-test comparing rimantadine treated mice with control treated mice (* $p < 0.0001$). *In vivo* assay kindly carried out by Dr Daniella Lefteri and Dr Clive McKimmie.

4.7 Discussion

The role of M protein during ZIKV entry and in the virus particle has not previously been investigated. However, we hypothesised that ZIKV M forms oligomeric channels during virus entry within acidified endosomes, aiding *Flavivirus* uncoating. Uncoating is an under explored stage of the virus life cycle, with few published reports into its mechanism. Over the years, research has uncovered the necessity for acidic pH, the requirement for a non-degradative ubiquitination step and very recently a proposed role for Valosin-Containing Protein (VCP) and p97 to disassemble VCP/p97 ubiquitylated nucleocapsids (Gollins and Porterfield, 1986; Byk et al., 2016; Ramanathan et al., 2019). However, there is no defined role for M protein during virus entry, despite the protein residing in the virion. M is known to have a role in chaperoning envelope protein during virus assembly, although within this chapter we have identified a novel role for M during entry.

Chapter 3 described M protein forming hexameric channels in an *in silico* system, however it is important to validate these *in silico* predictions through using M in isolation. Viroporins with similar channel-forming properties have been successfully studied using prokaryotic recombinant expression systems using large soluble tags to aid purification. These include GST tags for alphavirus 6K (Melton et al., 2002), HCV p7 (Clarke et al., 2006), SV40 VP4 protein (Raghava et al., 2011), Maltose Binding Protein for picornavirus 2B (Nieva et al., 2003) and SUMO for HRSV SH (Carter et al., 2010). However, our own attempts at expressing M protein using GST and HIS tagged systems resulted in low levels of expression and subsequent purification difficulties.

To circumvent difficulties in recombinant protein expression, a commercially synthesised N-terminal truncated 55 residue M peptide was commissioned from AltaBioscience. The purified peptide illustrated the capability of M protein to form oligomers in a membrane mimetic detergent, the structures of these oligomers by TEM and the activity of these channels by a liposome-based assay, showing a novel oligomeric ZIKV M structure and activity.

Membrane mimetic detergents such as DH(6)PC and DH(7)PC have previously facilitated studies of viroporin oligomerisation, including p7 peptides (Luik et al., 2009), M2 peptide (Schnell and Chou, 2008) and FLAG-tagged SH (Carter et

al., 2010), by both native-PAGE or TEM. M protein underwent similar protocols with 300 mM DH(6)PC and, as shown in Figure 4.2A by native-PAGE, two Coomassie stained bands at around 45 and 66 kDa indicated oligomerisation took place in the membrane mimetic environment. Determining the molecular weight of the proteins within individual bands is ambiguous due to the limitations of native-PAGE. However, these could resemble hexameric and heptameric or larger oligomers, as the monomeric form of the M peptide is 6264 Da. These bands could have relevance to the different oligomer sizes seen by EM at different DH(6)PC concentrations (Figure 4.4). Additionally, these two sizes of oligomers could relate to heterogeneity of M protein, similarly seen with p7 (Clarke et al., 2006; Griffin, S.D. et al., 2003; Luik et al., 2009).

Further analysis of M protein in the DH(6)PC environment identified ring-like structures by TEM. The channel-like complexes appeared to have an average protein diameter of 8.8 nm in 150 mM DH(6)PC, and are reminiscent of p7 visualised by EM (Clarke et al., 2006; Luik et al., 2009). Previously visualised viroporins SH and p7 were 8.7-9.3 and 8.1 nm in diameter respectively (Carter et al., 2010; Luik et al., 2009). However, the diameter of the oligomer is likely to appear greater by TEM due to staining effects, as uranyl acetate has a grain size of 4 to 5 Å (Scarff et al., 2018; Haschemeyer, 1970).

Dimensions of M protein hexameric channels from MD simulations range from 7.6 to 8.9 nm for helix 2 pore-lining and 5.7 to 7.7 nm for channels with helix 3 pore-lining. Chapter 3 results led to a hypothesis of M protein forming hexameric channels with helix 3 lining the pore, and with each monomer rotated to maximise interactions with the adjacent protomer. However, this lipid-anchored structure has a hexameric channel width of only 5.7 nm, compared to 7.6-10.4 nm which reside in detergent micelles. A slight difference between these measurements is to be expected due to the membrane differences of lipids and detergents, and the likelihood of small differences between *in silico* data and *in vitro*.

Though as seen in section 4.2.2 the channels formed exhibit heterogeneity, in addition the use of a 2 % uranyl acetate stain will increase the size of the channel, due to its grain-size of 4 -5 Å (Scarff et al., 2018; Haschemeyer, 1970).

In comparison, HCV p7 hexamers are around 42 kDa and exhibit a diameter of 8.1 nm at their widest point when hexameric by EM (Luik et al., 2009) and 11.1 nm by MD (Chandler et al., 2012). Additionally, RSV SH channels are separated into two distinct channel conformations, measuring 8.7 nm or 9.3 nm by EM (Carter et al., 2010).

However, the properties of M protein in detergents may not wholly reflect their properties in the virion membrane. Detergents have shorter chain lengths than lipids and form micelles as opposed to bilayers. Although, detergent to protein ratio is crucial for the oligomerisation of viroporin monomers, and either p7 monomers or hexamers are seen in the literature, dependent on the protein to detergent ratio (Oestringer et al., 2019; Chen, W. et al., 2019).

Additionally, analysis of the amino acid charges within the M protein sequence revealed helix 1, which lies parallel to the membrane and perpendicular to the TMDs in the cryo-EM structure and MD simulations in chapter 3 (Sirohi et al., 2016; Sevvana et al., 2018), contains multiple positively charged residues and through the sum of negative and positively charged residue the overall positive charge +0.9 at pH 7.4. This positive charge will potentially attract to the negatively charged grid, theoretically helping to orientate channels in a single plane for visualisation. The linker region of the peptide contains no charged residues and therefore will not be as strongly attracted to the grid.

ZIKV M was further investigated in liposomes, which more closely resemble ZIKV virion membranes. The ability of ZIKV M protein to mediate the release of CF from liposomes (Figure 4.6) was the first demonstration *in vitro* of a function associated to M protein oligomerisation, and further reinforces the molecular dynamic data from chapter 3, identifying M as a novel member of the virus encoded channels or viroporins. Similarly to viroporins HRSV SH, HPV E5, HCV p7, and IAV M2 all previously were shown to have channel activity using the liposome-based assay (Carter et al., 2010; Wetherill et al., 2012; StGelais et al., 2007; Atkins et al., 2014; Scott et al., 2020).

In M peptide liposome assays (Figure 4.4) the plotted endpoint fluorescence never reached the maximum fluorescence set by the Triton X-100 control, indicating CF was not released from a proportion of the liposomes and the protein to lipid ratio was the limiting step of CF release. Additionally, a dose-

dependent effect of the endpoint fluorescence occurred upon increasing M peptide concentration. Furthermore, HCV p7, HRSV SH and HPV E5 all display dose-dependent effects when added to liposomes and were optimised to avoid maximum CF release (StGelais et al., 2007; Carter et al., 2010; Wetherill et al., 2012). However, at high concentrations, greater than 5 μ M, M may form protein aggregates as is reported with HPV E5 and rhinovirus VP4, destabilising liposomal membranes (Davis et al., 2008; Wetherill et al., 2012). Therefore, amounts of M peptide that allowed sufficient CF release but did not cause membrane destabilisation were used in this assay (780 nM) evidenced by inhibition at these concentrations with small molecules.

Additionally, if time permitted it would be of interest to determine the approximate hydrodynamic radius of the M peptide channels within liposomes, using a dextran size exclusion assay (Wetherill et al., 2012; StGelais et al., 2007; Shukla et al., 2015). This would be done in conjunction with future TEM analysis of channel complexes. Furthermore, membrane flotation assays on sucrose gradients would determine whether M integrated within liposome membranes by incorporation of high pH washes and detergent treatment (StGelais et al., 2007; StGelais et al., 2009; Wetherill et al., 2012; Panjwani et al., 2014).

Viroporin functions have been associated with several stages during the virus life cycle, including: entry (Ruigrok et al., 1991), assembly (Ye, Y. and Hogue, 2007) or release (Beaton et al., 2002), and viroporins involved in virus entry are found within the virus particle (Gonzalez and Carrasco, 2003) as is seen with M proteins presence in the virus membrane.

The presence of viroporin channels is known to alter membrane permeability within host cells and subcellular compartments. HCV p7 and IAV M2 sense proton electrochemical potentials and are gated by a decrease in pH (Sarkar et al., 2001; Pinto et al., 1997; Wang, C. et al., 1995; StGelais et al., 2007; Wozniak et al., 2010; Atkins et al., 2014). Amino acids arginine, lysine, and histidine detect variations in the pH and can become protonated and change conformation upon a decrease in pH (Bezanilla, 2008).

Similarly, decreasing the pH to mimic the physiological endosomal environment during virus entry, resulted in a significant increase in M peptide channel activity

at pH 6.2 and 6.7, compared to pH 7.4 (Figure 4.7). We speculate that a change in external pH may result in protonation of HIS28, as investigated by simulations in chapter 3, causing extended opening and or stabilisation of the channel.

It is known that protonation of M2 HIS37 leads to a conformational change in gating residue TRP41. In addition, it has been reported some genotypes of HCV p7 may use a similar gating motif as M2 (Meshkat et al., 2009). However, mutations of the p7 HIS17 and TYR21 to ALA did not affect particle production and although HIS17 is highly conserved, TYR21 is not conserved throughout HCV genotypes (Montserret et al., 2010). Additionally, it is highly unlikely for two structurally unrelated viroporins to have the same gating motif and it has been suggested the gating residue could be PHE25 (Foster et al., 2014). Furthermore, proton-sensing properties of HCV p7 are not present across all HCV genotypes, for example HCV-H77 (Atkins et al., 2014).

Unlike M2 & p7 which have pore-lining HIS residues, ZIKV M HIS28 is present on the N-terminal helix of M protein peptide and so is not luminal. Thus, HIS28 being cytosolic is more similar to HPV E5, where HIS75/77 are present at the channel opening (Wetherill et al., 2012). It is plausible these histidines can also act as a pH sensor. Additionally, there is a second histidine in ZIKV M protein, however this lies further towards the N-terminus in the unstructured region, which is absent from our peptide and the model used for MD simulations in Chapter 3. Interestingly DENV-2 M protein contains an additional histidine residue to ZIKV M at residue 39, which when mutated results in loss of virus infectivity (Pryor et al., 2004). If DENV-2 M also forms channels, this would be located at the neck of the channel, between helix 1 and helix 2.

The data showing M protein channel activity increasing upon a reduction of pH, align with the published data showing ZIKV fusion during virus entry is likely to occur in late endosomes. Data shows ZIKV co-localises with both Rab5 of early endosomes and Rab7 of late endosomes, raising speculation that ZIKV is transported through the endocytic pathway and the late endosome pH is suitable for ZIKV RNA release (Li, M. et al., 2020; Owczarek et al., 2019). Additionally, ZIKV hemifusion is sensitive to pH and is greatest at a pH of 5.5-5 (Rawle et al., 2018). Furthermore, blocking endocytosis inhibits ZIKV infection in cell culture (Delvecchio et al., 2016; Li, M. et al., 2020).

Although ZIKV M channel activity has not been previously reported, DENV M channel activity has been measured. C-terminal peptides were reconstituted into voltage clamped suspended bilayers, and the conductance of sodium and potassium ions was measured. Additionally, this current was blocked by the adamantane compound, amantadine hydrochloride. Conversely, M proton channel activity has been disputed. Voltage clamping of *Xenopus laevis* oocytes producing DENV prM/M did not vary in proton conductance compared to non-expressing oocytes. Additionally, conductance did not vary with changes to the surrounding pH. However the form of DENV prM/M at the oocyte membrane was not validated (Premkumar et al., 2005; Wong et al., 2011).

The DENV M peptide used by Premkumar *et al.* was 40 amino acids in length, containing only helix 2 and 3 (Premkumar et al., 2005). By contrast, the ZIKV M peptide used in this chapter was 55 amino acids, ZIKV peptides retained helices 1, 2 and 3 as they are required for channel formation as discovered through M protein MD simulations (data not shown). Suggesting, unlike DENV M, ZIKV M protein channel formation and activity *in vitro* requires helix 1, possibly due to the presence of HIS28 on ZIKV M helix 1, whereas DENV contains an additional HIS39.

Viroporins are attractive targets for antiviral therapy and identifying M protein as a viroporin in the liposome-based assay highlights a new ZIKV antiviral target, which upon further development could be applied across the *Flaviviruses*. The TEM data IN section 4.2.2 and MD results from Chapter 3 highlight that the model of a hexameric M protein channel, support that future structural studies might be feasible.

We tested rimantadine against M protein, a licenced IAV M2 inhibitor and known inhibitor of other viroporins (Griffin, S. et al., 2008; Wetherill et al., 2012; Hay et al., 1985), a strategy used to identify druggable sites, followed by further development to identify suitable compounds. Previously, rimantadine has shown viroporin inhibitory activity in the liposome-based assay and in virus culture, however not previously with ZIKV.

Rimantadine had a dose dependent effect (Figure 4.8 and Figure 4.9), and was inhibitory at very low concentrations, suggestive of binding specificity. However, at high concentrations, rimantadine caused artefactual increases in the release

of CF from liposomes when added alongside protein. This phenomenon has been observed previously with other compounds for other viroporins, including HMA when tested with M2 (SG, personal communication). The effect on CF release is not seen in the absence of protein, meaning that it is likely due to a drug-induced effect upon how M interacts with the membrane.

Inhibition of M using rimantadine results also translated into cell culture as seen in figure 4.5, the dose-dependent effect was seen between 5 and 80 μM , however not taken above this dose due to the cytotoxicity observed in Figure 4.13. However, DENV-2 growth in peripheral blood leukocytes was entirely suppressed when incubated in 116 μM rimantadine (Koff et al., 1981). Similar cytotoxicity effects of rimantadine have been observed. A ~5 % reduction of live cells at 80 μM and cytotoxic effects seen at concentrations over 40 μM in Madin-Darby Canine Kidney (MDCK) cells from two sources (Govorkova et al., 2004; Scott et al., 2020).

Rimantadine time of addition assays show the most pronounced effect on ZIKV inhibition to be prior to and during virus inoculation indicating rimantadine is likely to be inhibiting ZIKV replication via disruption of virus entry. However, there is little effect of rimantadine addition during and post inoculation and post inoculation. Addition of rimantadine after the inoculation period is likely to be less effective as the virus has already entered the cells and the first round of infection has started, furthermore the presence of rimantadine prior to and during infection allows rimantadine to be present in endosomes prior to cell entry, whereas addition of rimantadine solely during infection does not allow for this build-up of rimantadine within the cell prior to virus entry, and rimantadine does not appear to have an effect on virus post-entry steps.

Considering the successful inhibition of ZIKV infection by rimantadine in cell culture we took to replicate the results in a murine mouse model *in vivo*. As described previously (section 4.6) the ZIKV rimantadine *in vivo* experiment involved treating mice subcutaneously with rimantadine 20 mg/kg 30 min prior to ZIKV infection and 5 hr post infection. This treatment plan was chosen due to prior literature searching as described above totalling 40 mg/kg in the 24 hr experiment. However, to prevent ZIKV infection being cleared by mice we used transient treatment with an anti IFNAR1 blocking antibody (Grant et al., 2016).

Additionally, to enhance the viral infection the site of injection was also subjected to up to five mosquito bites (Pingen et al., 2016). After 24 hr post infection, titres of ZIKV in the serum of rimantadine treated mice were dramatically lower than those in the untreated mice, however due to time limitations this was carried out only once and exhibited low plaque counts.

Rimantadine use in murine mouse models has been well documented via the treatment of IAV. For example, during a transmission study, rimantadine was given to infected mice 40-60 mg/kg/day. Uninfected mice were then placed in the same cage as rimantadine treated or untreated mice. It was observed fewer infected mice became infected when kept alongside treated mice (Schulman, 1968). Additionally, more recent drug combination studies have been carried out with up to 30 and 80 mg/kg rimantadine per day in mice (Simeonova et al., 2012; Bantia et al., 2010). Moreover, mice have been given 40 mg/kg by IP and PO and did not mention issues with the health or symptoms of treated mice (Hoffman et al., 1988; Herrmann et al., 1989). Our *in vivo* dosing regime was based on the treatments used in these studies.

Furthermore, a clinical trial in 1981 tested healthy adults for symptoms after giving rimantadine or amantadine for 4.5 days and either 200 or 300 mg/day. Patients in the 300 mg/day group were given 200 mg in the morning and 100 mg in the afternoon. At lower concentrations both drugs were well tolerated. At higher concentrations a greater percentage of patients treated with amantadine complained of central nervous system symptoms including nervousness, lightheaded, insomnia and fatigue. This gave way to preferential treatment with rimantadine (Hayden et al., 1981), however treatment with 300 mg/day equates to 5 mg/kg for a 60 kg human. Many previous experiments have used much higher concentrations of rimantadine in mice up to around 40 mg/kg. Rimantadine was used at 20 mg/kg in the ZIKV *in vivo* assay described in section 4.6, thus at a much higher translated concentration in humans than in the aforementioned trials. Therefore, providing a rationale to find an improved drug to be used at a suitable concentration.

This novel function of ZIKV M as an ion channel active during virus entry could reveal the mechanism behind virus uncoating, not only for ZIKV but also translated across the *Flavivirus* genus. Interestingly we have shown

commonality between previously identified viroporins and ZIKV M, including pH sensing, reminiscent ring conformations and inhibition by prototypic inhibitors. Furthermore, we have identified a novel ZIKV drug target, for future drug development.

Chapter 5 Rational development of improved inhibitors targeting M protein channel activity

5.1 Introduction

Currently, there are no licensed ZIKV vaccines available for prevention or treatment of infection. There are a number of vaccines in phase I and II clinical trials (Dowd et al., 2016; Larocca et al., 2016; Abbink et al., 2016; Xu, K. et al., 2018; Richner et al., 2017; Pardi et al., 2017; Brault, A.C. et al., 2017). However, there are challenges to overcome, including antibody-dependent enhancement of DENV and ZIKV due to their similarity and resultant cross-reactivity of non-neutralising antisera (Bardina et al., 2017; Stettler et al., 2016; Fowler et al., 2018; George et al., 2017). Additionally, there are no currently available antivirals targeting ZIKV, or other related *Flaviviruses*, despite extensive *de novo* design and efforts to repurpose candidates from drug libraries against both viral and cellular targets. However, targeting ZIKV M protein has not previously been investigated (Devillers, 2018; Han and Mesplede, 2018). The identification of a ZIKV targeting therapeutic would be highly valuable in reducing disease severity, particularly neurological effects such as microcephaly and Guillian-Barré syndrome.

A number of viral proteins comprise ideal enzymatic drug targets, primarily the ZIKV NS5 polymerase. Nucleoside analogue drugs selectively target viral polymerases to prevent genome replication, usually via their misincorporation and ensuing termination of nascent nucleotide chains. They are also highly specific for viral RdRp compared with cellular RNA polymerases (Eyer et al., 2016; Lu et al., 2017; Hercik et al., 2017). Several ZIKV polymerase inhibitor compounds have been identified in preclinical studies, including a nucleoside analogue BCX4430 (aka Galidesivir, Biocryst), and the nucleotide analogue prodrug, Sofosbuvir (Gilead), which is approved by the U.S Food and Drug Administration (FDA), Medicines and Health products Regulatory Agency (MHRA) and European Medicines Agency (EMA) for treatment of HCV infection (Eyer et al., 2016; Hercik et al., 2017; Zmurko et al., 2016; Julander et al., 2017; Bullard-Feibelman et al., 2017). BCX4430 (Galidesivir, BioCryst Pharma) is currently in Phase I clinical trials (NCT03800173). Other viral proteins exhibiting methyltransferase (NS5), protease (NS2B-NS3) and helicase (NS3) activity are

also being explored as potential drug targets (Coutard et al., 2017; Lee, H. et al., 2017; Cao et al., 2016). An ideal therapy would involve targeting a combination of these proteins, mitigating the emergence of resistance mutations.

The newly identified viroporin activity exhibited by the M protein in chapters 3 & 4 presents an opportunity for the development of new ZIKV and *Flavivirus* therapeutics.

Viroporin inhibitors have been used previously to treat virus infected patients, with the first approved in the 1960's. The adamantane compounds amantadine, and later rimantadine, were used to treat IAV (Davies et al., 1964; Dawkins et al., 1968; Togo et al., 1968; Wingfield et al., 1969; Sabin, 1967), although it was many years later that their mode of action targeting the M2 viroporin was discovered; adamantane mediated prevention of M2 proton conductance inhibits viral uncoating during entry (Hay et al., 1985; Pinto et al., 1992; Sugrue and Hay, 1991). Adamantanes have since displayed genotype-specific inhibitory effects against the HCV viroporin, p7 (StGelais et al., 2009; Griffin, S. et al., 2008) and combination therapy comprising amantadine, ribavirin and interferon has been tested using small treatment groups as a HCV combination therapy in clinical trials and a slight increase in efficacy was observed. Genotype 1a patients saw the most promising results, however genotype 1b patients exhibited L20F mutations, which locate to the peripheral adamantane binding site and have been shown experimentally to represent genuine resistance polymorphisms (Berg et al., 2003; Brillanti et al., 2000; Foster et al., 2014; Foster et al., 2011; Mihm et al., 2006; Castelain et al., 2007).

Viroporins have also been targeted using amiloride derivatives (e.g. hexamethylene amiloride (HMA) and BIT225). Previously HMA was used as a HIV therapeutic (Karlsson et al. 1993; Ewart et al. 2004) due to targeting viroporin vpu (Ewart et al. 2002). Similarly to adamantanes, HMA can also block other viroporins including HCV p7 *in vitro* (Premkumar et al. 2004) and in a pH monitoring cell-based assay (Wozniak et al. 2010). Furthermore, HMA also inhibits viroporins encoded by the E proteins of human coronavirus 229 (HCoV-229), Severe acute respiratory syndrome 1 (SARS1) and mouse hepatitis virus (MHV) (Pervushin et al., 2009; Wilson et al., 2006). However, HMA is relatively

toxic, leading to a need for derivative development (Steinmann et al., 2007b; Chang et al., 2009). The inhibition of M2 by HMA was studied, however its inhibition was improved upon by the production of novel HMA derivatives, in addition to improved cytotoxicity (Jalily et al., 2016). Compound BIT225 reportedly also has inhibitory activity against HCV p7 and specifically HIV-1 in monocyte-derived macrophages. The latter has led to phase II clinical trials within South East Asia, predominantly, comparing combination therapy of naïve HIV-1 patients with antiretrovirals and BIT225 or a placebo. The trials report a statistically significant benefit to patients CD8+ and activated CD4 T cell populations (Wilkinson et al., 2016).

The effectiveness of antivirals targeting RNA viruses as monotherapies is limited. RNA viruses evolve quickly and administering viroporin inhibitors as a monotherapy potentially will become clinically unsuitable due to the selection of resistance mutations (Foster et al., 2011; Griffin, S.D., 2009). M2 and p7 gained resistance mutations to adamantane compounds, which were located to predicted binding sites (Pabbaraju et al., 2008; Castelain et al., 2007; Mihm et al., 2006; StGelais et al., 2009). However, the emergence of resistance of IAV M2 to amantadine was suppressed when given alongside neuraminidase-targeting antiviral Oseltamivir (Ilyushina et al., 2006). Therefore, it remains important that the number of drug targets is expanded as even drugs with relatively low genetic barriers to resistance might have potential within combination therapies, and the lack of treatments to prevent or treat *Flavivirus* infection needs to be addressed.

The development of new viroporin inhibitors is hindered by the difficulty in determining their structure and working with membrane proteins in high-throughput systems. Therefore, our programme of drug development employed a rational approach involving structural information, *in silico* molecular models and compound docking software (Foster et al., 2014). This chapter describes our approach to discover compounds targeting using the *in silico* M protein hexamer model from chapter 1 as a structural template, and subsequent validation using the liposome-based dye-release channel activity assays used in chapter 2 and virus replication in cell culture.

5.2 M protein shows differential sensitivity to structurally distinct viroporin inhibitors

Rimantadine inhibits the activity of sensitive variants of the M2 and p7 viroporins (Wang, C. et al., 1993; Schnell and Chou, 2008; StGelais et al., 2007). Now, based upon our findings (section 4.4, 4.5 & 4.6), we can place ZIKV M as another rimantadine-sensitive member of the viroporin family.

Our previous work on viroporins has utilised rimantadine and other prototypic inhibitors to identify druggable sites upon channel complexes, which, in turn, are amenable to the development of more bespoke, and so more potent inhibitory series. Thus, we explored whether additional inhibitory compounds identified during previous viroporin studies could similarly block M protein channel activity.

Whilst the effects of rimantadine appeared specific, its promiscuity made it desirable to ensure that the liposome assay was capable of discriminating effective inhibitory compounds from those lacking activity targeting M. Thus, we capitalised upon the availability of distinct compound series targeting a well-characterised peripheral binding site upon the HCV p7 viroporin channel complex (Foster et al., 2014; Shaw et al., 2019).

The series contains rationally developed compounds, with a defined structure activity relationship (SAR) versus the peripheral site and dramatically improved drug-like qualities. Thus, we predicted that the structural differences between hexameric M and heptameric p7 channel complexes should result in distinct patterns of activity for such compounds when tested functionally against M peptides.

Small molecules designed to inhibit other viroporins were tested for inhibitory effects against M protein channels, these include 'JK' compounds. JK compounds are second generation compounds designed to target HCV p7 channels, composed of an oxindole core, an N-alkyl substituent and a benzyl group. JK3/32 was the most active compound against HCV p7 (Shaw et al., 2019), and is thought to target a peripheral p7 site. However, against ZIKV M JK3/34 and JK3/42 were the most effective. Although, these compounds were assayed in cell culture against p7, whereas they were tested against M in liposomes. In Figure 5.2 Rimantadine and JK3/42 significantly reduced channel

activity to 75% and 42 % respectively, however JK3/34 reduced activity to 51 %. Conversely, JK3/40 did not reduce channel activity in either assay.

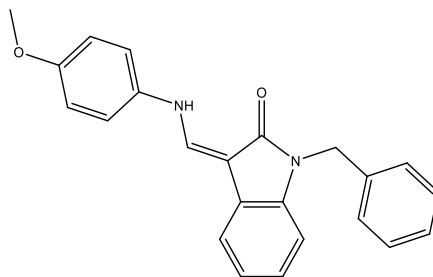


Figure 5.1 Representative JK compound chemical composition

JK3/32 shown representing the p7 second generation compounds containing an oxindole core, an N/alkyl substituent and a benzyl group.

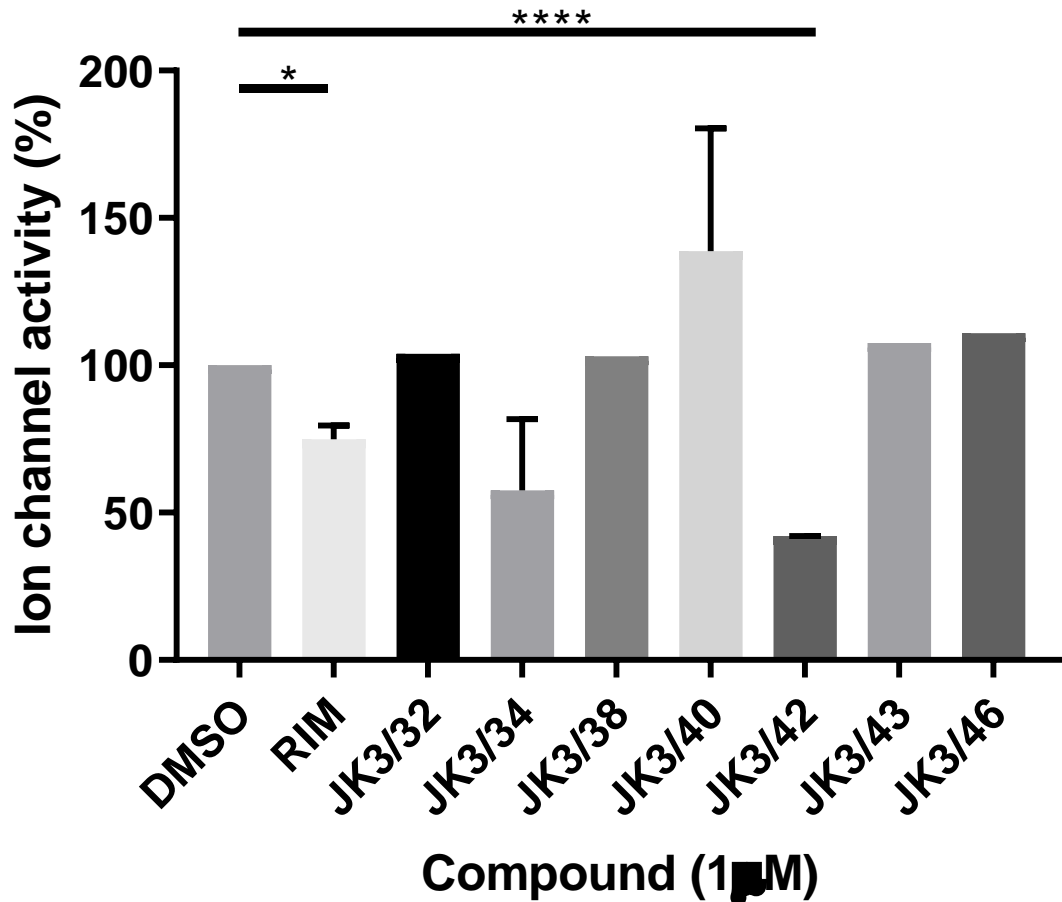


Figure 5.2 Inhibition of M protein channel activity by small molecules

The Liposome-based channel activity assay was used to determine the activity of compounds against M protein channels. A. Inhibition of M protein channels by second generation p7 inhibitors alongside Rimantadine. Rimantadine, JK3/34 and JK3/42 reduced activity to 75, 51 and 42 % respectively. Data shown, JK3/32, JK3/40, JK3/42, DMSO and Rimantadine n=2 biological repeats, JK3/38, JK3/42 and JK3/46 n=1 biological repeat. Error bars represent standard deviation of the mean. Statistical significance was determined using an unpaired t test, ****p value JK3/42 <0.0001, *p value rimantadine 0.0167

5.3 Identification of candidate drug binding sites and docking of adamantanes into M protein channel models *in silico*

Whilst no crystallographic, NMR or cryo-EM oligomeric M protein channel structure is available, the optimal *in silico* model generated and simulated in chapter 3 could comprise a surrogate template for the design and/or *in silico* screening of potential inhibitors, depending upon its accuracy. In this regard, previous studies utilising *de novo* models of both HCV p7 and HPV16 E5 channel complexes enabled the design of bespoke inhibitory compounds (Foster et al., 2011; Wetherill et al., 2012). Thus, the *in silico* hexameric 'helix 3 pore-lining rotated' model was scrutinised using Maestro software and SiteMap tool to identify potential drug binding sites (Halgren, 2009).

SiteMap provides two analyses of potential binding sites, SiteScore and Druggability (Dscore). Sites with a SiteScore of >0.8 are classed as a possible binding pocket, and those with a score >1.0 are identified as binding sites with particular importance. Druggability categorises sites as either very druggable >1.0, druggable 1.0-0.8, intermediate 0.8-0.7 and difficult <0.7.

The most favourable site, site L1 (GLU59, LYS60, VAL61, LEU64), was located within the channel lumen. This had a SiteScore of 1.111 and druggability score of 1.222, suggesting that this site had considerable potential for the development of novel ligands. Other drug binding sites (sites L2 and L3) identified within the lumen were less favourable according to prediction software, and were located towards the helix 1 neck of the lumen (site L2), and at the linker region between the TMDs at the opening of the pore (site L3) (Table 5.1).

Binding site	SiteMap	Druggability
L1	1.111	1.222
L2	0.875	0.944
L3	0.730	0.629

Table 5.1 SiteMap and druggability scores of Luminal binding sites

Rimantadine was predicted to bind most strongly to site L1. Rimantadine, docked into this site using Maestro software, was predicted to make hydrophobic interactions with VAL61, LEU64, VAL65 and LEU68 (Figure 5.4A).

However, unlike some docking packages, the SiteMap tool does not effectively identify binding sites that incur significant hydrophobic penalties for bound ligands, such as those upon the membrane-exposed surface of the M channel complex. Prior experience of other viroporin inhibitor binding sites (Foster et al., 2011) and the use of protein surface representation in visualisation software led us to select a peripheral cavity (P1) as an additional binding site of residues TYR63, LEU64, VAL65, MET66, ILE67 & LEU68 (Figure 5.3B).

Docking of rimantadine into the identified binding sites, accounting for hydrophobic penalties, found it preferentially docked into L1 site, which had the highest SiteMap and druggability scores. The adamantyl cage of rimantadine was shown to form the interactions with the cavity, as did amantadine (Figure 5.4B). Additionally, derivatives of rimantadine (N-methyl rimantadine and N-acetyl rimantadine) bound to the same luminal site. However, these compounds posed in the opposite direction with their adamantane cages facing the lumen, seen in Figure 5.4B, C, D and E, this could be due to less hydrophobic R-groups.

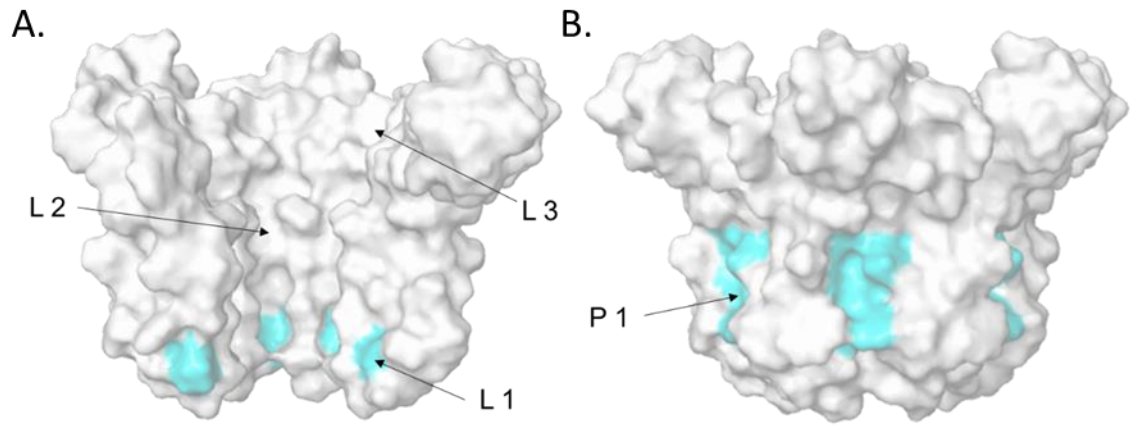


Figure 5.3 Identified drug binding sites on *in silico* M protein hexameric model

Surface representation of M protein model in white with the chosen drug binding sites highlighted in blue, and other binding sites identified. A. Identified luminal binding cavities 1, 2 and 3 (Table 5.1), two protomers hidden for representation and favoured luminal site 1 highlighted in blue. B. Peripheral drug binding site 1 highlighted in blue.

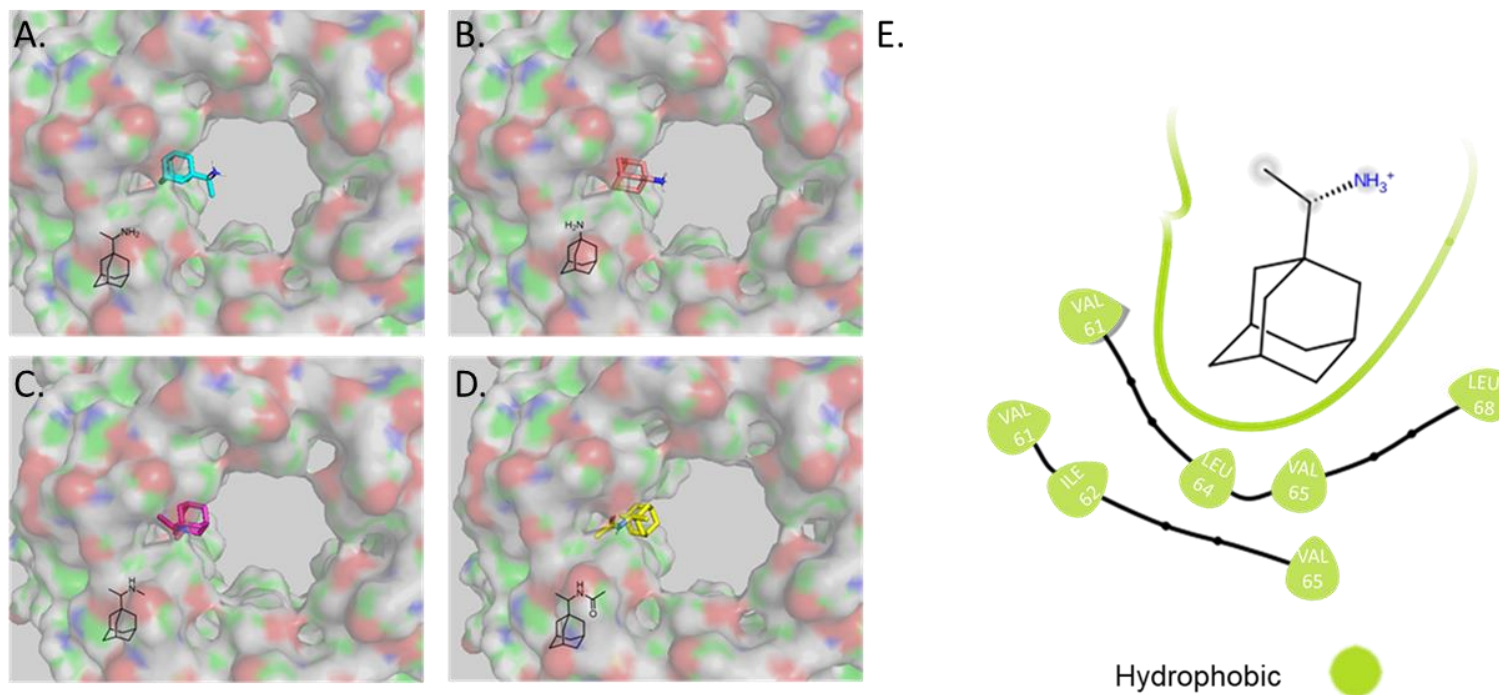


Figure 5.4 Docking of adamantane compounds into the luminal 1 site of optimal hexameric M protein *in silico* model

Adamantane compounds docked into luminal (L) 1 site of the optimal *in silico* model, protein displayed top-down with the linker region facing up. A. Rimantadine docked with adamantane cage interacting with the luminal cavity. B. Amantadine docked into model displayed top-down, with adamantane cage interacting with the luminal cavity. C. methyl-rimantadine docked into model displayed top-down, with methyl group interacting with the luminal cavity. D. acetyl-rimantadine docked into model displayed top-down, with methyl group interacting with the luminal cavity. E. Visualisation of interactions between protein and compound with Rimantadine docked.

images kindly done by DR Ravi Singh.

5.4 Identification and HTS targeting of peripheral and luminal binding sites

Identification of potential drug binding sites on ZIKV M protein led to screening of the structurally distinct targets with possible novel inhibitors. As rimantadine was not amenable to modification (Figure 5.4), and the previously screened JK compounds series didn't prove promising (Figure 5.2), compounds identified in section 5.3 were screened *in silico* by Dr Ravi Singh.

A TOCRIS drug-repurposing library was screened against L1 and P1 binding sites on the M protein *in silico* model. Of the 1280 compounds in the library the top ~50 docked compounds were picked to be assayed using the liposome-based channel activity assay. These compounds were ranked using Glide by docking score and GlideScore. In the selection of the top 50 compounds per binding site, those common to both lists were eliminated, followed by a process of attrition to identify the compounds with the best molecular fit, through analysis of binding energies. Additionally, the lowest scoring compound of the *in silico* screening was selected as a negative control for each binding site. All the selected compounds are listed in Table 5.2 and Table 5.3

5.4.1 Screening *in silico* selected compounds using dye release assays

The top 50 compounds ranked by docking score for both drug binding sites, were tested using the liposome-based channel activity assay (section 2.6.3 & 4.3). Compounds reconstituted in DMSO were assayed at 1 μ M against M peptide alongside the positive control rimantadine, and negative control DMSO.

"Rank"	Compound Name	Tocris ID	glide gscore	Description
N1	Mifepristone	1479	0.286	antiprogesterogenic steroid
N2	NAB 2	5131	0.603	Anti α -synuclein toxicity
1	FR 139317	1210	-10.227	ET _A antagonist
2	ZCL 278	4794	-9.294	Cdc42 inhibitor
3	Elinogrel	5316	-8.829	P2Y ₁₂ antagonist
4	Taxol	1097	-8.711	Promotes microtubules
5	UK 356618	4187	-8.401	MMP-3 inhibitor
7	TC-1 15	4527	-8.216	α 2 β 1 inhibitor
8	AS 2034178	5035	-8.032	FFA1 (GPR40) agonist
9	CP 775146	4190	-7.963	PPAR α agonist
10	GW 6471	4618	-9.092	PPAR α antagonist
11	Pravastatin sodium salt	2318	-7.825	HMG-CoA reductase inhibitor
12	Fluvastatin sodium	3309	-7.717	HMG-CoA reductase inhibitor
13	TC NTR1 17	5087	-7.683	NTS1 partial agonist
14	VER 155008	3803	-7.686	Hsp70 inhibitor
15	AMG PERK 44	5517	-7.618	PERK inhibitor
16	Glibenclamide	0911	-7.537	K _{ATP} channel blocker
17	Argatroban	1637	-7.454	Thrombin inhibitor
18	KB SRC 4	4660	-7.444	c-Src inhibitor
19	GBR 12909 dihydrochloride	0421	-7.965	DA uptake inhibitor
20	(\pm)-NBI 74330	4528	-7.366	CXCR3 antagonist
21	CU CPT 4a	4883	-7.331	TLR3 inhibitor
22	A 887826	4249	-7.315	voltage-dependent NaV1.8 channel blocker
23	SR 2640 hydrochloride	1804	-7.296	LTD ₄ /LTE ₄ receptor antagonist
24	NSC 74859	4655	-7.258	STAT3 inhibitor
25	RWJ 67657	2999	-7.217	p38 α and p38 β inhibitor
26	Lu AA 47070	4783	-7.659	adenosine A2A receptor antagonist
27	Edaglitazone	4784	-7.176	PPAR γ agonist; antidiabetic
29	GSK 1562590 hydrochloride	5110	-7.11	urotensin II (UT) receptor antagonist
30	Flurizan	4495	-7.098	γ -secretase inhibitor
31	GW 9508	2649	-7.096	FFA1 (GPR40) agonist
32	GSK 269962	4009	-7.051	ROCK inhibitor
33	AC 5216	5281	-6.986	TSPO ligand
34	DBZ	4489	-6.973	γ -secretase inhibitor
35	PF 04418948	4818	-6.957	EP ₂ receptor antagonist
36	GSK 2837808A	5189	-6.942	LDHA inhibitor
37	Sal 003	3657	-6.935	Inhibitor of eIF2 α
38	PD 173212	3552	-7.029	Ca _v 2.2 blocker
39	NTRC 824	5438	-9.012	NTS ₂ antagonist
40	ONO AE3 208	3565	-6.889	EP4 antagonist
41	RS 17053 hydrochloride	0985	-6.88	α _{1A} antagonist
42	Pitavastatin calcium	4942	-6.864	HMG-CoA reductase inhibitor
43	L-161,982	2514	-6.858	EP ₄ receptor antagonist
44	AMN 082 dihydrochloride	2385	-6.871	mGlu7 agonist
45	TC-N 1752	4435	-6.815	Na _v channel blocker
46	PF 431396	4278	-6.799	Dual FAK/PYK2 inhibitor
47	GNF 5837	4559	-6.754	Trk inhibitor
48	KS 176	4169	-6.731	BCRP inhibitor
49	Sarpogrelate hydrochloride	3739	-6.769	5-HT _{2A} antagonist
50	GKA 50	5133	-6.689	Glucokinase activator

Table 5.2 top 50 Luminal *in silico* HTS compounds

The top 50 compounds selected for the luminal binding site are listed. As identified by glide. The two compounds identified as the least likely inhibitors by the *in silico* screen were selected as the two negative compounds, named N1 and N2. The compounds are ranked according to docking score, the displayed glide score is the approximate ligand binding free energy. Channel activity colour coding: <30 % green, >30 % <70 % yellow, >70 % red.

"Rank"	Compound	Tocris ID	glide gscore	Description
N2	AMG 548	3920	0.471	p38 α inhibitor
1	RWJ 21757	2719	-6.475	TLR7 agonist
2	Ferrostatin 1	5180	-6.309	inhibitor of erastin induced ferroptosis
3	AA 29504	3972	-6.31	Positive allosteric modulator of GABA _A receptors
4	L-732,138	0868	-6.167	NK1 antagonist
5	API-2	2151	-6.158	Inhibitor of Akt/PKB signaling
6	5-BDBD	3579	-6.13	P2X ₄ antagonist
7	LY 225910	1018	-6.082	CCK ₂ antagonist
8	Formoterol hemifumarate	1448	-6.065	β_2 agonist
9	TC-S 7006	5240	-5.979	Tpl2 inhibitor
10	TCS 2210	3877	-6.005	Inducer of neuronal differentiation in MSCs
11	Sumatriptan succinate	3586	-5.952	5-HT _{1A} , 5-HT _{1B} and 5-HT _{1D} agonist
12	MRS 3777 hemioxalate	2403	-6.964	A ₃ antagonist
13	Thiamet G	4390	-6.079	O-GlcNAcase inhibitor
14	Abacavir hemisulfate	4148	-5.894	Reverse transcriptase inhibitor
15	DDR1-IN-1	5077	-5.99	DDR1 inhibitor
16	Fexofenadine hydrochloride	2429	-5.859	H ₁ receptor antagonist
17	6-Chloromelatonin	0443	-5.844	Melatonin agonist
18	GSK 0660	3433	-5.864	PPAR δ antagonist
19	PCA 4248	0571	-5.783	PAF receptor antagonist
20	Axitinib	4350	-5.765	VEGFR-1, -2 and -3 inhibitor
21	DSR 6434	4809	-5.971	TLR7 agonist
22	Necrostatin-1	2324	-5.756	RIP1 kinase inhibitor
23	Trifluorothymidine	4460	-5.838	Thymidylate synthetase inhibitor
24	Cilnidipine	2629	-5.729	Dual Cav1.x and Cav2.x blocker
25	Efonidipine hydrochloride monoethanolate	3733	-5.693	Cav1.x and Cav3.x blocker
26	ITE	1803	-5.69	Endogenous agonist for the transcription factor aryl hydrocarbon receptor
27	L-165,041	1856	-5.689	PPAR δ agonist
28	EB 47	4140	-6.033	PARP-1 inhibitor
29	GSK 2830371	5140	-5.657	allosteric inhibitor of Wip1 phosphatase
30	AZD 1480	5617	-5.738	JAK2 inhibitor
32	Amlodipine besylate	2571	-5.638	Cav1.x blocker
33	Melatonin	3550	-5.628	agonist at MT ₁ and MT ₂
34	Fludarabine	3495	-5.626	Purine analog
35	PF 06447475	5716	-5.609	LRRK2 inhibitor
36	SU 6668	3335	-5.608	PDGFR, VEGFR and FGFR inhibitor
37	AZD 5438	3968	-5.836	Cdk inhibitor
38	SU 11274	4101	-6.145	Inhibitor of MET tyrosine kinase activity
39	FPL 64176	1403	-5.543	Cav1.x activator
40	Sunitinib malate	3768	-5.543	VEGFR, PDGFR β and KIT inhibitor
41	YK 4-279	4067	-5.535	RNA helicase inhibitor
42	Ralfinamide mesylate	4029	-5.678	Na ⁺ channel blocker
43	ML 298 hydrochloride	4895	-5.504	PLD2 inhibitor
44	FH 1	5254	-5.485	Enhances iPSC-derived hepatocyte differentiation and maturation

45	PLX 647 dihydrochloride	5102	-6.23	dual Fms/KIT inhibitor
46	GPI 688	3967	-5.438	Allosteric glycogen phosphorylase inhibitor
47	CP 94253 hydrochloride	1317	-5.441	5-HT _{1B} agonist
48	CGP 57380	2731	-5.44	Mnk1 inhibitor
49	BW 723C86 hydrochloride	1059	-5.433	5-HT _{2B} agonist
50	LY 364947	2718	-5.84	TGF- β RI inhibitor

Table 5.3 Peripheral HTS *in silico* top 50 compounds

The top 50 compounds selected for the peripheral P1 binding site are listed. As identified by glide. The two compounds identified as the least likely inhibitors by the *in silico* screen were selected as the two negative compounds, named N1 and N2. The compounds are ranked according to docking score, the displayed glide score is the approximate ligand binding free energy. : <50 % green, >50 % <70 % yellow, >70 % red.

5.4.1.1 Screening of compounds docked to the luminal binding site

The top 50 compounds predicted to bind *in silico* to the M protein luminal cavity, as ranked by glidescore, are listed in Table 5.2. The activity of these compounds was first assessed using the liposome-based channel activity assay (Figure 5.4) (section 2.6.3 & 4.1).

Of the 50 compounds, several increased the fluorescence release from liposomes containing M protein, potentially fluorescing, activating the channels or disrupting liposome membranes similar to high concentrations of rimantadine (Figure 4.9). These included: GBR 12909, a dopamine reuptake inhibitor; KS 176 a Breast Cancer Resistance Protein inhibitor; PF 04418948, a prostaglandin E₂ receptor antagonist; and PF 431396, a focal adhesion kinase and proline-rich tyrosine kinase 2 inhibitor. However, most compounds reduced the fluorescence released from liposomes and 26 % of compounds reduced fluorescence by over 50 %, presumably through inhibiting M protein channels. The most active of these compounds included (±)-NBI 74330 a CCRX3 antagonist (Piotrowska et al., 2018), GNF 5837 a Trk inhibitor (Albaugh et al., 2012) and GSK2837808A a lactate dehydrogenase A (LDHA) inhibitor (Thongon et al., 2018). A cut-off of 50 % channel activity was used to choose compounds to be tested in cell culture. Of the 13 compounds below this cut off, which all improved upon rimantadine by over 25% channel activity inhibition, three were taken forward: GNF 5837, GSK2837808A and KB SRC 4. These compounds were selected from others below the cut-off based on their rapid commercial availability. However, in Figure 5.5 the negative control compounds Mifepristone and NAB 2 also reduced channel activity by over 50%, showing the docking process is not flawless, and only refines a list of compounds into those most likely to bind into identified sites.

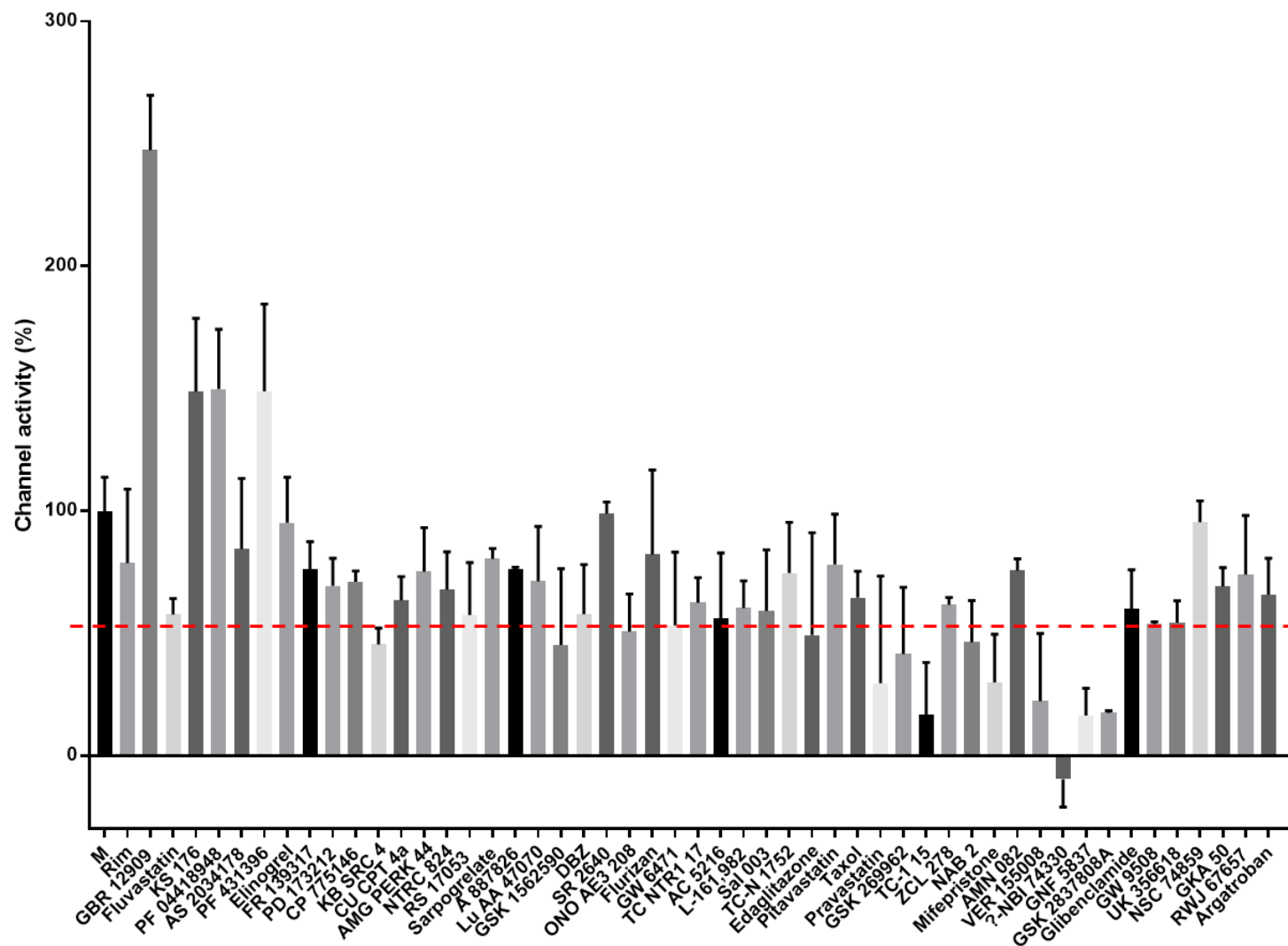


Figure 5.5 Inhibition of M peptide channels by lumen-targeting compounds using liposome-based channel activity assay

Compounds identified by *in silico* docking to the L1 site were used in the liposome-based channel activity assay at 1 μ M alongside M protein at 390 nM. Released fluorescence of M was normalised to 100 % and the inhibitory effects of compounds were compared. Assay cut off shown in red at 50%. N=3 biological repeats.

5.4.1.2 Screening of compounds docked to the peripheral binding site

The top 50 ranked compounds docked into the M protein membrane-facing peripheral cavity are listed in Table 5.3. Screening of these 50 compounds against M by the *in vitro* liposome-based channel activity assay (Figure 5.5) (section 2.6.3) similarly showed some compounds at 1 μ M increased fluorescence similarly to the effects of high rimantadine concentrations. These included: abacavir, a nucleoside analogue reverse-transcriptase inhibitor; ferrostatin 1, an inhibitor of non-apoptotic cell death; and ralfinamide mesylate, a sodium channel blocker. However, a variety of compounds also reduced fluorescence release, although not to the same extent as a proportion of the luminal compounds. The compounds which reduced levels of CF released included formoterol hemifumarate, a β 2-adrenoceptor agonist licensed for treatment of chronic asthma and Chronic obstructive pulmonary disease (Descalzi et al., 2008), AA 29504 an allosteric modulator of GABAA receptors (Hoestgaard-Jensen et al., 2010) and L 732,138, a tachykinin NK1 receptor antagonist (Munoz et al., 2010). A cut-off of 55% channel activity was used to choose compounds to be tested in cell culture and the negative control AMG 548 resulted in a channel activity of almost 100%. Of the 6 compounds below this cut off 3 were taken forward: AA 29504, Formoterol hemifumarate, L-732 138. These compounds were selected from others below the cut-off based on their commercial availability.

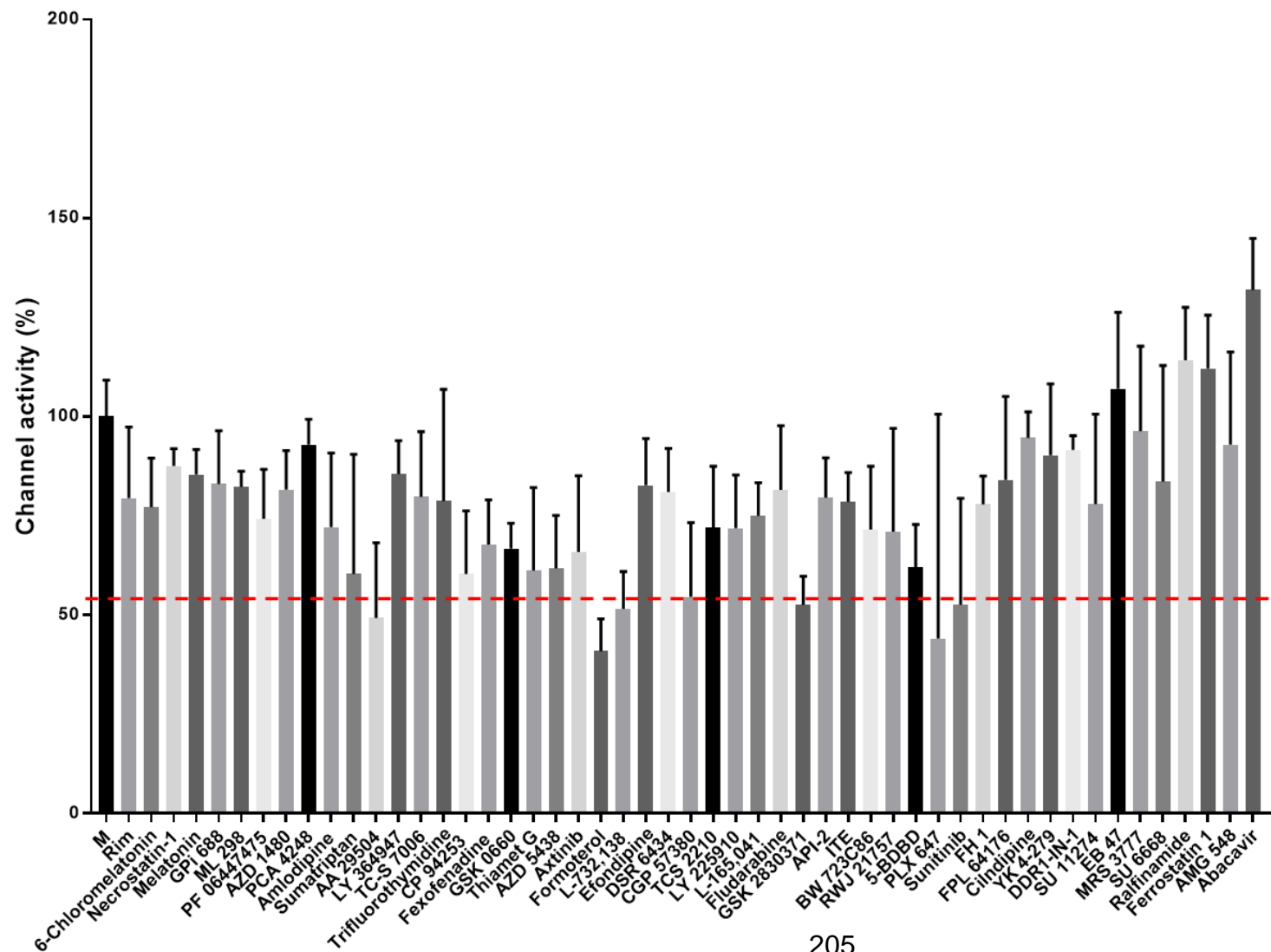


Figure 5.6 Inhibition of M peptide channels by peripherally targeting compounds using liposome-based channel activity assay

Compounds identified by *in silico* docking to P1 site were used in the liposome based channel activity assay at 1 μ M alongside M protein at 390 nM. Released fluorescence of M was normalised to 100 % and the inhibitory effects of compounds were compared. Assay cut off shown in red at 55%. N=3 biological repeats.

5.4.2 *In silico* docking of generic hits into ZIKV M viroporin model

Three of the top hits from each of the binding sites were chosen for further testing. In Figure 5.7 and Figure 5.8 the structures of these compounds and the orientation in which they are predicted to bind to the cavities of M protein *in silico* structure are presented. In Figure 5.9 and Figure 5.10 the interactions the compounds are predicted to make with the M protein hexamer are shown, carried out by Dr Ravi Singh.

All compounds are shown to make at least one hydrogen bond with M protein, shown by a pink line. Luminal compounds are predicted to form a hydrogen bond with THR57 on either one or two monomers per interacting compound. Peripheral compounds are predicted to form a hydrogen bond with TYR63 in addition to ALA43 for formoterol. Furthermore, aromatic rings of L 732, 138 and AA 29504 interact through a non-covalent interaction with the aromatic ring of TRP51 and TYR63 respectively forming π - π stacking interactions shown in by green lines. The conservation of these binding site-defined residues varies; ALA43 is highly conserved throughout the *Flavivirus* genus (Figure 3.1), whilst TRP51 and TYR63 are partially conserved, found in WNV, and WNV/DENV4 respectively. However, DENV2 and DENV4 retain residues with similar aromatic properties. Conversely, THR57 is not conserved across closely related viruses. As for ALA43, TRP51 and TYR63 are more highly conserved the peripheral site may be a more robust binding site, reducing the risk of resistance mutations.

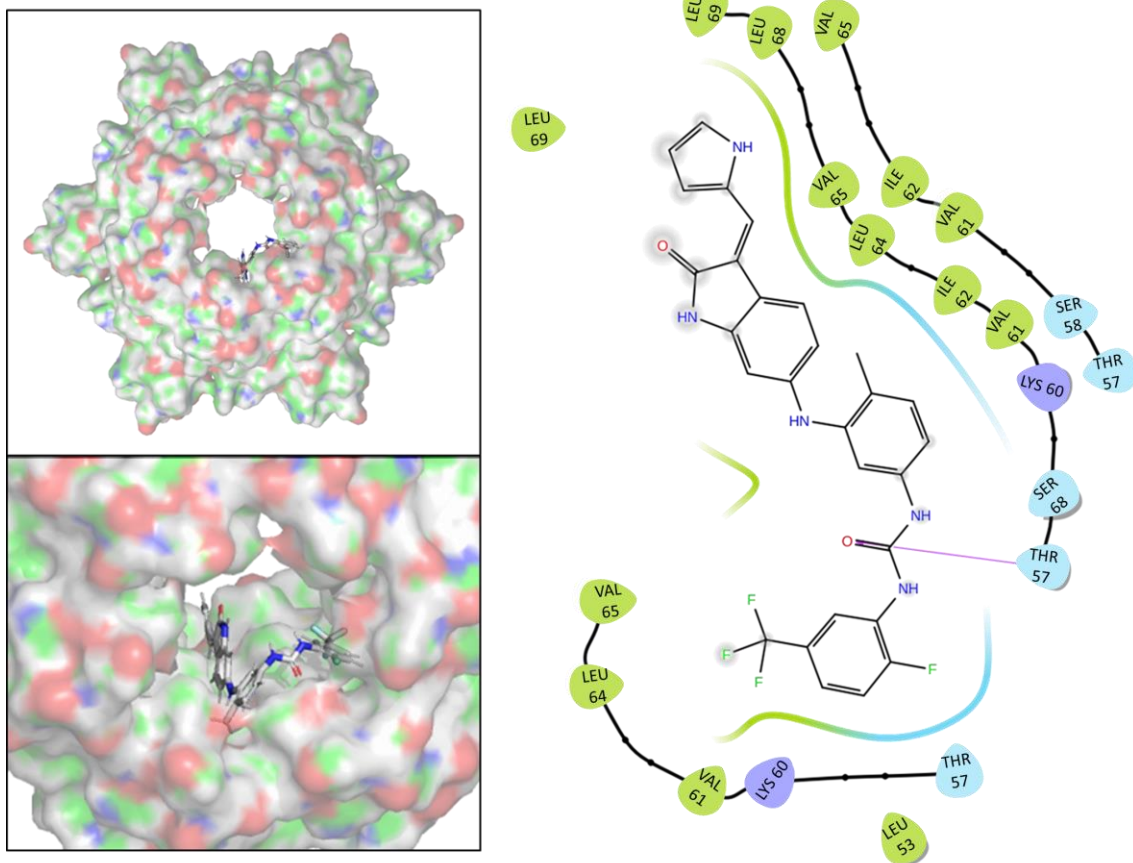


Figure 5.7 GNF 5837 and M protein predicted interaction data

A. Surface plot of M protein hexamer *in silico* model with the GNF 5837 shown docked into the lumenal cavity, represented as sticks in white, orientated towards the linker region. B. Predicted interactions between GNF 5837 and M protein lumenal cavity in Maestro software. Hydrophobic residues highlighted in green, positively charge residues in dark blue, polar residues in light blue and hydrogen bonds shown as pink lines. Maestro image kindly generated by Dr Ravi Singh.

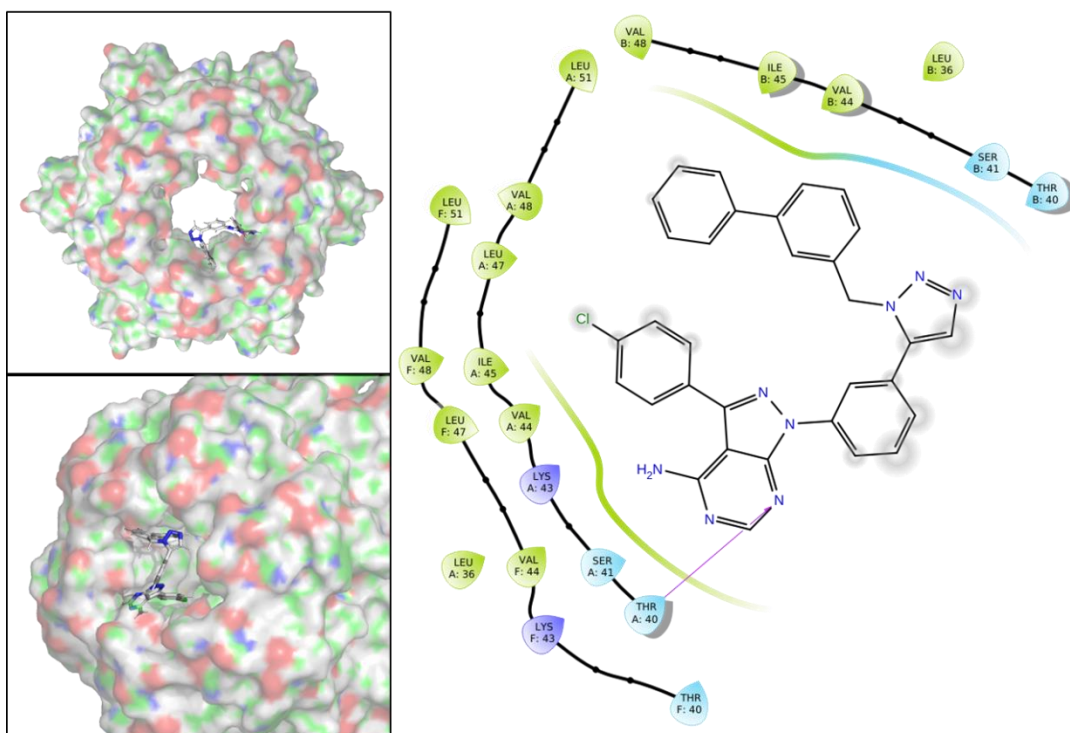


Figure 5.9 KB SRC 4 and M protein predicted interaction data

A. Surface plot of M protein hexamer *in silico* model with the KB SRC 4 shown docked into the lumenal cavity represented as sticks in white, orientated towards the linker region. B. Predicted interactions between KB SRC 4 and M protein lumenal cavity in Maestro software. Hydrophobic residues highlighted in green, positively charge residues in dark blue, polar residues in light blue and hydrogen bonds shown as pink lines. Maestro image kindly generated by Dr Ravi Singh.

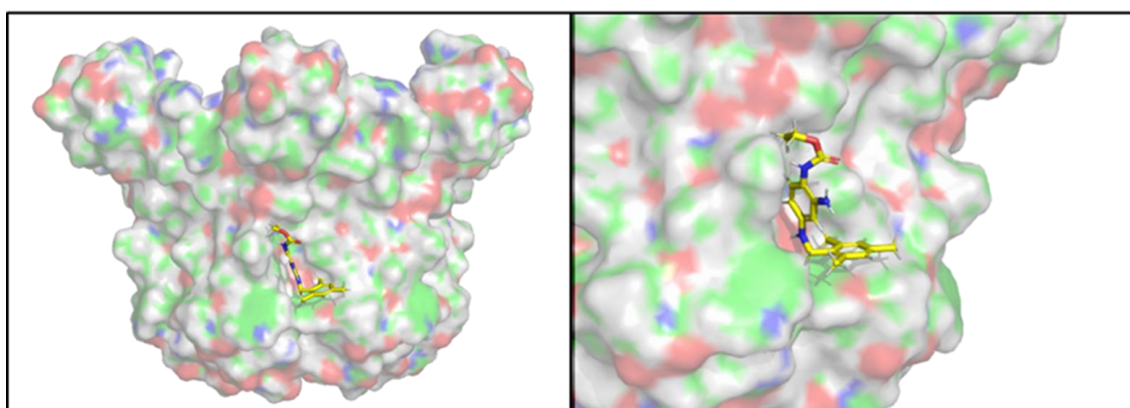
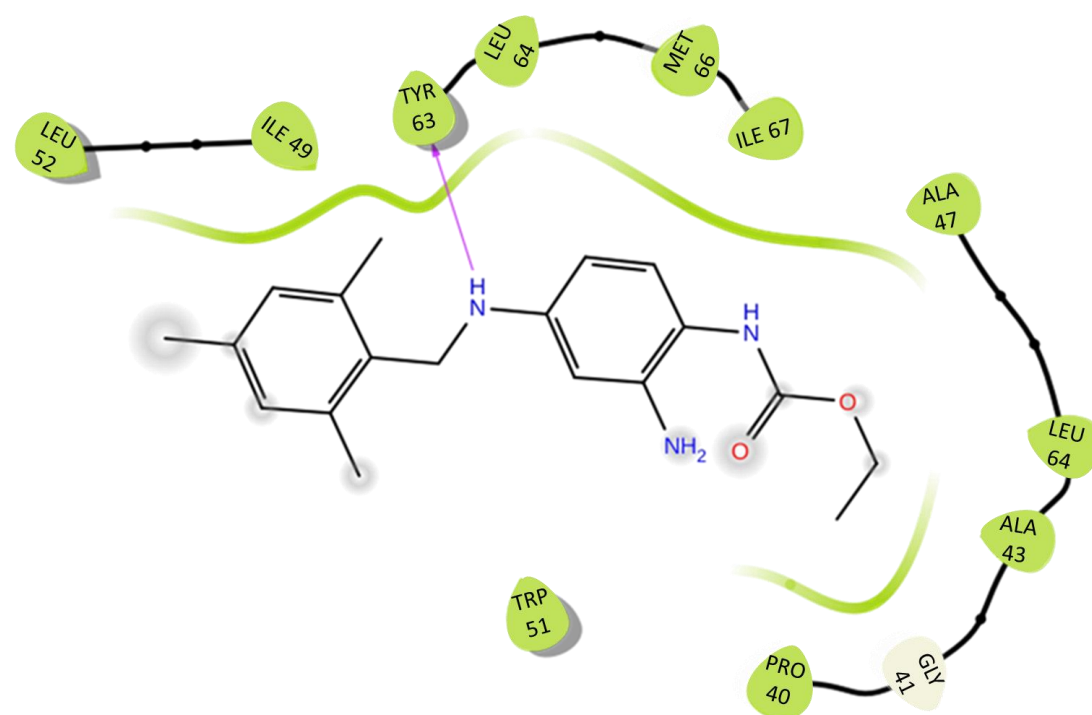


Figure 5.10 AA 29504 and M protein predicted interaction data

A. Surface plot of M protein hexamer *in silico* model with the AA 29504 shown docked into the peripheral cavity represented as sticks in yellow, orientated towards the linker region. B. Predicted interactions between AA 29504 and M protein peripheral cavity in Maestro software. Hydrophobic residues highlighted in green, glycine highlighted in white and hydrogen bonds shown as pink lines. Maestro image kindly generated by Dr Ravi Singh.

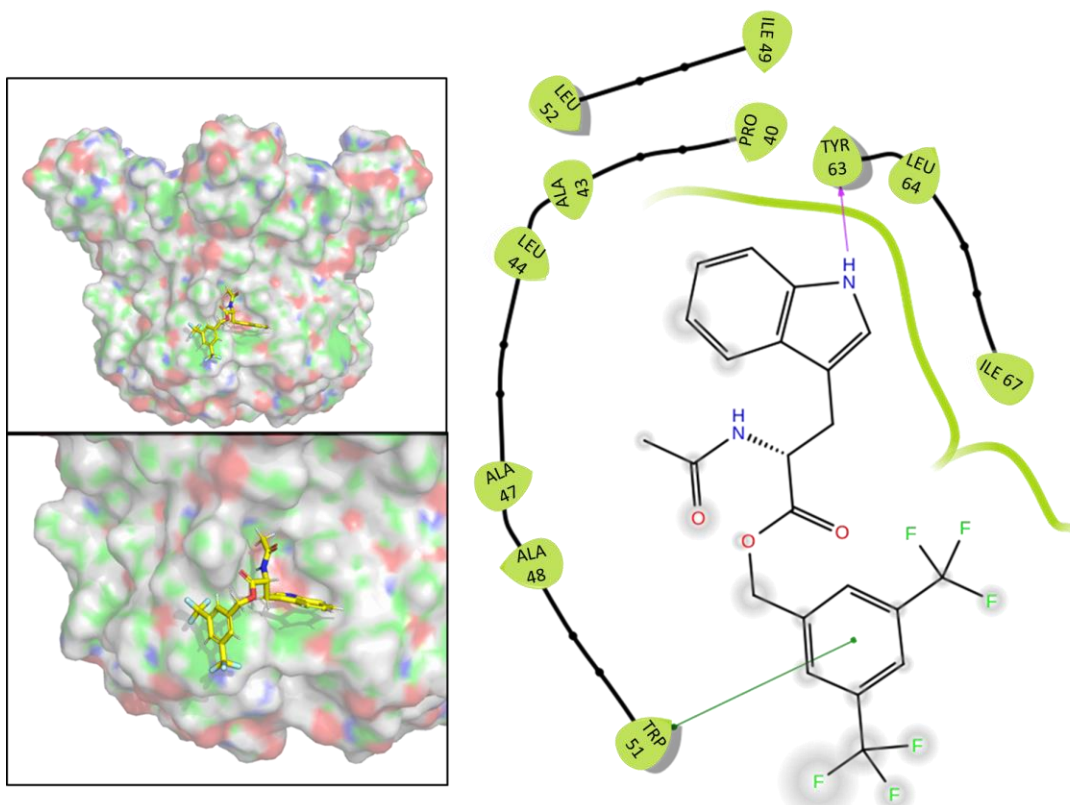


Figure 5.11 L-732, 183 and M protein predicted interaction data

A. Surface plot of M protein hexamer *in silico* model with the L-732, 183 shown docked into the peripheral cavity represented as sticks in yellow, orientated towards the linker region. B. Predicted interactions between L-732, 183 and M protein peripheral cavity in Maestro software. Hydrophobic residues highlighted in green, hydrogen bonds shown as pink lines and π - π stacking interactions shown in green. Maestro image kindly generated by Dr Ravi Singh.

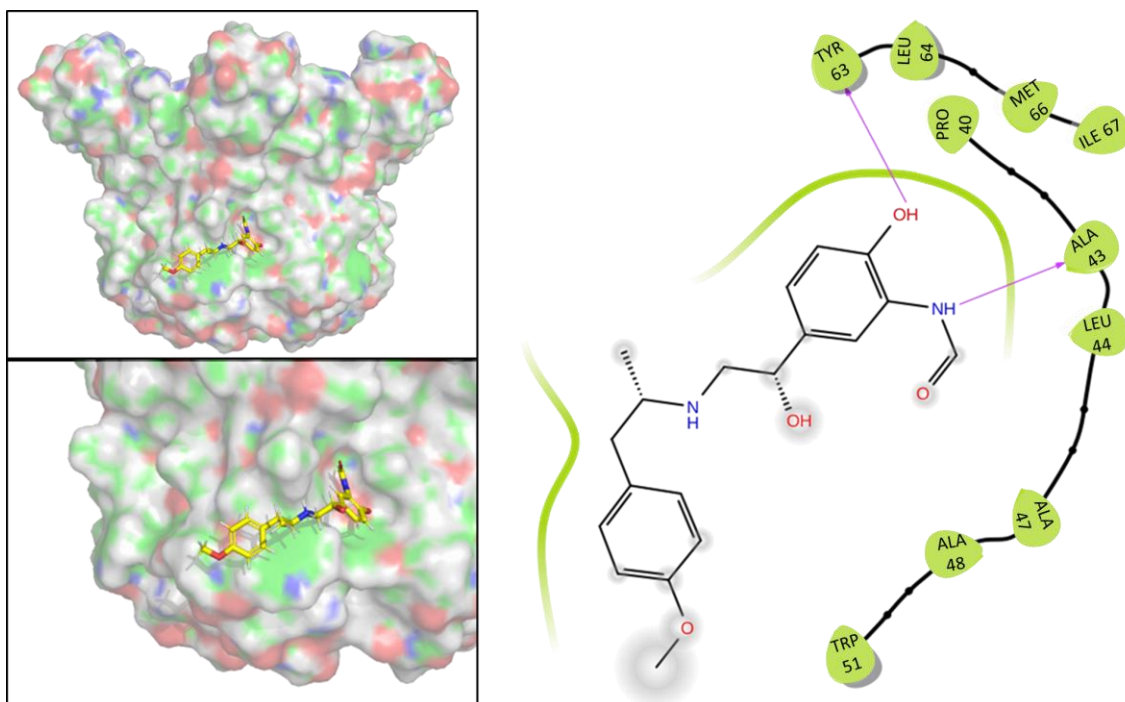


Figure 5.12 Formoterol and M protein predicted interaction data

A. Surface plot of M protein hexamer *in silico* model with the Formoterol shown docked into the peripheral cavity represented as sticks in yellow, orientated towards the linker region. B. Predicted interactions between Formoterol and M protein peripheral cavity in Maestro software. Hydrophobic residues highlighted in green and hydrogen bonds shown as pink lines. Maestro image kindly generated by Dr Ravi Singh.

5.4.3 Testing selected screened compounds in cell culture

The *in silico* screen of 100 TOCRIS library identified a number of compounds which reduced M protein channel activity *in vitro*. Three of the top inhibitory compounds which had a greater than 50 % reduction of M protein channel activity *in vitro* from both sites were selected to be further tested in cell culture. Compounds selected targeting the Luminal site comprised: GNF 5837, GSK 2837808A and KB SRC 4. Peripherally targeting selected compounds were AA 29504, formoterol hemifumarate and L-732,138.

Additionally, the effects of JK3/34 and JK3/42 (section 5.2) in viral cell culture was investigated, however upon addition to cell culture media the compounds were toxic and caused media discolouration at low concentrations.

The TOCRIS repurposing library contains previously licensed generic compounds and biologically active compounds shown to have activity against GPCRs, ion channels, kinases, enzymes, nuclear receptors and transporters. The effect of these compounds on Vero cells was investigated, to determine the concentrations used in the future cell culture screening against ZIKV. MTT assays were used to quantify the effect of the compounds on cell viability (section 2.2.4).

Selected lumen-targeting compounds for cell culture assays were found to have no adverse effects upon cellular metabolism when applied to cells across the μM range, with the exception of GNF 5837, which was only tolerated by cells at nM concentrations (Figure 5.13). Similarly, the majority of chosen peripherally targeting compounds did not affect cell viability at μM (Figure 5.14). Chosen concentrations are shown in Table 5.3.

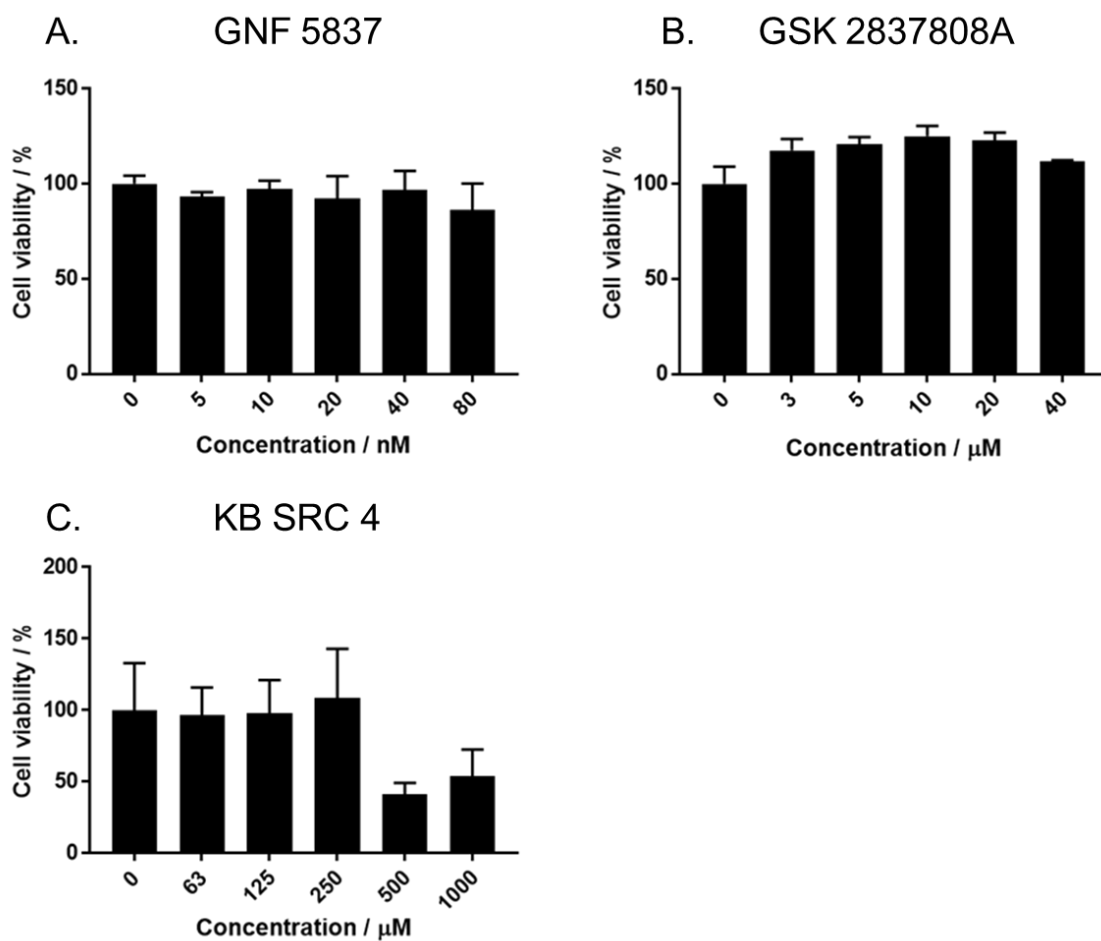


Figure 5.13 The effect of lumen-targeting TOCRIS selected compounds on cell viability

A. The effect of GNF 5837 on cell viability at 48 hr between 0 and 80 nM. B. The effect of GSK 2837808A on cell viability at 48 hr between 1 and 40 μM. C. The effect of KB SRC 4 on cell viability at 48 hr between 0 and 1 mM.

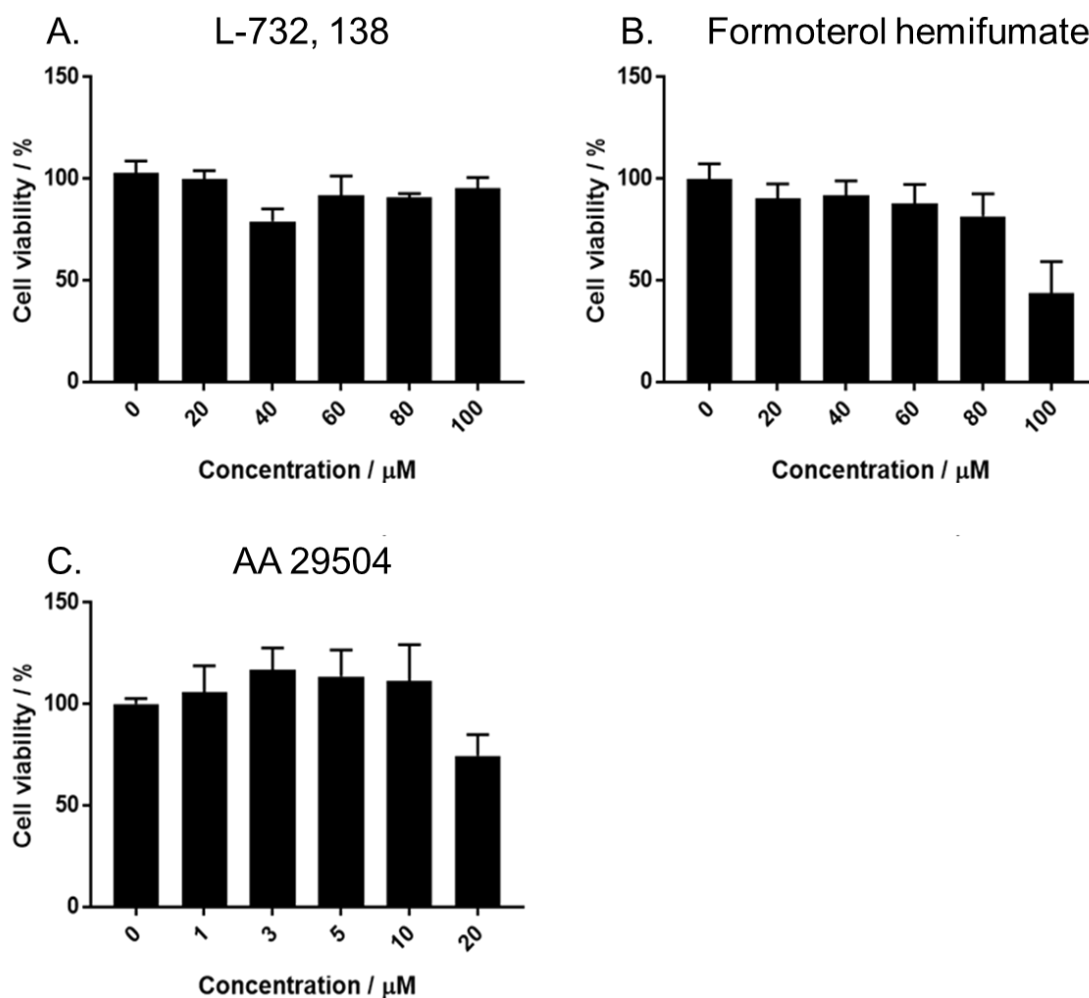


Figure 5.14 The effect of peripherally targeting TOCRIS selected compounds on cell viability

A. The effect of L-732, 138 on vero cell viability at 48 hr between 0 and 100 μM .
 B. The effect of formoterol hemifumate on vero cell viability at 48 hr between 0 and 100 μM .
 C. The effect of AA 29504 on vero cell viability at 48 hr between 0 and 20 μM .

Compound	Concentration (μM)
GNF 5837	0.08
GSK 2837808A	40
KB SRC 4	0.25
L-732, 138	40
Formoterol	80
AA 29504	10

Table 5.4 Concentrations of screened compounds for use in cell culture

5.4.3.1 Do selected TOCRIS compounds target ZIKV in cell culture?

The selected six compounds were assayed in cell culture to determine their effect on ZIKV infection. (section 2.3.4.2) Cell viability assays as shown in section 2.2.4 led us to suitable concentrations. Compounds were all reconstituted in DMSO and were added to both plaque assay virus inoculae and overlay.

Figure 5.15 shows the results from the plaque assay of the six different compounds, showing ZIKV infected cells treated with GNF 5837 and AA 29504 significantly inhibited ZIKV in cell culture at 10 μ M and 80 nM respectively. Notably these concentrations are a considerable improvement on rimantadine, used at 80 μ M to achieve similar antiviral effects. Additionally, when these two compounds thought to target different sites were used in combination at the previously described concentrations, they did not have a synergistic effect, however a smaller significant inhibitory effect was still observed. For comparison, a negative control, JK3/32, was chosen due to its lack of activity against M protein channels using the liposome-based dye release assay, furthermore this compound did also not have an effect on ZIKV infection in cell culture.

Throughout this chapter, we have researched the potential for repurposed compounds to inhibit ZIKV M protein *in vitro* and cell culture. When tested *in vitro* more compounds predicted to target M protein luminal cavity were inhibitory compared to those targeting the peripheral cavity. However, of the six compounds taken forward into cell culture luminal targeting AA 29504 and peripheral targeting GNF 5837 were the most potent ZIKV inhibitors of the drug repurposing library.

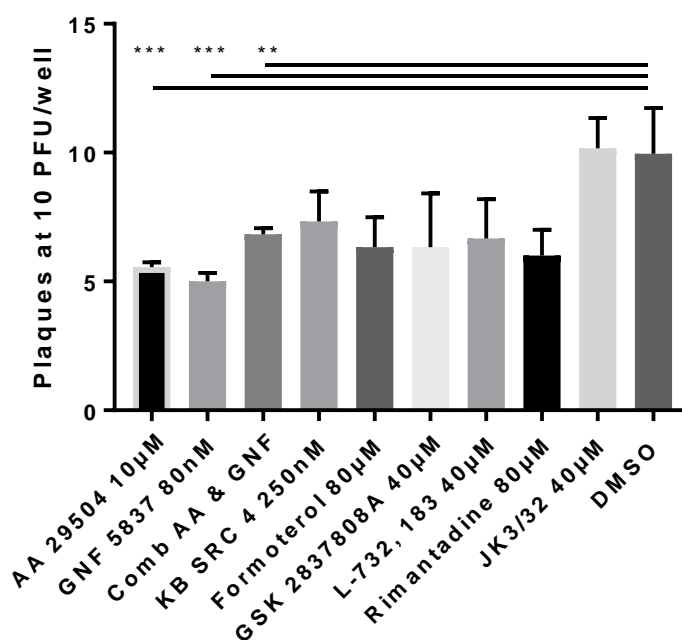


Figure 5.15 Effects of selected TOCRIS compounds on viral titre

TOCRIS compounds were added to cells at the same time as cells were inoculated with virus. Compounds were used at the following concentrations: AA 29504 10 µM, GNF 5837 80 nM, KB SRC 4 250nM, Formoterol hemifumate 80 µM, GSK 2837808A 40 µM, L-732, 183 40 µM, Rimantadine 80 µM, and negative control JK3/32 40 µM. Data shown of triplicate wells from one experiment, except for AA 29504 and GNF 5837 which contain 3 biological repeats of triplicate wells. Data shown from three biological replicates subjected to T tests of the mean. AA 29504, p value=0.0005, GNF 5837 p value=0.0002. Combined AA29504 and GNF 5837 treatment data is from two biological replicates, p value=0.0032.

5.5 Discussion

The current treatment of ZIKV infection is solely best supportive care, therefore will not prevent the virus crossing the placenta of pregnant women and establishing an *in utero* infection. There are compounds undergoing research and testing for their ability to treat ZIKV infected patients, however no therapies are currently licensed for the treatment of ZIKV. Additionally, the current ZIKV vaccine development is ongoing, and a vaccine may not address the need for a treatment preventing cross-placental infection prior to the third trimester.

We have previously identified M protein channels as a novel target throughout chapter 3 and 4. However, the lack of structural data has prevented screening and identification of new or repurposed compounds, capable of inhibiting M protein. We have avoided the inherent problems associated with hydrophobic membrane protein purification and adopted a rational approach to identifying repurposed drugs capable of inhibiting M protein channels, providing progress in the *Flavivirus* antiviral development field.

The licensed M2 viroporin inhibitor rimantadine was screened *in vitro*, in cell culture and *in vivo*, and inhibited M protein and ZIKV infection respectively in a dose-dependent manner (chapter 4). Additionally, in the liposome-based assay the levels of rimantadine needed to inhibit the channel were similar to those used for p7 inhibition (1 μM) (StGelais et al., 2007; StGelais et al., 2009), whereas inhibition of E5 required much higher concentrations (>400 μM) (Wetherill et al., 2012).

M protein activity was reduced to ~60 % by 1 μM rimantadine. Rimantadine is known to target multiple viroporins and is therefore relatively promiscuous. Thus, we used the liposome-based channel activity assay to test other compounds previously used or developed against viroporins. The compounds included JK3 compounds developed as potential p7 inhibitors (Shaw et al., 2019). The repeated testing of these compounds at 1 μM found the most active and repeatable being JK3/42. JK3/32, which has been identified as a potent p7 inhibitor does not show any inhibitory effects on ZIKV M protein and was subsequently used as a negative control (Figure 5.15) (Shaw et al., 2019).

Small molecules with greater efficacies for ZIKV M are clearly needed and a rational approach was taken to identifying potential compounds from a

repurposing library. The drug-repurposing library from TOCRIS is made up of 1280 compounds, which are known to target, GPCRs (27%), kinases (20%), enzymes (19%), ion channels (14%), cell biology (10%), nuclear receptors (5%), transporters and other pharmacology (5%).

Although an atomic channel structure remains elusive, our work *in silico* constructing and simulating a model has provided us with a template for rational drug library screening. Our first step utilised computational tools to identify potential binding cavities to go forth and screen the large repurposing library.

Our preferred *in silico* model of ZIKV M protein hexameric channel was studied to identify potential drug binding sites. *In silico* software Maestro identified rimantadine is predicted to bind to a luminal cavity of the model, with a promising glide/binding score compared to other binding sites identified on the model. Rimantadine is predicted to bind to this cavity positioned with its adamantyl cage away from the channel lumen (Figure 5.4A), similarly rimantadine docks to the HPV E5 channels in a lipophilic luminal binding site, although with the adamantyl cage facing the lumen pocket, however the binding of rimantadine onto HCV p7 resides on the periphery (Foster et al., 2011; Wetherill et al., 2012). Similarly, amantadine docked in the same predicted orientation to rimantadine, however *N*-acetyl and *N*-methyl rimantadine were positioned with their adamantyl cage towards the lumen (Figure 5.4) this could be due to more hydrophobic R-groups. Furthermore, rimantadine is shown to interact most closely with VAL61, LEU64, VAL65 and LEU68. These pore lining residues, particularly LEU64 and 68 were found in Chapter 2 to be consistently involved with closure of the MD simulation channels.

Additionally, Maestro software was not capable of considering the peripheral-membrane, so we identified a potential peripheral cavity, which bared a resemblance to the peripheral rimantadine binding cavity of p7 (Foster et al., 2014). Furthermore, these two binding sites were taken forward for *in silico* drug screening.

After screening the 1280 compounds against the two binding sites *in silico* the top 50 ranked according to binding capacity were screened *in vitro* using the liposome dye release assay, the liposome assay has been previously used and published with other viroporins (StGelais et al., 2007; Carter et al., 2010;

StGelais et al., 2009; Wetherill et al., 2012). This system has also been used as a high throughput *in vitro* screen of a Pharmaceutical company drug library, although some components of the liposomes were altered to improve stability (Gervais et al., 2011). A higher proportion of luminal targeting compounds effectively inhibited M protein than periphery-targeting, this could be due to the hydrophobic and polar interactions of lumenally targeting compounds. Also due to the biased nature of this screen by utilising *in silico* screening, the success rate of these compounds was much higher than a blind drug screen (Lionta et al., 2014).

Three of the top lumen-targeting compounds and peripherally targeting compounds were taken forward for testing in cell culture against ZIKV infection. However, AA 29504 and GNF 5837 showed the highest level of ZIKV inhibition, which are known as an allosteric modulator of GABAA receptors (Hoestgaard-Jensen et al., 2010) and a Trk inhibitor respectively (Albaugh et al., 2012).

The *in silico* predicted interaction data between the compounds and its binding cavities interestingly shown rimantadine is not predicted to form any hydrogen bonds or π - π stacking interactions with the residues in the luminal cavity. However, the six identified compounds taken forward into cell culture all form at least one hydrogen bond with the cavity, namely THR57 for the three luminal compounds, with two THR57 hydrogen bonds forming for one molecule of GSK 2837808A. For periphery targeting compounds TYR63 forms a hydrogen bond to all compounds in addition to ALA43 for formoterol. Furthermore, π - π stacking interactions are also found for AA 29504 and L-732, 138 between TYR63 and TRP51 respectively. The presence of these bonds would suggest the compounds are more likely to strongly inhibit M protein viroporins in comparison to the weak binding of Rimantadine.

AA 29504 a triamino-benzene compound enters the brain modulating GABAA receptors and is effective *in vivo*. Additionally, *in vivo* dosing has been carried out in rats at 4 mg/kg and 10 mg/kg successfully (Hoestgaard-Jensen et al., 2010). AA29504 is predicted to bind to the periphery of the M protein viroporin complex by virtue of its planar composition (Figure 5.10), and successfully reduced ZIKV plaque formation in cell culture by ~50 % at a concentration of 10 μ M (Figure 5.15).

GNF 5837 is an orally-administered potent and selective TRK-inhibitor, which inhibits mice Xenograft tumour growth (Albaugh, 2012). Interestingly GNF 5837 is also a planar compound, but contains an oxindole core, similar to the p7-targeted JK compound series. However, GNF 5837 was predicted to bind to the luminal cavity of ZIKV M protein channels (Figure 5.7), and similarly to AA 29504 was seen to reduce ZIKV infection in cell culture by ~50 %. Moreover, GNF 5837 was used at a 1000-fold lower concentration than rimantadine, indicative of a promising improvement in inhibitory properties.

The *in silico* approach undertaken to identify inhibitors of the ZIKV M protein viroporin was validated, as compounds AA 29504 and GNF 5837 exhibited specific, inhibition of M peptide viroporin activity *in vitro* and in cell culture. These compounds could represent the first step towards ZIKV M protein viroporin inhibitors.

Chapter 6 Final Conclusion

Controversy over the channel activity of *Flavivirus* M proteins exists due to conflicting published DENV data. Previous work with DENV-2 M protein C-terminal peptides supported cation channel activity *in vitro*, sensitive to prototypic viroporin inhibitors, amantadine and hexamethylene amiloride. In addition, amantadine and rimantadine have also inhibited DENV infection *in vitro* (Koff et al., 1980; Koff et al., 1981). However, no evidence was found supporting the ability of M to act as a proton channel in electrophysiology studies using *Xenopus* oocytes (Premkumar et al., 2005; Wong et al., 2011).

This study has demonstrated ZIKV M protein can form oligomeric channels through work *in silico*, *in vitro*, in cell culture and *in vivo*. MD simulations have shown M protein can dimerise within a lipid bilayer in different orientations and can be influenced by lipid composition and structural restraints. Furthermore, MD simulations have shown M can remain stable as a hexameric oligomer and possess a water channel with helix 3 lining the pore. In addition, rotating the monomers to increase interactions causes the pore to remain open for a greater proportion of time upon HIS28 protonation; this may be reflective of the physiological environment experienced by the virus during endocytosis.

The first indication *in vitro* of M protein oligomers was seen in a DH(6)PC detergent environment using native-PAGE, where oligomers suggestive of hexamers or heptamers were seen on a Coomassie-stained gel. Subsequent visualisation by TEM of M protein channels in this detergent environment showed that varying the detergent concentrations generated protein oligomers in different orientations and oligomeric sizes. Unfortunately, the stoichiometry could not be determined.

M protein channel activity was demonstrated in an *in vitro* liposome assay, used previously with many other viroporins. The assay showed M peptide concentration-dependent activity and dose-dependent inhibition with rimantadine.

Discovery of rimantadine as an inhibitor of ZIKV M protein was successfully translated to cell culture and *in vivo*. Mice infected with ZIKV and treated with rimantadine showed significant reduction in serum viral titre by plaque assay.

These results show M protein as a successful drug target *in vivo*, however as rimantadine did not reduce viral titre fully and due to its promiscuity, history and simplicity. This pipeline was applied to discover other potential M protein inhibitors.

Thus, the most favourable *in silico* model comprising the rotated M protein channel with the pore lined by helix-3 was used to identify potential inhibitor binding sites. These two identified sites L1 and P1 are found in the lumen and periphery respectively. The chemistry department assisted the TOCRIS drug repurposing library *in silico* screening for potential hits, the top 50 appropriate hits were taken forward per binding site.

The *in vitro* liposome assay was used for a rapid throughput screen based upon *in silico* enrichment, which highlighted several promising compounds. Implementation of the pipeline using six compounds identified *in vitro*, confirmed the activity of two compounds in cell culture, one for each P1 (AA 29504) and L1 (GNF 5837) binding sites were seen to have significant ZIKV infection inhibitory effects at 10-fold and 1000-fold reduction in concentration.

Future work testing these compounds ensuring they have no off-target effects and testing *in vivo* is crucial to determining their role in targeting ZIKV infection, however the nature of the library reduces the likelihood of this. Furthermore, looking at the effect of targeting ZIKV M protein *in utero* with Rimantadine and the identified AA29504 and GNF5837 would prove instrumental at displaying the effect of a drug targeting ZIKV M in a clinical anti-microcephaly setting. Moreover, determining the stoichiometry and structure of ZIKV M protein oligomers by cryo-electron microscopy would provide not only functional information, but also serve as an improved template for further development of inhibitors.

Abbink, P., Larocca, R.A., De La Barrera, R.A., Bricault, C.A., Moseley, E.T., Boyd, M., Kirilova, M., Li, Z., Ng'ang'a, D., Nanayakkara, O., Nityanandam, R., Mercado, N.B., Borducchi, E.N., Agarwal, A., Brinkman, A.L., Cabral, C., Chandrashekar, A., Giglio, P.B., Jetton, D., Jimenez, J., Lee, B.C., Mojta, S., Molloy, K., Shetty, M., Neubauer, G.H., Stephenson, K.E., Peron, J.P., Zanutto, P.M., Misamore, J., Finneyfrock, B., Lewis, M.G., Alter, G., Modjarrad, K., Jarman, R.G., Eckels, K.H., Michael, N.L., Thomas, S.J. and Barouch, D.H. 2016. Protective efficacy of multiple vaccine platforms against Zika virus challenge in rhesus monkeys. *Science*. **353**(6304), pp.1129-1132.

Abraham, M., Murtola, T., Schulz, R., Páll, S., Smith, J., Hess, B. and Lindahl, E. 2015. GROMACS: High performance molecular simulations through multi-level parallelism from laptops to supercomputers. *SoftwareX*. **1**.

Ackermann, M. and Padmanabhan, R. 2001. De novo synthesis of RNA by the dengue virus RNA-dependent RNA polymerase exhibits temperature dependence at the initiation but not elongation phase. *J Biol Chem*. **276**(43), pp.39926-39937.

Acosta, E.G., Castilla, V. and Damonte, E.B. 2009. Alternative infectious entry pathways for dengue virus serotypes into mammalian cells. *Cell Microbiol*. **11**(10), pp.1533-1549.

Adams Waldorf, K.M., Stencel-Baerenwald, J.E., Kapur, R.P., Studholme, C., Boldenow, E., Vornhagen, J., Baldessari, A., Dighe, M.K., Thiel, J., Merillat, S., Armistead, B., Tisoncik-Go, J., Green, R.R., Davis, M.A., Dewey, E.C., Fairgrieve, M.R., Gatenby, J.C., Richards, T., Garden, G.A., Diamond, M.S., Juul, S.E., Grant, R.F., Kuller, L., Shaw, D.W., Ogle, J., Gough, G.M., Lee, W., English, C., Hevner, R.F., Dobyns, W.B., Gale, M., Jr. and Rajagopal, L. 2016. Fetal brain lesions after subcutaneous inoculation of Zika virus in a pregnant nonhuman primate. *Nat Med*. **22**(11), pp.1256-1259.

Akey, D.L., Brown, W.C., Dutta, S., Konwerski, J., Jose, J., Jurkiw, T.J., DelProposto, J., Ogata, C.M., Skinotis, G., Kuhn, R.J. and Smith, J.L. 2014. Flavivirus NS1 structures reveal surfaces for associations with membranes and the immune system. *Science*. **343**(6173), pp.881-885.

Akey, D.L., Brown, W.C., Jose, J., Kuhn, R.J. and Smith, J.L. 2015. Structure-guided insights on the role of NS1 in flavivirus infection. *Bioessays*. **37**(5), pp.489-494.

Aktepe, T.E. and Mackenzie, J.M. 2018. Shaping the flavivirus replication complex: It is curvaceous! *Cell Microbiol*. **20**(8), pe12884.

Albaugh, P., Fan, Y., Mi, Y., Sun, F., Adrian, F., Li, N., Jia, Y., Sarkisova, Y., Kreusch, A., Hood, T., Lu, M., Liu, G., Huang, S., Liu, Z., Loren, J., Tuntland, T., Karanewsky, D.S., Seidel, H.M. and Molteni, V. 2012. Discovery of GNF-5837, a Selective TRK Inhibitor with Efficacy in Rodent Cancer Tumor Models. *ACS Med Chem Lett*. **3**(2), pp.140-145.

Alcantara, D. and O'Driscoll, M. 2014. Congenital microcephaly. *Am J Med Genet C Semin Med Genet*. **166C**(2), pp.124-139.

Alcendor, D.J. 2017. Zika Virus Infection of the Human Glomerular Cells: Implications for Viral Reservoirs and Renal Pathogenesis. *J Infect Dis*. **216**(2), pp.162-171.

Althouse, B.M., Vasilakis, N., Sall, A.A., Diallo, M., Weaver, S.C. and Hanley, K.A. 2016. Potential for Zika Virus to Establish a Sylvatic Transmission Cycle in the Americas. *PLoS Negl Trop Dis*. **10**(12), pe0005055.

Amberg, S.M., Nestorowicz, A., McCourt, D.W. and Rice, C.M. 1994. NS2B-3 proteinase-mediated processing in the yellow fever virus structural region: in vitro and in vivo studies. *J Virol.* **68**(6), pp.3794-3802.

Ambrose, R.L. and Mackenzie, J.M. 2011. West Nile virus differentially modulates the unfolded protein response to facilitate replication and immune evasion. *J Virol.* **85**(6), pp.2723-2732.

Andreas, L.B., Eddy, M.T., Pielak, R.M., Chou, J. and Griffin, R.G. 2010. Magic angle spinning NMR investigation of influenza A M2(18-60): support for an allosteric mechanism of inhibition. *J Am Chem Soc.* **132**(32), pp.10958-10960.

Antoine, A.F., Montpellier, C., Cailliau, K., Browaeys-Poly, E., Vilain, J.P. and Dubuisson, J. 2007. The alphavirus 6K protein activates endogenous ionic conductances when expressed in *Xenopus* oocytes. *J Membr Biol.* **215**(1), pp.37-48.

Araujo, G.C., Silva, R.H., Scott, L.P., Araujo, A.S., Souza, F.P. and de Oliveira, R.J. 2016. Structure and functional dynamics characterization of the ion channel of the human respiratory syncytial virus (hRSV) small hydrophobic protein (SH) transmembrane domain by combining molecular dynamics with excited normal modes. *J Mol Model.* **22**(12), p286.

Assenberg, R., Mastrangelo, E., Walter, T.S., Verma, A., Milani, M., Owens, R.J., Stuart, D.I., Grimes, J.M. and Mancini, E.J. 2009. Crystal structure of a novel conformational state of the flavivirus NS3 protein: implications for polyprotein processing and viral replication. *J Virol.* **83**(24), pp.12895-12906.

Atkins, E., Tatineni, R., Li, H., Gretch, D., Harris, M. and Griffin, S. 2014. The stability of secreted, acid-labile H77/JFH-1 hepatitis C virus (HCV) particles is altered by patient isolate genotype 1a p7 sequences. *Virology.* **448**, pp.117-124.

Atkinson, B., Hearn, P., Afrough, B., Lumley, S., Carter, D., Aarons, E.J., Simpson, A.J., Brooks, T.J. and Hewson, R. 2016. Detection of Zika Virus in Semen. *Emerg Infect Dis.* **22**(5), p940.

Avirutnan, P., Punyadee, N., Noisakran, S., Komoltri, C., Thiemmecca, S., Auethavornanan, K., Jairungsri, A., Kanlaya, R., Tangthawornchaikul, N., Puttikhunt, C., Pattanakitsakul, S.N., Yenchitsomanus, P.T., Mongkolsapaya, J., Kasinrerak, W., Sittisombut, N., Husmann, M., Blettner, M., Vasana-wathana, S., Bhakdi, S. and Malasit, P. 2006. Vascular leakage in severe dengue virus infections: a potential role for the nonstructural viral protein NS1 and complement. *J Infect Dis.* **193**(8), pp.1078-1088.

Bagasra, O., Addanki, K.C., Goodwin, G.R., Hughes, B.W., Pandey, P. and McLean, E. 2017. Cellular Targets and Receptor of Sexual Transmission of Zika Virus. *Appl Immunohistochem Mol Morphol.* **25**(10), pp.679-686.

Bagneris, C., DeCaen, P.G., Naylor, C.E., Pryde, D.C., Nobeli, I., Clapham, D.E. and Wallace, B.A. 2014. Prokaryotic NavMs channel as a structural and functional model for eukaryotic sodium channel antagonism. *Proc Natl Acad Sci U S A.* **111**(23), pp.8428-8433.

Baker, L.M., Shock, M.P. and Iezzoni, D.G. 1969. The therapeutic efficacy of Symmetrel (amantadine hydrochloride) in naturally occurring influenza A2 respiratory illness. *J Am Osteopath Assoc.* **68**(12), pp.1244-1250.

Bantia, S., Kellogg, D., Parker, C.D. and Babu, Y.S. 2010. Combination of peramivir and rimantadine demonstrate synergistic antiviral effects in sub-lethal influenza A (H3N2) virus mouse model. *Antiviral Res.* **88**(3), pp.276-280.

Bardina, S.V., Bunduc, P., Tripathi, S., Duehr, J., Frere, J.J., Brown, J.A., Nachbagauer, R., Foster, G.A., Krysztof, D., Tortorella, D., Stramer, S.L., Garcia-Sastre, A., Krammer, F. and Lim, J.K. 2017. Enhancement of Zika virus

pathogenesis by preexisting antinflavivirus immunity. *Science*. **356**(6334), pp.175-180.

Barthel, A., Gourinat, A.C., Cazorla, C., Joubert, C., Dupont-Rouzeyrol, M. and Descloux, E. 2013. Breast milk as a possible route of vertical transmission of dengue virus? *Clin Infect Dis*. **57**(3), pp.415-417.

Bauer, C.M., Pinto, L.H., Cross, T.A. and Lamb, R.A. 1999. The influenza virus M2 ion channel protein: probing the structure of the transmembrane domain in intact cells by using engineered disulfide cross-linking. *Virology*. **254**(1), pp.196-209.

Bayer, A., Lennemann, N.J., Ouyang, Y., Bramley, J.C., Morosky, S., Marques, E.T., Jr., Cherry, S., Sadovsky, Y. and Coyne, C.B. 2016. Type III Interferons Produced by Human Placental Trophoblasts Confer Protection against Zika Virus Infection. *Cell Host Microbe*. **19**(5), pp.705-712.

Bayless, N.L., Greenberg, R.S., Swigut, T., Wysocka, J. and Blish, C.A. 2016. Zika Virus Infection Induces Cranial Neural Crest Cells to Produce Cytokines at Levels Detrimental for Neurogenesis. *Cell Host Microbe*. **20**(4), pp.423-428.

Beaton, A.R., Rodriguez, J., Reddy, Y.K. and Roy, P. 2002. The membrane trafficking protein calpactin forms a complex with bluetongue virus protein NS3 and mediates virus release. *Proc Natl Acad Sci U S A*. **99**(20), pp.13154-13159.

Belokrinitskaya, T.Y., Trubitsyna, A.Y. and Ionouchene, S.V. 2012. H1N1 2009 influenza virus infection among pregnant women in Transbaikal, Russia. *Int J Gynaecol Obstet*. **118**(3), pp.251-252.

Bentham, M.J., Foster, T.L., McCormick, C. and Griffin, S. 2013. Mutations in hepatitis C virus p7 reduce both the egress and infectivity of assembled particles via impaired proton channel function. *J Gen Virol*. **94**(Pt 10), pp.2236-2248.

Bera, A.K., Kuhn, R.J. and Smith, J.L. 2007. Functional characterization of cis and trans activity of the Flavivirus NS2B-NS3 protease. *J Biol Chem*. **282**(17), pp.12883-12892.

Berg, T., Sarrazin, C., Herrmann, E., Hinrichsen, H., Gerlach, T., Zachoval, R., Wiedenmann, B., Hopf, U. and Zeuzem, S. 2003. Prediction of treatment outcome in patients with chronic hepatitis C: significance of baseline parameters and viral dynamics during therapy. *Hepatology*. **37**(3), pp.600-609.

Bernsel, A., Viklund, H., Hennerdal, A. and Elofsson, A. 2009. TOPCONS: consensus prediction of membrane protein topology. *Nucleic Acids Res*. **37**(Web Server issue), pp.W465-468.

Besnard, M., Lastere, S., Teissier, A., Cao-Lormeau, V. and Musso, D. 2014. Evidence of perinatal transmission of Zika virus, French Polynesia, December 2013 and February 2014. *Euro Surveill*. **19**(13).

Betakova, T. and Kollerova, E. 2006. pH modulating activity of ion channels of influenza A, B, and C viruses. *Acta Virol*. **50**(3), pp.187-193.

Bezanilla, F. 2008. How membrane proteins sense voltage. *Nat Rev Mol Cell Biol*. **9**(4), pp.323-332.

Black, R.A., Rota, P.A., Gorodkova, N., Cramer, A., Klenk, H.D. and Kendal, A.P. 1993. Production of the M2 protein of influenza A virus in insect cells is enhanced in the presence of amantadine. *J Gen Virol*. **74** (Pt 8), pp.1673-1677.

Boorman, J.P. and Porterfield, J.S. 1956. A simple technique for infection of mosquitoes with viruses; transmission of Zika virus. *Trans R Soc Trop Med Hyg*. **50**(3), pp.238-242.

Boson, B., Granio, O., Bartenschlager, R. and Cosset, F.L. 2011. A concerted action of hepatitis C virus p7 and nonstructural protein 2 regulates core

localization at the endoplasmic reticulum and virus assembly. *PLoS Pathog.* **7**(7), pe1002144.

Bowen, J.R., Zimmerman, M.G. and Suthar, M.S. 2018. Taking the defensive: Immune control of Zika virus infection. *Virus Res.* **254**, pp.21-26.

Brault, A.C., Domi, A., McDonald, E.M., Talmi-Frank, D., McCurley, N., Basu, R., Robinson, H.L., Hellerstein, M., Duggal, N.K., Bowen, R.A. and Guirakhoo, F. 2017. A Zika Vaccine Targeting NS1 Protein Protects Immunocompetent Adult Mice in a Lethal Challenge Model. *Sci Rep.* **7**(1), p14769.

Brault, J.B., Khou, C., Basset, J., Coquand, L., Fraissier, V., Frenkiel, M.P., Goud, B., Manuguerra, J.C., Pardigon, N. and Baffet, A.D. 2016. Comparative Analysis Between Flaviviruses Reveals Specific Neural Stem Cell Tropism for Zika Virus in the Mouse Developing Neocortex. *EBioMedicine.* **10**, pp.71-76.

Breitinger, U., Farag, N.S., Ali, N.K. and Breitinger, H.G. 2016. Patch-Clamp Study of Hepatitis C p7 Channels Reveals Genotype-Specific Sensitivity to Inhibitors. *Biophys J.* **110**(11), pp.2419-2429.

Bressanelli, S., Stiasny, K., Allison, S.L., Stura, E.A., Duquerroy, S., Lescar, J., Heinz, F.X. and Rey, F.A. 2004. Structure of a flavivirus envelope glycoprotein in its low-pH-induced membrane fusion conformation. *EMBO J.* **23**(4), pp.728-738.

Brillanti, S., Levantesi, F., Masi, L., Folli, M. and Bolondi, L. 2000. Triple antiviral therapy as a new option for patients with interferon nonresponsive chronic hepatitis C. *Hepatology.* **32**(3), pp.630-634.

Brito, C.A.A., Henriques-Souza, A., Soares, C.R.P., Castanha, P.M.S., Machado, L.C., Pereira, M.R., Sobral, M.C.M., Lucena-Araujo, A.R., Wallau, G.L. and Franca, R.F.O. 2018. Persistent detection of Zika virus RNA from an infant with severe microcephaly - a case report. *BMC Infect Dis.* **18**(1), p388.

Bukreyev, A., Whitehead, S.S., Murphy, B.R. and Collins, P.L. 1997. Recombinant respiratory syncytial virus from which the entire SH gene has been deleted grows efficiently in cell culture and exhibits site-specific attenuation in the respiratory tract of the mouse. *J Virol.* **71**(12), pp.8973-8982.

Bullard-Feibelman, K.M., Govero, J., Zhu, Z., Salazar, V., Veselinovic, M., Diamond, M.S. and Geiss, B.J. 2017. The FDA-approved drug sofosbuvir inhibits Zika virus infection. *Antiviral Res.* **137**, pp.134-140.

Burlaud-Gaillard, J., Sellin, C., Georgeault, S., Uzbekov, R., Lebos, C., Guillaume, J.M. and Roingard, P. 2014. Correlative scanning-transmission electron microscopy reveals that a chimeric flavivirus is released as individual particles in secretory vesicles. *PLoS One.* **9**(3), pe93573.

Bussi, G., Donadio, D. and Parrinello, M. 2007. Canonical sampling through velocity rescaling. *J Chem Phys.* **126**(1), p014101.

Butcher, S.J., Grimes, J.M., Makeyev, E.V., Bamford, D.H. and Stuart, D.I. 2001. A mechanism for initiating RNA-dependent RNA polymerization. *Nature.* **410**(6825), pp.235-240.

Byk, L.A., Iglesias, N.G., De Maio, F.A., Gebhard, L.G., Rossi, M. and Gamarnik, A.V. 2016. Dengue Virus Genome Uncoating Requires Ubiquitination. *MBio.* **7**(3).

Byrd, C.M., Dai, D., Grosenbach, D.W., Berhanu, A., Jones, K.F., Cardwell, K.B., Schneider, C., Wineinger, K.A., Page, J.M., Harver, C., Stavale, E., Tyavanagimatt, S., Stone, M.A., Bartenschlager, R., Scaturro, P., Hruby, D.E. and Jordan, R. 2013. A novel inhibitor of dengue virus replication that targets the capsid protein. *Antimicrob Agents Chemother.* **57**(1), pp.15-25.

Cady, S., Wang, T. and Hong, M. 2011. Membrane-dependent effects of a cytoplasmic helix on the structure and drug binding of the influenza virus M2 protein. *J Am Chem Soc.* **133**(30), pp.11572-11579.

Cady, S.D., Schmidt-Rohr, K., Wang, J., Soto, C.S., Degrado, W.F. and Hong, M. 2010. Structure of the amantadine binding site of influenza M2 proton channels in lipid bilayers. *Nature.* **463**(7281), pp.689-692.

Cady, S.D., Wang, J., Wu, Y., DeGrado, W.F. and Hong, M. 2011. Specific binding of adamantane drugs and direction of their polar amines in the pore of the influenza M2 transmembrane domain in lipid bilayers and dodecylphosphocholine micelles determined by NMR spectroscopy. *J Am Chem Soc.* **133**(12), pp.4274-4284.

Cao-Lormeau, V.M. and Musso, D. 2014. Emerging arboviruses in the Pacific. *Lancet.* **384**(9954), pp.1571-1572.

Cao-Lormeau, V.M., Roche, C., Teissier, A., Robin, E., Berry, A.L., Mallet, H.P., Sall, A.A. and Musso, D. 2014. Zika virus, French polynesia, South pacific, 2013. *Emerg Infect Dis.* **20**(6), pp.1085-1086.

Cao, X., Li, Y., Jin, X., Li, Y., Guo, F. and Jin, T. 2016. Molecular mechanism of divalent-metal-induced activation of NS3 helicase and insights into Zika virus inhibitor design. *Nucleic Acids Res.* **44**(21), pp.10505-10514.

Carrasco, L. 1995. Modification of membrane permeability by animal viruses. *Adv Virus Res.* **45**, pp.61-112.

Carrere-Kremer, S., Montpellier-Pala, C., Cocquerel, L., Wychowski, C., Penin, F. and Dubuisson, J. 2002. Subcellular localization and topology of the p7 polypeptide of hepatitis C virus. *J Virol.* **76**(8), pp.3720-3730.

Carrere-Kremer, S., Montpellier, C., Lorenzo, L., Brulin, B., Cocquerel, L., Belouzard, S., Penin, F. and Dubuisson, J. 2004. Regulation of hepatitis C virus polyprotein processing by signal peptidase involves structural determinants at the p7 sequence junctions. *J Biol Chem.* **279**(40), pp.41384-41392.

Carter, S.D., Dent, K.C., Atkins, E., Foster, T.L., Verow, M. and Gorny, P. 2010. Direct visualization of the small hydrophobic protein of human respiratory syncytial virus reveals the structural basis for membrane permeability. *FEBS Lett.* **584**.

Castelain, S., Bonte, D., Penin, F., Francois, C., Capron, D., Dedeurwaerder, S., Zawadzki, P., Morel, V., Wychowski, C. and Duverlie, G. 2007. Hepatitis C Virus p7 membrane protein quasispecies variability in chronically infected patients treated with interferon and ribavirin, with or without amantadine. *J Med Virol.* **79**(2), pp.144-154.

Castrucci, M.R., Hughes, M., Calzoletti, L., Donatelli, I., Wells, K., Takada, A. and Kawaoka, Y. 1997. The cysteine residues of the M2 protein are not required for influenza A virus replication. *Virology.* **238**(1), pp.128-134.

Catanese, M.T., Uryu, K., Kopp, M., Edwards, T.J., Andrus, L., Rice, W.J., Silvestry, M., Kuhn, R.J. and Rice, C.M. 2013. Ultrastructural analysis of hepatitis C virus particles. *Proc Natl Acad Sci U S A.* **110**(23), pp.9505-9510.

Catteau, A., Kalinina, O., Wagner, M.C., Deubel, V., Courageot, M.P. and Despres, P. 2003. Dengue virus M protein contains a proapoptotic sequence referred to as ApoptoM. *J Gen Virol.* **84**(Pt 10), pp.2781-2793.

Cerbino-Neto, J., Mesquita, E.C., Souza, T.M., Parreira, V., Wittlin, B.B., Durovni, B., Lemos, M.C., Vizzoni, A., Bispo de Filippis, A.M., Sampaio, S.A., Goncalves Bde, S. and Bozza, F.A. 2016. Clinical Manifestations of Zika Virus Infection, Rio de Janeiro, Brazil, 2015. *Emerg Infect Dis.* **22**(7), pp.1318-1320.

Cervantes-Salazar, M., Angel-Ambrocio, A.H., Soto-Acosta, R., Bautista-Carbajal, P., Hurtado-Monzon, A.M., Alcaraz-Estrada, S.L., Ludert, J.E. and Del Angel, R.M. 2015. Dengue virus NS1 protein interacts with the ribosomal protein RPL18: this interaction is required for viral translation and replication in Huh-7 cells. *Virology*. **484**, pp.113-126.

Chambers, T.J., McCourt, D.W. and Rice, C.M. 1989. Yellow fever virus proteins NS2A, NS2B, and NS4B: identification and partial N-terminal amino acid sequence analysis. *Virology*. **169**(1), pp.100-109.

Chambers, T.J., McCourt, D.W. and Rice, C.M. 1990. Production of yellow fever virus proteins in infected cells: identification of discrete polyprotein species and analysis of cleavage kinetics using region-specific polyclonal antisera. *Virology*. **177**(1), pp.159-174.

Chandler, D.E., Penin, F., Schulten, K. and Chipot, C. 2012. The p7 protein of hepatitis C virus forms structurally plastic, minimalist ion channels. *PLoS Comput Biol*. **8**(9), pe1002702.

Chang, J., Wang, L., Ma, D., Qu, X., Guo, H., Xu, X., Mason, P.M., Bourne, N., Moriarty, R., Gu, B., Guo, J.T. and Block, T.M. 2009. Novel imino sugar derivatives demonstrate potent antiviral activity against flaviviruses. *Antimicrob Agents Chemother*. **53**(4), pp.1501-1508.

Chen, J., Yang, Y.F., Yang, Y., Zou, P., Chen, J., He, Y., Shui, S.L., Cui, Y.R., Bai, R., Liang, Y.J., Hu, Y., Jiang, B., Lu, L., Zhang, X., Liu, J. and Xu, J. 2018. AXL promotes Zika virus infection in astrocytes by antagonizing type I interferon signalling. *Nat Microbiol*. **3**(3), pp.302-309.

Chen, M., Aoki-Utsubo, C., Kameoka, M., Deng, L., Terada, Y., Kamitani, W., Sato, K., Koyanagi, Y., Hijikata, M., Shindo, K., Noda, T., Kohara, M. and Hotta, H. 2017. Broad-spectrum antiviral agents: secreted phospholipase A2 targets viral envelope lipid bilayers derived from the endoplasmic reticulum membrane. *Sci Rep*. **7**(1), p15931.

Chen, W., OuYang, B. and Chou, J.J. 2018. Chen et al. reply. *Nature*. **562**(7727), pp.E19-E20.

Chen, W., OuYang, B. and Chou, J.J. 2019. Critical Effect of the Detergent:Protein Ratio on the Formation of the Hepatitis C Virus p7 Channel. *Biochemistry*. **58**(37), pp.3834-3837.

Chew, C.F., Vijayan, R., Chang, J., Zitzmann, N. and Biggin, P.C. 2009. Determination of pore-lining residues in the hepatitis C virus p7 protein. *Biophys J*. **96**(2), pp.L10-12.

Chizhnikov, I.V., Geraghty, F.M., Ogden, D.C., Hayhurst, A., Antoniou, M. and Hay, A.J. 1996. Selective proton permeability and pH regulation of the influenza virus M2 channel expressed in mouse erythroleukaemia cells. *J Physiol*. **494** (Pt 2), pp.329-336.

Chu, J.J. and Ng, M.L. 2004. Infectious entry of West Nile virus occurs through a clathrin-mediated endocytic pathway. *J Virol*. **78**(19), pp.10543-10555.

Ciampor, F., Thompson, C.A., Grambas, S. and Hay, A.J. 1992. Regulation of pH by the M2 protein of influenza A viruses. *Virus Res*. **22**(3), pp.247-258.

Clarke, D., Griffin, S., Beales, L., Gelais, C.S., Burgess, S., Harris, M. and Rowlands, D. 2006. Evidence for the formation of a heptameric ion channel complex by the hepatitis C virus p7 protein in vitro. *J Biol Chem*. **281**(48), pp.37057-37068.

Cleaves, G.R., Ryan, T.E. and Schlesinger, R.W. 1981. Identification and characterization of type 2 dengue virus replicative intermediate and replicative form RNAs. *Virology*. **111**(1), pp.73-83.

Clum, S., Ebner, K.E. and Padmanabhan, R. 1997. Cotranslational membrane insertion of the serine proteinase precursor NS2B-NS3(Pro) of dengue virus type 2 is required for efficient in vitro processing and is mediated through the hydrophobic regions of NS2B. *J Biol Chem.* **272**(49), pp.30715-30723.

Clyde, K. and Harris, E. 2006. RNA secondary structure in the coding region of dengue virus type 2 directs translation start codon selection and is required for viral replication. *J Virol.* **80**(5), pp.2170-2182.

Coady, M.J., Daniel, N.G., Tiganos, E., Allain, B., Friborg, J., Lapointe, J.Y. and Cohen, E.A. 1998. Effects of Vpu expression on *Xenopus* oocyte membrane conductance. *Virology.* **244**(1), pp.39-49.

Cocucci, E., Gaudin, R. and Kirchhausen, T. 2014. Dynamin recruitment and membrane scission at the neck of a clathrin-coated pit. *Mol Biol Cell.* **25**(22), pp.3595-3609.

Cohen, E.A., Terwilliger, E.F., Sodroski, J.G. and Haseltine, W.A. 1988. Identification of a protein encoded by the vpu gene of HIV-1. *Nature.* **334**(6182), pp.532-534.

Collins, P.L. and Mottet, G. 1993. Membrane orientation and oligomerization of the small hydrophobic protein of human respiratory syncytial virus. *J Gen Virol.* **74 (Pt 7)**, pp.1445-1450.

Cook, G.A., Dawson, L.A., Tian, Y. and Opella, S.J. 2013. Three-dimensional structure and interaction studies of hepatitis C virus p7 in 1,2-dihexanoyl-sn-glycero-3-phosphocholine by solution nuclear magnetic resonance. *Biochemistry.* **52**(31), pp.5295-5303.

Cortese, M., Goellner, S., Acosta, E.G., Neufeldt, C.J., Oleksiuk, O., Lampe, M., Haselmann, U., Funaya, C., Schieber, N., Ronchi, P., Schorb, M., Pruunsild, P., Schwab, Y., Chatel-Chaix, L., Ruggieri, A. and Bartenschlager, R. 2017. Ultrastructural Characterization of Zika Virus Replication Factories. *Cell Rep.* **18**(9), pp.2113-2123.

Coutard, B., Barral, K., Lichiere, J., Selisko, B., Martin, B., Aouadi, W., Lombardia, M.O., Debart, F., Vasseur, J.J., Guillemot, J.C., Canard, B. and Decroly, E. 2017. Zika Virus Methyltransferase: Structure and Functions for Drug Design Perspectives. *J Virol.* **91**(5).

Cross, K.J., Wharton, S.A., Skehel, J.J., Wiley, D.C. and Steinhauer, D.A. 2001. Studies on influenza haemagglutinin fusion peptide mutants generated by reverse genetics. *EMBO J.* **20**(16), pp.4432-4442.

Cruz-Oliveira, C., Freire, J.M., Conceicao, T.M., Higa, L.M., Castanho, M.A. and Da Poian, A.T. 2015. Receptors and routes of dengue virus entry into the host cells. *FEMS Microbiol Rev.* **39**(2), pp.155-170.

Daelemans, D., Pauwels, R., De Clercq, E. and Pannecouque, C. 2011. A time-of-drug addition approach to target identification of antiviral compounds. *Nat Protoc.* **6**(6), pp.925-933.

Daffis, S., Szretter, K.J., Schriewer, J., Li, J., Youn, S., Errett, J., Lin, T.Y., Schneller, S., Züst, R., Dong, H., Thiel, V., Sen, G.C., Fensterl, V., Klimstra, W.B., Pierson, T.C., Buller, R.M., Gale, M., Jr., Shi, P.Y. and Diamond, M.S. 2010. 2'-O methylation of the viral mRNA cap evades host restriction by IFIT family members. *Nature.* **468**(7322), pp.452-456.

Dai, L., Song, J., Lu, X., Deng, Y.Q., Musyoki, A.M., Cheng, H., Zhang, Y., Yuan, Y., Song, H., Haywood, J., Xiao, H., Yan, J., Shi, Y., Qin, C.F., Qi, J. and Gao, G.F. 2016. Structures of the Zika Virus Envelope Protein and Its Complex with a Flavivirus Broadly Protective Antibody. *Cell Host Microbe.* **19**(5), pp.696-704.

- Danthi, P., Tosteson, M., Li, Q.H. and Chow, M. 2003. Genome delivery and ion channel properties are altered in VP4 mutants of poliovirus. *J Virol.* **77**(9), pp.5266-5274.
- Darwish, M.A., Hoogstraal, H., Roberts, T.J., Ahmed, I.P. and Omar, F. 1983. A sero-epidemiological survey for certain arboviruses (Togaviridae) in Pakistan. *Trans R Soc Trop Med Hyg.* **77**(4), pp.442-445.
- Davies, W.L., Grunert, R.R., Haff, R.F., McGahen, J.W., Neumayer, E.M., Paulshock, M., Watts, J.C., Wood, T.R., Hermann, E.C. and Hoffmann, C.E. 1964. Antiviral Activity of 1-Adamantanamine (Amantadine). *Science.* **144**(3620), pp.862-863.
- Davis, M.P., Bottley, G., Beales, L.P., Killington, R.A., Rowlands, D.J. and Tuthill, T.J. 2008. Recombinant VP4 of human rhinovirus induces permeability in model membranes. *J Virol.* **82**(8), pp.4169-4174.
- Dawkins, A.T., Jr., Gallager, L.R., Togo, Y., Hornick, R.B. and Harris, B.A. 1968. Studies on induced influenza in man. II. Double-blind study designed to assess the prophylactic efficacy of an analogue of amantadine hydrochloride. *JAMA.* **203**(13), pp.1095-1099.
- de Jong, D.H., Singh, G., Bennett, W.F., Arnarez, C., Wassenaar, T.A., Schafer, L.V., Periole, X., Tieleman, D.P. and Marrink, S.J. 2013. Improved Parameters for the Martini Coarse-Grained Protein Force Field. *J Chem Theory Comput.* **9**(1), pp.687-697.
- de Oliveira Dos Santos Soares, R., Bortot, L.O., van der Spoel, D. and Caliri, A. 2017. Membrane vesiculation induced by proteins of the dengue virus envelope studied by molecular dynamics simulations. *J Phys Condens Matter.* **29**(50), p504002.
- de Oliveira, W.K., Carmo, E.H., Henriques, C.M., Coelho, G., Vazquez, E., Cortez-Escalante, J., Molina, J., Aldighieri, S., Espinal, M.A. and Dye, C. 2017a. Zika Virus Infection and Associated Neurologic Disorders in Brazil. *N Engl J Med.* **376**(16), pp.1591-1593.
- de Oliveira, W.K., de Franca, G.V.A., Carmo, E.H., Duncan, B.B., de Souza Kuchenbecker, R. and Schmidt, M.I. 2017b. Infection-related microcephaly after the 2015 and 2016 Zika virus outbreaks in Brazil: a surveillance-based analysis. *Lancet.* **390**(10097), pp.861-870.
- Decroly, E., Ferron, F., Lescar, J. and Canard, B. 2011. Conventional and unconventional mechanisms for capping viral mRNA. *Nat Rev Microbiol.* **10**(1), pp.51-65.
- Delvecchio, R., Higa, L.M., Pezzuto, P., Valadao, A.L., Garcez, P.P., Monteiro, F.L., Loiola, E.C., Dias, A.A., Silva, F.J., Aliota, M.T., Caine, E.A., Osorio, J.E., Bellio, M., O'Connor, D.H., Rehen, S., de Aguiar, R.S., Savarino, A., Campanati, L. and Tanuri, A. 2016. Chloroquine, an Endocytosis Blocking Agent, Inhibits Zika Virus Infection in Different Cell Models. *Viruses.* **8**(12).
- Descalzi, D., Folli, C., Nicolini, G., Riccio, A.M., Gamalero, C., Scordamaglia, F. and Canonica, G.W. 2008. Anti-proliferative and anti-remodelling effect of beclomethasone dipropionate, formoterol and salbutamol alone or in combination in primary human bronchial fibroblasts. *Allergy.* **63**(4), pp.432-437.
- Devillers, J. 2018. Repurposing drugs for use against Zika virus infection. *SAR QSAR Environ Res.* **29**(2), pp.103-115.
- Dick, G.W., Kitchen, S.F. and Haddow, A.J. 1952. Zika virus. I. Isolations and serological specificity. *Trans R Soc Trop Med Hyg.* **46**(5), pp.509-520.
- DiMaio, D. and Petti, L.M. 2013. The E5 proteins. *Virology.* **445**(1-2), pp.99-114.

Ding, W., Palaiokostas, M., Wang, W. and Orsi, M. 2015. Effects of Lipid Composition on Bilayer Membranes Quantified by All-Atom Molecular Dynamics. *J Phys Chem B*. **119**(49), pp.15263-15274.

Donald, C.L., Brennan, B., Cumberworth, S.L., Rezelj, V.V., Clark, J.J., Cordeiro, M.T., Freitas de Oliveira Franca, R., Pena, L.J., Wilkie, G.S., Da Silva Filipe, A., Davis, C., Hughes, J., Varjak, M., Selinger, M., Zuvanov, L., Owsianka, A.M., Patel, A.H., McLauchlan, J., Lindenbach, B.D., Fall, G., Sall, A.A., Biek, R., Rehwinkel, J., Schnettler, E. and Kohl, A. 2016. Full Genome Sequence and sfRNA Interferon Antagonist Activity of Zika Virus from Recife, Brazil. *PLoS Negl Trop Dis*. **10**(10), pe0005048.

Dong, H., Fink, K., Zust, R., Lim, S.P., Qin, C.F. and Shi, P.Y. 2014. Flavivirus RNA methylation. *J Gen Virol*. **95**(Pt 4), pp.763-778.

Dowd, K.A., Ko, S.Y., Morabito, K.M., Yang, E.S., Pelc, R.S., DeMaso, C.R., Castilho, L.R., Abbink, P., Boyd, M., Nityanandam, R., Gordon, D.N., Gallagher, J.R., Chen, X., Todd, J.P., Tsybovsky, Y., Harris, A., Huang, Y.S., Higgs, S., Vanlandingham, D.L., Andersen, H., Lewis, M.G., De La Barrera, R., Eckels, K.H., Jarman, R.G., Nason, M.C., Barouch, D.H., Roederer, M., Kong, W.P., Mascola, J.R., Pierson, T.C. and Graham, B.S. 2016. Rapid development of a DNA vaccine for Zika virus. *Science*. **354**(6309), pp.237-240.

Dowd, K.A., Mukherjee, S., Kuhn, R.J. and Pierson, T.C. 2014. Combined effects of the structural heterogeneity and dynamics of flaviviruses on antibody recognition. *J Virol*. **88**(20), pp.11726-11737.

Drakopoulos, A., Tzitzoglaki, C., McGuire, K., Hoffmann, A., Konstantinidi, A., Kolokouris, D., Ma, C., Freudenberger, K., Hutterer, J., Gauglitz, G., Wang, J., Schmidtke, M., Busath, D.D. and Kolocouris, A. 2018. Unraveling the Binding, Proton Blockage, and Inhibition of Influenza M2 WT and S31N by Rimantadine Variants. *ACS Med Chem Lett*. **9**(3), pp.198-203.

Du, Q.S., Huang, R.B., Wang, C.H., Li, X.M. and Chou, K.C. 2009. Energetic analysis of the two controversial drug binding sites of the M2 proton channel in influenza A virus. *J Theor Biol*. **259**(1), pp.159-164.

Dudley, D.M., Aliota, M.T., Mohr, E.L., Weiler, A.M., Lehrer-Brey, G., Weisgrau, K.L., Mohns, M.S., Breitbach, M.E., Rasheed, M.N., Newman, C.M., Gellerup, D.D., Moncla, L.H., Post, J., Schultz-Darken, N., Schotzko, M.L., Hayes, J.M., Eudailey, J.A., Moody, M.A., Permar, S.R., O'Connor, S.L., Rakasz, E.G., Simmons, H.A., Capuano, S., Golos, T.G., Osorio, J.E., Friedrich, T.C. and O'Connor, D.H. 2016. A rhesus macaque model of Asian-lineage Zika virus infection. *Nat Commun*. **7**, p12204.

Duff, K.C. and Ashley, R.H. 1992. The transmembrane domain of influenza A M2 protein forms amantadine-sensitive proton channels in planar lipid bilayers. *Virology*. **190**(1), pp.485-489.

Duffy, M.R., Chen, T.H., Hancock, W.T., Powers, A.M., Kool, J.L., Lanciotti, R.S., Pretrick, M., Marfel, M., Holzbauer, S., Dubray, C., Guillaumot, L., Griggs, A., Bel, M., Lambert, A.J., Laven, J., Kosoy, O., Panella, A., Biggerstaff, B.J., Fischer, M. and Hayes, E.B. 2009. Zika virus outbreak on Yap Island, Federated States of Micronesia. *N Engl J Med*. **360**(24), pp.2536-2543.

Edgil, D., Polacek, C. and Harris, E. 2006. Dengue virus utilizes a novel strategy for translation initiation when cap-dependent translation is inhibited. *J Virol*. **80**(6), pp.2976-2986.

Egloff, M.P., Benarroch, D., Selisko, B., Romette, J.L. and Canard, B. 2002. An RNA cap (nucleoside-2'-O-)-methyltransferase in the flavivirus RNA polymerase

NS5: crystal structure and functional characterization. *EMBO J.* **21**(11), pp.2757-2768.

Elshuber, S., Allison, S.L., Heinz, F.X. and Mandl, C.W. 2003. Cleavage of protein prM is necessary for infection of BHK-21 cells by tick-borne encephalitis virus. *J Gen Virol.* **84**(Pt 1), pp.183-191.

Eurosurveillance editorial, t. 2016. Resources and latest news about Zika virus disease available from ECDC. *Euro Surveill.* **21**(5), p32.

Ewart, G.D., Mills, K., Cox, G.B. and Gage, P.W. 2002. Amiloride derivatives block ion channel activity and enhancement of virus-like particle budding caused by HIV-1 protein Vpu. *Eur Biophys J.* **31**(1), pp.26-35.

Ewart, G.D., Sutherland, T., Gage, P.W. and Cox, G.B. 1996. The Vpu protein of human immunodeficiency virus type 1 forms cation-selective ion channels. *J Virol.* **70**(10), pp.7108-7115.

Eyer, L., Nencka, R., Huvarova, I., Palus, M., Joao Alves, M., Gould, E.A., De Clercq, E. and Ruzek, D. 2016. Nucleoside Inhibitors of Zika Virus. *J Infect Dis.* **214**(5), pp.707-711.

Fagbami, A. 1977. Epidemiological investigations on arbovirus infections at Igbo-Ora, Nigeria. *Trop Geogr Med.* **29**(2), pp.187-191.

Fairman-Williams, M.E., Guenther, U.P. and Jankowsky, E. 2010. SF1 and SF2 helicases: family matters. *Curr Opin Struct Biol.* **20**(3), pp.313-324.

Falgout, B. and Markoff, L. 1995. Evidence that flavivirus NS1-NS2A cleavage is mediated by a membrane-bound host protease in the endoplasmic reticulum. *J Virol.* **69**(11), pp.7232-7243.

Falgout, B., Pethel, M., Zhang, Y.M. and Lai, C.J. 1991. Both nonstructural proteins NS2B and NS3 are required for the proteolytic processing of dengue virus nonstructural proteins. *J Virol.* **65**(5), pp.2467-2475.

Ferreira-de-Brito, A., Ribeiro, I.P., Miranda, R.M., Fernandes, R.S., Campos, S.S., Silva, K.A., Castro, M.G., Bonaldo, M.C., Brasil, P. and Lourenco-de-Oliveira, R. 2016. First detection of natural infection of *Aedes aegypti* with Zika virus in Brazil and throughout South America. *Mem Inst Oswaldo Cruz.* **111**(10), pp.655-658.

Ferreira, A.C., Zaverucha-do-Valle, C., Reis, P.A., Barbosa-Lima, G., Vieira, Y.R., Mattos, M., Silva, P.P., Sacramento, C., de Castro Faria Neto, H.C., Campanati, L., Tanuri, A., Bruning, K., Bozza, F.A., Bozza, P.T. and Souza, T.M.L. 2017. Sofosbuvir protects Zika virus-infected mice from mortality, preventing short- and long-term sequelae. *Sci Rep.* **7**(1), p9409.

Filomatori, C.V., Lodeiro, M.F., Alvarez, D.E., Samsa, M.M., Pietrasanta, L. and Gamarnik, A.V. 2006. A 5' RNA element promotes dengue virus RNA synthesis on a circular genome. *Genes Dev.* **20**(16), pp.2238-2249.

Fink, S.L., Vojtech, L., Wagoner, J., Slivinski, N.S.J., Jackson, K.J., Wang, R., Khadka, S., Luthra, P., Basler, C.F. and Polyak, S.J. 2018. The Antiviral Drug Arbidol Inhibits Zika Virus. *Sci Rep.* **8**(1), p8989.

Firth, A.E. and Atkins, J.F. 2009. A conserved predicted pseudoknot in the NS2A-encoding sequence of West Nile and Japanese encephalitis flaviviruses suggests NS1' may derive from ribosomal frameshifting. *Virology.* **6**, p14.

Firth, A.E., Blitvich, B.J., Wills, N.M., Miller, C.L. and Atkins, J.F. 2010. Evidence for ribosomal frameshifting and a novel overlapping gene in the genomes of insect-specific flaviviruses. *Virology.* **399**(1), pp.153-166.

Fiser, A. and Sali, A. 2003. Modeller: generation and refinement of homology-based protein structure models. *Methods Enzymol.* **374**, pp.461-491.

Flamand, M., Megret, F., Mathieu, M., Lepault, J., Rey, F.A. and Deubel, V. 1999. Dengue virus type 1 nonstructural glycoprotein NS1 is secreted from mammalian cells as a soluble hexamer in a glycosylation-dependent fashion. *J Virol.* **73**(7), pp.6104-6110.

Fontaine, K.A., Leon, K.E., Khalid, M.M., Tomar, S., Jimenez-Morales, D., Dunlap, M., Kaye, J.A., Shah, P.S., Finkbeiner, S., Krogan, N.J. and Ott, M. 2018. The Cellular NMD Pathway Restricts Zika Virus Infection and Is Targeted by the Viral Capsid Protein. *mBio.* **9**(6).

Foo, S.S., Chen, W., Chan, Y., Bowman, J.W., Chang, L.C., Choi, Y., Yoo, J.S., Ge, J., Cheng, G., Bonnin, A., Nielsen-Saines, K., Brasil, P. and Jung, J.U. 2017. Asian Zika virus strains target CD14(+) blood monocytes and induce M2-skewed immunosuppression during pregnancy. *Nat Microbiol.* **2**(11), pp.1558-1570.

Foster, T.L., Thompson, G.S., Kalverda, A.P., Kankanala, J., Bentham, M., Wetherill, L.F., Thompson, J., Barker, A.M., Clarke, D., Noerenberg, M., Pearson, A.R., Rowlands, D.J., Homans, S.W., Harris, M., Foster, R. and Griffin, S. 2014. Structure-guided design affirms inhibitors of hepatitis C virus p7 as a viable class of antivirals targeting virion release. *Hepatology.* **59**(2), pp.408-422.

Foster, T.L., Verow, M., Wozniak, A.L., Bentham, M.J., Thompson, J., Atkins, E., Weinman, S.A., Fishwick, C., Foster, R., Harris, M. and Griffin, S. 2011. Resistance mutations define specific antiviral effects for inhibitors of the hepatitis C virus p7 ion channel. *Hepatology.* **54**(1), pp.79-90.

Fowler, A.M., Tang, W.W., Young, M.P., Mamidi, A., Viramontes, K.M., McCauley, M.D., Carlin, A.F., Schooley, R.T., Swanstrom, J., Baric, R.S., Govero, J., Diamond, M.S. and Shresta, S. 2018. Maternally Acquired Zika Antibodies Enhance Dengue Disease Severity in Mice. *Cell Host Microbe.* **24**(5), pp.743-750 e745.

Foy, B.D., Kobylinski, K.C., Chilson Foy, J.L., Blitvich, B.J., Travassos da Rosa, A., Haddow, A.D., Lanciotti, R.S. and Tesh, R.B. 2011. Probable non-vector-borne transmission of Zika virus, Colorado, USA. *Emerg Infect Dis.* **17**(5), pp.880-882.

Fragoso, P., Armijo, A., Gomez, D., Gomez, C., Bugueno, M., Sanchez, G. and Venegas, J. 2018. Molecular Characterization of the cry Gene profile of *Bacillus thuringiensis* Isolated from a Caribbean Region of Colombia. *Pol J Microbiol.* **67**(1), pp.19-26.

Fricks, C.E. and Hogle, J.M. 1990. Cell-induced conformational change in poliovirus: externalization of the amino terminus of VP1 is responsible for liposome binding. *J Virol.* **64**(5), pp.1934-1945.

Fuentes, S., Tran, K.C., Luthra, P., Teng, M.N. and He, B. 2007. Function of the respiratory syncytial virus small hydrophobic protein. *J Virol.* **81**(15), pp.8361-8366.

Gan, S.W., Ng, L., Lin, X., Gong, X. and Torres, J. 2008. Structure and ion channel activity of the human respiratory syncytial virus (hRSV) small hydrophobic protein transmembrane domain. *Protein Sci.* **17**(5), pp.813-820.

Gan, S.W., Surya, W., Vararattanavech, A. and Torres, J. 2014. Two different conformations in hepatitis C virus p7 protein account for proton transport and dye release. *PLoS One.* **9**(1), pe78494.

Gan, S.W., Tan, E., Lin, X., Yu, D., Wang, J. and Tan, G.M. 2012. The small hydrophobic protein of the human respiratory syncytial virus forms pentameric ion channels. *J Biol Chem.* **287**.

Garcez, P.P., Loiola, E.C., Madeiro da Costa, R., Higa, L.M., Trindade, P., Delvecchio, R., Nascimento, J.M., Brindeiro, R., Tanuri, A. and Rehen, S.K. 2016. Zika virus impairs growth in human neurospheres and brain organoids. *Science*. **352**(6287), pp.816-818.

Garcia-Blanco, M.A., Vasudevan, S.G., Bradrick, S.S. and Nicchitta, C. 2016. Flavivirus RNA transactions from viral entry to genome replication. *Antiviral Res.* **134**, pp.244-249.

Gastaminza, P., Cheng, G., Wieland, S., Zhong, J., Liao, W. and Chisari, F.V. 2008. Cellular determinants of hepatitis C virus assembly, maturation, degradation, and secretion. *J Virol.* **82**(5), pp.2120-2129.

Gaudinski, M.R., Houser, K.V., Morabito, K.M., Hu, Z., Yamshchikov, G., Rothwell, R.S., Berkowitz, N., Mendoza, F., Saunders, J.G., Novik, L., Hendel, C.S., Holman, L.A., Gordon, I.J., Cox, J.H., Edupuganti, S., McArthur, M.A., Roupheal, N.G., Lyke, K.E., Cummings, G.E., Sitar, S., Bailer, R.T., Foreman, B.M., Burgomaster, K., Pelc, R.S., Gordon, D.N., DeMaso, C.R., Dowd, K.A., Laurencot, C., Schwartz, R.M., Mascola, J.R., Graham, B.S., Pierson, T.C., Ledgerwood, J.E., Chen, G.L., Vrc and teams, V.R.C.s. 2018. Safety, tolerability, and immunogenicity of two Zika virus DNA vaccine candidates in healthy adults: randomised, open-label, phase 1 clinical trials. *Lancet*. **391**(10120), pp.552-562.

George, J., Valiant, W.G., Mattapallil, M.J., Walker, M., Huang, Y.S., Vanlandingham, D.L., Misamore, J., Greenhouse, J., Weiss, D.E., Verthelyi, D., Higgs, S., Andersen, H., Lewis, M.G. and Mattapallil, J.J. 2017. Prior Exposure to Zika Virus Significantly Enhances Peak Dengue-2 Viremia in Rhesus Macaques. *Sci Rep.* **7**(1), p10498.

Gervais, C., Do, F., Cantin, A., Kukolj, G., White, P.W., Gauthier, A. and Vaillancourt, F.H. 2011. Development and validation of a high-throughput screening assay for the hepatitis C virus p7 viroporin. *J Biomol Screen.* **16**(3), pp.363-369.

Geschwind, D.H. and Rakic, P. 2013. Cortical evolution: judge the brain by its cover. *Neuron.* **80**(3), pp.633-647.

Gieswein, C.E., Sharom, F.J. and Wildeman, A.G. 2003. Oligomerization of the E5 protein of human papillomavirus type 16 occurs through multiple hydrophobic regions. *Virology.* **313**(2), pp.415-426.

Gillespie, L.K., Hoenen, A., Morgan, G. and Mackenzie, J.M. 2010. The endoplasmic reticulum provides the membrane platform for biogenesis of the flavivirus replication complex. *J Virol.* **84**(20), pp.10438-10447.

Gollins, S.W. and Porterfield, J.S. 1986. The uncoating and infectivity of the flavivirus West Nile on interaction with cells: effects of pH and ammonium chloride. *J Gen Virol.* **67 (Pt 9)**, pp.1941-1950.

Goncalves, R.B., Mendes, Y.S., Soares, M.R., Katpally, U., Smith, T.J., Silva, J.L. and Oliveira, A.C. 2007. VP4 protein from human rhinovirus 14 is released by pressure and locked in the capsid by the antiviral compound WIN. *J Mol Biol.* **366**(1), pp.295-306.

Gong, Z., Xu, X. and Han, G.Z. 2017. The Diversification of Zika Virus: Are There Two Distinct Lineages? *Genome Biol Evol.* **9**(11), pp.2940-2945.

Gonzalez, M.E. and Carrasco, L. 2003. Viroporins. *FEBS Lett.* **552**(1), pp.28-34.

Gorman, M.J., Caine, E.A., Zaitsev, K., Begley, M.C., Weger-Lucarelli, J., Uccellini, M.B., Tripathi, S., Morrison, J., Yount, B.L., Dinno, K.H., 3rd, Ruckert, C., Young, M.C., Zhu, Z., Robertson, S.J., McNally, K.L., Ye, J., Cao, B., Mysorekar, I.U., Ebel, G.D., Baric, R.S., Best, S.M., Artyomov, M.N., Garcia-

Sastre, A. and Diamond, M.S. 2018. An Immunocompetent Mouse Model of Zika Virus Infection. *Cell Host Microbe*. **23**(5), pp.672-685 e676.

Govorkova, E.A., Fang, H.B., Tan, M. and Webster, R.G. 2004. Neuraminidase inhibitor-rimantadine combinations exert additive and synergistic anti-influenza virus effects in MDCK cells. *Antimicrob Agents Chemother*. **48**(12), pp.4855-4863.

Grambas, S. and Hay, A.J. 1992. Maturation of influenza A virus hemagglutinin-estimates of the pH encountered during transport and its regulation by the M2 protein. *Virology*. **190**(1), pp.11-18.

Grant, A., Ponia, S.S., Tripathi, S., Balasubramaniam, V., Miorin, L., Sourisseau, M., Schwarz, M.C., Sanchez-Seco, M.P., Evans, M.J., Best, S.M. and Garcia-Sastre, A. 2016. Zika Virus Targets Human STAT2 to Inhibit Type I Interferon Signaling. *Cell Host Microbe*. **19**(6), pp.882-890.

Grantham, M.L., Stewart, S.M., Lalime, E.N. and Pekosz, A. 2010. Tyrosines in the influenza A virus M2 protein cytoplasmic tail are critical for production of infectious virus particles. *J Virol*. **84**(17), pp.8765-8776.

Grice, A.L., Kerr, I.D. and Sansom, M.S. 1997. Ion channels formed by HIV-1 Vpu: a modelling and simulation study. *FEBS Lett*. **405**(3), pp.299-304.

Griffin, S., Clarke, D., McCormick, C., Rowlands, D. and Harris, M. 2005. Signal peptide cleavage and internal targeting signals direct the hepatitis C virus p7 protein to distinct intracellular membranes. *J Virol*. **79**(24), pp.15525-15536.

Griffin, S., Stgelais, C., Owsianka, A.M., Patel, A.H., Rowlands, D. and Harris, M. 2008. Genotype-dependent sensitivity of hepatitis C virus to inhibitors of the p7 ion channel. *Hepatology*. **48**(6), pp.1779-1790.

Griffin, S.D. 2009. Plugging the holes in hepatitis C virus antiviral therapy. *Proc Natl Acad Sci U S A*. **106**(31), pp.12567-12568.

Griffin, S.D., Beales, L.P., Clarke, D.S., Worsfold, O., Evans, S.D., Jaeger, J., Harris, M.P. and Rowlands, D.J. 2003. The p7 protein of hepatitis C virus forms an ion channel that is blocked by the antiviral drug, Amantadine. *FEBS Lett*. **535**(1-3), pp.34-38.

Griffin, S.D., Harvey, R., Clarke, D.S., Barclay, W.S., Harris, M. and Rowlands, D.J. 2004. A conserved basic loop in hepatitis C virus p7 protein is required for amantadine-sensitive ion channel activity in mammalian cells but is dispensable for localization to mitochondria. *J Gen Virol*. **85**(Pt 2), pp.451-461.

Gutsche, I., Coulibaly, F., Voss, J.E., Salmon, J., d'Alayer, J., Ermonval, M., Larquet, E., Charneau, P., Krey, T., Megret, F., Guittet, E., Rey, F.A. and Flamand, M. 2011. Secreted dengue virus nonstructural protein NS1 is an atypical barrel-shaped high-density lipoprotein. *Proc Natl Acad Sci U S A*. **108**(19), pp.8003-8008.

Guyatt, K.J., Westaway, E.G. and Khromykh, A.A. 2001. Expression and purification of enzymatically active recombinant RNA-dependent RNA polymerase (NS5) of the flavivirus Kunjin. *J Virol Methods*. **92**(1), pp.37-44.

Hackett, B.A. and Cherry, S. 2018. Flavivirus internalization is regulated by a size-dependent endocytic pathway. *Proc Natl Acad Sci U S A*. **115**(16), pp.4246-4251.

Haddow, A.D., Schuh, A.J., Yasuda, C.Y., Kasper, M.R., Heang, V., Huy, R., Guzman, H., Tesh, R.B. and Weaver, S.C. 2012. Genetic characterization of Zika virus strains: geographic expansion of the Asian lineage. *PLoS Negl Trop Dis*. **6**(2), pe1477.

Halbert, C.L. and Galloway, D.A. 1988. Identification of the E5 open reading frame of human papillomavirus type 16. *J Virol*. **62**(3), pp.1071-1075.

Halgren, T.A. 2009. Identifying and characterizing binding sites and assessing druggability. *J Chem Inf Model.* **49**(2), pp.377-389.

Hamel, R., Dejarnac, O., Wichit, S., Ekcharyawat, P., Neyret, A., Luplertlop, N., Perera-Lecoin, M., Surasombatpattana, P., Talignani, L., Thomas, F., Cao-Lormeau, V.M., Choumet, V., Briant, L., Despres, P., Amara, A., Yssel, H. and Misse, D. 2015. Biology of Zika Virus Infection in Human Skin Cells. *J Virol.* **89**(17), pp.8880-8896.

Hamel, R., Ferraris, P., Wichit, S., Diop, F., Talignani, L., Pompon, J., Garcia, D., Liegeois, F., Sall, A.A., Yssel, H. and Misse, D. 2017. African and Asian Zika virus strains differentially induce early antiviral responses in primary human astrocytes. *Infect Genet Evol.* **49**, pp.134-137.

Han, Y. and Mesplede, T. 2018. Investigational drugs for the treatment of Zika virus infection: a preclinical and clinical update. *Expert Opin Investig Drugs.* **27**(12), pp.951-962.

Hanners, N.W., Eitson, J.L., Usui, N., Richardson, R.B., Wexler, E.M., Konopka, G. and Schoggins, J.W. 2016. Western Zika Virus in Human Fetal Neural Progenitors Persists Long Term with Partial Cytopathic and Limited Immunogenic Effects. *Cell Rep.* **15**(11), pp.2315-2322.

Harrison, S.C. 2008. The pH sensor for flavivirus membrane fusion. *J Cell Biol.* **183**(2), pp.177-179.

Haschemeyer, R.H. 1970. Electron microscopy of enzymes. *Adv Enzymol Relat Areas Mol Biol.* **33**, pp.71-118.

Hay, A.J., Wolstenholme, A.J., Skehel, J.J. and Smith, M.H. 1985. The molecular basis of the specific anti-influenza action of amantadine. *EMBO J.* **4**(11), pp.3021-3024.

Hayashida, E., Ling, Z.L., Ashhurst, T.M., Viengkhou, B., Jung, S.R., Songkhunawej, P., West, P.K., King, N.J.C. and Hofer, M.J. 2019. Zika virus encephalitis in immunocompetent mice is dominated by innate immune cells and does not require T or B cells. *J Neuroinflammation.* **16**(1), p177.

Hayden, F.G., Gwaltney, J.M., Jr., Van de Castle, R.L., Adams, K.F. and Giordani, B. 1981. Comparative toxicity of amantadine hydrochloride and rimantadine hydrochloride in healthy adults. *Antimicrob Agents Chemother.* **19**(2), pp.226-233.

Hayes, E.B. 2009. Zika virus outside Africa. *Emerg Infect Dis.* **15**(9), pp.1347-1350.

Helenius, A. 1992. Unpacking the incoming influenza virus. *Cell.* **69**(4), pp.577-578.

Hercik, K., Kozak, J., Sala, M., Dejmek, M., Hrebabecky, H., Zbornikova, E., Smola, M., Ruzek, D., Nencka, R. and Boura, E. 2017. Adenosine triphosphate analogs can efficiently inhibit the Zika virus RNA-dependent RNA polymerase. *Antiviral Res.* **137**, pp.131-133.

Herrmann, J.E., Bruns, M., West, K. and Ennis, F.A. 1989. Efficacy of rimantadine hydrochloride in the treatment of influenza infection of mice. *Antiviral Res.* **11**(3), pp.127-135.

Hess, B., Bekker, H., Berendsen, H.J.C. and Fraaije, J.G.E.M. 1997. LINCS: A linear constraint solver for molecular simulations. *Journal of Computational Chemistry.* **18**(12), pp.1463-1472.

Hinckley, A.F., O'Leary, D.R. and Hayes, E.B. 2007. Transmission of West Nile virus through human breast milk seems to be rare. *Pediatrics.* **119**(3), pp.e666-671.

Hodge, K., Tunghirun, C., Kamkaew, M., Limjindaporn, T., Yenchitsomanus, P.T. and Chimnaronk, S. 2016. Identification of a Conserved RNA-dependent RNA Polymerase (RdRp)-RNA Interface Required for Flaviviral Replication. *J Biol Chem.* **291**(33), pp.17437-17449.

Hoestgaard-Jensen, K., Dalby, N.O., Wolinsky, T.D., Murphey, C., Jones, K.A., Rottlander, M., Frederiksen, K., Watson, W.P., Jensen, K. and Ebert, B. 2010. Pharmacological characterization of a novel positive modulator at alpha 4 beta 3 delta-containing extrasynaptic GABA(A) receptors. *Neuropharmacology.* **58**(4-5), pp.702-711.

Hoffman, H.E., Gaylord, J.C., Blasecki, J.W., Shalaby, L.M. and Whitney, C.C., Jr. 1988. Pharmacokinetics and metabolism of rimantadine hydrochloride in mice and dogs. *Antimicrob Agents Chemother.* **32**(11), pp.1699-1704.

Holsinger, L.J. and Lamb, R.A. 1991. Influenza virus M2 integral membrane protein is a homotetramer stabilized by formation of disulfide bonds. *Virology.* **183**(1), pp.32-43.

Holsinger, L.J., Shaughnessy, M.A., Micko, A., Pinto, L.H. and Lamb, R.A. 1995. Analysis of the posttranslational modifications of the influenza virus M2 protein. *J Virol.* **69**(2), pp.1219-1225.

Hout, D.R., Gomez, M.L., Pacyniak, E., Gomez, L.M., Fegley, B., Mulcahy, E.R., Hill, M.S., Culley, N., Pinson, D.M., Nothnick, W., Powers, M.F., Wong, S.W. and Stephens, E.B. 2006. Substitution of the transmembrane domain of Vpu in simian-human immunodeficiency virus (SHIVKU1bMC33) with that of M2 of influenza A results in a virus that is sensitive to inhibitors of the M2 ion channel and is pathogenic for pig-tailed macaques. *Virology.* **344**(2), pp.541-559.

Hsu, K., Seharaseyon, J., Dong, P., Bour, S. and Marban, E. 2004. Mutual functional destruction of HIV-1 Vpu and host TASK-1 channel. *Mol Cell.* **14**(2), pp.259-267.

Hu, F., Luo, W., Cady, S.D. and Hong, M. 2011. Conformational plasticity of the influenza A M2 transmembrane helix in lipid bilayers under varying pH, drug binding, and membrane thickness. *Biochim Biophys Acta.* **1808**(1), pp.415-423.

Huang, J. and MacKerell, A.D., Jr. 2013. CHARMM36 all-atom additive protein force field: validation based on comparison to NMR data. *J Comput Chem.* **34**(25), pp.2135-2145.

Huotari, J. and Helenius, A. 2011. Endosome maturation. *EMBO J.* **30**(17), pp.3481-3500.

Hyser, J.M. 2015. Viroporins. *Electrophysiology of Unconventional Channels and Pores.* **18**, pp.153-181.

Ilyushina, N.A., Bovin, N.V., Webster, R.G. and Govorkova, E.A. 2006. Combination chemotherapy, a potential strategy for reducing the emergence of drug-resistant influenza A variants. *Antiviral Res.* **70**(3), pp.121-131.

Issur, M., Geiss, B.J., Bougie, I., Picard-Jean, F., Despins, S., Mayette, J., Hobdey, S.E. and Bisailon, M. 2009. The flavivirus NS5 protein is a true RNA guanylyltransferase that catalyzes a two-step reaction to form the RNA cap structure. *RNA.* **15**(12), pp.2340-2350.

Ito, T., Gorman, O.T., Kawaoka, Y., Bean, W.J. and Webster, R.G. 1991. Evolutionary analysis of the influenza A virus M gene with comparison of the M1 and M2 proteins. *J Virol.* **65**(10), pp.5491-5498.

Jackman, J.A., Costa, V.V., Park, S., Real, A., Park, J.H., Cardozo, P.L., Ferhan, A.R., Olmo, I.G., Moreira, T.P., Bambirra, J.L., Queiroz, V.F., Queiroz-Junior, C.M., Foureaux, G., Souza, D.G., Ribeiro, F.M., Yoon, B.K.,

Wynendaele, E., De Spiegeleer, B., Teixeira, M.M. and Cho, N.J. 2018. Therapeutic treatment of Zika virus infection using a brain-penetrating antiviral peptide. *Nat Mater.* **17**(11), pp.971-977.

Jalily, P.H., Eldstrom, J., Miller, S.C., Kwan, D.C., Tai, S.S., Chou, D., Niikura, M., Tietjen, I. and Fedida, D. 2016. Mechanisms of Action of Novel Influenza A/M2 Viroprotein Inhibitors Derived from Hexamethylene Amiloride. *Mol Pharmacol.* **90**(2), pp.80-95.

Jan, C., Languillat, G., Renaudet, J. and Robin, Y. 1978. [A serological survey of arboviruses in Gabon]. *Bull Soc Pathol Exot Filiales.* **71**(2), pp.140-146.

Jarsch, I.K., Daste, F. and Gallop, J.L. 2016. Membrane curvature in cell biology: An integration of molecular mechanisms. *J Cell Biol.* **214**(4), pp.375-387.

Jensen, M.O. and Mouritsen, O.G. 2004. Lipids do influence protein function-the hydrophobic matching hypothesis revisited. *Biochim Biophys Acta.* **1666**(1-2), pp.205-226.

Jin, H., Cheng, X., Zhou, H.Z., Li, S. and Seddiqui, A. 2000. Respiratory syncytial virus that lacks open reading frame 2 of the M2 gene (M2-2) has altered growth characteristics and is attenuated in rodents. *J Virol.* **74**(1), pp.74-82.

Jirasko, V., Montserret, R., Appel, N., Janvier, A., Eustachi, L., Brohm, C., Steinmann, E., Pietschmann, T., Penin, F. and Bartenschlager, R. 2008. Structural and functional characterization of nonstructural protein 2 for its role in hepatitis C virus assembly. *J Biol Chem.* **283**(42), pp.28546-28562.

Jirasko, V., Montserret, R., Lee, J.Y., Gouttenoire, J., Moradpour, D., Penin, F. and Bartenschlager, R. 2010. Structural and functional studies of nonstructural protein 2 of the hepatitis C virus reveal its key role as organizer of virion assembly. *PLoS Pathog.* **6**(12), pe1001233.

Johnson, B.K., Chanas, A.C., Shockley, P., Squires, E.J., Gardner, P., Wallace, C., Simpson, D.I., Bowen, E.T., Platt, G.S., Way, H., Parsons, J. and Grainger, W.E. 1977. Arbovirus isolations from, and serological studies on, wild and domestic vertebrates from Kano Plain, Kenya. *Trans R Soc Trop Med Hyg.* **71**(6), pp.512-517.

Jones, M.S., 2nd, Harrach, B., Ganac, R.D., Gozum, M.M., Dela Cruz, W.P., Riedel, B., Pan, C., Delwart, E.L. and Schnurr, D.P. 2007. New adenovirus species found in a patient presenting with gastroenteritis. *J Virol.* **81**(11), pp.5978-5984.

Julander, J.G., Siddharthan, V., Evans, J., Taylor, R., Tolbert, K., Apuli, C., Stewart, J., Collins, P., Gebre, M., Neilson, S., Van Wettere, A., Lee, Y.M., Sheridan, W.P., Morrey, J.D. and Babu, Y.S. 2017. Efficacy of the broad-spectrum antiviral compound BCX4430 against Zika virus in cell culture and in a mouse model. *Antiviral Res.* **137**, pp.14-22.

Junjhon, J., Lausumpao, M., Supasa, S., Noisakran, S., Songjaeng, A., Saraithong, P., Chaichoun, K., Utaipat, U., Keelapang, P., Kanjanahaluethai, A., Puttikhunt, C., Kasinrerak, W., Malasit, P. and Sittisombut, N. 2008. Differential modulation of prM cleavage, extracellular particle distribution, and virus infectivity by conserved residues at nonfurin consensus positions of the dengue virus pr-M junction. *J Virol.* **82**(21), pp.10776-10791.

Junjhon, J., Pennington, J.G., Edwards, T.J., Perera, R., Lanman, J. and Kuhn, R.J. 2014. Ultrastructural characterization and three-dimensional architecture of replication sites in dengue virus-infected mosquito cells. *J Virol.* **88**(9), pp.4687-4697.

Kalko, S.G., Cachau, R.E. and Silva, A.M. 1992. Ion channels in icosahedral virus: a comparative analysis of the structures and binding sites at their fivefold axes. *Biophys J.* **63**(4), pp.1133-1145.

Kall, L., Krogh, A. and Sonnhammer, E.L. 2004. A combined transmembrane topology and signal peptide prediction method. *J Mol Biol.* **338**(5), pp.1027-1036.

Kall, L., Krogh, A. and Sonnhammer, E.L. 2007. Advantages of combined transmembrane topology and signal peptide prediction--the Phobius web server. *Nucleic Acids Res.* **35**(Web Server issue), pp.W429-432.

Kato, F., Ishida, Y., Oishi, S., Fujii, N., Watanabe, S., Vasudevan, S.G., Tajima, S., Takasaki, T., Suzuki, Y., Ichiyama, K., Yamamoto, N., Yoshii, K., Takashima, I., Kobayashi, T., Miura, T., Igarashi, T. and Hishiki, T. 2016. Novel antiviral activity of bromocriptine against dengue virus replication. *Antiviral Res.* **131**, pp.141-147.

Katpally, U., Fu, T.M., Freed, D.C., Casimiro, D.R. and Smith, T.J. 2009. Antibodies to the buried N terminus of rhinovirus VP4 exhibit cross-serotypic neutralization. *J Virol.* **83**(14), pp.7040-7048.

Kaufusi, P.H., Kelley, J.F., Yanagihara, R. and Nerurkar, V.R. 2014. Induction of endoplasmic reticulum-derived replication-competent membrane structures by West Nile virus non-structural protein 4B. *PLoS One.* **9**(1), pe84040.

Khurana, E., Dal Peraro, M., DeVane, R., Vemparala, S., DeGrado, W.F. and Klein, M.L. 2009. Molecular dynamics calculations suggest a conduction mechanism for the M2 proton channel from influenza A virus. *Proc Natl Acad Sci U S A.* **106**(4), pp.1069-1074.

Kim, C.R., Counotte, M., Bernstein, K., Deal, C., Mayaud, P., Low, N., Broutet, N. and Sexual Transmission of Zika virus Expert Meeting, p. 2018. Investigating the sexual transmission of Zika virus. *Lancet Glob Health.* **6**(1), pp.e24-e25.

Klein, D.E., Choi, J.L. and Harrison, S.C. 2013. Structure of a dengue virus envelope protein late-stage fusion intermediate. *J Virol.* **87**(4), pp.2287-2293.

Koff, W.C., Elm, J.L., Jr. and Halstead, S.B. 1980. Inhibition of dengue virus replication by amantadine hydrochloride. *Antimicrob Agents Chemother.* **18**(1), pp.125-129.

Koff, W.C., Elm, J.L., Jr. and Halstead, S.B. 1981. Suppression of dengue virus replication in vitro by rimantadine hydrochloride. *Am J Trop Med Hyg.* **30**(1), pp.184-189.

Koff, W.C. and Knight, V. 1979. Inhibition of influenza virus uncoating by rimantadine hydrochloride. *J Virol.* **31**(1), pp.261-263.

Kozakov, D., Chuang, G.Y., Beglov, D. and Vajda, S. 2010. Where does amantadine bind to the influenza virus M2 proton channel? *Trends Biochem Sci.* **35**(9), pp.471-475.

Krauer, F., Riesen, M., Reveiz, L., Oladapo, O.T., Martinez-Vega, R., Porgo, T.V., Haefliger, A., Broutet, N.J., Low, N. and Group, W.H.O.Z.C.W. 2017. Zika Virus Infection as a Cause of Congenital Brain Abnormalities and Guillain-Barre Syndrome: Systematic Review. *PLoS Med.* **14**(1), pe1002203.

Kuhn, R.J., Zhang, W., Rossmann, M.G., Pletnev, S.V., Corver, J., Lenches, E., Jones, C.T., Mukhopadhyay, S., Chipman, P.R., Strauss, E.G., Baker, T.S. and Strauss, J.H. 2002. Structure of dengue virus: implications for flavivirus organization, maturation, and fusion. *Cell.* **108**(5), pp.717-725.

Kurscheidt, F.A., Mesquita, C.S.S., Damke, G., Damke, E., Carvalho, A., Suehiro, T.T., Teixeira, J.J.V., da Silva, V.R.S., Souza, R.P. and Consolaro,

M.E.L. 2019. Persistence and clinical relevance of Zika virus in the male genital tract. *Nat Rev Urol.* **16**(4), pp.211-230.

Kuwabara, S. 2004. Guillain-Barre syndrome: epidemiology, pathophysiology and management. *Drugs.* **64**(6), pp.597-610.

Lamb, R.A., Zebedee, S.L. and Richardson, C.D. 1985. Influenza virus M2 protein is an integral membrane protein expressed on the infected-cell surface. *Cell.* **40**(3), pp.627-633.

Lanciotti, R.S., Kosoy, O.L., Laven, J.J., Velez, J.O., Lambert, A.J., Johnson, A.J., Stanfield, S.M. and Duffy, M.R. 2008. Genetic and serologic properties of Zika virus associated with an epidemic, Yap State, Micronesia, 2007. *Emerg Infect Dis.* **14**(8), pp.1232-1239.

Larocca, R.A., Abbink, P., Peron, J.P., Zanotto, P.M., Lampietro, M.J., Badamchi-Zadeh, A., Boyd, M., Ng'ang'a, D., Kirilova, M., Nityanandam, R., Mercado, N.B., Li, Z., Moseley, E.T., Bricault, C.A., Borducchi, E.N., Giglio, P.B., Jetton, D., Neubauer, G., Nkolola, J.P., Maxfield, L.F., De La Barrera, R.A., Jarman, R.G., Eckels, K.H., Michael, N.L., Thomas, S.J. and Barouch, D.H. 2016. Vaccine protection against Zika virus from Brazil. *Nature.* **536**(7617), pp.474-478.

Lazear, H.M. and Diamond, M.S. 2016. Zika Virus: New Clinical Syndromes and Its Emergence in the Western Hemisphere. *J Virol.* **90**(10), pp.4864-4875.

Lazear, H.M., Govero, J., Smith, A.M., Platt, D.J., Fernandez, E., Miner, J.J. and Diamond, M.S. 2016. A Mouse Model of Zika Virus Pathogenesis. *Cell Host Microbe.* **19**(5), pp.720-730.

Lee, H., Ren, J., Nocadello, S., Rice, A.J., Ojeda, I., Light, S., Minasov, G., Vargas, J., Nagarathnam, D., Anderson, W.F. and Johnson, M.E. 2017. Identification of novel small molecule inhibitors against NS2B/NS3 serine protease from Zika virus. *Antiviral Res.* **139**, pp.49-58.

Lee, J.L., Loe, M.W.C., Lee, R.C.H. and Chu, J.J.H. 2019. Antiviral activity of pinocembrin against Zika virus replication. *Antiviral Res.* **167**, pp.13-24.

Leier, H.C., Weinstein, J.B., Kyle, J.E., Lee, J.-Y., Bramer, L.M., Stratton, K.G., Kempthorne, D., Navratil, A.R., Tafesse, E.G., Hornemann, T., Messer, W.B., Dennis, E.A., Metz, T.O., Barklis, E. and Tafesse, F.G. 2020. A global lipid map defines a network essential for Zika virus replication. *bioRxiv.* p2020.2001.2027.910919.

Li, C., Xu, D., Ye, Q., Hong, S., Jiang, Y., Liu, X., Zhang, N., Shi, L., Qin, C.F. and Xu, Z. 2016a. Zika Virus Disrupts Neural Progenitor Development and Leads to Microcephaly in Mice. *Cell Stem Cell.* **19**(5), p672.

Li, C., Xu, D., Ye, Q., Hong, S., Jiang, Y., Liu, X., Zhang, N., Shi, L., Qin, C.F. and Xu, Z. 2016b. Zika Virus Disrupts Neural Progenitor Development and Leads to Microcephaly in Mice. *Cell Stem Cell.* **19**(1), pp.120-126.

Li, F., Hu, Y., Wang, Y., Ma, C. and Wang, J. 2017. Expedient Lead Optimization of Isoxazole-Containing Influenza A Virus M2-S31N Inhibitors Using the Suzuki-Miyaura Cross-Coupling Reaction. *J Med Chem.* **60**(4), pp.1580-1590.

Li, F., Ma, C., DeGrado, W.F. and Wang, J. 2016a. Discovery of Highly Potent Inhibitors Targeting the Predominant Drug-Resistant S31N Mutant of the Influenza A Virus M2 Proton Channel. *J Med Chem.* **59**(3), pp.1207-1216.

Li, F., Ma, C., Hu, Y., Wang, Y. and Wang, J. 2016b. Discovery of Potent Antivirals against Amantadine-Resistant Influenza A Viruses by Targeting the M2-S31N Proton Channel. *ACS Infect Dis.* **2**(10), pp.726-733.

Li, H., Atkins, E., Bruckner, J., McArdle, S., Qiu, W.C., Thomassen, L.V., Scott, J., Shuhart, M.C., Livingston, S., Townshend-Bulson, L., McMahon, B.J., Harris, M., Griffin, S. and Gretch, D.R. 2012. Genetic and functional heterogeneity of the hepatitis C virus p7 ion channel during natural chronic infection. *Virology*. **423**(1), pp.30-37.

Li, J., Lim, S.P., Beer, D., Patel, V., Wen, D., Tumanut, C., Tully, D.C., Williams, J.A., Jiricek, J., Priestle, J.P., Harris, J.L. and Vasudevan, S.G. 2005. Functional profiling of recombinant NS3 proteases from all four serotypes of dengue virus using tetrapeptide and octapeptide substrate libraries. *J Biol Chem*. **280**(31), pp.28766-28774.

Li, K., Phoo, W.W. and Luo, D. 2014. Functional interplay among the flavivirus NS3 protease, helicase, and cofactors. *Viol Sin*. **29**(2), pp.74-85.

Li, L., Lok, S.M., Yu, I.M., Zhang, Y., Kuhn, R.J., Chen, J. and Rossmann, M.G. 2008. The flavivirus precursor membrane-envelope protein complex: structure and maturation. *Science*. **319**(5871), pp.1830-1834.

Li, M., Zhang, D., Li, C., Zheng, Z., Fu, M., Ni, F., Liu, Y., Du, T., Wang, H., Griffin, G.E., Zhang, M. and Hu, Q. 2020. Characterization of Zika Virus Endocytic Pathways in Human Glioblastoma Cells. *Front Microbiol*. **11**, p242.

Li, P., Wei, Y., Mei, M., Tang, L., Sun, L., Huang, W., Zhou, J., Zou, C., Zhang, S., Qin, C.F., Jiang, T., Dai, J., Tan, X. and Zhang, Q.C. 2018. Integrative Analysis of Zika Virus Genome RNA Structure Reveals Critical Determinants of Viral Infectivity. *Cell Host Microbe*. **24**(6), pp.875-886 e875.

Li, Q., Yafal, A.G., Lee, Y.M., Hogle, J. and Chow, M. 1994. Poliovirus neutralization by antibodies to internal epitopes of VP4 and VP1 results from reversible exposure of these sequences at physiological temperature. *J Virol*. **68**(6), pp.3965-3970.

Li, X.D., Ye, H.Q., Deng, C.L., Liu, S.Q., Zhang, H.L., Shang, B.D., Shi, P.Y., Yuan, Z.M. and Zhang, B. 2015. Genetic interaction between NS4A and NS4B for replication of Japanese encephalitis virus. *J Gen Virol*. **96**(Pt 6), pp.1264-1275.

Li, X.F., Dong, H.L., Huang, X.Y., Qiu, Y.F., Wang, H.J., Deng, Y.Q., Zhang, N.N., Ye, Q., Zhao, H., Liu, Z.Y., Fan, H., An, X.P., Sun, S.H., Gao, B., Fa, Y.Z., Tong, Y.G., Zhang, F.C., Gao, G.F., Cao, W.C., Shi, P.Y. and Qin, C.F. 2016. Characterization of a 2016 Clinical Isolate of Zika Virus in Non-human Primates. *EBioMedicine*. **12**, pp.170-177.

Li, Y., Liu, H., Xia, M. and Gong, H. 2016. Lysine and the Na⁺/K⁺ Selectivity in Mammalian Voltage-Gated Sodium Channels. *PLoS One*. **11**(9), pe0162413.

Li, Y., To, J., Verdía-Baguena, C., Dossena, S., Surya, W., Huang, M., Paulmichl, M., Liu, D.X., Aguilera, V.M. and Torres, J. 2014. Inhibition of the human respiratory syncytial virus small hydrophobic protein and structural variations in a bicelle environment. *J Virol*. **88**(20), pp.11899-11914.

Liang, Q., Luo, Z., Zeng, J., Chen, W., Foo, S.S., Lee, S.A., Ge, J., Wang, S., Goldman, S.A., Zlokovic, B.V., Zhao, Z. and Jung, J.U. 2016. Zika Virus NS4A and NS4B Proteins Deregulate Akt-mTOR Signaling in Human Fetal Neural Stem Cells to Inhibit Neurogenesis and Induce Autophagy. *Cell Stem Cell*. **19**(5), pp.663-671.

Liao, M., Sanchez-San Martin, C., Zheng, A. and Kielian, M. 2010. In vitro reconstitution reveals key intermediate states of trimer formation by the dengue virus membrane fusion protein. *J Virol*. **84**(11), pp.5730-5740.

Lim, S.P., Koh, J.H., Seh, C.C., Liew, C.W., Davidson, A.D., Chua, L.S., Chandrasekaran, R., Cornvik, T.C., Shi, P.Y. and Lescar, J. 2013a. A crystal

structure of the dengue virus non-structural protein 5 (NS5) polymerase delineates interdomain amino acid residues that enhance its thermostability and de novo initiation activities. *J Biol Chem.* **288**(43), pp.31105-31114.

Lim, S.P., Wang, Q.Y., Noble, C.G., Chen, Y.L., Dong, H., Zou, B., Yokokawa, F., Nilar, S., Smith, P., Beer, D., Lescar, J. and Shi, P.Y. 2013b. Ten years of dengue drug discovery: progress and prospects. *Antiviral Res.* **100**(2), pp.500-519.

Limjindaporn, T., Netsawang, J., Noisakran, S., Thiemmecca, S., Wongwiwat, W., Sudsaward, S., Avirutnan, P., Puttikhunt, C., Kasinrerak, W., Sriburi, R., Sittisombut, N., Yenichitsomanus, P.T. and Malasit, P. 2007. Sensitization to Fas-mediated apoptosis by dengue virus capsid protein. *Biochem Biophys Res Commun.* **362**(2), pp.334-339.

Lin, C., Amberg, S.M., Chambers, T.J. and Rice, C.M. 1993. Cleavage at a novel site in the NS4A region by the yellow fever virus NS2B-3 proteinase is a prerequisite for processing at the downstream 4A/4B signalase site. *J Virol.* **67**(4), pp.2327-2335.

Lin, C., Lindenbach, B.D., Pragai, B.M., McCourt, D.W. and Rice, C.M. 1994. Processing in the hepatitis C virus E2-NS2 region: identification of p7 and two distinct E2-specific products with different C termini. *J Virol.* **68**(8), pp.5063-5073.

Lin, C.C. and Chen, W.C. 2016. Treatment Effectiveness of Amantadine Against Dengue Virus Infection. *Am J Case Rep.* **17**, pp.921-924.

Lin, J., Lee, L.Y., Roivainen, M., Filman, D.J., Hogle, J.M. and Belnap, D.M. 2012. Structure of the Fab-labeled "breathing" state of native poliovirus. *J Virol.* **86**(10), pp.5959-5962.

Lionta, E., Spyrou, G., Vassilatis, D.K. and Cournia, Z. 2014. Structure-based virtual screening for drug discovery: principles, applications and recent advances. *Curr Top Med Chem.* **14**(16), pp.1923-1938.

Liu, J., Kline, B.A., Kenny, T.A., Smith, D.R., Soloveva, V., Beitzel, B., Pang, S., Lockett, S., Hess, H.F., Palacios, G., Kuhn, J.H., Sun, M.G. and Zeng, X. 2018. A novel sheet-like virus particle array is a hallmark of Zika virus infection. *Emerg Microbes Infect.* **7**(1), p69.

Liu, W.J., Wang, X.J., Clark, D.C., Lobigs, M., Hall, R.A. and Khromykh, A.A. 2006. A single amino acid substitution in the West Nile virus nonstructural protein NS2A disables its ability to inhibit alpha/beta interferon induction and attenuates virus virulence in mice. *J Virol.* **80**(5), pp.2396-2404.

Lorenz, I.C., Allison, S.L., Heinz, F.X. and Helenius, A. 2002. Folding and dimerization of tick-borne encephalitis virus envelope proteins prM and E in the endoplasmic reticulum. *J Virol.* **76**(11), pp.5480-5491.

Lu, G., Bluemling, G.R., Collop, P., Hager, M., Kuiper, D., Gurale, B.P., Painter, G.R., De La Rosa, A. and Kolykhalov, A.A. 2017. Analysis of Ribonucleotide 5'-Triphosphate Analogs as Potential Inhibitors of Zika Virus RNA-Dependent RNA Polymerase by Using Nonradioactive Polymerase Assays. *Antimicrob Agents Chemother.* **61**(3).

Luik, P., Chew, C., Aittoniemi, J., Chang, J., Wentworth, P., Jr., Dwek, R.A., Biggin, P.C., Venien-Bryan, C. and Zitzmann, N. 2009. The 3-dimensional structure of a hepatitis C virus p7 ion channel by electron microscopy. *Proc Natl Acad Sci U S A.* **106**(31), pp.12712-12716.

Lum, F.M., Lee, D., Chua, T.K., Tan, J.J.L., Lee, C.Y.P., Liu, X., Fang, Y., Lee, B., Yee, W.X., Rickett, N.Y., Chia, P.Y., Lim, V., Leo, Y.S., Matthews, D.A., Hiscox, J.A. and Ng, L.F.P. 2018. Zika Virus Infection Preferentially

Counterbalances Human Peripheral Monocyte and/or NK Cell Activity. *mSphere*. **3**(2).

Ma, W., Li, S., Ma, S., Jia, L., Zhang, F., Zhang, Y., Zhang, J., Wong, G., Zhang, S., Lu, X., Liu, M., Yan, J., Li, W., Qin, C., Han, D., Qin, C., Wang, N., Li, X. and Gao, G.F. 2017. Zika Virus Causes Testis Damage and Leads to Male Infertility in Mice. *Cell*. **168**(3), p542.

Mackenzie, J.M., Khromykh, A.A., Jones, M.K. and Westaway, E.G. 1998. Subcellular localization and some biochemical properties of the flavivirus Kunjin nonstructural proteins NS2A and NS4A. *Virology*. **245**(2), pp.203-215.

Mackenzie, J.M., Khromykh, A.A. and Parton, R.G. 2007. Cholesterol manipulation by West Nile virus perturbs the cellular immune response. *Cell Host Microbe*. **2**(4), pp.229-239.

Macnamara, F.N. 1954. Zika virus: a report on three cases of human infection during an epidemic of jaundice in Nigeria. *Trans R Soc Trop Med Hyg*. **48**(2), pp.139-145.

Madan, V., Sanchez-Martinez, S., Vedovato, N., Rispoli, G., Carrasco, L. and Nieva, J.L. 2007. Plasma membrane-porating domain in poliovirus 2B protein. A short peptide mimics viroporin activity. *J Mol Biol*. **374**(4), pp.951-964.

Magalhaes-Barbosa, M.C., Prata-Barbosa, A., Robaina, J.R., Raymundo, C.E., Lima-Setta, F. and Cunha, A.J. 2016. Trends of the microcephaly and Zika virus outbreak in Brazil, January-July 2016. *Travel Med Infect Dis*. **14**(5), pp.458-463.

Magnus, M.M., Esposito, D.L.A., Costa, V.A.D., Melo, P.S., Costa-Lima, C., Fonseca, B. and Addas-Carvalho, M. 2018. Risk of Zika virus transmission by blood donations in Brazil. *Hematol Transfus Cell Ther*. **40**(3), pp.250-254.

Manzano, M., Reichert, E.D., Polo, S., Falgout, B., Kasprzak, W., Shapiro, B.A. and Padmanabhan, R. 2011. Identification of cis-acting elements in the 3'-untranslated region of the dengue virus type 2 RNA that modulate translation and replication. *J Biol Chem*. **286**(25), pp.22521-22534.

Marchette, N.J., Garcia, R. and Rudnick, A. 1969. Isolation of Zika virus from *Aedes aegypti* mosquitoes in Malaysia. *Am J Trop Med Hyg*. **18**(3), pp.411-415.

Martin-Acebes, M.A., Merino-Ramos, T., Blazquez, A.B., Casas, J., Escribano-Romero, E., Sobrino, F. and Saiz, J.C. 2014. The composition of West Nile virus lipid envelope unveils a role of sphingolipid metabolism in flavivirus biogenesis. *J Virol*. **88**(20), pp.12041-12054.

Maxfield, F.R. and Yamashiro, D.J. 1987. Endosome acidification and the pathways of receptor-mediated endocytosis. *Adv Exp Med Biol*. **225**, pp.189-198.

Mazeaud, C., Freppel, W. and Chatel-Chaix, L. 2018. The Multiples Fates of the Flavivirus RNA Genome During Pathogenesis. *Front Genet*. **9**, p595.

McCown, M.F. and Pekosz, A. 2005. The influenza A virus M2 cytoplasmic tail is required for infectious virus production and efficient genome packaging. *J Virol*. **79**(6), pp.3595-3605.

McCown, M.F. and Pekosz, A. 2006. Distinct domains of the influenza a virus M2 protein cytoplasmic tail mediate binding to the M1 protein and facilitate infectious virus production. *J Virol*. **80**(16), pp.8178-8189.

McLean, J.E., Wudzinska, A., Datan, E., Quaglino, D. and Zakeri, Z. 2011. Flavivirus NS4A-induced autophagy protects cells against death and enhances virus replication. *J Biol Chem*. **286**(25), pp.22147-22159.

Meertens, L., Labeau, A., Dejarnac, O., Cipriani, S., Sinigaglia, L., Bonnet-Madin, L., Le Charpentier, T., Hafirassou, M.L., Zamborlini, A., Cao-Lormeau, V.M., Couplier, M., Misse, D., Jouvenet, N., Tabibiazar, R., Gressens, P.,

Schwartz, O. and Amara, A. 2017. Axl Mediates ZIKA Virus Entry in Human Glial Cells and Modulates Innate Immune Responses. *Cell Rep.* **18**(2), pp.324-333.

Melian, E.B., Hinzman, E., Nagasaki, T., Firth, A.E., Wills, N.M., Nouwens, A.S., Blitvich, B.J., Leung, J., Funk, A., Atkins, J.F., Hall, R. and Khromykh, A.A. 2010. NS1' of flaviviruses in the Japanese encephalitis virus serogroup is a product of ribosomal frameshifting and plays a role in viral neuroinvasiveness. *J Virol.* **84**(3), pp.1641-1647.

Melton, J.V., Ewart, G.D., Weir, R.C., Board, P.G., Lee, E. and Gage, P.W. 2002. Alphavirus 6K proteins form ion channels. *J Biol Chem.* **277**(49), pp.46923-46931.

Meredith, L.W., Zitzmann, N. and McKeating, J.A. 2013. Differential effect of p7 inhibitors on hepatitis C virus cell-to-cell transmission. *Antiviral Res.* **100**(3), pp.636-639.

Merfeld, E., Ben-Avi, L., Kennon, M. and Cervený, K.L. 2017. Potential mechanisms of Zika-linked microcephaly. *Wiley Interdiscip Rev Dev Biol.* **6**(4).

Meshkat, Z., Audsley, M., Beyer, C., Gowans, E.J. and Haqshenas, G. 2009. Reverse genetic analysis of a putative, influenza virus M2 HXXXW-like motif in the p7 protein of hepatitis C virus. *J Viral Hepat.* **16**(3), pp.187-194.

Michlmayr, D., Andrade, P., Gonzalez, K., Balmaseda, A. and Harris, E. 2017. CD14(+)CD16(+) monocytes are the main target of Zika virus infection in peripheral blood mononuclear cells in a paediatric study in Nicaragua. *Nat Microbiol.* **2**(11), pp.1462-1470.

Microcephaly Epidemic Research, G. 2016. Microcephaly in Infants, Pernambuco State, Brazil, 2015. *Emerg Infect Dis.* **22**(6), pp.1090-1093.

Mihm, U., Grigorian, N., Welsch, C., Herrmann, E., Kronenberger, B., Teuber, G., von Wagner, M., Hofmann, W.P., Albrecht, M., Lengauer, T., Zeuzem, S. and Sarrazin, C. 2006. Amino acid variations in hepatitis C virus p7 and sensitivity to antiviral combination therapy with amantadine in chronic hepatitis C. *Antivir Ther.* **11**(4), pp.507-519.

Miller, S., Kastner, S., Krijnse-Locker, J., Buhler, S. and Bartenschlager, R. 2007. The non-structural protein 4A of dengue virus is an integral membrane protein inducing membrane alterations in a 2K-regulated manner. *J Biol Chem.* **282**(12), pp.8873-8882.

Miller, S., Sparacio, S. and Bartenschlager, R. 2006. Subcellular localization and membrane topology of the Dengue virus type 2 Non-structural protein 4B. *J Biol Chem.* **281**(13), pp.8854-8863.

Miner, J.J., Cao, B., Govero, J., Smith, A.M., Fernandez, E., Cabrera, O.H., Garber, C., Noll, M., Klein, R.S., Noguchi, K.K., Mysorekar, I.U. and Diamond, M.S. 2016. Zika Virus Infection during Pregnancy in Mice Causes Placental Damage and Fetal Demise. *Cell.* **165**(5), pp.1081-1091.

Mizushima, H., Hijikata, M., Asabe, S., Hirota, M., Kimura, K. and Shimotohno, K. 1994. Two hepatitis C virus glycoprotein E2 products with different C termini. *J Virol.* **68**(10), pp.6215-6222.

Modhiran, N., Watterson, D., Muller, D.A., Panetta, A.K., Sester, D.P., Liu, L., Hume, D.A., Stacey, K.J. and Young, P.R. 2015. Dengue virus NS1 protein activates cells via Toll-like receptor 4 and disrupts endothelial cell monolayer integrity. *Sci Transl Med.* **7**(304), p304ra142.

Modis, Y., Ogata, S., Clements, D. and Harrison, S.C. 2004. Structure of the dengue virus envelope protein after membrane fusion. *Nature.* **427**(6972), pp.313-319.

Modis, Y., Ogata, S., Clements, D. and Harrison, S.C. 2005. Variable surface epitopes in the crystal structure of dengue virus type 3 envelope glycoprotein. *J Virol.* **79**(2), pp.1223-1231.

Moller, S., Croning, M.D. and Apweiler, R. 2001. Evaluation of methods for the prediction of membrane spanning regions. *Bioinformatics.* **17**(7), pp.646-653.

Montserret, R., Saint, N., Vanbelle, C., Salvay, A.G., Simorre, J.P., Ebel, C., Sapay, N., Renisio, J.G., Bockmann, A., Steinmann, E., Pietschmann, T., Dubuisson, J., Chipot, C. and Penin, F. 2010. NMR structure and ion channel activity of the p7 protein from hepatitis C virus. *J Biol Chem.* **285**(41), pp.31446-31461.

Moore, D.L., Causey, O.R., Carey, D.E., Reddy, S., Cooke, A.R., Akinkugbe, F.M., David-West, T.S. and Kemp, G.E. 1975. Arthropod-borne viral infections of man in Nigeria, 1964-1970. *Ann Trop Med Parasitol.* **69**(1), pp.49-64.

Morrison, T.E. and Diamond, M.S. 2017. Animal Models of Zika Virus Infection, Pathogenesis, and Immunity. *J Virol.* **91**(8).

Mukhopadhyay, S., Kuhn, R.J. and Rossmann, M.G. 2005. A structural perspective of the flavivirus life cycle. *Nat Rev Microbiol.* **3**(1), pp.13-22.

Muller, D.A., Landsberg, M.J., Bletchly, C., Rothnagel, R., Waddington, L., Hankamer, B. and Young, P.R. 2012. Structure of the dengue virus glycoprotein non-structural protein 1 by electron microscopy and single-particle analysis. *J Gen Virol.* **93**(Pt 4), pp.771-779.

Munoz-Jordan, J.L., Laurent-Rolle, M., Ashour, J., Martinez-Sobrido, L., Ashok, M., Lipkin, W.I. and Garcia-Sastre, A. 2005. Inhibition of alpha/beta interferon signaling by the NS4B protein of flaviviruses. *J Virol.* **79**(13), pp.8004-8013.

Munoz-Jordan, J.L., Sanchez-Burgos, G.G., Laurent-Rolle, M. and Garcia-Sastre, A. 2003. Inhibition of interferon signaling by dengue virus. *Proc Natl Acad Sci U S A.* **100**(24), pp.14333-14338.

Munoz, M., Rosso, M., Gonzalez-Ortega, A. and Covenas, R. 2010. The NK-1 Receptor Antagonist L-732,138 Induces Apoptosis and Counteracts Substance P-Related Mitogenesis in Human Melanoma Cell Lines. *Cancers (Basel).* **2**(2), pp.611-623.

Musharrafieh, R., Lagarias, P.I., Ma, C., Tan, G.S., Kolocouris, A. and Wang, J. 2019. The L46P mutant confers a novel allosteric mechanism of resistance toward the influenza A virus M2 S31N proton channel blockers. *Mol Pharmacol.* **96**(2), pp.148-157.

Musso, D., Roche, C., Robin, E., Nhan, T., Teissier, A. and Cao-Lormeau, V.M. 2015. Potential sexual transmission of Zika virus. *Emerg Infect Dis.* **21**(2), pp.359-361.

Mysorekar, I.U. 2017. Zika Virus Takes a Transplacental Route to Infect Fetuses: Insights from an Animal Model. *Mo Med.* **114**(3), pp.168-170.

Mysorekar, I.U. and Diamond, M.S. 2016. Modeling Zika Virus Infection in Pregnancy. *N Engl J Med.* **375**(5), pp.481-484.

Nawa, M., Takasaki, T., Yamada, K., Kurane, I. and Akatsuka, T. 2003. Interference in Japanese encephalitis virus infection of Vero cells by a cationic amphiphilic drug, chlorpromazine. *J Gen Virol.* **84**(Pt 7), pp.1737-1741.

Nayak, V., Dessau, M., Kucera, K., Anthony, K., Ledizet, M. and Modis, Y. 2009. Crystal structure of dengue virus type 1 envelope protein in the postfusion conformation and its implications for membrane fusion. *J Virol.* **83**(9), pp.4338-4344.

Neil, S.J., Zang, T. and Bieniasz, P.D. 2008. Tetherin inhibits retrovirus release and is antagonized by HIV-1 Vpu. *Nature.* **451**(7177), pp.425-430.

Netsawang, J., Noisakran, S., Puttikhunt, C., Kasinrerak, W., Wongwiwat, W., Malasit, P., Yenchitsomanus, P.T. and Limjindaporn, T. 2010. Nuclear localization of dengue virus capsid protein is required for DAXX interaction and apoptosis. *Virus Res.* **147**(2), pp.275-283.

Ngueyen, T.T.N., Kim, S.J., Lee, J.Y. and Myoung, J. 2019. Zika Virus Proteins NS2A and NS4A Are Major Antagonists that Reduce IFN-beta Promoter Activity Induced by the MDA5/RIG-I Signaling Pathway. *J Microbiol Biotechnol.* **29**(10), pp.1665-1674.

Nieva, J.L., Agirre, A., Nir, S. and Carrasco, L. 2003. Mechanisms of membrane permeabilization by picornavirus 2B viroporin. *FEBS Lett.* **552**(1), pp.68-73.

Nowakowski, T.J., Pollen, A.A., Di Lullo, E., Sandoval-Espinosa, C., Bershteyn, M. and Kriegstein, A.R. 2016. Expression Analysis Highlights AXL as a Candidate Zika Virus Entry Receptor in Neural Stem Cells. *Cell Stem Cell.* **18**(5), pp.591-596.

Nugent, T. and Jones, D.T. 2009. Transmembrane protein topology prediction using support vector machines. *BMC Bioinformatics.* **10**, p159.

Oehler, E., Watrin, L., Larre, P., Leparac-Goffart, I., Lastere, S., Valour, F., Baudouin, L., Mallet, H., Musso, D. and Ghawche, F. 2014. Zika virus infection complicated by Guillain-Barre syndrome--case report, French Polynesia, December 2013. *Euro Surveill.* **19**(9).

Oestringer, B.P., Bolivar, J.H., Claridge, J.K., Almanea, L., Chipot, C., Dehez, F., Holzmann, N., Schnell, J.R. and Zitzmann, N. 2019. Hepatitis C virus sequence divergence preserves p7 viroporin structural and dynamic features. *Sci Rep.* **9**(1), p8383.

Oestringer, B.P., Bolivar, J.H., Hensen, M., Claridge, J.K., Chipot, C., Dehez, F., Holzmann, N., Zitzmann, N. and Schnell, J.R. 2018. Re-evaluating the p7 viroporin structure. *Nature.* **562**(7727), pp.E8-E18.

Ogawa, K., Hishiki, T., Shimizu, Y., Funami, K., Sugiyama, K., Miyanari, Y. and Shimotohno, K. 2009. Hepatitis C virus utilizes lipid droplet for production of infectious virus. *Proc Jpn Acad Ser B Phys Biol Sci.* **85**(7), pp.217-228.

Ohigashi, Y., Ma, C., Jing, X., Balannick, V., Pinto, L.H. and Lamb, R.A. 2009. An amantadine-sensitive chimeric BM2 ion channel of influenza B virus has implications for the mechanism of drug inhibition. *Proc Natl Acad Sci U S A.* **106**(44), pp.18775-18779.

Okada, A., Miura, T. and Takeuchi, H. 2001. Protonation of histidine and histidine-tryptophan interaction in the activation of the M2 ion channel from influenza A virus. *Biochemistry.* **40**(20), pp.6053-6060.

Olson, J.G., Ksiazek, T.G., Suhandiman and Triwibowo. 1981. Zika virus, a cause of fever in Central Java, Indonesia. *Trans R Soc Trop Med Hyg.* **75**(3), pp.389-393.

Olsthoorn, R.C. and Bol, J.F. 2001. Sequence comparison and secondary structure analysis of the 3' noncoding region of flavivirus genomes reveals multiple pseudoknots. *RNA.* **7**(10), pp.1370-1377.

Orlikowski, D., Prigent, H., Sharshar, T., Lofaso, F. and Raphael, J.C. 2004. Respiratory dysfunction in Guillain-Barre Syndrome. *Neurocrit Care.* **1**(4), pp.415-422.

OuYang, B., Xie, S., Berardi, M.J., Zhao, X., Dev, J., Yu, W., Sun, B. and Chou, J.J. 2013. Unusual architecture of the p7 channel from hepatitis C virus. *Nature.* **498**(7455), pp.521-525.

- Owczarek, K., Chykunova, Y., Jassoy, C., Maksym, B., Rajfur, Z. and Pyrc, K. 2019. Zika virus: mapping and reprogramming the entry. *Cell Commun Signal.* **17**(1), p41.
- Pabbaraju, K., Ho, K.C., Wong, S., Shokoples, S., Pang, X.L., Fonseca, K. and Fox, J.D. 2008. Adamantane resistance in circulating human influenza A viruses from Alberta, Canada (1970-2007). *Antiviral Res.* **79**(2), pp.81-86.
- Panjwani, A., Asfor, A.S. and Tuthill, T.J. 2016. The conserved N-terminus of human rhinovirus capsid protein VP4 contains membrane pore-forming activity and is a target for neutralizing antibodies. *J Gen Virol.* **97**(12), pp.3238-3242.
- Panjwani, A., Strauss, M., Gold, S., Wenham, H., Jackson, T., Chou, J.J., Rowlands, D.J., Stonehouse, N.J., Hogle, J.M. and Tuthill, T.J. 2014. Capsid protein VP4 of human rhinovirus induces membrane permeability by the formation of a size-selective multimeric pore. *PLoS Pathog.* **10**(8), pe1004294.
- Pardi, N., Hogan, M.J., Pelc, R.S., Muramatsu, H., Andersen, H., DeMaso, C.R., Dowd, K.A., Sutherland, L.L., Scearce, R.M., Parks, R., Wagner, W., Granados, A., Greenhouse, J., Walker, M., Willis, E., Yu, J.S., McGee, C.E., Sempowski, G.D., Mui, B.L., Tam, Y.K., Huang, Y.J., Vanlandingham, D., Holmes, V.M., Balachandran, H., Sahu, S., Lifton, M., Higgs, S., Hensley, S.E., Madden, T.D., Hope, M.J., Kariko, K., Santra, S., Graham, B.S., Lewis, M.G., Pierson, T.C., Haynes, B.F. and Weissman, D. 2017. Zika virus protection by a single low-dose nucleoside-modified mRNA vaccination. *Nature.* **543**(7644), pp.248-251.
- Park, E.K., Castrucci, M.R., Portner, A. and Kawaoka, Y. 1998. The M2 ectodomain is important for its incorporation into influenza A virions. *J Virol.* **72**(3), pp.2449-2455.
- Parra, B., Lizarazo, J., Jimenez-Arango, J.A., Zea-Vera, A.F., Gonzalez-Manrique, G., Vargas, J., Angarita, J.A., Zuniga, G., Lopez-Gonzalez, R., Beltran, C.L., Rizcala, K.H., Morales, M.T., Pacheco, O., Ospina, M.L., Kumar, A., Cornblath, D.R., Munoz, L.S., Osorio, L., Barreras, P. and Pardo, C.A. 2016. Guillain-Barre Syndrome Associated with Zika Virus Infection in Colombia. *N Engl J Med.* **375**(16), pp.1513-1523.
- Parrinello, M. and Rahman, A. 1981. Polymorphic transitions in single crystals: A new molecular dynamics method. **52**(12), pp.7182-7190.
- Patterson, J., Sammon, M. and Garg, M. 2016. Dengue, Zika and Chikungunya: Emerging Arboviruses in the New World. *West J Emerg Med.* **17**(6), pp.671-679.
- Paul, D. and Bartenschlager, R. 2013. Architecture and biogenesis of plus-strand RNA virus replication factories. *World J Virol.* **2**(2), pp.32-48.
- Pauwels, R., Andries, K., Desmyter, J., Schols, D., Kukla, M.J., Breslin, H.J., Raeymaeckers, A., Van Gelder, J., Woestenborghs, R., Heykants, J. and et al. 1990. Potent and selective inhibition of HIV-1 replication in vitro by a novel series of TIBO derivatives. *Nature.* **343**(6257), pp.470-474.
- Pavlovic, D., Neville, D.C., Argaud, O., Blumberg, B., Dwek, R.A., Fischer, W.B. and Zitzmann, N. 2003. The hepatitis C virus p7 protein forms an ion channel that is inhibited by long-alkyl-chain iminosugar derivatives. *Proc Natl Acad Sci U S A.* **100**(10), pp.6104-6108.
- Paz-Bailey, G., Rosenberg, E.S., Doyle, K., Munoz-Jordan, J., Santiago, G.A., Klein, L., Perez-Padilla, J., Medina, F.A., Waterman, S.H., Gubern, C.G., Alvarado, L.I. and Sharp, T.M. 2018. Persistence of Zika Virus in Body Fluids - Final Report. *N Engl J Med.* **379**(13), pp.1234-1243.

Perez, M., Garcia-Barreno, B., Melero, J.A., Carrasco, L. and Guinea, R. 1997. Membrane permeability changes induced in Escherichia coli by the SH protein of human respiratory syncytial virus. *Virology*. **235**(2), pp.342-351.

Persaud, M., Martinez-Lopez, A., Buffone, C., Porcelli, S.A. and Diaz-Griffero, F. 2018. Infection by Zika viruses requires the transmembrane protein AXL, endocytosis and low pH. *Virology*. **518**, pp.301-312.

Pervushin, K., Tan, E., Parthasarathy, K., Lin, X., Jiang, F.L., Yu, D., Vararattanavech, A., Soong, T.W., Liu, D.X. and Torres, J. 2009. Structure and inhibition of the SARS coronavirus envelope protein ion channel. *PLoS Pathog.* **5**(7), pe1000511.

Peterson, A.T., Osorio, J., Qiao, H. and Escobar, L.E. 2016. Zika Virus, Elevation, and Transmission Risk. *PLoS Curr.* **8**.

Pfaender, S., Heyden, J., Friesland, M., Ciesek, S., Ejaz, A., Steinmann, J., Steinmann, J., Malarski, A., Stoiber, H., Tsiavaliaris, G., Bader, W., Jahreis, G., Pietschmann, T. and Steinmann, E. 2013. Inactivation of hepatitis C virus infectivity by human breast milk. *J Infect Dis.* **208**(12), pp.1943-1952.

Pham, T., Perry, J.L., Dosey, T.L., Delcour, A.H. and Hyser, J.M. 2017. The Rotavirus NSP4 Viroporin Domain is a Calcium-conducting Ion Channel. *Sci Rep.* **7**, p43487.

Pichlmair, A., Schulz, O., Tan, C.P., Naslund, T.I., Liljestrom, P., Weber, F. and Reis e Sousa, C. 2006. RIG-I-mediated antiviral responses to single-stranded RNA bearing 5'-phosphates. *Science*. **314**(5801), pp.997-1001.

Pielak, R.M., Oxenoid, K. and Chou, J.J. 2011. Structural investigation of rimantadine inhibition of the AM2-BM2 chimera channel of influenza viruses. *Structure*. **19**(11), pp.1655-1663.

Pielak, R.M., Schnell, J.R. and Chou, J.J. 2009. Mechanism of drug inhibition and drug resistance of influenza A M2 channel. *Proc Natl Acad Sci U S A.* **106**(18), pp.7379-7384.

Pijlman, G.P., Funk, A., Kondratieva, N., Leung, J., Torres, S., van der Aa, L., Liu, W.J., Palmenberg, A.C., Shi, P.Y., Hall, R.A. and Khromykh, A.A. 2008. A highly structured, nuclease-resistant, noncoding RNA produced by flaviviruses is required for pathogenicity. *Cell Host Microbe*. **4**(6), pp.579-591.

Pim, D., Collins, M. and Banks, L. 1992. Human papillomavirus type 16 E5 gene stimulates the transforming activity of the epidermal growth factor receptor. *Oncogene*. **7**(1), pp.27-32.

Pingen, M., Bryden, S.R., Pondeville, E., Schnettler, E., Kohl, A., Merits, A., Fazakerley, J.K., Graham, G.J. and McKimmie, C.S. 2016. Host Inflammatory Response to Mosquito Bites Enhances the Severity of Arbovirus Infection. *Immunity*. **44**(6), pp.1455-1469.

Pinto, L.H., Dieckmann, G.R., Gandhi, C.S., Papworth, C.G., Braman, J., Shaughnessy, M.A., Lear, J.D., Lamb, R.A. and DeGrado, W.F. 1997. A functionally defined model for the M2 proton channel of influenza A virus suggests a mechanism for its ion selectivity. *Proc Natl Acad Sci U S A.* **94**(21), pp.11301-11306.

Pinto, L.H., Holsinger, L.J. and Lamb, R.A. 1992. Influenza virus M2 protein has ion channel activity. *Cell*. **69**(3), pp.517-528.

Piotrowska, A., Rojewska, E., Pawlik, K., Kreiner, G., Ciechanowska, A., Makuch, W., Zychowska, M. and Mika, J. 2018. Pharmacological blockade of CXCR3 by (+/-)-NBI-74330 reduces neuropathic pain and enhances opioid effectiveness - Evidence from in vivo and in vitro studies. *Biochim Biophys Acta Mol Basis Dis.* **1864**(10), pp.3418-3437.

Polacek, C., Friebe, P. and Harris, E. 2009. Poly(A)-binding protein binds to the non-polyadenylated 3' untranslated region of dengue virus and modulates translation efficiency. *J Gen Virol.* **90**(Pt 3), pp.687-692.

Poland, G.A. 2018. Influenza vaccine failure: failure to protect or failure to understand? *Expert Rev Vaccines.* **17**(6), pp.495-502.

Pong, W.L., Huang, Z.S., Teoh, P.G., Wang, C.C. and Wu, H.N. 2011. RNA binding property and RNA chaperone activity of dengue virus core protein and other viral RNA-interacting proteins. *FEBS Lett.* **585**(16), pp.2575-2581.

Potisopon, S., Ferron, F., Fattorini, V., Selisko, B. and Canard, B. 2017. Substrate selectivity of Dengue and Zika virus NS5 polymerase towards 2'-modified nucleotide analogues. *Antiviral Res.* **140**, pp.25-36.

Potisopon, S., Priet, S., Collet, A., Decroly, E., Canard, B. and Selisko, B. 2014. The methyltransferase domain of dengue virus protein NS5 ensures efficient RNA synthesis initiation and elongation by the polymerase domain. *Nucleic Acids Res.* **42**(18), pp.11642-11656.

Prasad, V.M., Miller, A.S., Klose, T., Sirohi, D., Buda, G., Jiang, W., Kuhn, R.J. and Rossmann, M.G. 2017. Structure of the immature Zika virus at 9 Å resolution. *Nat Struct Mol Biol.* **24**(2), pp.184-186.

Premkumar, A., Horan, C.R. and Gage, P.W. 2005. Dengue virus M protein C-terminal peptide (DVM-C) forms ion channels. *J Membr Biol.* **204**(1), pp.33-38.

Premkumar, A., Wilson, L., Ewart, G.D. and Gage, P.W. 2004. Cation-selective ion channels formed by p7 of hepatitis C virus are blocked by hexamethylene amiloride. *FEBS Lett.* **557**(1-3), pp.99-103.

Pryor, M.J., Azzola, L., Wright, P.J. and Davidson, A.D. 2004. Histidine 39 in the dengue virus type 2 M protein has an important role in virus assembly. *J Gen Virol.* **85**(Pt 12), pp.3627-3636.

Pujhari, S., Brustolin, M., Macias, V.M., Nissly, R.H., Nomura, M., Kuchipudi, S.V. and Rasgon, J.L. 2019. Heat shock protein 70 (Hsp70) mediates Zika virus entry, replication, and egress from host cells. *Emerg Microbes Infect.* **8**(1), pp.8-16.

Qian, X., Nguyen, H.N., Jacob, F., Song, H. and Ming, G.L. 2017. Using brain organoids to understand Zika virus-induced microcephaly. *Development.* **144**(6), pp.952-957.

Quicke, K.M., Bowen, J.R., Johnson, E.L., McDonald, C.E., Ma, H., O'Neal, J.T., Rajakumar, A., Wrammert, J., Rimawi, B.H., Pulendran, B., Schinazi, R.F., Chakraborty, R. and Suthar, M.S. 2016. Zika Virus Infects Human Placental Macrophages. *Cell Host Microbe.* **20**(1), pp.83-90.

Raghava, S., Giorda, K.M., Romano, F.B., Heuck, A.P. and Herbert, D.N. 2011. The SV40 late protein VP4 is a viroporin that forms pores to disrupt membranes for viral release. *Plos Pathog.* **7**.

Rajan, A., Kelly, R.J., Trepel, J.B., Kim, Y.S., Alarcon, S.V., Kummar, S., Gutierrez, M., Crandon, S., Zein, W.M., Jain, L., Mannargudi, B., Figg, W.D., Houk, B.E., Shnaidman, M., Brega, N. and Giaccone, G. 2011. A phase I study of PF-04929113 (SNX-5422), an orally bioavailable heat shock protein 90 inhibitor, in patients with refractory solid tumor malignancies and lymphomas. *Clin Cancer Res.* **17**(21), pp.6831-6839.

Rakic, P. 2009. Evolution of the neocortex: a perspective from developmental biology. *Nat Rev Neurosci.* **10**(10), pp.724-735.

Ramanathan, H.N., Zhang, S., Douam, F., Chang, J., Yang, P.L., Ploss, A. and Lindenbach, B.D. 2019. A Sensitive Yellow Fever Virus Entry Reporter Identifies

Valosin-Containing Protein (VCP/p97) as an Essential Host Factor for Flavivirus Uncoating. p814764.

Rasmussen, S.A., Jamieson, D.J., Honein, M.A. and Petersen, L.R. 2016. Zika Virus and Birth Defects--Reviewing the Evidence for Causality. *N Engl J Med.* **374**(20), pp.1981-1987.

Rasul, A., Millimouno, F.M., Ali Eltayb, W., Ali, M., Li, J. and Li, X. 2013. Pinocembrin: a novel natural compound with versatile pharmacological and biological activities. *Biomed Res Int.* **2013**, p379850.

Rawle, R.J., Webster, E.R., Jelen, M., Kasson, P.M. and Boxer, S.G. 2018. pH Dependence of Zika Membrane Fusion Kinetics Reveals an Off-Pathway State. *ACS Cent Sci.* **4**(11), pp.1503-1510.

Ray, D., Shah, A., Tilgner, M., Guo, Y., Zhao, Y., Dong, H., Deas, T.S., Zhou, Y., Li, H. and Shi, P.Y. 2006. West Nile virus 5'-cap structure is formed by sequential guanine N-7 and ribose 2'-O methylations by nonstructural protein 5. *J Virol.* **80**(17), pp.8362-8370.

Richner, J.M., Himansu, S., Dowd, K.A., Butler, S.L., Salazar, V., Fox, J.M., Julander, J.G., Tang, W.W., Shrestha, S., Pierson, T.C., Ciaramella, G. and Diamond, M.S. 2017. Modified mRNA Vaccines Protect against Zika Virus Infection. *Cell.* **169**(1), p176.

Roach, T. and Alcendor, D.J. 2017. Zika virus infection of cellular components of the blood-retinal barriers: implications for viral associated congenital ocular disease. *J Neuroinflammation.* **14**(1), p43.

Robin, Y. and Mouchet, J. 1975. [Serological and entomological study on yellow fever in Sierra Leone]. *Bull Soc Pathol Exot Filiales.* **68**(3), pp.249-258.

Roby, J.A., Setoh, Y.X., Hall, R.A. and Khromykh, A.A. 2015. Post-translational regulation and modifications of flavivirus structural proteins. *J Gen Virol.* **96**(Pt 7), pp.1551-1569.

Rodenhuis-Zybert, I.A., Wilschut, J. and Smit, J.M. 2011. Partial maturation: an immune-evasion strategy of dengue virus? *Trends Microbiol.* **19**(5), pp.248-254.

Roosendaal, J., Westaway, E.G., Khromykh, A. and Mackenzie, J.M. 2006. Regulated cleavages at the West Nile virus NS4A-2K-NS4B junctions play a major role in rearranging cytoplasmic membranes and Golgi trafficking of the NS4A protein. *J Virol.* **80**(9), pp.4623-4632.

Rosenberg, M.R. and Casarotto, M.G. 2010. Coexistence of two adamantane binding sites in the influenza A M2 ion channel. *Proc Natl Acad Sci U S A.* **107**(31), pp.13866-13871.

Rossi, S.L., Tesh, R.B., Azar, S.R., Muruato, A.E., Hanley, K.A., Auguste, A.J., Langsjoen, R.M., Paessler, S., Vasilakis, N. and Weaver, S.C. 2016. Characterization of a Novel Murine Model to Study Zika Virus. *Am J Trop Med Hyg.* **94**(6), pp.1362-1369.

Rossmann, J.S., Jing, X., Leser, G.P. and Lamb, R.A. 2010. Influenza virus M2 protein mediates ESCRT-independent membrane scission. *Cell.* **142**(6), pp.902-913.

Rossmann, J.S. and Lamb, R.A. 2013. Viral membrane scission. *Annu Rev Cell Dev Biol.* **29**, pp.551-569.

Roth, A., Mercier, A., Lepers, C., Hoy, D., Duituturaga, S., Benyon, E., Guillaumot, L. and Souares, Y. 2014. Concurrent outbreaks of dengue, chikungunya and Zika virus infections - an unprecedented epidemic wave of mosquito-borne viruses in the Pacific 2012-2014. *Euro Surveill.* **19**(41).

Ruigrok, R.W., Hirst, E.M. and Hay, A.J. 1991. The specific inhibition of influenza A virus maturation by amantadine: an electron microscopic examination. *J Gen Virol.* **72 (Pt 1)**, pp.191-194.

Russell, R.F., McDonald, J.U., Ivanova, M., Zhong, Z., Bukreyev, A. and Tregoning, J.S. 2015. Partial Attenuation of Respiratory Syncytial Virus with a Deletion of a Small Hydrophobic Gene Is Associated with Elevated Interleukin-1beta Responses. *J Virol.* **89(17)**, pp.8974-8981.

Sabin, A.B. 1967. Amantadine hydrochloride. Analysis of data related to its proposed use for prevention of A2 influenza virus disease in human beings. *JAMA.* **200(11)**, pp.943-950.

Sager, G., Gabaglio, S., Sztul, E. and Belov, G.A. 2018. Role of Host Cell Secretory Machinery in Zika Virus Life Cycle. *Viruses.* **10(10)**.

Saint, N., Montserret, R., Chipot, C. and Penin, F. 2009. Structural and functional analysis of the HCV p7 protein. *Methods Mol Biol.* **510**, pp.125-143.

Saiz, J.C. and Martin-Acebes, M.A. 2017. The Race To Find Antivirals for Zika Virus. *Antimicrob Agents Chemother.* **61(6)**.

Saiz, J.C., Vazquez-Calvo, A., Blazquez, A.B., Merino-Ramos, T., Escribano-Romero, E. and Martin-Acebes, M.A. 2016. Zika Virus: the Latest Newcomer. *Front Microbiol.* **7**, p496.

Sakaguchi, T., Tu, Q., Pinto, L.H. and Lamb, R.A. 1997. The active oligomeric state of the minimalistic influenza virus M2 ion channel is a tetramer. *Proc Natl Acad Sci U S A.* **94(10)**, pp.5000-5005.

Salam, A.P. and Horby, P. 2018. Isolation of viable Zika virus from spermatozoa. *Lancet Infect Dis.* **18(2)**, p144.

Saluzzo, J.F., Gonzalez, J.P., Herve, J.P. and Georges, A.J. 1981. [Serological survey for the prevalence of certain arboviruses in the human population of the south-east area of Central African Republic (author's transl)]. *Bull Soc Pathol Exot Filiales.* **74(5)**, pp.490-499.

Samsa, M.M., Mondotte, J.A., Iglesias, N.G., Assuncao-Miranda, I., Barbosa-Lima, G., Da Poian, A.T., Bozza, P.T. and Gamarnik, A.V. 2009. Dengue virus capsid protein usurps lipid droplets for viral particle formation. *PLoS Pathog.* **5(10)**, pe1000632.

Samuel, G.H., Wiley, M.R., Badawi, A., Adelman, Z.N. and Myles, K.M. 2016. Yellow fever virus capsid protein is a potent suppressor of RNA silencing that binds double-stranded RNA. *Proc Natl Acad Sci U S A.* **113(48)**, pp.13863-13868.

Sanz, M.A., Perez, L. and Carrasco, L. 1994. Semliki Forest virus 6K protein modifies membrane permeability after inducible expression in Escherichia coli cells. *J Biol Chem.* **269(16)**, pp.12106-12110.

Sarkar, S., Miwa, N., Kominami, H., Igarashi, N., Hayashi, S., Okada, T., Jahangeer, S. and Nakamura, S. 2001. Regulation of mammalian phospholipase D2: interaction with and stimulation by G(M2) activator. *Biochem J.* **359(Pt 3)**, pp.599-604.

Satchidanandam, V., Uchil, P.D. and Kumar, P. 2006. Organization of flaviviral replicase proteins in virus-induced membranes: a role for NS1' in Japanese encephalitis virus RNA synthesis. *Novartis Found Symp.* **277**, pp.136-145; discussion 145-138, 251-133.

Saunier, B., Triyatni, M., Ulianich, L., Maruvada, P., Yen, P. and Kohn, L.D. 2003. Role of the asialoglycoprotein receptor in binding and entry of hepatitis C virus structural proteins in cultured human hepatocytes. *J Virol.* **77(1)**, pp.546-559.

Scarff, C.A., Fuller, M.J.G., Thompson, R.F. and Iadanza, M.G. 2018. Variations on Negative Stain Electron Microscopy Methods: Tools for Tackling Challenging Systems. *J Vis Exp.* (132).

Scaturro, P., Cortese, M., Chatel-Chaix, L., Fischl, W. and Bartenschlager, R. 2015. Dengue Virus Non-structural Protein 1 Modulates Infectious Particle Production via Interaction with the Structural Proteins. *PLoS Pathog.* **11**(11), pe1005277.

Scaturro, P., Kastner, A.L. and Pichlmair, A. 2019. Chasing Intracellular Zika Virus Using Proteomics. *Viruses.* **11**(9).

Scaturro, P., Stukalov, A., Haas, D.A., Cortese, M., Draganova, K., Plaszczyca, A., Bartenschlager, R., Gotz, M. and Pichlmair, A. 2018. An orthogonal proteomic survey uncovers novel Zika virus host factors. *Nature.* **561**(7722), pp.253-257.

Schmidt, A.G., Yang, P.L. and Harrison, S.C. 2010. Peptide inhibitors of dengue-virus entry target a late-stage fusion intermediate. *PLoS Pathog.* **6**(4), pe1000851.

Schnell, J.R. and Chou, J.J. 2008. Structure and mechanism of the M2 proton channel of influenza A virus. *Nature.* **451**(7178), pp.591-595.

Schnirring, L. 2016. *Brazil confirms blood-transfusion Zika; PAHO calls for global support.* [Online]. Available from: <http://www.cidrap.umn.edu/news-perspective/2016/02/brazil-confirms-blood-transfusion-zika-paho-calls-global-support>

Schonberger, L.B., Bregman, D.J., Sullivan-Bolyai, J.Z., Keenlyside, R.A., Ziegler, D.W., Retalliau, H.F., Eddins, D.L. and Bryan, J.A. 1979. Guillain-Barre syndrome following vaccination in the National Influenza Immunization Program, United States, 1976--1977. *Am J Epidemiol.* **110**(2), pp.105-123.

Schubert, U., Ferrer-Montiel, A.V., Oblatt-Montal, M., Henklein, P., Strebel, K. and Montal, M. 1996. Identification of an ion channel activity of the Vpu transmembrane domain and its involvement in the regulation of virus release from HIV-1-infected cells. *FEBS Lett.* **398**(1), pp.12-18.

Schulman, J.L. 1968. Effect of 1-Amantanamine Hydrochloride (Amantadine Hci) and Methyl-1-Adamantanethylamine Hydrochloride (Rimantadine Hci) on Transmission of Influenza Virus Infection in Mice. *Proceedings of the Society for Experimental Biology and Medicine.* **128**(4), pp.1173-&.

Scott, C. and Griffin, S. 2015. Viroporins: structure, function and potential as antiviral targets. *J Gen Virol.* **96**(8), pp.2000-2027.

Scott, C., Kankanala, J., Foster, T.L., Goldhill, D.H., Bao, P., Simmons, K., Pinggen, M., Bentham, M., Atkins, E., Loundras, E., Elderfield, R., Claridge, J.K., Thompson, J., Stilwell, P.R., Tathineni, R., McKimmie, C.S., Targett-Adams, P., Schnell, J.R., Cook, G.P., Evans, S., Barclay, W.S., Foster, R. and Griffin, S. 2020. Site-directed M2 proton channel inhibitors enable synergistic combination therapy for rimantadine-resistant pandemic influenza. *PLoS Pathog.* **16**(8), pe1008716.

Sevvana, M., Long, F., Miller, A.S., Klose, T., Buda, G., Sun, L., Kuhn, R.J. and Rossmann, M.G. 2018. Refinement and Analysis of the Mature Zika Virus Cryo-EM Structure at 3.1 Å Resolution. *Structure.* **26**(9), pp.1169-1177 e1163.

Sharma, M., Li, C., Busath, D.D., Zhou, H.X. and Cross, T.A. 2011. Drug sensitivity, drug-resistant mutations, and structures of three conductance domains of viral porins. *Biochim Biophys Acta.* **1808**(2), pp.538-546.

Sharma, M., Yi, M., Dong, H., Qin, H., Peterson, E., Busath, D.D., Zhou, H.X. and Cross, T.A. 2010. Insight into the mechanism of the influenza A proton channel from a structure in a lipid bilayer. *Science*. **330**(6003), pp.509-512.

Shaw, J., Gosein, R., Kalita, M.M., Foster, T.L., Kankanala, J., Mahato, D.R., Scott, C., King, B.J., Brown, E., Bentham, M.J., Wetherill, L., Bloy, A., Samson, A., Harris, M., Mankouri, J., Rowlands, D., Macdonald, A., Tarr, A.W., Fischer, W.B., Foster, R. and Griffin, S. 2019. Rationally derived inhibitors of hepatitis C virus (HCV) p7 channel activity reveal prospect for bimodal antiviral therapy. p374793.

Sheng, Z.Y., Gao, N., Wang, Z.Y., Cui, X.Y., Zhou, D.S., Fan, D.Y., Chen, H., Wang, P.G. and An, J. 2017. Sertoli Cells Are Susceptible to ZIKV Infection in Mouse Testis. *Front Cell Infect Microbiol*. **7**, p272.

Shimbo, K., Brassard, D.L., Lamb, R.A. and Pinto, L.H. 1996. Ion selectivity and activation of the M2 ion channel of influenza virus. *Biophys J*. **70**(3), pp.1335-1346.

Shiryaev, S.A., Chernov, A.V., Aleshin, A.E., Shiryaeva, T.N. and Strongin, A.Y. 2009. NS4A regulates the ATPase activity of the NS3 helicase: a novel cofactor role of the non-structural protein NS4A from West Nile virus. *J Gen Virol*. **90**(Pt 9), pp.2081-2085.

Shuck, K., Lamb, R.A. and Pinto, L.H. 2000. Analysis of the pore structure of the influenza A virus M(2) ion channel by the substituted-cysteine accessibility method. *J Virol*. **74**(17), pp.7755-7761.

Shukla, A., Dey, D., Banerjee, K., Nain, A. and Banerjee, M. 2015. The C-terminal region of the non-structural protein 2B from Hepatitis A Virus demonstrates lipid-specific viroporin-like activity. *Sci Rep*. **5**, p15884.

Siemann, D.N., Strange, D.P., Maharaj, P.N., Shi, P.Y. and Verma, S. 2017. Zika Virus Infects Human Sertoli Cells and Modulates the Integrity of the In Vitro Blood-Testis Barrier Model. *J Virol*. **91**(22).

Simeonova, L., Gegova, G. and Galabov, A.S. 2012. Prophylactic and therapeutic combination effects of rimantadine and oseltamivir against influenza virus A (H3N2) infection in mice. *Antiviral Res*. **95**(2), pp.172-181.

Simpson, D.I. 1964. Zika Virus Infection in Man. *Trans R Soc Trop Med Hyg*. **58**, pp.335-338.

Sirohi, D., Chen, Z., Sun, L., Klose, T., Pierson, T.C., Rossmann, M.G. and Kuhn, R.J. 2016. The 3.8 Å resolution cryo-EM structure of Zika virus. *Science*. **352**(6284), pp.467-470.

Sirohi, D. and Kuhn, R.J. 2017. Zika Virus Structure, Maturation, and Receptors. *J Infect Dis*. **216**(suppl_10), pp.S935-S944.

Slon-Campos, J.L., Dejnirattisai, W., Jagger, B.W., Lopez-Camacho, C., Wongwiwat, W., Durnell, L.A., Winkler, E.S., Chen, R.E., Reyes-Sandoval, A., Rey, F.A., Diamond, M.S., Mongkolsapaya, J. and Screaton, G.R. 2019. A protective Zika virus E-dimer-based subunit vaccine engineered to abrogate antibody-dependent enhancement of dengue infection. *Nat Immunol*. **20**(10), pp.1291-1298.

Smithburn, K.C. 1952. Neutralizing antibodies against certain recently isolated viruses in the sera of human beings residing in East Africa. *J Immunol*. **69**(2), pp.223-234.

Song, Y., Mugavero, J., Stauff, C.B. and Wimmer, E. 2019. Dengue and Zika Virus 5' Untranslated Regions Harbor Internal Ribosomal Entry Site Functions. *MBio*. **10**(2).

Sorkin, A. and Waters, C.M. 1993. Endocytosis of growth factor receptors. *Bioessays*. **15**(6), pp.375-382.

Stadler, K., Allison, S.L., Schalich, J. and Heinz, F.X. 1997. Proteolytic activation of tick-borne encephalitis virus by furin. *J Virol*. **71**(11), pp.8475-8481.

Stefanik, M., Formanova, P., Bily, T., Vancova, M., Eyer, L., Palus, M., Salat, J., Braconi, C.T., Zanotto, P.M.A., Gould, E.A. and Ruzek, D. 2018. Characterisation of Zika virus infection in primary human astrocytes. *BMC Neurosci*. **19**(1), p5.

Steinmann, E., Penin, F., Kallis, S., Patel, A.H., Bartenschlager, R. and Pietschmann, T. 2007a. Hepatitis C virus p7 protein is crucial for assembly and release of infectious virions. *PLoS Pathog*. **3**(7), pe103.

Steinmann, E., Whitfield, T., Kallis, S., Dwek, R.A., Zitzmann, N., Pietschmann, T. and Bartenschlager, R. 2007b. Antiviral effects of amantadine and iminosugar derivatives against hepatitis C virus. *Hepatology*. **46**(2), pp.330-338.

Stern, O., Hung, Y.F., Valdau, O., Yaffe, Y., Harris, E., Hoffmann, S., Willbold, D. and Sklan, E.H. 2013. An N-terminal amphipathic helix in dengue virus nonstructural protein 4A mediates oligomerization and is essential for replication. *J Virol*. **87**(7), pp.4080-4085.

Stettler, K., Beltramello, M., Espinosa, D.A., Graham, V., Cassotta, A., Bianchi, S., Vanzetta, F., Minola, A., Jaconi, S., Mele, F., Foglierini, M., Pedotti, M., Simonelli, L., Dowall, S., Atkinson, B., Percivalle, E., Simmons, C.P., Varani, L., Blum, J., Baldanti, F., Camerini, E., Hewson, R., Harris, E., Lanzavecchia, A., Sallusto, F. and Corti, D. 2016. Specificity, cross-reactivity, and function of antibodies elicited by Zika virus infection. *Science*. **353**(6301), pp.823-826.

Stewart, H., Bartlett, C., Ross-Thriepland, D., Shaw, J., Griffin, S. and Harris, M. 2015. A novel method for the measurement of hepatitis C virus infectious titres using the IncuCyte ZOOM and its application to antiviral screening. *J Virol Methods*. **218**, pp.59-65.

StGelais, C., Foster, T.L., Verow, M., Atkins, E., Fishwick, C.W., Rowlands, D., Harris, M. and Griffin, S. 2009. Determinants of hepatitis C virus p7 ion channel function and drug sensitivity identified in vitro. *J Virol*. **83**(16), pp.7970-7981.

StGelais, C., Tuthill, T.J., Clarke, D.S., Rowlands, D.J., Harris, M. and Griffin, S. 2007. Inhibition of hepatitis C virus p7 membrane channels in a liposome-based assay system. *Antiviral Res*. **76**(1), pp.48-58.

Stiasny, K., Fritz, R., Pangerl, K. and Heinz, F.X. 2011. Molecular mechanisms of flavivirus membrane fusion. *Amino Acids*. **41**(5), pp.1159-1163.

Stouffer, A.L., Ma, C., Cristian, L., Ohigashi, Y., Lamb, R.A., Lear, J.D., Pinto, L.H. and DeGrado, W.F. 2008. The interplay of functional tuning, drug resistance, and thermodynamic stability in the evolution of the M2 proton channel from the influenza A virus. *Structure*. **16**(7), pp.1067-1076.

Strauss, M., Levy, H.C., Bostina, M., Filman, D.J. and Hogle, J.M. 2013. RNA transfer from poliovirus 135S particles across membranes is mediated by long umbilical connectors. *J Virol*. **87**(7), pp.3903-3914.

Strebel, K., Klimkait, T. and Martin, M.A. 1988. A novel gene of HIV-1, vpu, and its 16-kilodalton product. *Science*. **241**(4870), pp.1221-1223.

Sugrue, R.J. and Hay, A.J. 1991. Structural characteristics of the M2 protein of influenza A viruses: evidence that it forms a tetrameric channel. *Virology*. **180**(2), pp.617-624.

Sun, G., Larsen, C.N., Baumgarth, N., Klem, E.B. and Scheuermann, R.H. 2017. Comprehensive Annotation of Mature Peptides and Genotypes for Zika Virus. *PLoS One*. **12**(1), pe0170462.

Sun, X., Hua, S., Chen, H.R., Ouyang, Z., Einkauf, K., Tse, S., Ard, K., Ciaranello, A., Yawetz, S., Sax, P., Rosenberg, E.S., Lichterfeld, M. and Yu, X.G. 2017. Transcriptional Changes during Naturally Acquired Zika Virus Infection Render Dendritic Cells Highly Conducive to Viral Replication. *Cell Rep.* **21**(12), pp.3471-3482.

Suprynowicz, F.A., Krawczyk, E., Hebert, J.D., Sudarshan, S.R., Simic, V., Kamonjoh, C.M. and Schlegel, R. 2010. The human papillomavirus type 16 E5 oncoprotein inhibits epidermal growth factor trafficking independently of endosome acidification. *J Virol.* **84**(20), pp.10619-10629.

Surana, P., Satchidanandam, V. and Nair, D.T. 2014. RNA-dependent RNA polymerase of Japanese encephalitis virus binds the initiator nucleotide GTP to form a mechanistically important pre-initiation state. *Nucleic Acids Res.* **42**(4), pp.2758-2773.

Tabata, K., Arimoto, M., Arakawa, M., Nara, A., Saito, K., Omori, H., Arai, A., Ishikawa, T., Konishi, E., Suzuki, R., Matsuura, Y. and Morita, E. 2016. Unique Requirement for ESCRT Factors in Flavivirus Particle Formation on the Endoplasmic Reticulum. *Cell Rep.* **16**(9), pp.2339-2347.

Tabata, T., Pettit, M., Puerta-Guardo, H., Michlmayr, D., Wang, C., Fang-Hoover, J., Harris, E. and Pereira, L. 2016. Zika Virus Targets Different Primary Human Placental Cells, Suggesting Two Routes for Vertical Transmission. *Cell Host Microbe.* **20**(2), pp.155-166.

Taguwa, S., Yeh, M.T., Rainbolt, T.K., Nayak, A., Shao, H., Gestwicki, J.E., Andino, R. and Frydman, J. 2019. Zika Virus Dependence on Host Hsp70 Provides a Protective Strategy against Infection and Disease. *Cell Rep.* **26**(4), pp.906-920 e903.

Tai, W., Voronin, D., Chen, J., Bao, W., Kessler, D.A., Shaz, B., Jiang, S., Yazdanbakhsh, K. and Du, L. 2019. Transfusion-Transmitted Zika Virus Infection in Pregnant Mice Leads to Broad Tissue Tropism With Severe Placental Damage and Fetal Demise. *Front Microbiol.* **10**, p29.

Takahashi, H., Takahashi, C., Moreland, N.J., Chang, Y.T., Sawasaki, T., Ryo, A., Vasudevan, S.G., Suzuki, Y. and Yamamoto, N. 2012. Establishment of a robust dengue virus NS3-NS5 binding assay for identification of protein-protein interaction inhibitors. *Antiviral Res.* **96**(3), pp.305-314.

Takamatsu, Y., Okamoto, K., Dinh, D.T., Yu, F., Hayasaka, D., Uchida, L., Nabeshima, T., Buerano, C.C. and Morita, K. 2014. NS1' protein expression facilitates production of Japanese encephalitis virus in avian cells and embryonated chicken eggs. *J Gen Virol.* **95**(Pt 2), pp.373-383.

Tan, T.Y., Fibriansah, G., Kostyuchenko, V.A., Ng, T.S., Lim, X.X., Zhang, S., Lim, X.N., Wang, J., Shi, J., Morais, M.C., Corti, D. and Lok, S.M. 2020. Capsid protein structure in Zika virus reveals the flavivirus assembly process. *Nat Commun.* **11**(1), p895.

Tang, H., Hammack, C., Ogden, S.C., Wen, Z., Qian, X., Li, Y., Yao, B., Shin, J., Zhang, F., Lee, E.M., Christian, K.M., Didier, R.A., Jin, P., Song, H. and Ming, G.L. 2016. Zika Virus Infects Human Cortical Neural Progenitors and Attenuates Their Growth. *Cell Stem Cell.* **18**(5), pp.587-590.

Tebas, P., Roberts, C.C., Muthumani, K., Reuschel, E.L., Kudchodkar, S.B., Zaidi, F.I., White, S., Khan, A.S., Racine, T., Choi, H., Boyer, J., Park, Y.K., Trottier, S., Remigio, C., Krieger, D., Spruill, S.E., Bagarazzi, M., Kobinger, G.P., Weiner, D.B. and Maslow, J.N. 2017. Safety and Immunogenicity of an Anti-Zika Virus DNA Vaccine - Preliminary Report. *N Engl J Med.*

- Teo, C.S. and Chu, J.J. 2014. Cellular vimentin regulates construction of dengue virus replication complexes through interaction with NS4A protein. *J Virol.* **88**(4), pp.1897-1913.
- Thomas, S.M., Obermayr, U., Fischer, D., Kreyling, J. and Beierkuhnlein, C. 2012. Low-temperature threshold for egg survival of a post-diapause and non-diapause European aedine strain, *Aedes albopictus* (Diptera: Culicidae). *Parasit Vectors.* **5**, p100.
- Thomaston, J.L. and DeGrado, W.F. 2016. Crystal structure of the drug-resistant S31N influenza M2 proton channel. *Protein Sci.* **25**(8), pp.1551-1554.
- Thongon, N., Zucal, C., D'Agostino, V.G., Tebaldi, T., Ravera, S., Zamporlini, F., Piacente, F., Moschoi, R., Raffaelli, N., Quattrone, A., Nencioni, A., Peyron, J.F. and Provenzani, A. 2018. Cancer cell metabolic plasticity allows resistance to NAMPT inhibition but invariably induces dependence on LDHA. *Cancer Metab.* **6**, p1.
- Tian, H., Ji, X., Yang, X., Zhang, Z., Lu, Z., Yang, K., Chen, C., Zhao, Q., Chi, H., Mu, Z., Xie, W., Wang, Z., Lou, H., Yang, H. and Rao, Z. 2016. Structural basis of Zika virus helicase in recognizing its substrates. *Protein Cell.* **7**(8), pp.562-570.
- Tobler, K., Kelly, M.L., Pinto, L.H. and Lamb, R.A. 1999. Effect of cytoplasmic tail truncations on the activity of the M(2) ion channel of influenza A virus. *J Virol.* **73**(12), pp.9695-9701.
- Togo, Y., Hornick, R.B. and Dawkins, A.T., Jr. 1968. Studies on induced influenza in man. I. Double-blind studies designed to assess prophylactic efficacy of amantadine hydrochloride against a2/Rockville/1/65 strain. *JAMA.* **203**(13), pp.1089-1094.
- Tomar, P.P.S., Oren, R., Krugliak, M. and Arkin, I.T. 2019. Potential Viroporin Candidates From Pathogenic Viruses Using Bacteria-Based Bioassays. *Viruses.* **11**(7).
- Torres, J., Maheswari, U., Parthasarathy, K., Ng, L., Liu, D.X. and Gong, X. 2007. Conductance and amantadine binding of a pore formed by a lysine-flanked transmembrane domain of SARS coronavirus envelope protein. *Protein Sci.* **16**(9), pp.2065-2071.
- Tuthill, T.J., Bubeck, D., Rowlands, D.J. and Hogle, J.M. 2006. Characterization of early steps in the poliovirus infection process: receptor-decorated liposomes induce conversion of the virus to membrane-anchored entry-intermediate particles. *J Virol.* **80**(1), pp.172-180.
- Tuthill, T.J., Groppelli, E., Hogle, J.M. and Rowlands, D.J. 2010. Picornaviruses. *Curr Top Microbiol Immunol.* **343**, pp.43-89.
- Ulmschneider, M.B., Bagneris, C., McCusker, E.C., Decaen, P.G., Delling, M., Clapham, D.E., Ulmschneider, J.P. and Wallace, B.A. 2013. Molecular dynamics of ion transport through the open conformation of a bacterial voltage-gated sodium channel. *Proc Natl Acad Sci U S A.* **110**(16), pp.6364-6369.
- Umareddy, I., Chao, A., Sampath, A., Gu, F. and Vasudevan, S.G. 2006. Dengue virus NS4B interacts with NS3 and dissociates it from single-stranded RNA. *J Gen Virol.* **87**(Pt 9), pp.2605-2614.
- van der Schaar, H.M., Rust, M.J., Chen, C., van der Ende-Metselaar, H., Wilschut, J., Zhuang, X. and Smit, J.M. 2008. Dissecting the cell entry pathway of dengue virus by single-particle tracking in living cells. *PLoS Pathog.* **4**(12), pe1000244.
- Vieyres, G., Brohm, C., Friesland, M., Gentzsch, J., Wolk, B., Roingeard, P., Steinmann, E. and Pietschmann, T. 2013. Subcellular localization and function

of an epitope-tagged p7 viroporin in hepatitis C virus-producing cells. *J Virol.* **87**(3), pp.1664-1678.

ViralZone.

Wang, C., Lamb, R.A. and Pinto, L.H. 1994. Direct measurement of the influenza A virus M2 protein ion channel activity in mammalian cells. *Virology.* **205**(1), pp.133-140.

Wang, C., Lamb, R.A. and Pinto, L.H. 1995. Activation of the M2 ion channel of influenza virus: a role for the transmembrane domain histidine residue. *Biophys J.* **69**(4), pp.1363-1371.

Wang, C., Takeuchi, K., Pinto, L.H. and Lamb, R.A. 1993. Ion channel activity of influenza A virus M2 protein: characterization of the amantadine block. *J Virol.* **67**(9), pp.5585-5594.

Wang, J., Ma, C., Wang, J., Jo, H., Canturk, B., Fiorin, G., Pinto, L.H., Lamb, R.A., Klein, M.L. and DeGrado, W.F. 2013. Discovery of novel dual inhibitors of the wild-type and the most prevalent drug-resistant mutant, S31N, of the M2 proton channel from influenza A virus. *J Med Chem.* **56**(7), pp.2804-2812.

Wang, L., Liang, R., Gao, Y., Li, Y., Deng, X., Xiang, R., Zhang, Y., Ying, T., Jiang, S. and Yu, F. 2019. Development of Small-Molecule Inhibitors Against Zika Virus Infection. *Front Microbiol.* **10**, p2725.

Wang, Y., Hu, Y., Xu, S., Zhang, Y., Musharrafieh, R., Hau, R.K., Ma, C. and Wang, J. 2018. In Vitro Pharmacokinetic Optimizations of AM2-S31N Channel Blockers Led to the Discovery of Slow-Binding Inhibitors with Potent Antiviral Activity against Drug-Resistant Influenza A Viruses. *J Med Chem.* **61**(3), pp.1074-1085.

Wang, Z.Y., Wang, Z., Zhen, Z.D., Feng, K.H., Guo, J., Gao, N., Fan, D.Y., Han, D.S., Wang, P.G. and An, J. 2017. Axl is not an indispensable factor for Zika virus infection in mice. *J Gen Virol.* **98**(8), pp.2061-2068.

Wassenaar, T.A., Ingolfsson, H.I., Bockmann, R.A., Tieleman, D.P. and Marrink, S.J. 2015. Computational Lipidomics with insane: A Versatile Tool for Generating Custom Membranes for Molecular Simulations. *J Chem Theory Comput.* **11**(5), pp.2144-2155.

Wassenaar, T.A., Pluhackova, K., Bockmann, R.A., Marrink, S.J. and Tieleman, D.P. 2014. Going Backward: A Flexible Geometric Approach to Reverse Transformation from Coarse Grained to Atomistic Models. *J Chem Theory Comput.* **10**(2), pp.676-690.

Webb, B. and Sali, A. 2016. Comparative Protein Structure Modeling Using MODELLER. *Curr Protoc Bioinformatics.* **54**, pp.5 6 1-5 6 37.

Wells, M.F., Salick, M.R., Wiskow, O., Ho, D.J., Worringer, K.A., Ihry, R.J., Komminen, S., Bilican, B., Klim, J.R., Hill, E.J., Kane, L.T., Ye, C., Kaykas, A. and Eggan, K. 2016. Genetic Ablation of AXL Does Not Protect Human Neural Progenitor Cells and Cerebral Organoids from Zika Virus Infection. *Cell Stem Cell.* **19**(6), pp.703-708.

Welsch, S., Miller, S., Romero-Brey, I., Merz, A., Bleck, C.K. and Walther, P. 2009. Composition and three-dimensional architecture of the dengue virus replication and assembly sites. *Cell Host Microbe.* **5**.

Wetherill, L.F., Holmes, K.K., Verow, M., Muller, M., Howell, G., Harris, M., Fishwick, C., Stonehouse, N., Foster, R., Blair, G.E., Griffin, S. and Macdonald, A. 2012. High-risk human papillomavirus E5 oncoprotein displays channel-forming activity sensitive to small-molecule inhibitors. *J Virol.* **86**(9), pp.5341-5351.

- Wetherill, L.F., Wasson, C.W., Swinscoe, G., Kealy, D., Foster, R., Griffin, S. and Macdonald, A. 2018. Alkyl-imino sugars inhibit the pro-oncogenic ion channel function of human papillomavirus (HPV) E5. *Antiviral Res.* **158**, pp.113-121.
- Wewer, C.R. and Khandelia, H. 2018. Different footprints of the Zika and dengue surface proteins on viral membranes. *Soft Matter.* **14**(27), pp.5615-5621.
- Whitehead, S.S., Bukreyev, A., Teng, M.N., Firestone, C.Y., St Claire, M., Elkins, W.R., Collins, P.L. and Murphy, B.R. 1999. Recombinant respiratory syncytial virus bearing a deletion of either the NS2 or SH gene is attenuated in chimpanzees. *J Virol.* **73**(4), pp.3438-3442.
- Whitfield, T., Miles, A.J., Scheinost, J.C., Offer, J., Wentworth, P., Jr., Dwek, R.A., Wallace, B.A., Biggin, P.C. and Zitzmann, N. 2011. The influence of different lipid environments on the structure and function of the hepatitis C virus p7 ion channel protein. *Mol Membr Biol.* **28**(5), pp.254-264.
- Wilkinson, J., Ewart, G., Luscombe, C., McBride, K., Ratanasuwan, W., Miller, M. and Murphy, R.L. 2016. A Phase 1b/2a study of the safety, pharmacokinetics and antiviral activity of BIT225 in patients with HIV-1 infection. *J Antimicrob Chemother.* **71**(3), pp.731-738.
- Willey, R.L., Maldarelli, F., Martin, M.A. and Strebel, K. 1992a. Human immunodeficiency virus type 1 Vpu protein induces rapid degradation of CD4. *J Virol.* **66**(12), pp.7193-7200.
- Willey, R.L., Maldarelli, F., Martin, M.A. and Strebel, K. 1992b. Human immunodeficiency virus type 1 Vpu protein regulates the formation of intracellular gp160-CD4 complexes. *J Virol.* **66**(1), pp.226-234.
- Wilson, L., Gage, P. and Ewart, G. 2006. Hexamethylene amiloride blocks E protein ion channels and inhibits coronavirus replication. *Virology.* **353**(2), pp.294-306.
- Wilson, L., McKinlay, C., Gage, P. and Ewart, G. 2004. SARS coronavirus E protein forms cation-selective ion channels. *Virology.* **330**(1), pp.322-331.
- Wingfield, W.L., Pollack, D. and Grunert, R.R. 1969. Therapeutic efficacy of amantadine HCl and rimantadine HCl in naturally occurring influenza A2 respiratory illness in man. *N Engl J Med.* **281**(11), pp.579-584.
- Wong, S.S., Chebib, M., Haqshenas, G., Loveland, B. and Gowans, E.J. 2011. Dengue virus PrM/M proteins fail to show pH-dependent ion channel activity in *Xenopus* oocytes. *Virology.* **412**(1), pp.83-90.
- Wozniak, A.L., Griffin, S., Rowlands, D., Harris, M., Yi, M., Lemon, S.M. and Weinman, S.A. 2010. Intracellular proton conductance of the hepatitis C virus p7 protein and its contribution to infectious virus production. *PLoS Pathog.* **6**(9), pe1001087.
- Wu, R.H., Tsai, M.H., Chao, D.Y. and Yueh, A. 2015. Scanning mutagenesis studies reveal a potential intramolecular interaction within the C-terminal half of dengue virus NS2A involved in viral RNA replication and virus assembly and secretion. *J Virol.* **89**(8), pp.4281-4295.
- Wu, Y., Canturk, B., Jo, H., Ma, C., Gianti, E., Klein, M.L., Pinto, L.H., Lamb, R.A., Fiorin, G., Wang, J. and DeGrado, W.F. 2014. Flipping in the pore: discovery of dual inhibitors that bind in different orientations to the wild-type versus the amantadine-resistant S31N mutant of the influenza A virus M2 proton channel. *J Am Chem Soc.* **136**(52), pp.17987-17995.
- Xia, H., Luo, H., Shan, C., Muruato, A.E., Nunes, B.T.D., Medeiros, D.B.A., Zou, J., Xie, X., Giraldo, M.I., Vasconcelos, P.F.C., Weaver, S.C., Wang, T.,

- Rajsbaum, R. and Shi, P.Y. 2018. An evolutionary NS1 mutation enhances Zika virus evasion of host interferon induction. *Nat Commun.* **9**(1), p414.
- Xie, X., Zou, J., Puttikhunt, C., Yuan, Z. and Shi, P.Y. 2015. Two distinct sets of NS2A molecules are responsible for dengue virus RNA synthesis and virion assembly. *J Virol.* **89**(2), pp.1298-1313.
- Xu, H.T., Hassounah, S.A., Colby-Germinario, S.P., Oliveira, M., Fogarty, C., Quan, Y., Han, Y., Golubkov, O., Ibanescu, I., Brenner, B., Stranix, B.R. and Wainberg, M.A. 2017. Purification of Zika virus RNA-dependent RNA polymerase and its use to identify small-molecule Zika inhibitors. *J Antimicrob Chemother.* **72**(3), pp.727-734.
- Xu, K., Song, Y., Dai, L., Zhang, Y., Lu, X., Xie, Y., Zhang, H., Cheng, T., Wang, Q., Huang, Q., Bi, Y., Liu, W.J., Liu, W., Li, X., Qin, C., Shi, Y., Yan, J., Zhou, D. and Gao, G.F. 2018. Recombinant Chimpanzee Adenovirus Vaccine AdC7-M/E Protects against Zika Virus Infection and Testis Damage. *J Virol.* **92**(6).
- Xu, S., Ci, Y., Wang, L., Yang, Y., Zhang, L., Xu, C., Qin, C. and Shi, L. 2019. Zika virus NS3 is a canonical RNA helicase stimulated by NS5 RNA polymerase. *Nucleic Acids Res.*
- Xu, Z., Anderson, R. and Hobman, T.C. 2011. The capsid-binding nucleolar helicase DDX56 is important for infectivity of West Nile virus. *J Virol.* **85**(11), pp.5571-5580.
- Yang, M., Peyret, C., Shi, X.Q., Siron, N., Jang, J.H., Wu, S., Fournier, S. and Zhang, J. 2015. Evidence from Human and Animal Studies: Pathological Roles of CD8(+) T Cells in Autoimmune Peripheral Neuropathies. *Front Immunol.* **6**, p532.
- Yang, M.R., Lee, S.R., Oh, W., Lee, E.W., Yeh, J.Y., Nah, J.J., Joo, Y.S., Shin, J., Lee, H.W., Pyo, S. and Song, J. 2008. West Nile virus capsid protein induces p53-mediated apoptosis via the sequestration of HDM2 to the nucleolus. *Cell Microbiol.* **10**(1), pp.165-176.
- Ye, Q., Li, X.F., Zhao, H., Li, S.H., Deng, Y.Q., Cao, R.Y., Song, K.Y., Wang, H.J., Hua, R.H., Yu, Y.X., Zhou, X., Qin, E.D. and Qin, C.F. 2012. A single nucleotide mutation in NS2A of Japanese encephalitis-live vaccine virus (SA14-14-2) ablates NS1' formation and contributes to attenuation. *J Gen Virol.* **93**(Pt 9), pp.1959-1964.
- Ye, Y. and Hogue, B.G. 2007. Role of the coronavirus E viroporin protein transmembrane domain in virus assembly. *J Virol.* **81**(7), pp.3597-3607.
- Yeagle, P.L., Bennett, M., Lemaitre, V. and Watts, A. 2007. Transmembrane helices of membrane proteins may flex to satisfy hydrophobic mismatch. *Biochim Biophys Acta.* **1768**(3), pp.530-537.
- Yi, M., Ma, Y., Yates, J. and Lemon, S.M. 2007. Compensatory mutations in E1, p7, NS2, and NS3 enhance yields of cell culture-infectious intergenotypic chimeric hepatitis C virus. *J Virol.* **81**(2), pp.629-638.
- Yi, Z., Yuan, Z., Rice, C.M. and MacDonald, M.R. 2012. Flavivirus replication complex assembly revealed by DNAJC14 functional mapping. *J Virol.* **86**(21), pp.11815-11832.
- Yoon, K.J., Song, G., Qian, X., Pan, J., Xu, D., Rho, H.S., Kim, N.S., Habela, C., Zheng, L., Jacob, F., Zhang, F., Lee, E.M., Huang, W.K., Ringeling, F.R., Vissers, C., Li, C., Yuan, L., Kang, K., Kim, S., Yeo, J., Cheng, Y., Liu, S., Wen, Z., Qin, C.F., Wu, Q., Christian, K.M., Tang, H., Jin, P., Xu, Z., Qian, J., Zhu, H., Song, H. and Ming, G.L. 2017. Zika-Virus-Encoded NS2A Disrupts Mammalian

Cortical Neurogenesis by Degrading Adherens Junction Proteins. *Cell Stem Cell*. **21**(3), pp.349-358 e346.

Young, L.B., Melian, E.B. and Khromykh, A.A. 2013. NS1' colocalizes with NS1 and can substitute for NS1 in West Nile virus replication. *J Virol*. **87**(16), pp.9384-9390.

Yu, I.M., Holdaway, H.A., Chipman, P.R., Kuhn, R.J., Rossmann, M.G. and Chen, J. 2009. Association of the pr peptides with dengue virus at acidic pH blocks membrane fusion. *J Virol*. **83**(23), pp.12101-12107.

Yu, I.M., Zhang, W., Holdaway, H.A., Li, L., Kostyuchenko, V.A., Chipman, P.R., Kuhn, R.J., Rossmann, M.G. and Chen, J. 2008. Structure of the immature dengue virus at low pH primes proteolytic maturation. *Science*. **319**(5871), pp.1834-1837.

Yuan, L., Huang, X.Y., Liu, Z.Y., Zhang, F., Zhu, X.L., Yu, J.Y., Ji, X., Xu, Y.P., Li, G., Li, C., Wang, H.J., Deng, Y.Q., Wu, M., Cheng, M.L., Ye, Q., Xie, D.Y., Li, X.F., Wang, X., Shi, W., Hu, B., Shi, P.Y., Xu, Z. and Qin, C.F. 2017. A single mutation in the prM protein of Zika virus contributes to fetal microcephaly. *Science*. **358**(6365), pp.933-936.

Zhang, J., Lan, Y., Li, M.Y., Lamers, M.M., Fusade-Boyer, M., Klemm, E., Thiele, C., Ashour, J. and Sanyal, S. 2018. Flaviviruses Exploit the Lipid Droplet Protein AUP1 to Trigger Lipophagy and Drive Virus Production. *Cell Host Microbe*. **23**(6), pp.819-831 e815.

Zhang, Q., Hunke, C., Yau, Y.H., Seow, V., Lee, S., Tanner, L.B., Guan, X.L., Wenk, M.R., Fibriansah, G., Chew, P.L., Kukkaro, P., Biukovic, G., Shi, P.Y., Shochat, S.G., Gruber, G. and Lok, S.M. 2012. The stem region of premembrane protein plays an important role in the virus surface protein rearrangement during dengue maturation. *J Biol Chem*. **287**(48), pp.40525-40534.

Zhang, W., Chipman, P.R., Corver, J., Johnson, P.R., Zhang, Y., Mukhopadhyay, S., Baker, T.S., Strauss, J.H., Rossmann, M.G. and Kuhn, R.J. 2003. Visualization of membrane protein domains by cryo-electron microscopy of dengue virus. *Nat Struct Biol*. **10**(11), pp.907-912.

Zhang, W., Kaufmann, B., Chipman, P.R., Kuhn, R.J. and Rossmann, M.G. 2013. Membrane curvature in flaviviruses. *J Struct Biol*. **183**(1), pp.86-94.

Zhang, X., Li, Y. and Li, Y.J.B. 2009. Evaluating signal peptide prediction methods for Gram-positive bacteria. **64**(4), pp.655-659.

Zhang, X., Sheng, J., Austin, S.K., Hoornweg, T.E., Smit, J.M., Kuhn, R.J., Diamond, M.S. and Rossmann, M.G. 2015. Structure of acidic pH dengue virus showing the fusogenic glycoprotein trimers. *J Virol*. **89**(1), pp.743-750.

Zhang, X., Xie, X., Xia, H., Zou, J., Huang, L., Popov, V.L., Chen, X. and Shi, P.Y. 2019. Zika Virus NS2A-Mediated Virion Assembly. *mBio*. **10**(5).

Zhang, Y., Zhang, W., Ogata, S., Clements, D., Strauss, J.H., Baker, T.S., Kuhn, R.J. and Rossmann, M.G. 2004. Conformational changes of the flavivirus E glycoprotein. *Structure*. **12**(9), pp.1607-1618.

Zhao, B., Yi, G., Du, F., Chuang, Y.C., Vaughan, R.C., Sankaran, B., Kao, C.C. and Li, P. 2017. Structure and function of the Zika virus full-length NS5 protein. *Nat Commun*. **8**, p14762.

Zhao, Z., Yang, M., Azar, S.R., Soong, L., Weaver, S.C., Sun, J., Chen, Y., Rossi, S.L. and Cai, J. 2017. Viral Retinopathy in Experimental Models of Zika Infection. *Invest Ophthalmol Vis Sci*. **58**(10), pp.4355-4365.

Zhu, X., Ji, M.H., Li, S.M., Li, B., Mei, L. and Yang, J.J. 2019. Systemic Inflammation Impairs Mood Function by Disrupting the Resting-State Functional

Network in a Rat Animal Model Induced by Lipopolysaccharide Challenge. *Mediators Inflamm.* **2019**, p6212934.

Zhu, Z., Chan, J.F., Tee, K.M., Choi, G.K., Lau, S.K., Woo, P.C., Tse, H. and Yuen, K.Y. 2016. Comparative genomic analysis of pre-epidemic and epidemic Zika virus strains for virological factors potentially associated with the rapidly expanding epidemic. *Emerg Microbes Infect.* **5**, pe22.

Zika Cumulative Cases. 2018. [Online]. Available from: https://www.paho.org/hq/index.php?option=com_content&view=article&id=12390:zika-cumulative-cases&Itemid=42090&lang=en

ZIKA VIRUS MICROCEPHALY GUILLAIN-BARRÉ SYNDROME 2016.

Zmurko, J., Marques, R.E., Schols, D., Verbeken, E., Kaptein, S.J. and Neyts, J. 2016. The Viral Polymerase Inhibitor 7-Deaza-2'-C-Methyladenosine Is a Potent Inhibitor of In Vitro Zika Virus Replication and Delays Disease Progression in a Robust Mouse Infection Model. *PLoS Negl Trop Dis.* **10**(5), pe0004695.

Zou, J., Xie, X., Lee le, T., Chandrasekaran, R., Reynaud, A., Yap, L., Wang, Q.Y., Dong, H., Kang, C., Yuan, Z., Lescar, J. and Shi, P.Y. 2014. Dimerization of flavivirus NS4B protein. *J Virol.* **88**(6), pp.3379-3391.

Zou, J., Xie, X., Wang, Q.Y., Dong, H., Lee, M.Y., Kang, C., Yuan, Z. and Shi, P.Y. 2015. Characterization of dengue virus NS4A and NS4B protein interaction. *J Virol.* **89**(7), pp.3455-3470.

Zoueva, O.P., Bailly, J.E., Nicholls, R. and Brown, E.G. 2002. Aggregation of influenza virus ribonucleocapsids at low pH. *Virus Res.* **85**(2), pp.141-149.

Zust, R., Cervantes-Barragan, L., Habjan, M., Maier, R., Neuman, B.W., Ziebuhr, J., Szretter, K.J., Baker, S.C., Barchet, W., Diamond, M.S., Siddell, S.G., Ludewig, B. and Thiel, V. 2011. Ribose 2'-O-methylation provides a molecular signature for the distinction of self and non-self mRNA dependent on the RNA sensor Mda5. *Nat Immunol.* **12**(2), pp.137-143.

Appendix

Appendix A Recipes

A.1 Vero cell culture media:

DMEM + 10% FCS + 5% PenStrep

A.2 BHK-21 Cell culture media:

BHK-21 media + 10% FCS + 5% PenStrep

A.3 Freezing media:

Cell culture media + 10% DMSO

A.4 EBC lysis buffer

50 mM Tris HCl pH 8.0, 140 mM NaCl, 100 mM NaF, 200 μ m Na₃VO₄, 0.1 % SDS, 1 % Triton X100, 1 tablet protease inhibitor per 50 ml (complete ULTRA tablets, Roche)

A.5 2x Laemmli Buffer

100 mM Tris HCl pH 6.8, 4 % SDS, 20 % Glycerol, 10 mM DTT (Dithiothreitol), 0.025 % Bromophenol Blue

A.6 Tris Glycine running buffer

25 mM Tris base pH 8.0, 250 mM Glycine, 0.1 % SDS

A.7 Towbin

A.8

25mM Tris base, 250 mM Glycine, 20 % Methanol

A.9 Tris-buffered Saline

50 mM Tris HCl pH 7.5, 150 mM NaCl

A.10 ECL Solutions:

a. **Solution 1: 0.4 mM p-Coumaric acid, 2.5 mM Luminol, 0.1 Tris pH 8.5;**

b. **Solution 2: 0.02 % H₂O₂ 0.1 mM Tris pH 8.5**

A.11 Liposome Assay Buffer

10 mM HEPES pH 7.4 107 mM NaCl

A.12 Native-PAGE Loading Dye

150 mM Tris-Cl pH 7.0 30 % v/v Glycerol 0.05 % w/v bromophenol blue

A.13 Native-PAGE running buffer:

0.025 mM Tris-base 0.192 mM Glycine pH 8.5

A.14 Coomassie Blue Stain solution

0.1% Coomassie Blue, 10% acetic acid, 50% methanol, 40% H₂O

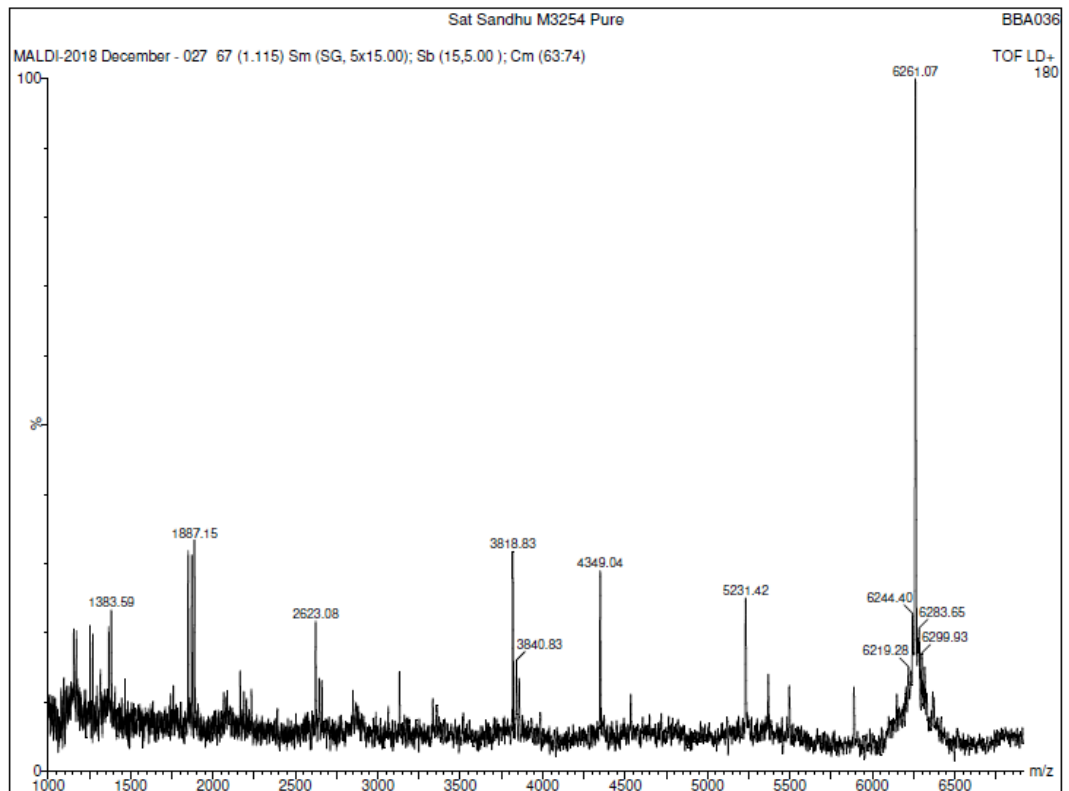
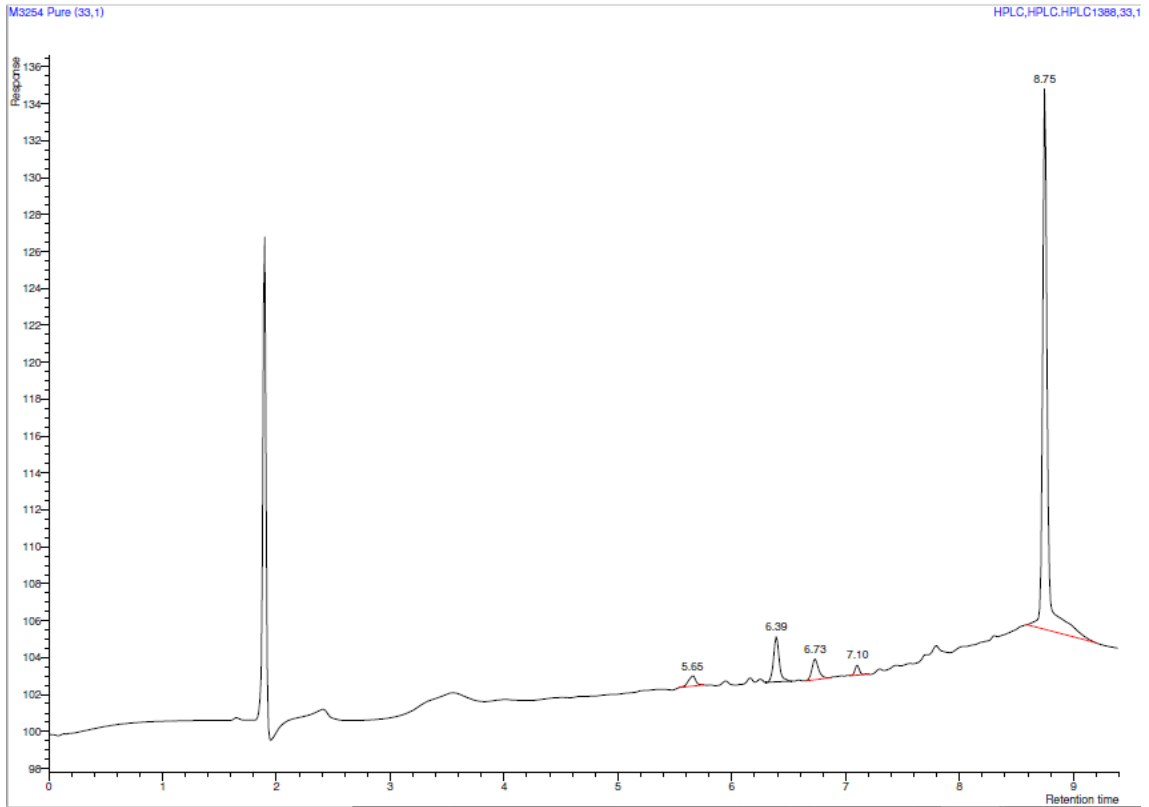
A.15 Coomassie Blue destain solution

10% acetic acid, 50% methanol, 40% H₂O

A.16 Carboxyfluorescein (CF) Buffer

50 mM CF 10 mM HEPES-NaOH pH 7.4 107 mM NaCl

M peptide HPLC and Mass Spec traces (Alta Bioscience).



Appendix B Supplementary Data

Simulating M protein in the absence of the second TMD

The linker region between the two transmembrane domains is only short, however the simulations of M protein with two TMDs shown in Figure 3.9 Monomeric M protein with two TMDs is stable in a POPC bilayer (Figure 3.9 and Figure 3.10) shows this region interacts with the lower leaflet of the lipid bilayer causing the membrane conformation to alter, pinching up due to the short length of the transmembrane domains. To determine whether this linker region alone, without the presence of the C-terminal TMD could still interact with the inner leaflet and cause the membrane conformational change we ran an additional set of simulations with M protein truncated at the C-termini of 20 amino acids, forming a 38 amino acid protein.

After 3 μ s of coarse grain simulation the absence of the C-terminal TMD did not affect the conformation or interactions of the truncated protein with the membrane (Figure B1.). The same membrane alterations occurred and there was less RMSF variation between repeated simulations (Figure B1). From this set of simulations, it appears H3 is not important for M protein to remain anchored within the membrane; H2 and the linker region alone results in this strong interaction.

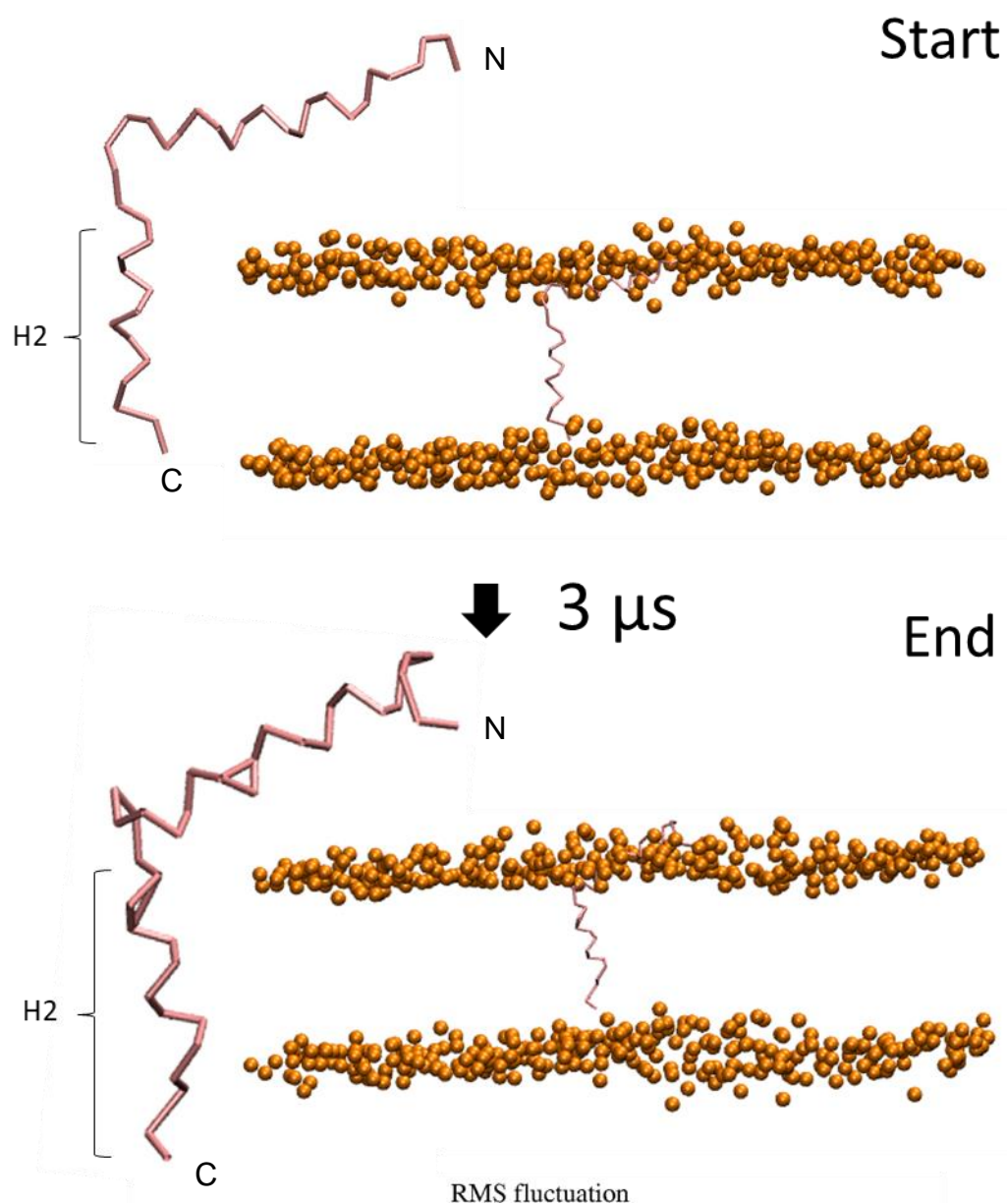


Figure B.1 Monomeric M protein truncated after the linker region is stable in a POPC bilayer

Conformations of monomeric H3-truncated M protein before and after 3 μs simulation. Protein backbone shown in pink and phospholipid bilayer heads shown in orange. **A.** Monomeric M protein simulation starting conformation, shown side on with and without phospholipid bilayer heads. **B.** Monomeric M protein simulation after 3 μs , shown side on with and without phospholipid bilayer heads.

B.2 Simulating heptameric M protein channels *in silico*

Oligomerisation of channels such as viroporins can result in multiple higher order structures forming. Previous work of HCV viroporin p7 displayed the capability of forming both hexameric and heptameric channels with the possibility of less favourable tetrameric and pentameric complexes additionally forming (Chandler et al., 2012). In light of this we additionally generated and simulated Heptameric M protein channels using the same protocol used in section 3.5 simulating Hexameric M protein channels.

B2.2 Helix 2 pore lining radial conformation

Heptameric channels with helix 2 pore-lining in the same radial conformation as mentioned in section 3.5.3.1 were simulated for 200 ns. Channels had a wider pore radius of 7.122 Å compared to the 3.2 Å pore radius of hexameric channels. Increasing the number of protomers forming these channels results in an increase in both pore size and interactions holding the channels together (Figure B.2.1). The residues lining the pore were LEU52, TRP51, ALA48, ALA45 and GLY41.

Analysis of simulations showed two of the channels remained open throughout the 200 ns with respective channel radius of 4.253 and 4.146 Å and the third began to close after 112 ns and fluctuated between open and closed for 28 ns before closing at 140 ns (Figure B.2.2).

However, protonation of the channels did not increase the duration they remained open, one channel closed after 25 ns, opening and closing twice before closing fully at 58 ns, the other channels remained open for 110 and 58 ns before closing fully. The protonated channels had an increased pore radius prior to simulation beginning with a radius of 7.43 Å, resulting in closure of all channels with end pore radii of 1.336, 0.940 and 1.823 Å respectively (Figure B.2.3).

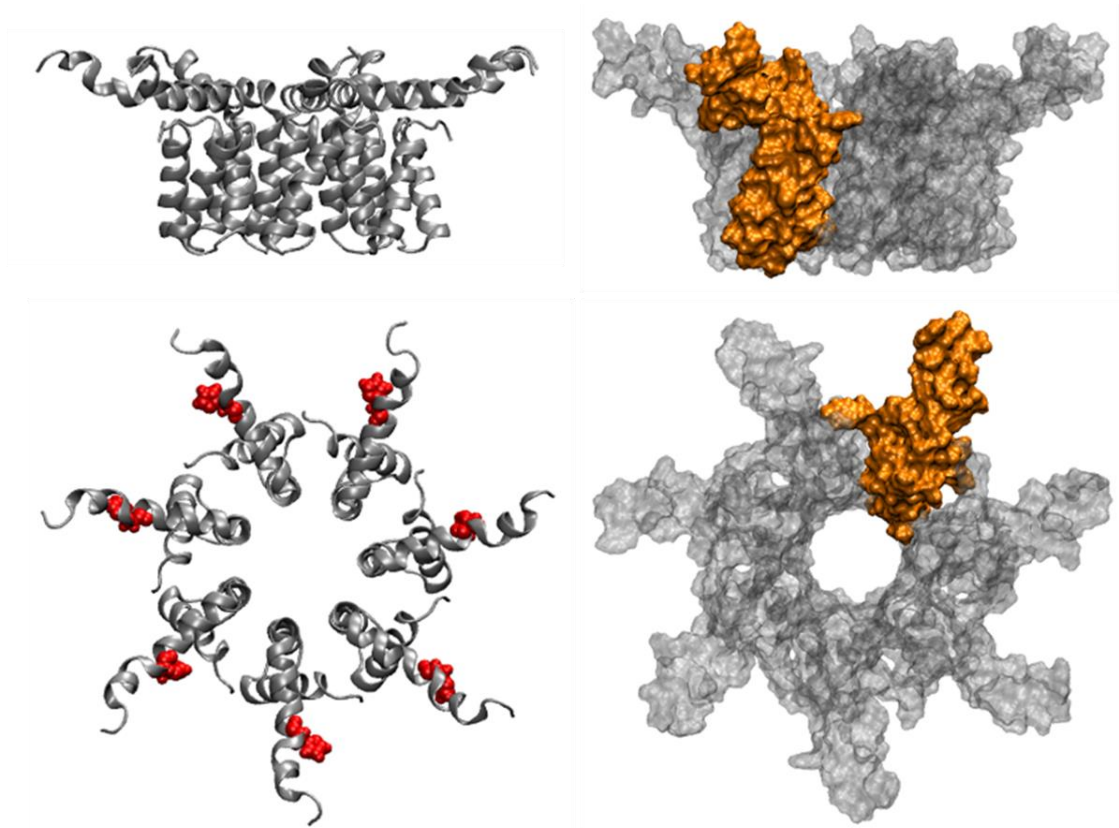


Figure B2.1 Heptameric Helix 2 pore-lining 'radial' channel starting conformations

A. Ribbon representation side on and from above with histidine residues highlighted in red. B. Surface representation side on and from above with one protomer highlighted in orange.

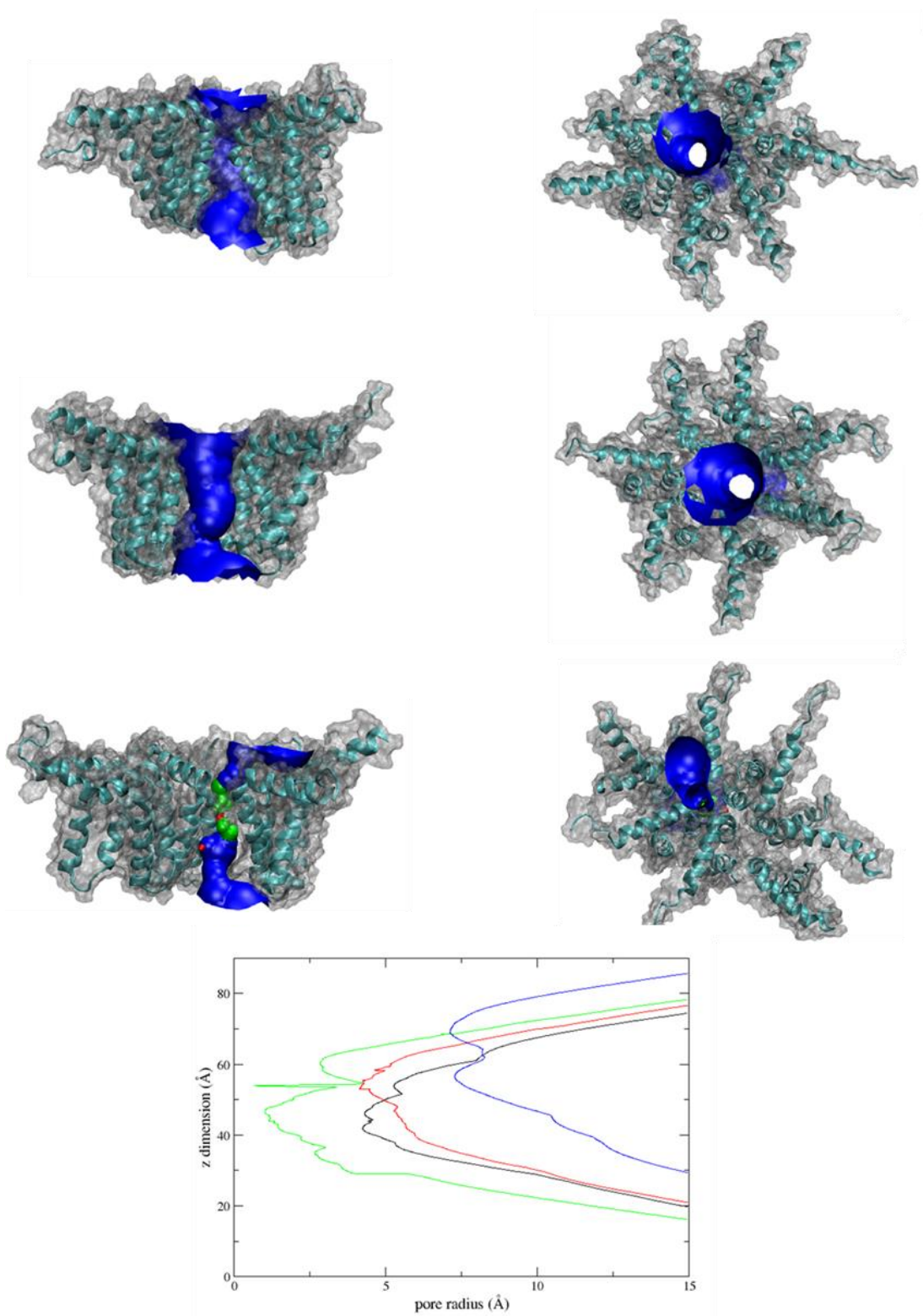


Figure B2.2 Heptameric Helix 2 pore-lining radial channel conformation after 200 ns simulation

A-C, Surface and Ribbon representation of simulations at 200ns from above and side (with one helix cut away) B. HOLE profile pore radius of simulations 1-3 and the starting conformation in black, red, green and blue respectively.

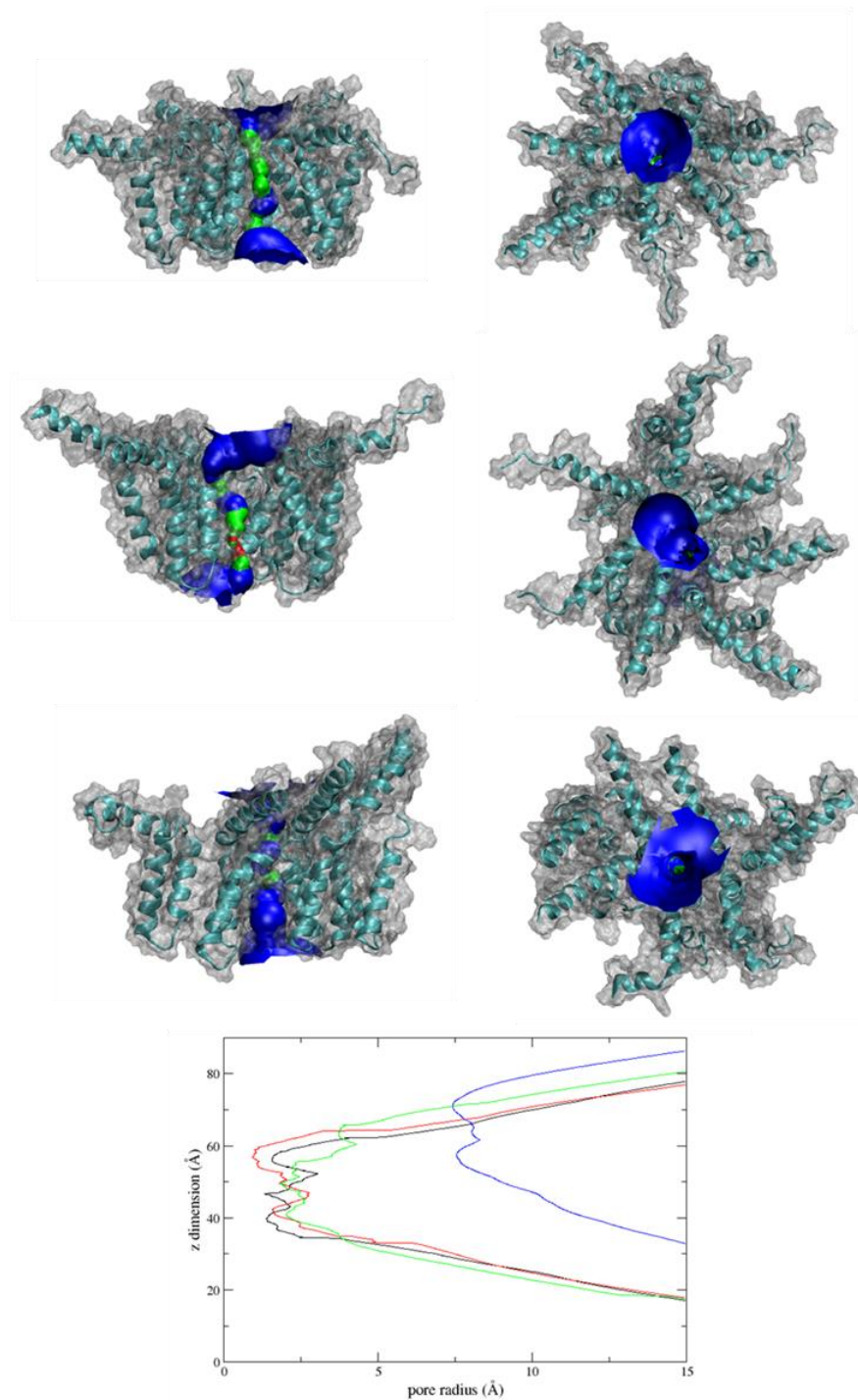


Figure B2.3 Heptameric Helix 2 pore-lining 'radial' protonated channel conformation after 200 ns simulation

A-C, Surface and Ribbon representation of simulations at 200ns from above and side (with one helix cut away) B. HOLE profile pore radius of simulations 1-3 and the starting conformation in black, red, green and blue respectively.

B2.3 Helix 2 pore lining compact conformation

The compact Helix 2 pore lining heptamer structure has a pore radius of 6.815 Å (Figure B2.4) at the start of the simulations with LEU52, ILE49, ALA48, ALA45, PHE42 and GLY41 lining the pore.

Over the 200 ns simulations two of the neutral pH channels remain open for over 200 ns and the remaining channel closed with a final pore radii of 2.85, 1.827 and 0.994 Å (Figure B2.5). After protonation the channel has an increased pore radius of 6.88 Å and remain open for 40, 200 and 23 ns with respective pore radii of 0.81, 2.9 and 0.66 Å respectively (Figure B2.6).

B2.4 Helix 3 pore lining radial conformation

As previously, heptameric channel conformations were arranged comparably to the hexameric channel conformation. However, this resulted in the pore radius decreasing to 2.41 Å, due to the angles of the pore-lining helices, allowing for closer placement of protomers without overlapping (figure B2.7). The residues lining the pore were LYS60, TRP63, LEU64, ILE67 and LEU68.

Despite the much smaller pore of the channel all three repeat simulations remained open for the 200 ns with respective pore radii of 4.64, 1.34 and 2.5 Å (Figure B2.8). Upon histidine protonation the simulations the starting pore radius was 2.35 and channels remained open for 195, 192 and 200 ns with pore radii of 0.46, 0.5 and 4.04 Å respectively (Figure B2.9)

B2.5 Helix 3 pore lining compact conformation

The rotated conformation of the Helix 3 pore lining channel is more compact in comparison to the radial conformation, resulting in increased interactions between protomers, particularly increasing the interactions between the N-terminal helices which are no longer as flexible, due to their proximity to the neighbouring protomer. The starting conformation of the channel exhibits a pore radius of 7.012 Å allowing many water molecules to fill the lumen with THR57, LYS60, VAL61, VAL65, LEU68, LEU69, PRO72 and ALA73 lining the pore (Figure B2.10).

After 200 ns of simulation two channels remained open with a water column and pore radii of 3.8 Å and 3.78 Å, however one channel did close after 75 ns resulting in a final pore radius of just 0.16 Å (Figure B2.11).

After protonation of the Helix 3 pore lining rotated channel the simulations started with a pore radius of 7.0 Å. Once more two of the three channels remained open with radii of 2.5 Å and 5.8 Å, and the remaining channel closed after 90 ns of simulation resulting in a pore radius of 0.8 Å (Figure B.12).

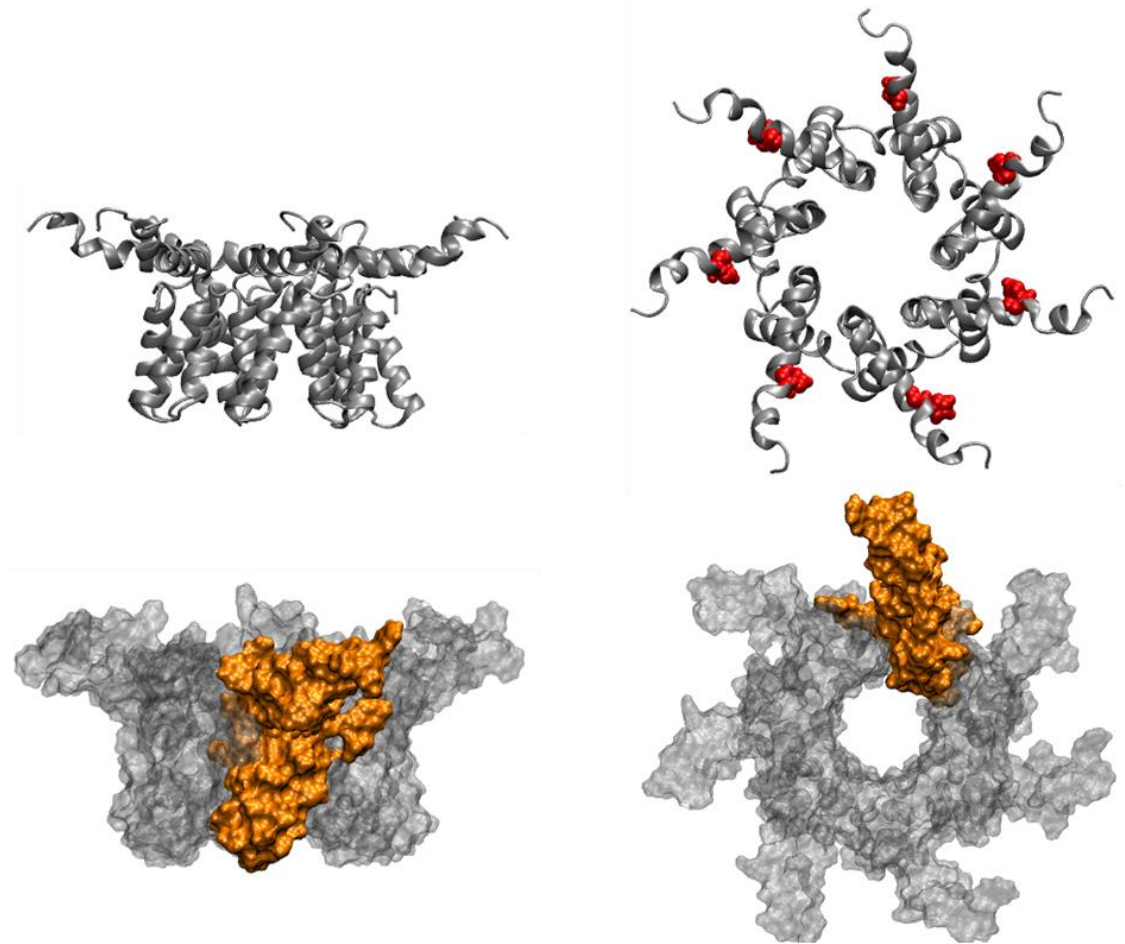


Figure B2.4 Heptameric Helix 2 pore-lining 'compact' channel starting conformations

A. Ribbon representation side on and from above with histidine residues highlighted in red. B. Surface representation side on and from above with one protomer highlighted in orange.

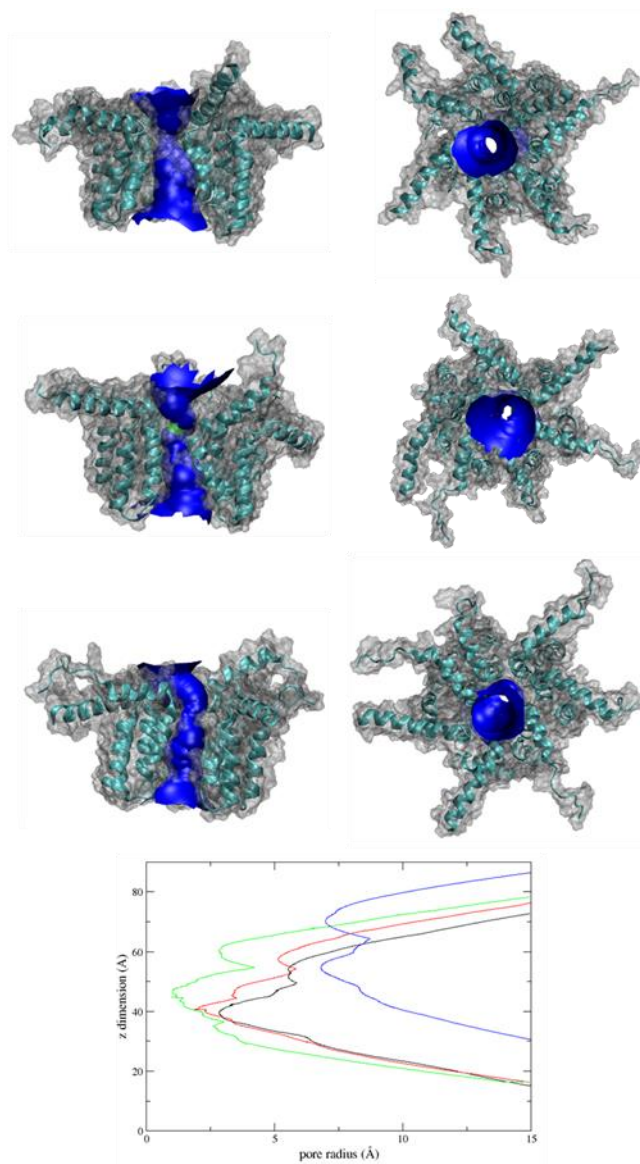


Figure B2.5 Heptameric Helix 2 pore-lining 'compact' channel conformation after 200 ns simulation

A-C, Surface and Ribbon representation of simulations at 200ns from above and side (with one helix cut away) B. HOLE profile pore radius of simulations 1-3 and the starting conformation in black, red, green and blue respectively.

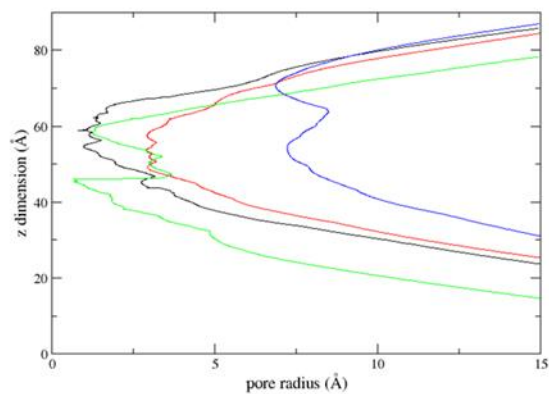
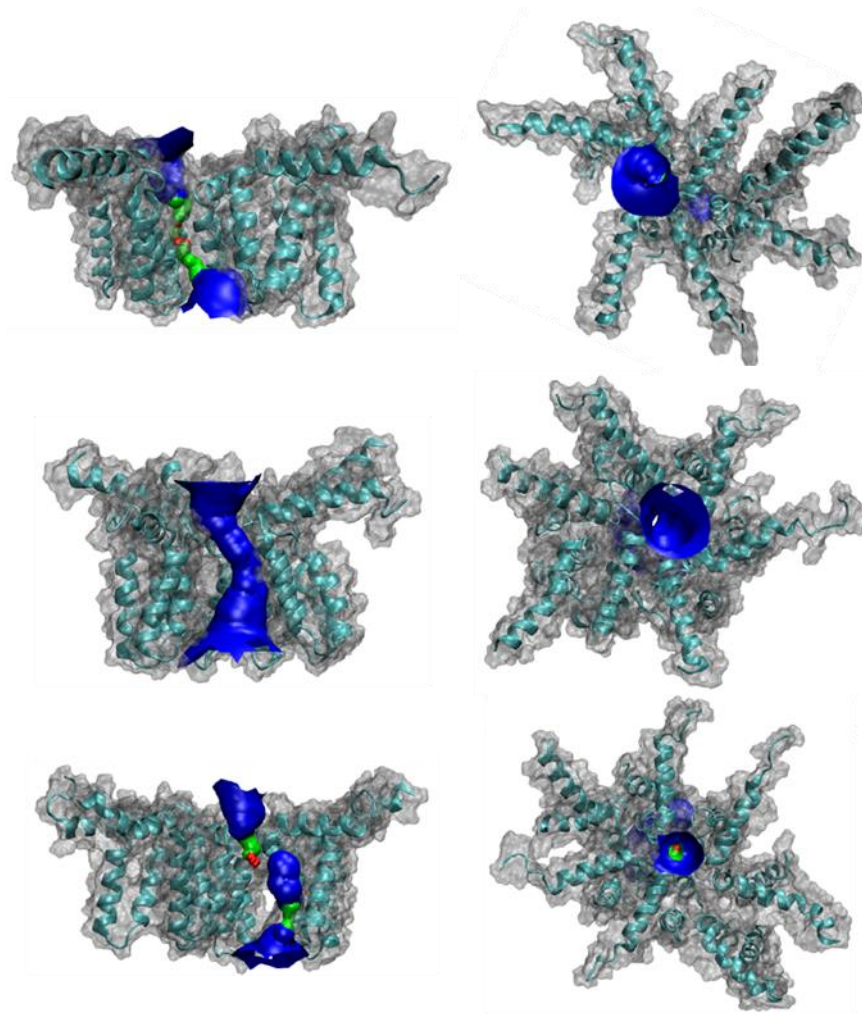


Figure B2.6 Heptameric Helix 2 pore-lining ‘compact’ protonated channel conformation after 200 ns simulation

A-C, Surface and Ribbon representation of simulations at 200ns from above and side (with one helix cut away) B. HOLE profile pore radius of simulations 1-3 and the starting conformation in black, red, green and blue respectively.

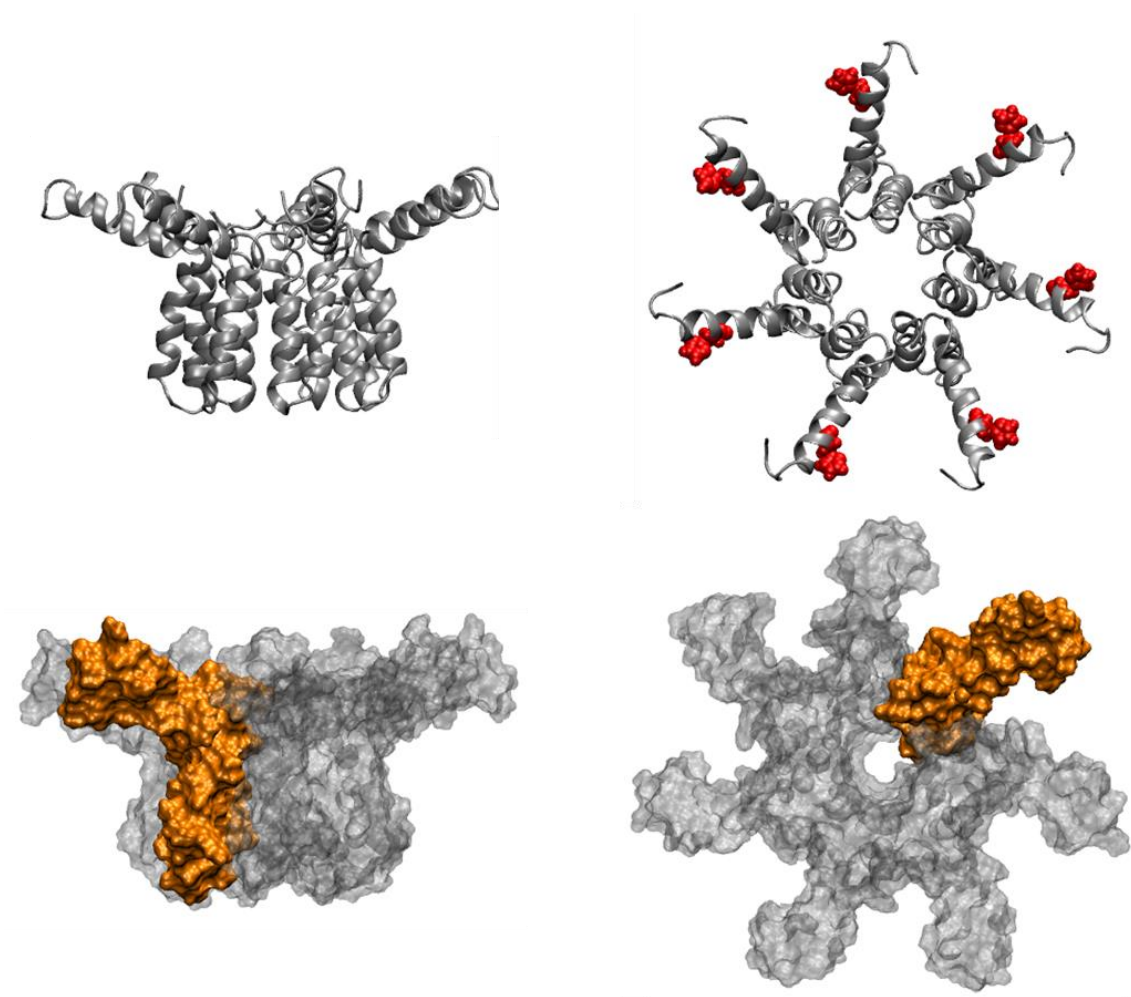


Figure B2.7 Heptameric Helix 3 pore-lining 'radial' channel starting conformations

A. Ribbon representation side on and from above with histidine residues highlighted in red. B. Surface representation side on and from above with one protomer highlighted in orange.

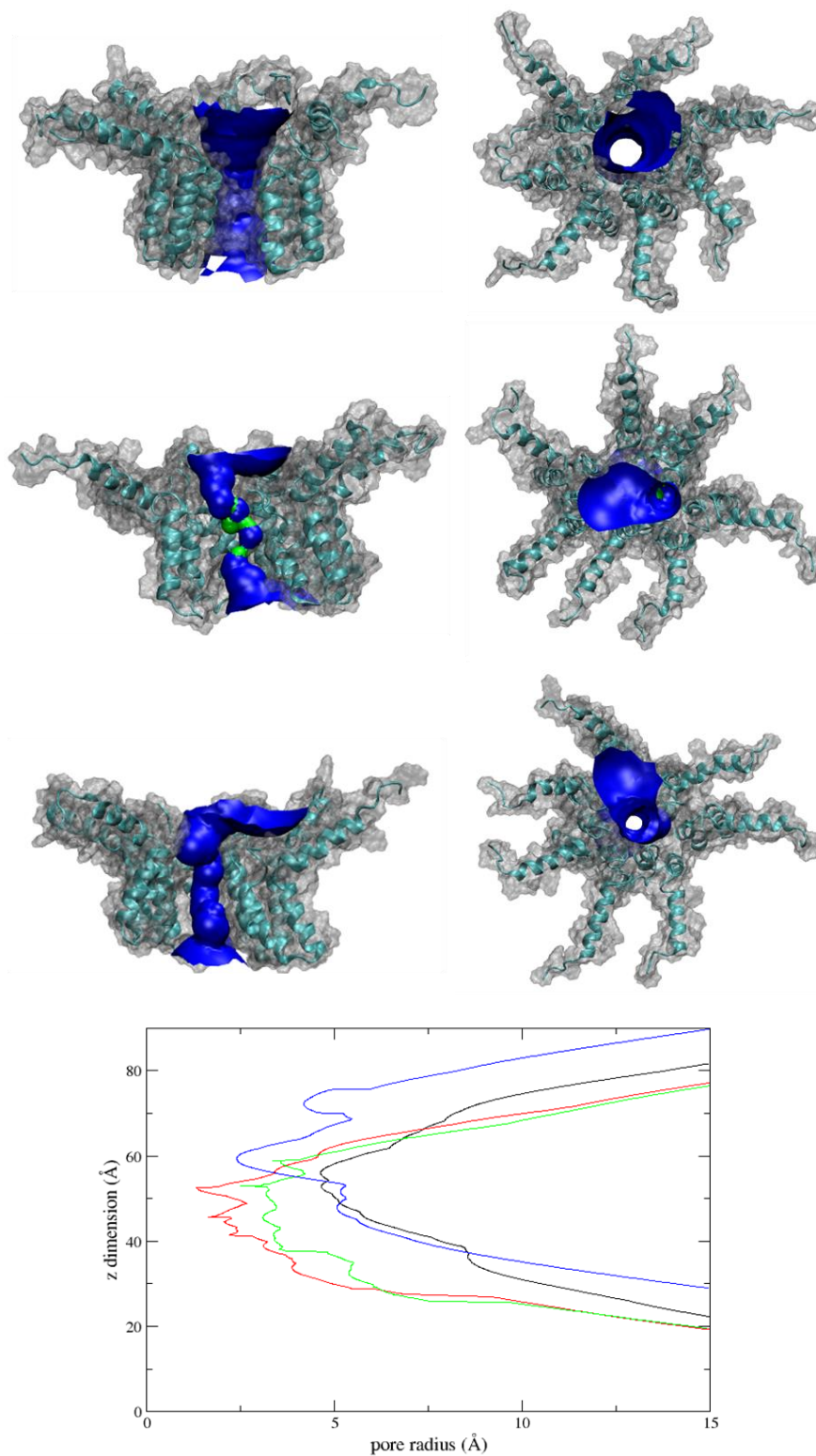


Figure B2.8 Heptameric Helix 3 pore-lining 'radial' channel conformation after 200 ns simulation

A-C, Surface and Ribbon representation of simulations at 200ns from above and side (with one helix cut away) B. HOLE profile pore radius of simulations 1-3 and the starting conformation in black, red, green and blue respectively

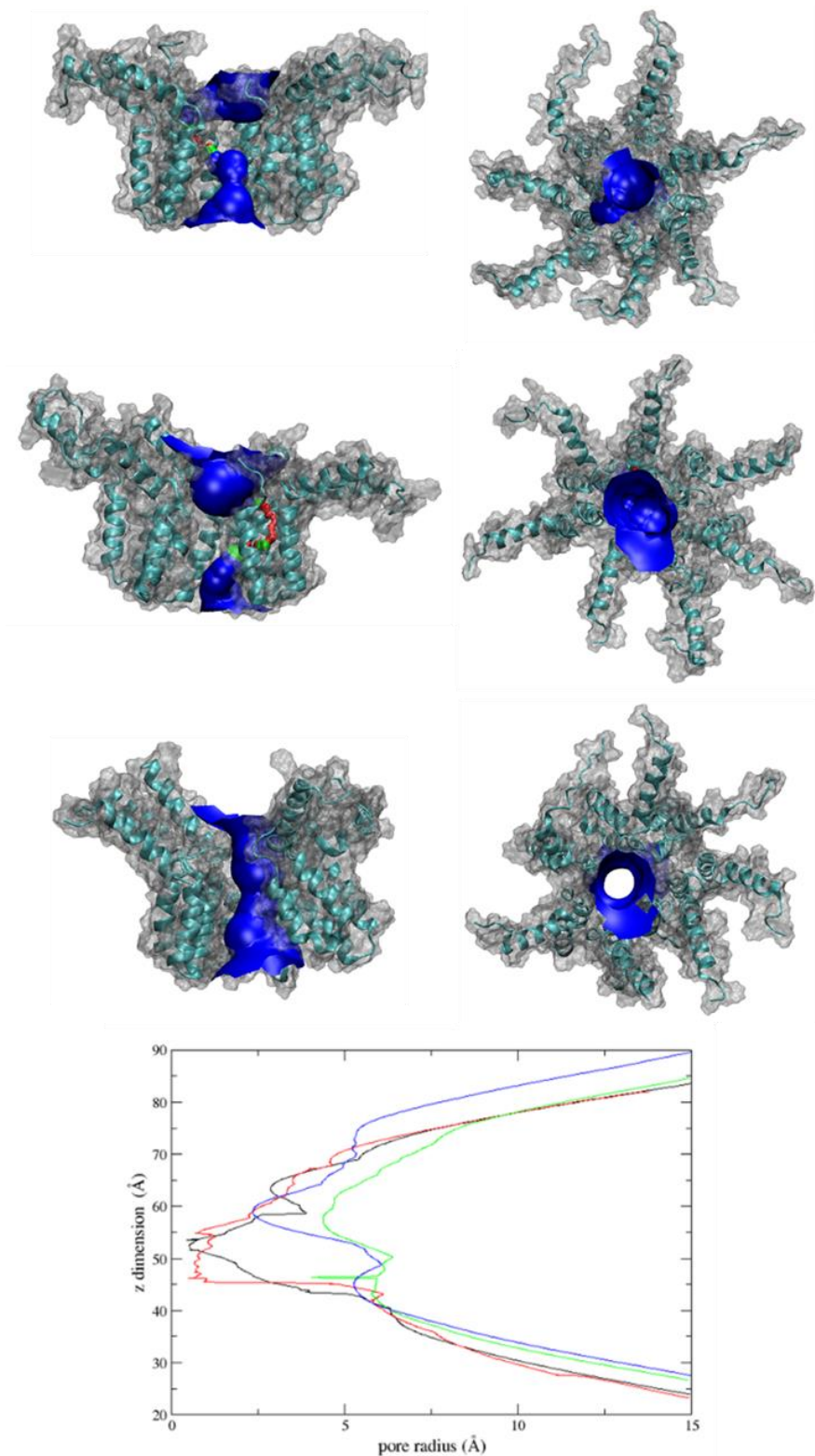


Figure B2.9 Heptameric Helix 3 pore-lining 'radial' protonated channel conformation after 200 ns simulation

A-C, Surface and Ribbon representation of simulations at 200ns from above and side (with one helix cut away) B. HOLE profile pore radius of simulations 1-3 and the starting conformation in black, red, green and blue respectively. C. RMSD of simulations in corresponding colours to B

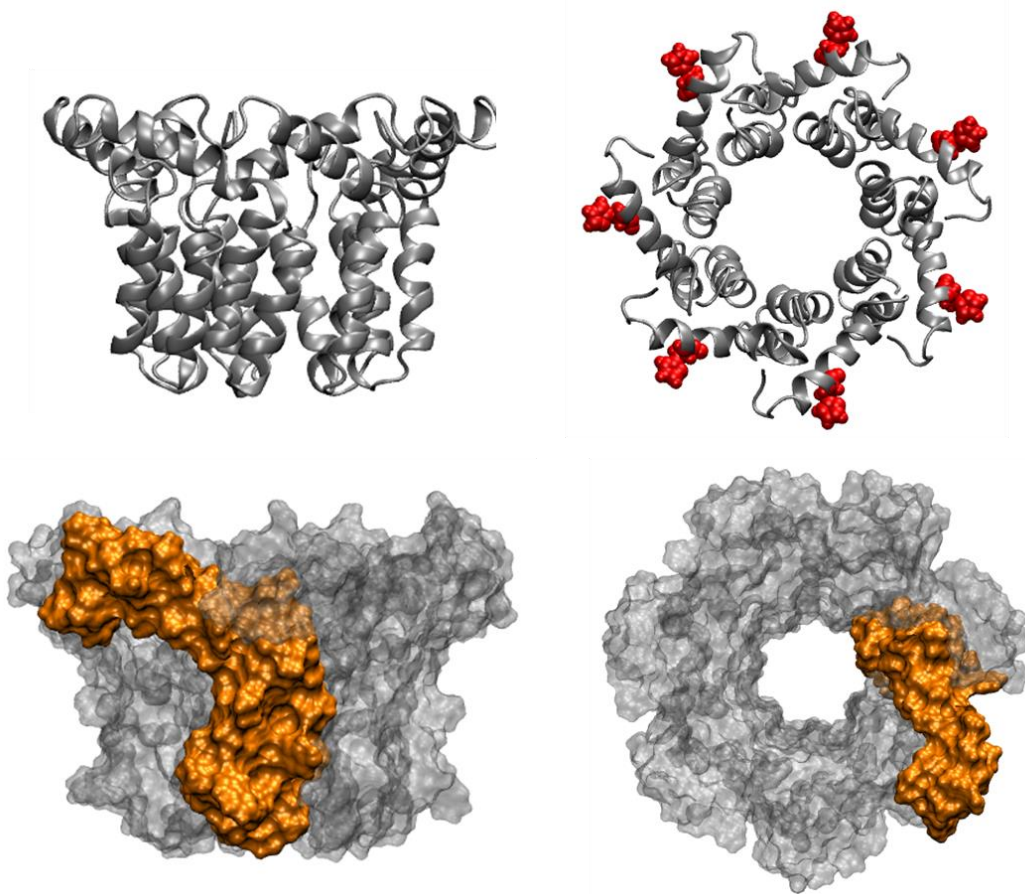


Figure B2.10 Heptameric Helix 3 pore-lining 'compact' channel starting conformations

A. Ribbon representation side on and from above with histidine residues highlighted in red. B. Surface representation side on and from above with one protomer highlighted in orange

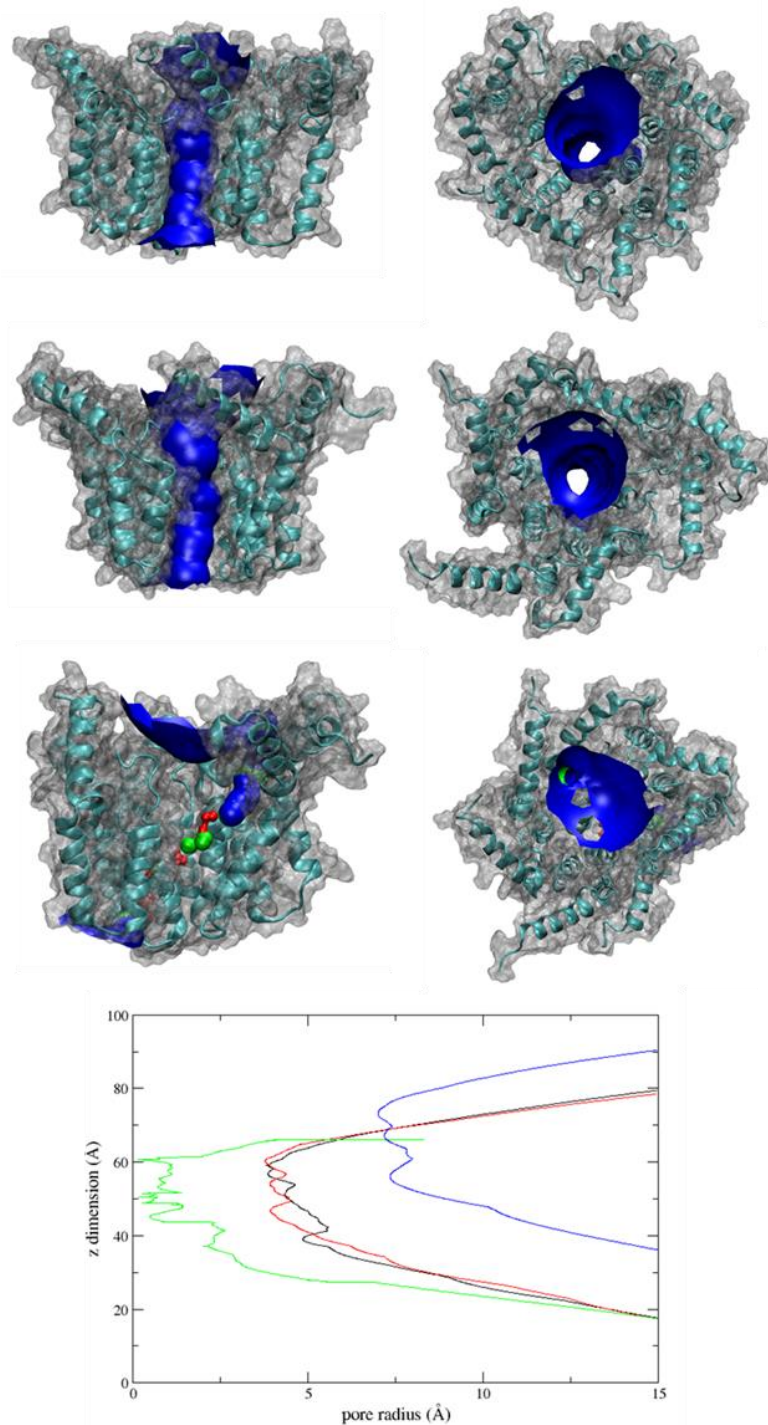


Figure B2.11 Heptameric Helix 3 pore-lining 'compact' channel conformation after 200 ns simulation

A-C, Surface and Ribbon representation of simulations at 200ns from above and side (with one helix cut away) B. HOLE profile pore radius of simulations 1-3 and the starting conformation in black, red, green and blue respectively.

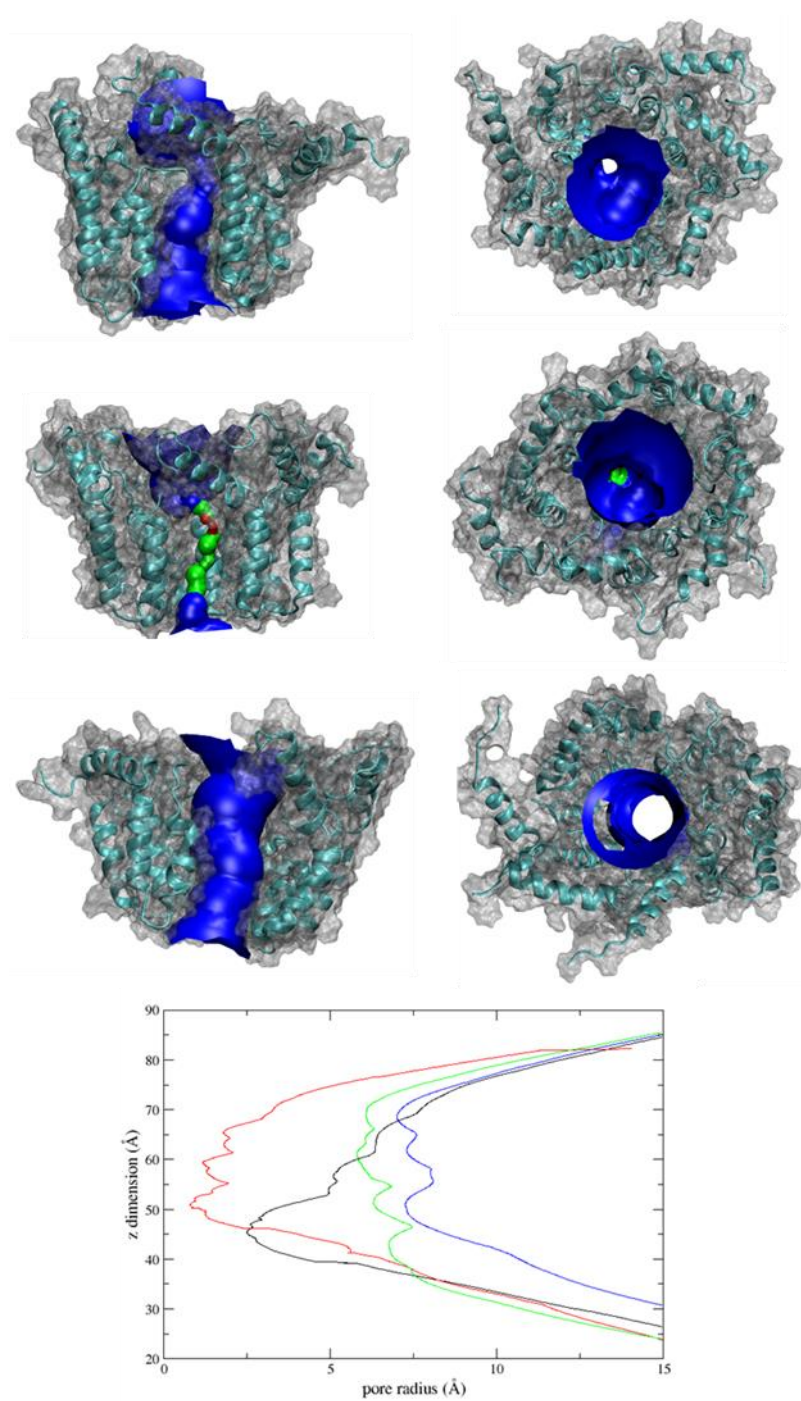


Figure B2.12 Heptameric Helix 3 pore-lining 'compact' protonated channel conformation after 200 ns simulation

A-C, Surface and Ribbon representation of simulations at 200ns from above and side (with one helix cut away) B. HOLE profile pore radius of simulations 1-3 and the starting conformation in black, red, green and blue respectively.